TREE-NUREG-1074
for U.S. Nuclear Regulatory Commission

IRRADIATION EFFECTS TEST SERIES
TEST IE-2
TEST RESULTS REPORT

C. M. ALLISON D. W. CROUCHER
S. A. PLOGER A. S. MEHNER

August 1977

EG&G Idaho, Inc.

IDAHO NATIONAL ENGINEERING LABORATORY

ENERGY RESEARCH AND DEVELOPMENT ADMINISTRATION

IDAHO OPERATIONS OFFICE UNDER CONTRACT EY-76-C-07-1570

DISCLAIMER

Printed in the United States of America
Available from
National Technical Information Service
U.S. Department of Commerce
5285 Port Royal Road
Springfield, Virginia 22161
Price: Printed Copy ~~$7.75~~ 9.00 Microfiche $3.00

"The NRC will make available data tapes and operational computer codes on research programs dealing with postulated loss-of-coolant accidents in light water reactors. Persons requesting this information must reimburse the NRC contractors for their expenses in preparing copies of the data tapes and the operational computer codes. Requests should be submitted to the Research Applications Branch, Office of Nuclear Regulatory Research, Nuclear Regulatory Commission, Washington, D.C. 20555."

TREE-NUREG-1074
IRRADIATION EFFECTS TEST SERIES
TEST IE-2
TEST RESULTS REPORT

Approved:

W. J. Quapp, Manager
Experiments Specification and Analysis Branch

J. G. Crocker, Manager
Thermal Fuels Behavior Program

J. O. Zane, Manager
Thermal Fuels Behavior Program

L. J. Ybarrondo, Director
Water Reactor Research Directorate

TREE-NUREG-1074

Distributed Under Category:
NRC-3
Water Reactor Safety Research
Fuel Behavior

IRRADIATION EFFECTS TEST SERIES

TEST IE-2

TEST RESULTS REPORT

By:

C. M. Allison
D. W. Croucher
A. S. Mehner
S. A. Ploger

EG&G IDAHO, INC.

Date Published - August 1977

PREPARED FOR THE

U.S. NUCLEAR REGULATORY COMMISSION

AND

ENERGY RESEARCH AND DEVELOPMENT ADMINISTRATION

IDAHO OPERATIONS OFFICE

UNDER CONTRACT NO. EY-76-C-07-1570

ABSTRACT

This report describes the results of the fourth test, Test IE-2, conducted by the Thermal Fuels Behavior Program of the Water Reactor Research Program of EG&G Idaho, Inc. The research is sponsored by the Nuclear Regulatory Commission and is part of the NRC's Irradiation Effects Test Series. This test used four, 0.97-m long, PWR-type fuel rods with differences in diametral gap and cladding irradiation. The objective of this test was to provide information about the effects of these differences on fuel rod behavior during quasi-equilibrium and film boiling operation.

The fuel rods were subjected to a series of preconditioning power cycles of less than 30 kW/m. Rod powers were then increased to 68 kW/m at a coolant mass flux of 4900 kg/s-m^2. After one hour at 68 kW/m, a power-cooling-mismatch sequence was initiated by a flow reduction at constant power. At a flow of 2550 kg/s-m^2, the onset of film boiling occurred on one rod, Rod IE-011. An additional flow reduction to 2245 kg/s-m^2 caused the onset of film boiling on the remaining three rods.

Data are presented on the behavior of fuel rods during quasi-equilibrium and during film boiling operation. The effects of initial gap size, cladding irradiation, rod power cycling, a rapid power increase, and sustained film boiling are discussed. These discussions are based on measured test data, preliminary postirradiation examination results, and comparisons of results with FRAP-T3 computer model calculations.

SUMMARY

This report describes the results of the fourth test, Test IE-2, in the Irradiation Effects Test Series, which is part of the Thermal Fuels Behavior Program being conducted at the Idaho National Engineering Laboratory by EG&G Idaho, Inc., to define the behavior of fuel rods during transient operating conditions. Research is being sponsored by the Fuel Behavior Program of the Nuclear Regulatory Commission. The objective of this test was to provide information about the effects of diametral gap and cladding irradiation on fuel rod behavior during quasi-equilibrium and film boiling operation.

Test IE-2 was conducted in October, 1976, in the Power Burst Facility (PBF) reactor at the Idaho National Engineering Laboratory. Four rods designated IE-011, IE-012, IE-013, and IE-014 were used. Rods IE-011 and IE-012 were fabricated from irradiated zircaloy-4 cladding, and Rods IE-013 and IE-014 were assembled from unirradiated zircaloy-4 cladding. All rods contained fresh fuel. The fuel pellet diameters were ground so that Rods IE-011 and IE-013 had small diametral gaps (0.10 mm) and Rods IE-012 and IE-014 had large diametral gaps (0.34 mm). The fuel rod upper end caps contained a pressure transducer. The rods were repressurized with an argon and helium gas mixture which had a thermal conductivity similar to fission gases extracted from similar Saxton fuel rods.

The four rods were mounted in the PBF in-pile tube which is connected to an external loop capable of providing PWR coolant conditions. Each of the rods was surrounded by a separate flow shroud so that they were hydraulically and thermally isolated from one another. The rods and the shroud assembly were instrumented to monitor fuel rod behavior and coolant conditions.

The first part of the test consisted of about thirty-seven hours of preconditioning at various peak rod powers not exceeding 30 kW/m. This period was followed by a power ramp to 68 kW/m at a ramp rate of 3 kW/m per minute. The rods were held at 68 kW/m for one hour and then were

subjected to a power-cooling-mismatch sequence initiated by a flow reduction to induce film boiling. At a coolant flow of 2550 kg/s-m^2, the onset of film boiling occurred on Rod IE-011. During a further flow reduction to 2245 kg/s-m^2, film boiling was indicated on the remaining rods. After one minute of film boiling on Rod IE-011, the reactor was rapidly shut down. Rod failure was not indicated by test instruments or found during the posttest examination.

The effects of the differences in gap sizes were readily apparent from both the experimental measurements and visual posttest examination. Measurements indicated that the rods with the small initial gaps (Rods IE-011 and IE-013) exhibited larger axial strains, lower internal pressures, and lower centerline temperatures than did the other rods during both the pre-film boiling and film boiling phases. Visual posttest examination revealed the collapse (radial) strain for Rods IE-011 and IE-013 was less than that for Rods IE-012 and IE-014. FRAP-T3 calculations also exhibited these effects.

The effects of cladding irradiation upon fuel rod behavior were minimal. Irradiation essentially affects only the mechanical properties of the cladding, so that no distinguishable variations in rod internal pressures, fuel centerline and cladding surface temperatures were expected or observed. "In-service" related differences between the previously irradiated and unirradiated cladding apparently resulted in a slight variation in the length of the film boiling zone. The effect of mechanical property changes, namely an increase in yield-point due to irradiation, was expected to cause a difference in cladding elongation but a difference could not be clearly identified. During the power cycles, no plastic deformation was observed. Evidence of any plastic deformation during the rapid power ramp was marked by fuel creep during and following the ramp and the subsequent film boiling operation.

CONTENTS

FIGURES

TABLES

1. INTRODUCTION

This document describes the results of the Irradiation Effects Test 2 (Test IE-2), the fourth test in the Irradiation Effects (IE) Test Series. The tests are being conducted at the Idaho National Engineering Laboratory under the Thermal Fuels Behavior Program by EG&G Idaho, Inc. This test series, part of the Nuclear Regulatory Commission's Fuel Behavior Program[1], is designed to study the behavior of irradiated and unirradiated fuel rods under abnormal reactor conditions. The results of these tests will be used in the development of verified analytical models for predicting the behavior of irradiated fuel rods. A more comprehensive discussion of the scope and objectives of this test series is given in the Irradiation Effects Experiment Requirements Document[2].

The objective of Test IE-2 was to provide information on fuel rods with differences in diametral gap size and cladding irradiation. The data include (a) steady-state data at various fuel rod power levels, (b) data on pellet-cladding mechanical interaction (PCI) during transient operating conditions, and (c) data for post-DNB fuel rod behavior at high power (approximately 68 kW/m peak).

Four PWR-type fuel rods were mounted in the in-pile tube in the Power Burst Facility (PBF) reactor. These rods, contained in individual cylindrical flow shrouds, were tested simultaneously under the same nominal operating conditions. The fuel rods and shroud assembly were instrumented to monitor fuel rod behavior and coolant conditions. A complete description of the fuel rods and test train is contained in Section 2.

The test consisted of a series of preconditioning power cycles followed by a rapid power ramp, high power steady-state period, and a power-cooling-mismatch (PCM) sequence initiated by a flow reduction to produce film boiling while at high power. A piggyback gap conductance test, which used a sinusoidal variation of reactor power to produce gap conductance data, was run early in the preconditioning period. The results from this piggyback test are presented in a separate report[3].

The description of the test conduct and the experimental results are contained in Sections 3 and 4.

The results of the visual postirradiation examination (PIE) are presented in Section 5. The balance of the PIE results will be reported separately, following completion of the examinations.

Section 6 contains an evaluation and a comparison of the calculated and experimental fuel rod behavior data.

Conclusions and a discussion of the test results and the comparisons made in Section 6 are provided in Section 7.

In Appendix A, an assessment of the instrumentation and data system errors is presented. The fuel rod characterization data are given in Appendix B. A description of the data reduction process and additional test data not presented in the main body of the text are given in Appendix C. The results of a detailed power calibration are presented in Appendix D.

2. EXPERIMENT DESCRIPTION

The PBF consists of an open-tank reactor vessel, a driver core region with an active length of 0.91 meter, a central flux trap region containing an in-pile tube (IPT), and a loop coolant system to provide the typical pressurized water reactor system conditions. The re-entrant IPT, which encloses the test space, has inlet and outlet connections for loop coolant flow located at its upper end above the driver core. The coolant flow enters the top of the IPT and is directed downward on the outside of a flow tube which surrounds the test assembly. At the bottom of the IPT, the coolant flow reverses direction and flows up through the test assembly and out the IPT outlet.

The four fuel rods tested in Test IE-2 were positioned vertically in the IPT. A separate flow shroud surrounded each fuel rod. Hence, the fuel rods were hydraulically and thermally isolated from interacting with one another, essentially allowing four single fuel rod tests to be conducted simultaneously.

Each fuel rod and flow shroud assembly was instrumented to monitor fuel rod behavior during nuclear operations. The fuel rods, test train, flow shroud, and associated instrumentation are described in this section.

2.1 Fuel Rods

The four fuel rods were designated Rods IE-011, IE-012, IE-013, and IE-014. Rods IE-011 and IE-012 were remotely fabricated from irradiated zircaloy-4 cladding, and Rods IE-013 and IE-014 were assembled from unirradiated zircaloy-4 cladding. All rods contained fresh 12.5 wt% $^{235}UO_2$ dished fuel pellets. The fuel rods were approximately 0.97-m long (not including the instrumented end cap) and had a nominal active fuel stack length of 0.884 m. A summary of selected information describing the fuel rods is contained in Table I. Complete cladding and fuel pellet characterization data for each fuel rod are given in Appendix B.

TABLE I

DESIGN AND TEST PARAMETERS FOR FUEL RODS USED IN TEST IE-2

Parameter	Rod			
	IE-011	IE-012	IE-013	IE-014
Rod Identification	M-15	M-19	925	929
Cladding Fluence (10^{20} n/cm^2)	4.7	5.2	0	0
Cladding Length (m)	0.97	0.97	0.97	0.97
Mean Cladding OD (mm)	9.997	9.967	9.925	9.939
Mean Cladding Thickness (mm)	0.630	0.617	0.592	0.600
Mean Diametral Gap (mm)	0.102	0.343	0.100	0.343
Measured Void Volume (ml)	6.6	9.2	7.7	10.2
Fill Gas Composition/Pressure (MPa) (at time of assembly)	76% He-24% Ar/2.51	76% He-24% Ar/2.50	76% He-24% Ar/2.69	76% He-24% Ar/2.67

2.1.1 Fuel Rods with Previously Irradiated Cladding. Rods IE-011 and IE-012 were remotely fabricated from MAPI[a] Rods, M-15 and M-19, irradiated in the Saxton reactor[b] to approximate burnups of 5110 and 5610 MWd/tU, respectively[4]. The cladding from these rods received neutron fluences at energies greater than 1 MeV of 4.7 and 5.2 x 10^{20} neutrons/cm^2, respectively[4]. The irradiated fuel within the rods was removed and replaced with unirradiated 12.5 wt% $^{235}UO_2$. The measured cladding outer diameter (OD) near the central region of the irradiated cladding was a maximum of 0.04 mm smaller than the nominal cladding OD of the unirradiated cladding. This small dimensional change was probably due to creep experienced during irradiation in the Saxton reactor.

The OD of the fuel pellets was ground to produce nominal diametral fuel-cladding gaps of 0.102 mm and 0.343 mm in Rods IE-011 and IE-012, respectively. One fuel pellet having an outside diameter of 8.11 mm, approximately 0.3-mm smaller than all other fuel pellets, was loaded into Rod IE-012 at the 0.58-m elevation[c]. Fuel pellets at the top of the stack were drilled to accommodate a centerline thermocouple. The upper end caps of the two rods were replaced with end caps containing a pressure transducer. A gas mixture of 76% helium and 24% argon was used to backfill the rods to a pressure of 2.5 MPa. This gas composition simulates the thermal conductivity of the gases in the irradiated Saxton fuel rods[2].

2.1.2 Fuel Rods with Unirradiated Cladding. Rods IE-013 and IE-014 were fabricated from cladding from unirradiated Saxton Rods 925 and 929 and from fresh 12.5 wt% $^{235}UO_2$ fuel. The fuel pellet diameters were ground to produce diametral fuel-cladding gaps of 0.100 mm in Rod IE-013 and 0.343 mm in Rod IE-014. The nominal wall thickness of the unirradiated cladding was 0.596 mm, approximately 5% thinner than the

---

[a] Mitsubishi Atomic Power Industries of Japan.

[b] The Saxton Reactor was designed by Westinghouse Electric Corporation for the USAEC. The reactor was a small, prototypic, pressurized water reactor.

[c] The smaller pellet was inadvertently loaded and could not be removed without severe schedular impact.

irradiated cladding of Rods IE-011 and IE-012. Pellets at the top of the fuel stack were drilled to accommodate an ultrasonic thermometer (UT) at the fuel centerline of both rods. The rods were fitted with upper end caps containing a pressure transducer. These rods were also backfilled with a 76% helium/24% argon gas mixture, but to approximately 2.7 MPa.

2.2 Test Train

The test train hardware symmetrically positions the four fuel rods in the PBF IPT as shown in Figure 1. A fuel rod mounted in a flow shroud with a full complement of instruments is depicted in Figure 2. A cross sectional view of the test train assembly presented in Figure 3 shows the relative location of each flow shroud and the self-powered neutron detector (SPND) support tubes. Figure 4 shows the relative positioning of the SPNDs in the test assembly.

2.3 Flow Shroud

The flow shrouds were fabricated from zircaloy-4. Each flow shroud had a nominal inside diameter of 16.31 mm and a wall thickness of 3.15 mm. The outside diameter of each fuel rod was nominally 9.96 mm. Resultant hydraulic and heated equivalent diameters were 6.35 and 16.75 mm, respectively. The four flow shrouds were positioned in the in-pile tube as shown in Figure 1.

2.4 Instrumentation

Instrumentation was provided to monitor fuel rod behavior and coolant conditions in each flow shroud during the test. A listing of the transducer calibrations and error analyses for the test instruments is given in Appendix A. The test instrumentation is divided into two classifications: test train instrumentation and fuel rod instrumentation.

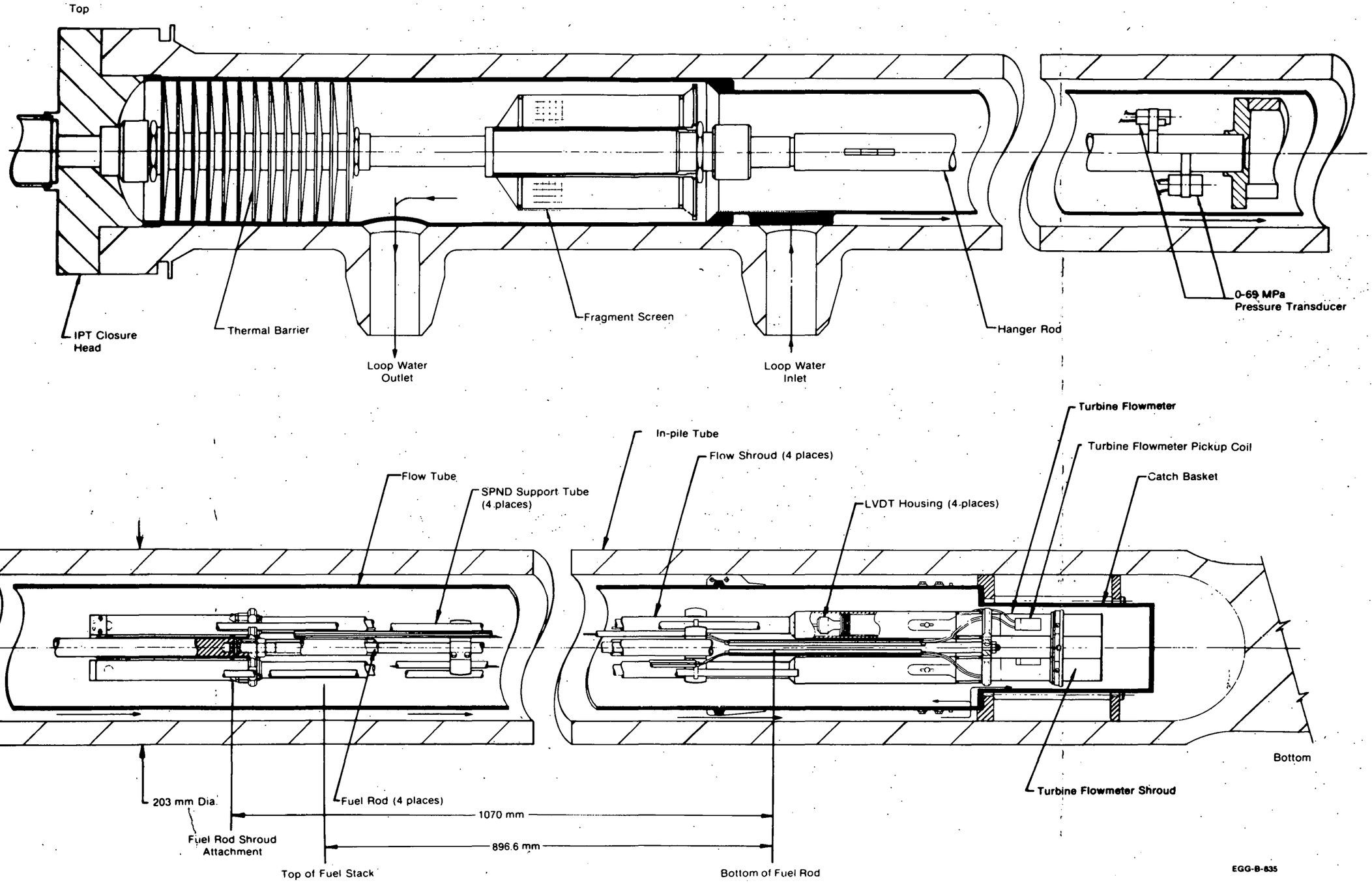

Fig. 1 Test IE-2 four rod experiment assembly and instrumentation shown installed in the PBF in-pile tube.

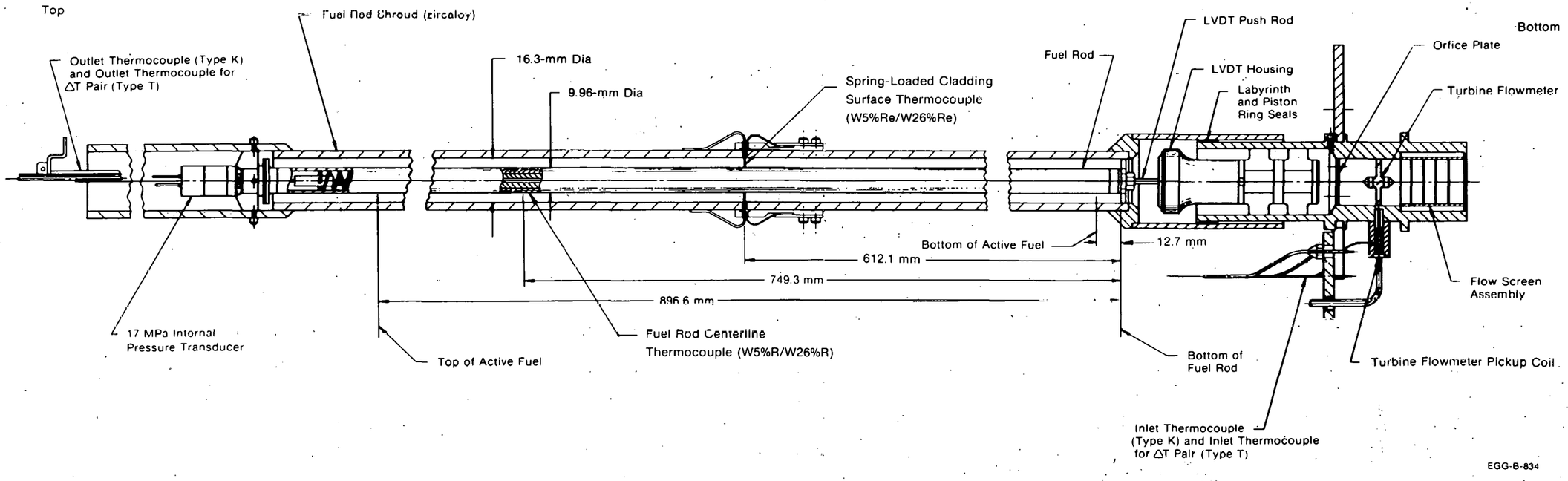

Fig. 2 Typical instrumented fuel rod for Test IE-2, shown installed in a flow shroud.

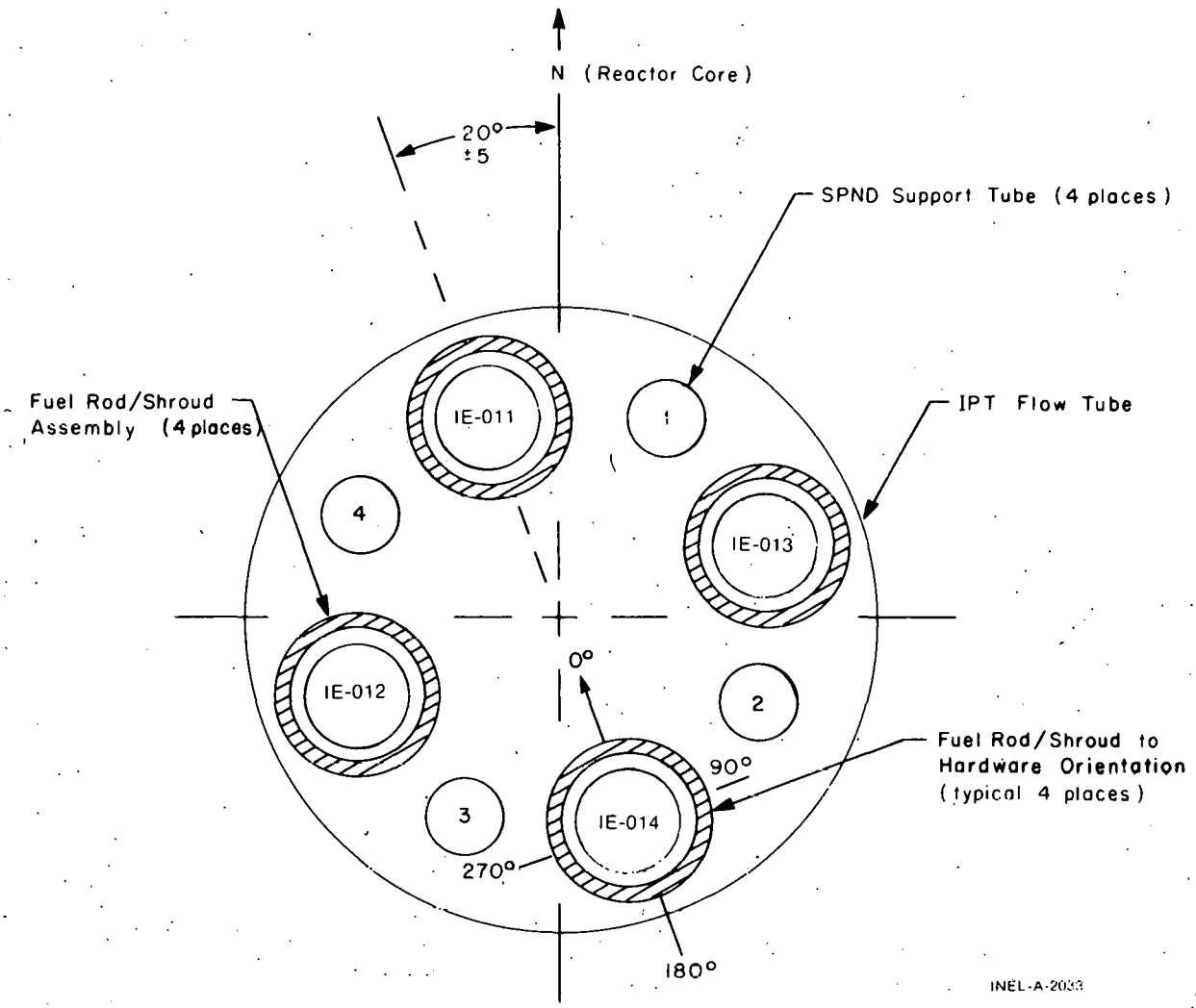

Fig. 3 Top view of Test IE-2 hardware orientation in the PBF in-pile tube. The zero degree position for each flow shroud is toward the center of the test assembly.

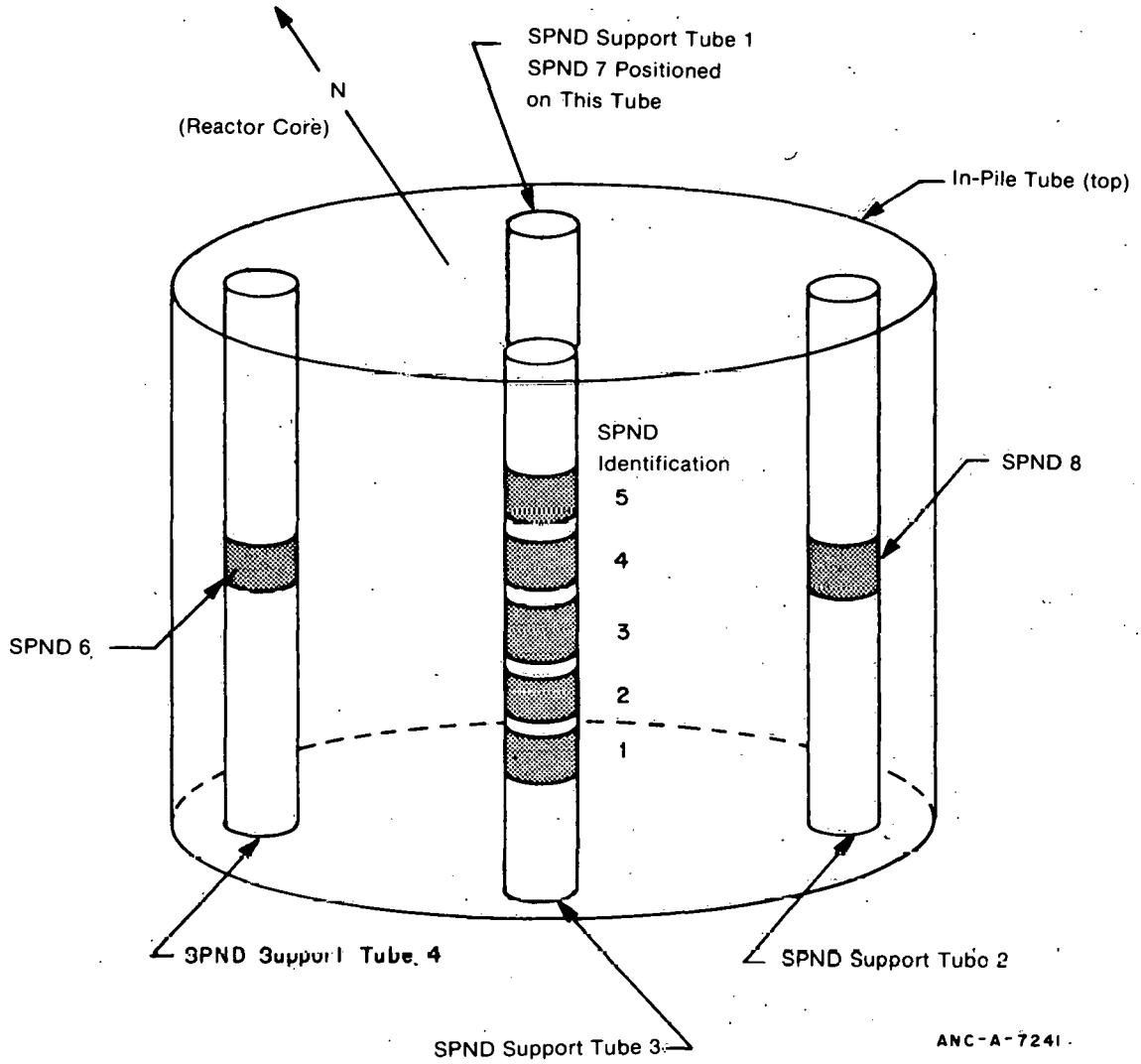

Fig. 4 Schematic orientation of IE-2 self-powered neutron detectors (SPND).

2.4.1 Test Train Instrumentation. The test train instrumentation consisted of the following:

(1) Two 69-MPa strain post-type pressure transducers were used to measure the system coolant pressure during the test. Both were positioned on the test train above the fuel rod assembly as shown in Figure 1.

(2) A turbine flowmeter at each flow shroud inlet was used to measure coolant flow through the shroud. This component is shown in Figure 5.

(3) A calibrated copper-constantan (Type T) differential thermocouple pair was provided to measure coolant temperature rise through each flow shroud.

(4) Two magnesium oxide insulated, Chromel-Alumel (Type K) thermocouples were positioned near the inlet of the test train assembly to measure the coolant inlet temperature. The coolant outlet temperature of each flow shroud was monitored with a similar Chromel-Alumel (Type K) thermocouple.

(5) One linear variable differential transformer (LVDT) was positioned at the bottom of each fuel rod to measure changes in fuel rod cladding length as shown in Figure 5.

(6) Eight, 10-cm long, cobalt self-powered neutron detectors (SPNDs) were mounted on support tubes in the test train assembly as shown in Figure 6. The locations of these devices relative to the test train are shown in Figure 3. Five of the detectors were mounted on the test train with centers at 0.16, 0.31, 0.47, 0.63, and 0.78 m from the bottom of the active core. These devices were employed to measure the relative axial neutron flux in the in-pile tube during the test. Three additional SPNDs were mounted at the 0.63-m location to provide a relative measure of the azimuthal neutron flux distribution across the test train.

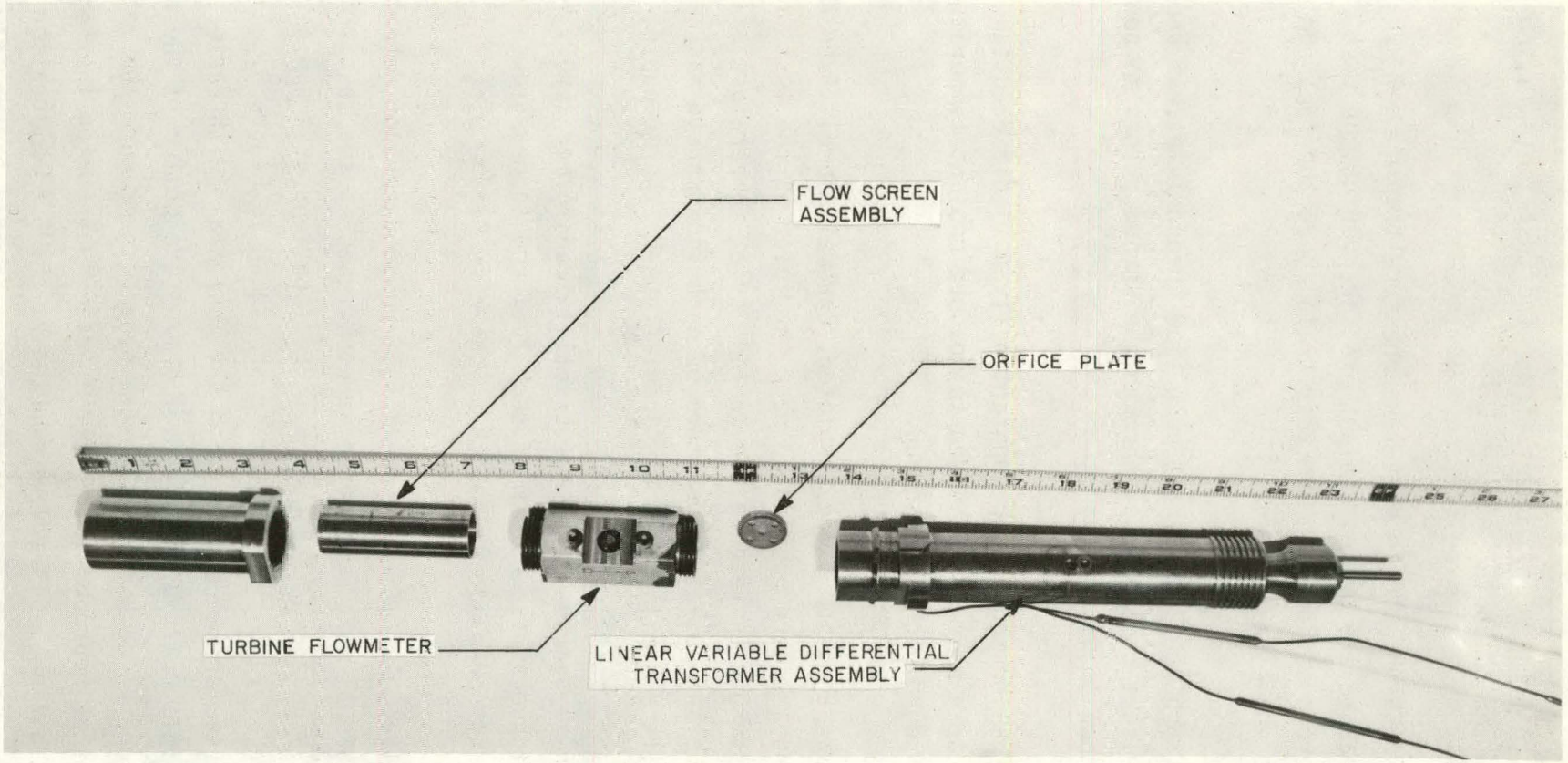

Fig. 5 Expanded layout of the linear variable differential transformer, coolant flow orifice plate, turbine flowmeter, and coolant flow screen assembly.

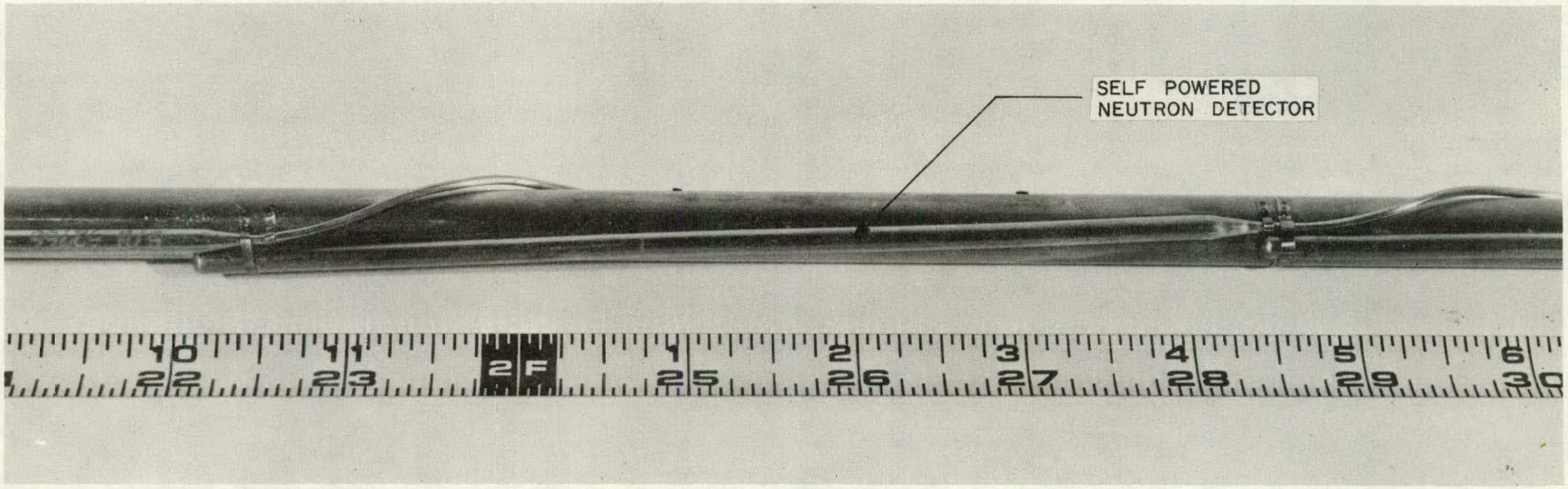

Fig. 6 Self-powered neutron detectors as mounted on support bar.

(7) A cobalt wire was mounted on the outside of each of three flow shrouds to monitor the axial neutron flux profile in the IPT. The cobalt wires were positioned to extend below the bottom and the top of the active core.

2.4.2 Fuel Rod Instrumentation. The following transducers were utilized to monitor the response of each fuel rod during the experiment:

(1) One 17-MPa strain post-type pressure transducer was mounted on the upper end cap of each rod to monitor internal pressure.

(2) A calibrated thermocouple composed of a tungsten-rhenium (W5%Re/W26%Re) alloy wire, with a hard-fired beryllium oxide insulation and a tantalum sheath, was provided to measure the fuel centerline temperature on Rods IE-011 and IE-012. These thermocouples were inserted from the top of the fuel stack through drilled fuel pellets. Temperature measurements were made at 0.75 m above the bottom of both fuel rods.

(3) An ultrasonic thermometer (UT) with an active length of 10 cm was used to measure the fuel centerline temperature in Rods IE-013 and IE-014. The UTs were inserted from the top of the fuel stack through drilled fuel pellets and centered at 0.61 m above the bottom of the fuel rod.

(4) Two grounded junction, beryllium oxide insulated, tungsten-rhenium (W5%Re/W26%Re) alloy wire, zircaloy sheathed thermocouples were used to measure cladding surface temperatures. These thermocouples, depicted in Figure 7, were spring-loaded against the outer surface of the cladding with an approximate three-pound preload. The thermocouples were located 0.61 m above the bottom of Rods IE-011 and IE-012.

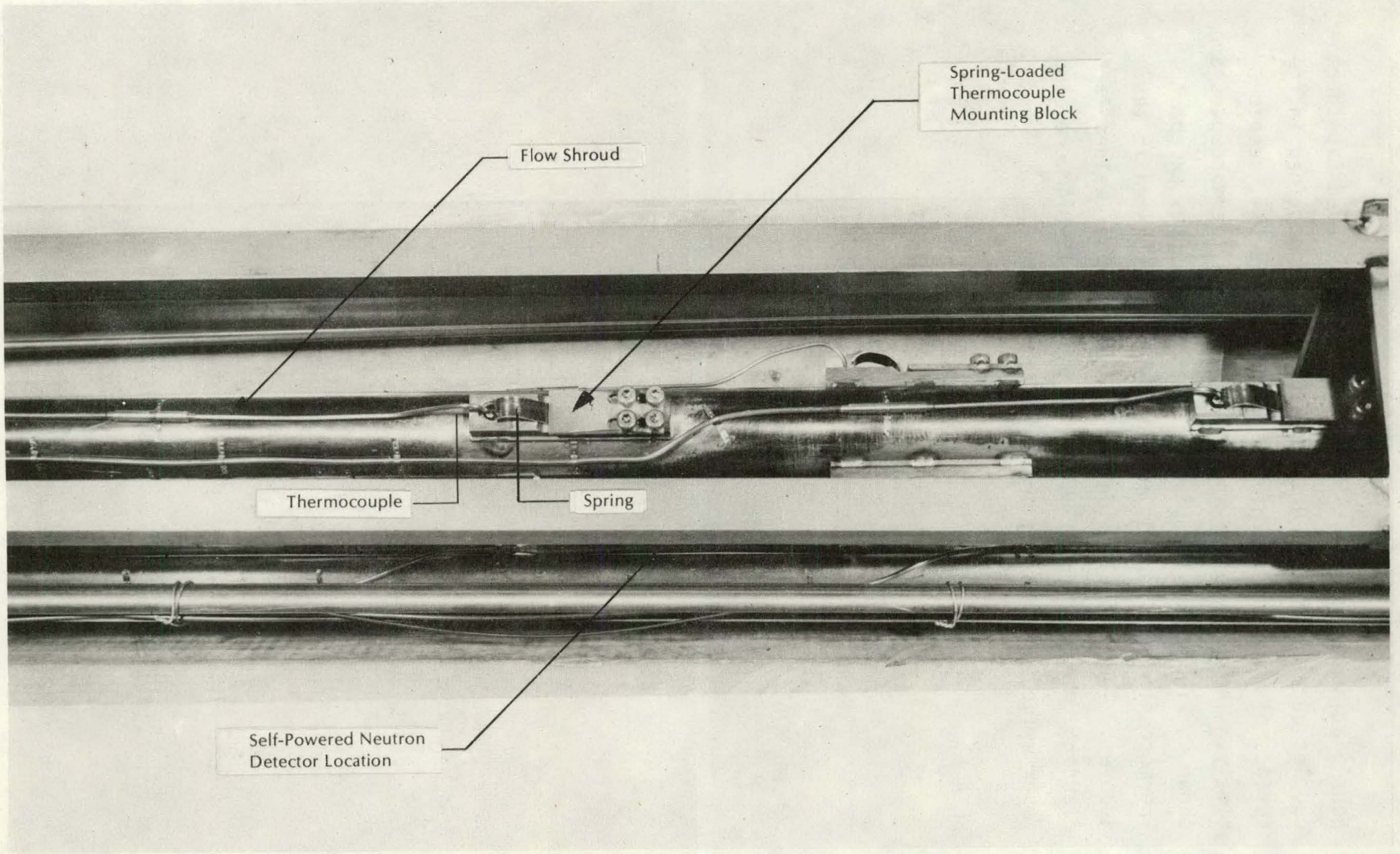

Fig. 7 Section of the test train, as assembled for insertion into the IPT.

(5) Four platinum/platinum 10% rhodium (Type S) spaded tip thermocouples were located in 0.25-mm-deep grooves machined in the surface of the cladding of Rods IE-013 and IE-014, respectively. The orientation and location of the thermocouples are shown in Figure 8. The tips of all thermocouples except Thermocouple A (Figure 8) on Rod IE-014 were brazed in the grooves. Thermocouple A on Rod IE-014 was laser welded to the cladding. Thermocouples B, C, and D of Rod IE-014 were also laser welded after being brazed to the cladding.

TC No	Orientation	Distance from Bottom of End Cap	Distance from Bottom of Fuel
A	0°	0.612 m	0.599 m
B	90°	0.511 m	0.498 m
C	180°	0.612 m	0.599 m
D	270°	0.714 m	0.701 m

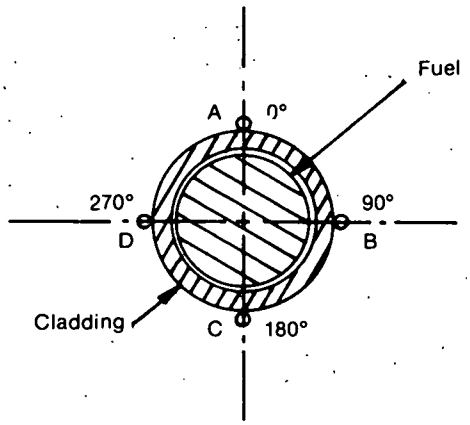

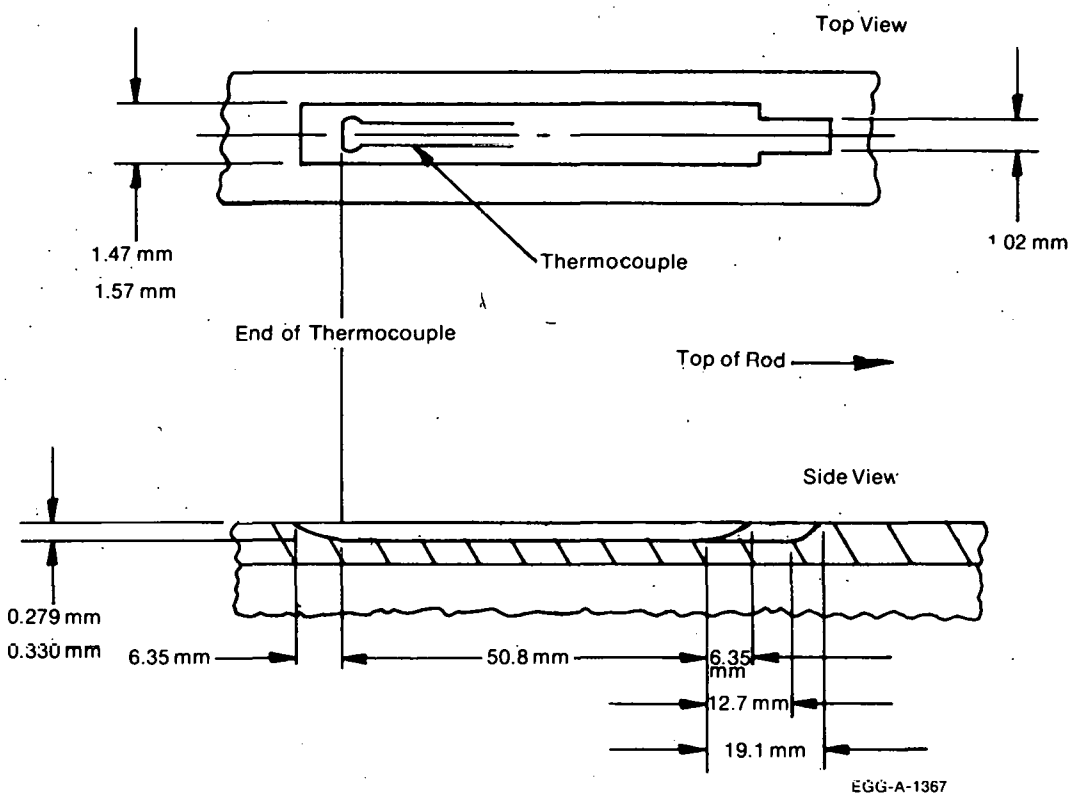

Fig. 8 Orientation and location of Type S thermocouples on Rods IE-013 and IE-014.

3. EXPERIMENT CONDUCT

Irradiation Effects Test 2 consisted of four phases, which spanned a total of 49 hours, including about 38 hours of nuclear operation:

(1) A preconditioning phase.

(2) A rapid power ramp phase.

(3) A steady-state operation phase in which the test rod power, inlet temperature, and coolant flow rate were held constant.

(4) A flow reduction phase which induced a film boiling transient.

During the 37-hour preconditioning phase, the fuel rods were subjected to different power cycles, which allowed for fuel restructuring. In these cycles a maximum power of 30 kW/m was reached. In the power ramp phase the peak fuel rod power was increased from 25 kW/m up to 68 kW/m at a rate of 3 kW/m per minute. The power ramp was used in the study of pellet-cladding mechanical interaction, known to be a principal factor in irradiated fuel rod failure. A one hour constant power phase followed the rapid power ramp to 68 kW/m. This period of steady-state operation allowed additional fuel restructuring and relaxation of the stresses between the fuel and its cladding. The final test phase was a forced flow reduction to study film boiling behavior by inducing a power-cooling-mismatch.

To avoid possible misunderstanding, a specific terminology is used to discuss test conduct. Since most of the test conditions (inlet temperature, flow rate, etc.) have small random variations, as shown in Figure 9, nominal values are used to describe these conditions. Fuel rod peak power is the peak linear heat rating (kW/m), whereas fuel rod average power is the linear heat rating averaged over the length of the rod. Fuel rod average peak power is used for the average of the fuel rod peak powers in all four rods. Fuel rod average powers were calculated using a thermal balance, whereas local power was calculated using data

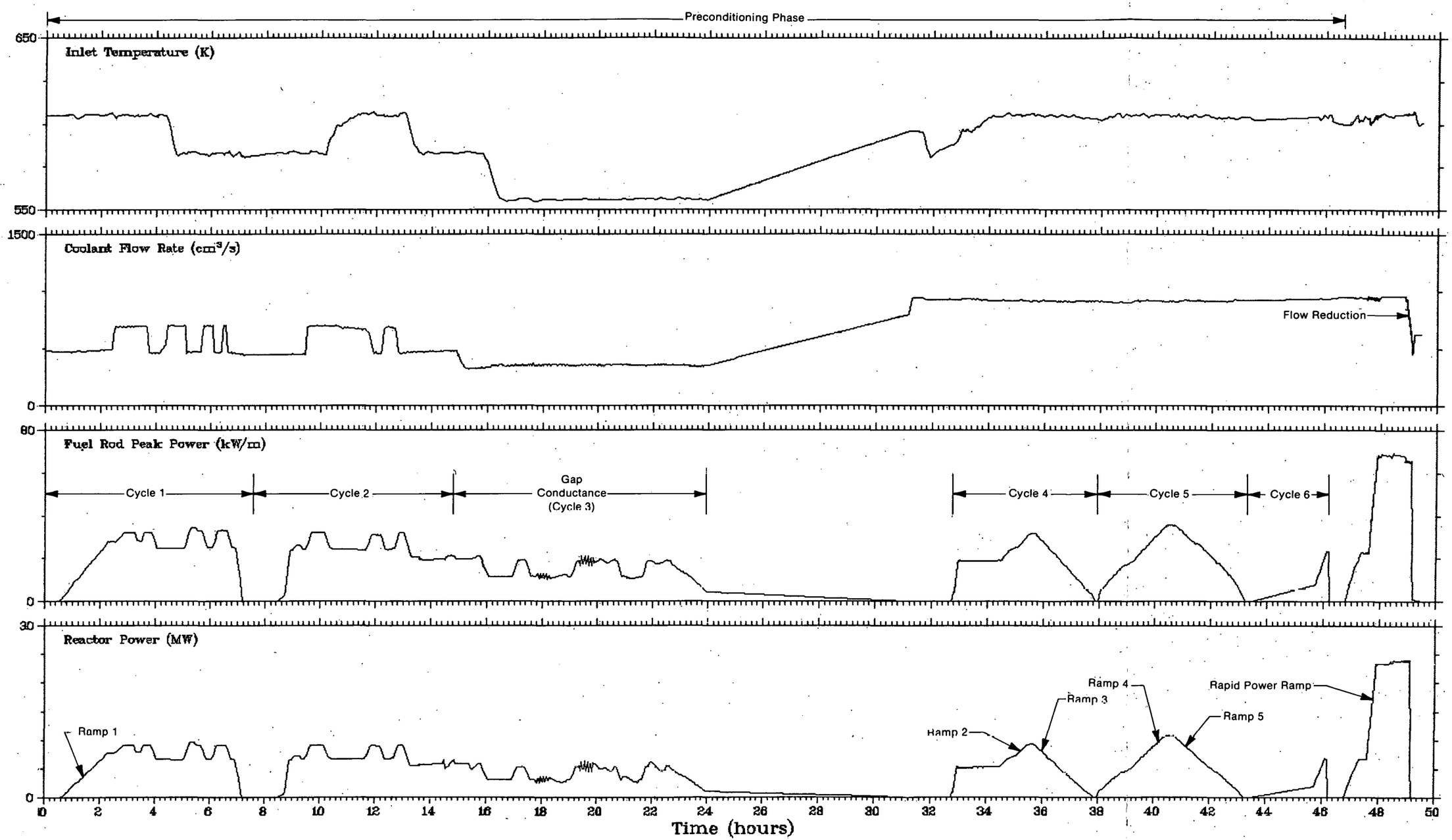

Fig. 9 Experiment conduct - inlet temperature, coolant flow rate, fuel rod peak power and reactor power for Test IE-2.

from three axially distributed SPNDs and two cobalt flux wires. The specific calculational techniques are discussed in Appendix D.

3.1 Preconditioning Phase. The first part of the test, the preconditioning phase, consisted of (a) two cycles designed to study the effects of coolant inlet temperature, coolant flow rate, reactor power, and time on fuel rod and test train measurements, (b) a gap conductance piggyback test, and (c) two additional cycles of slowly varying power.

The first two cycles consisted of 16 steps at all possible combinations of two levels of flow rate; 500 and 700 cm^3/s, inlet temperature; 585 and 606 K, and fuel rod peak power; 23 and 30 kW/m[a]. As shown in Figure 9, rod average power was slowly increased at a rate of 0.23 kW/m per minute up to the first power step. Subsequent scheduled power changes were completed at ramp rates of 0.5 kW/m per minute. Between Cycles 1 and 2 (7 hours after the start of the test) there was an unscheduled shutdown. The average rod power was decreased and increased at approximately 1.25 kW/m per minute for this shutdown and subsequent startup.

The gap conductance testing, described in another report[3], consisted of oscillations at nominal fuel rod peak power levels of 12 and 19 kW/m. The coolant flow rate and inlet temperature were varied from 500 to 300 cm^3/s and from 583 to 555 K, respectively. No attempt was made to retain the frequency content of the data during the oscillations for this report. These data, which show strong aliasing effects, were presented only to show the complete sequence of fuel rod preconditioning.

Following the gap conductance portion of the test, the reactor was shut down for instrument recalibration and range changes. The reactor

---

[a] The combination of flow rate, inlet temperature, and rod linear heat rating was chosen using a 2^3 factorial design with one complete replicate to provide estimates of variances. The steps were randomly arranged in time with a constraint on the inlet temperature as shown in Figure 9. The design was additionally constrained so that the effect of time, electronic drift, etc., was confounded with three factor interaction.

was returned to power after nine hours to complete two additional cycles of preconditioning. This period consisted of ramps from a rod average power of 0 kW/m to 30 kW/m at rates of either 0.25 or 1.25 kW/m per minute. Nominal coolant flow rate and inlet temperature were 1000 cm^3/s and 606 K, respectively. At the middle of Cycle 6, as the power was being increased to 24 kW/m, a loss of onsite power caused the reactor to scram. After startup, the preconditioning period was completed.

3.2 Power Ramp and Steady-State Operation. The preconditioning period ended with a steady-state fuel rod peak power of 24 kW/m. The rod peak power was then increased at a ramp rate of 3 kW/m per minute up to 68 kW/m. After a constant power level was reached, a calculation of fuel rod average power using coolant flow and temperature differential measurements determined that powers of 68.5, 65.0, 72.0, and 64.2 kW/m for Rods IE-011, IE-012, IE-013, and IE-014, respectively, had been attained.

3.3 Flow Reduction. After about one hour at constant power, coolant inlet temperature and flow, the flow reduction portion of the test was initiated. The fuel rod coolant flow rates, nominally the same for all four rods, were reduced in steps from an initial value of 1000 cm^3/s (4880 $kg/s\text{-}m^2$). Following each flow reduction step, flow was held constant for approximately one minute. At a flow of approximately 530 cm^3/s (2550 $kg/s\text{-}m^2$), the LVDT on Rod IE-011 indicated the onset of film boiling (DNB - departure from nucleate boiling). Concurrently, the flow rates for the other three rods were approximately 2700 $kg/s\text{-}m^2$ and slight indications of film boiling were observed on Rods IE-013 and IE-014. At this point, the flow for Rod IE-011 was further reduced to 460 cm^3/s (2245 $kg/s\text{-}m^2$). During this flow reduction, film boiling was indicated on the remaining fuel rods. After the flow reduction to 460 cm^3/s, the flow was held constant for about one minute after which the reactor was shut down. These events are summarized in Table II.

Film boiling ceased as the control rods were inserted into the reactor core. Rewetting of the fuel rods was indicated by the LVDTs, the fuel rod internal pressure transducers, cladding surface thermo-

TABLE II

MASS FLUX AND FUEL ROD POWER DURING TEST IE-2 FILM BOILING

Time after DNB (sec)	Rod	Mass Flux ($kg/s\text{-}m^2$)	Average Rod Power (kW/m)	Comments
0.0	IE-011	2550 ± 30	50.5 ± 1.5	First indications of DNB on Rods IE-011, IE-013, IE-014: (1) IE-011 - cladding elongation increases, (2) IE-013 - centerline temperature increases, slight increase in cladding temperatures at 0.61-m elevation. (3) IE-014 - increase in internal pressure and cladding surface temperatures at 0.61-m elevation.
	IE-012	2700 ± 30	49.1 ± 1.5	
	IE-013	2750 ± 30	54.0 ± 1.6	
	IE-014	2750 ± 30	49.3 ± 1.5	
18.0	(Same)	(Same)	(Same)	Start of final flow reduction; immediate change in slope on measurements listed above. Increase in pressure for Rods IE-011 and IE-013. Increase in cladding surface temperatures on Rods IE-013 and IE-014.
22.0	IE-012	2650 ± 50	(Same)	First indication of DNB on Rod IE-012.
24.0	IE-011	2220 ± 30	(Same)	Lowest flow.
	IE-012	2475 ± 30		
	IE-013	2360 ± 30		
	IE-014	2370 ± 30		
40.0-50.0	(Same)	(Same)	(Same)	Increases have leveled off, equilibrium has been reached.
62.0	(Same)	(Same)	(Same)	Cladding temperature at 0.61-m elevation and zero degree orientation on Rod IE-014 has dropped, indicating local collapse of vapor layer.
80.0	(Same)	(Same)	(Same)	Reduction in power started. Flow starting to increase. All measurements which were indicating film boiling start to decrease.
115.0	IE-011	2350 ± 30	14.3 ± 0.2	Measurements have reached pre-DNB levels.
	IE-012	2600 ± 30	14.4 ± 0.2	
	IE-013	2550 ± 30	14.1 ± 0.2	
	IE-014	2540 ± 30	15.0 ± 0.2	

couples on Rods IE-013 and IE-014, and a fuel centerline thermocouple on Rod IE-011.

Fuel rod internal pressure readings, loop fission monitor readings and subsequent postirradiation visual examination indicated that none of the fuel rods failed during or after the film boiling portion of the test.

4. EXPERIMENTAL RESULTS

The experimental results presented in this section and Section 6 have been divided into two parts; pre-film boiling behavior and film boiling behavior.

The raw experimental data, described in Appendix C, were reduced using a fairly complicated process to obtain the data presented in this section. One of the steps involved was to find the uncertainties associated with the data due to instrument calibration and data acquisition. These uncertainties are discussed in Appendix A. Another step, and probably the most important, was the correction of the data for known systematic instrument or data acquisition errors. Most of these corrections were minor except for those concerned with the rod internal pressure transducers.

The pressure transducers were corrected for large zero drifts due to instrument decalibration. The corrections were determined using a multiple regression analysis as discussed in Appendix C.

As discussed in the following paragraphs, transformations were made for parts of the plots in this section and Section 6 which show cladding elongation and rod internal pressure (Appendix C). These transformations were made to minimize the effects of instrument uncertainties and thermal expansion of the hardware for pressure and elongation, respectively.

Cladding elongation data are presented in terms of change in strain

$$\varepsilon - \varepsilon_o = \frac{\Delta L - \Delta L_o}{L} \qquad (1)$$

where

ε = cladding strain

ε_o = cladding strain at the start of the nuclear portion of the test as shown in Table III and at time zero in Figure 9

ΔL = cladding elongation

ΔL_o = cladding elongation at the start of the test

L = cladding cold length (970 mm).

Rod internal pressure is presented in terms of the fractional change in pressure,

$$\frac{P - P_o}{P_o} \qquad (2)$$

where

P = rod internal pressure

P_o = rod internal pressure at the start of the test after correction for decalibration of the pressure transducer (Table III).

TABLE III

REFERENCE INITIAL CLADDING STRAINS AND FUEL ROD INTERNAL PRESSURES FOR TEST IE-2

Rod	Initial Pressure, P_o (MPa)	Initial Cladding Strain, ε_o (mm/mm)
IE-011	5.07	1.18×10^{-3}
IE-012	5.05	0.89×10^{-3}
IE-013	5.43	-
IE-014	5.39	-0.03×10^{-3}
IE-011 (FRAP-T3)	2.211	1.47×10^{-3}
IE-014 (FRAP-T3)	5.246	1.51×10^{-3}

4.1 Pre-Film Boiling Experimental Results.

Prior to film boiling the fuel rods were essentially in thermodynamic equilibrium. The changes in rod power, inlet temperature, and flow rate were slow enough that any thermal lag in fuel rod temperature

or coolant temperature was negligible. The fuel rods were not in mechanical equilibrium due to fuel creep and slippage between fuel and cladding. Nonequilibrium effects were less pronounced at low powers (< 30 kW/m) but were quite evident during the one hour steady power period at 68 kW/m. For this reason, the mechanical data such as cladding elongation is more properly termed quasi-equilibrium during the pre-film boiling period.

Representative key measurements made on each rod are presented in Figures 10 through 13. Also, the mass fluxes and rod average powers for all four rods during the power ramp and steady-state operation are shown in Figures 14 and 15.

4.1.1 Cladding Elongation. Only three LVDTs, on Rods IE-011, IE-012, and IE-014[a], were operational during the test. The LVDT on Rod IE-013 failed prior to the test and could not be replaced without substantial schedule impact. The change in cladding strain versus power for Rod IE-011, which had a diametral gap of 0.102 mm, was consistently greater than the change in strain of Rods IE-012 and IE-014, which had gaps of 0.343 mm. "Hard"[b] pellet-cladding interaction was initiated at lower rod average powers on Rod IE-011, with a resultant increase in the slope of cladding strain versus rod power. This effect can be seen in Figures 16 through 18.

---

[a] Absolute cladding elongations on Rod IE-014 are not presented because of a change in sensitivity of the LVDT as discussed in Appendix A. Relative comparisons are included to indicate the variations in behavior between Rods IE-012 and IE-014.

[b] "Hard" PCI is differentiated from "soft" PCI which is characterized by isolated points of fuel-cladding interaction due to pellet fragments or misaligned pellets, and does not result in lockup between the fuel and the cladding. During "hard" PCI the cladding elongation approximates that of the fuel stack.

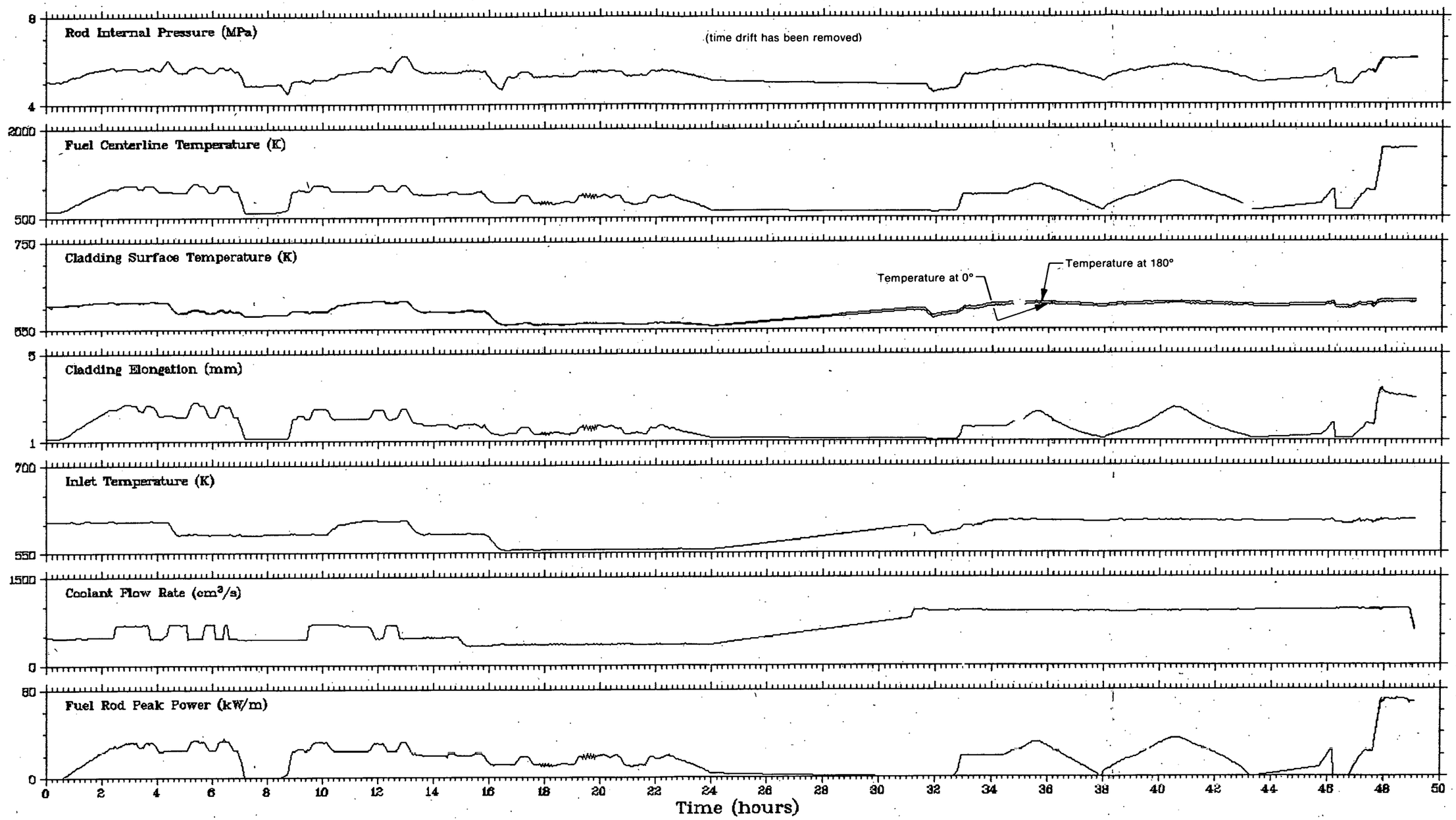

Fig. 10 Rod IE-011 behavioral data for pre-film boiling phase of Test IE-2.

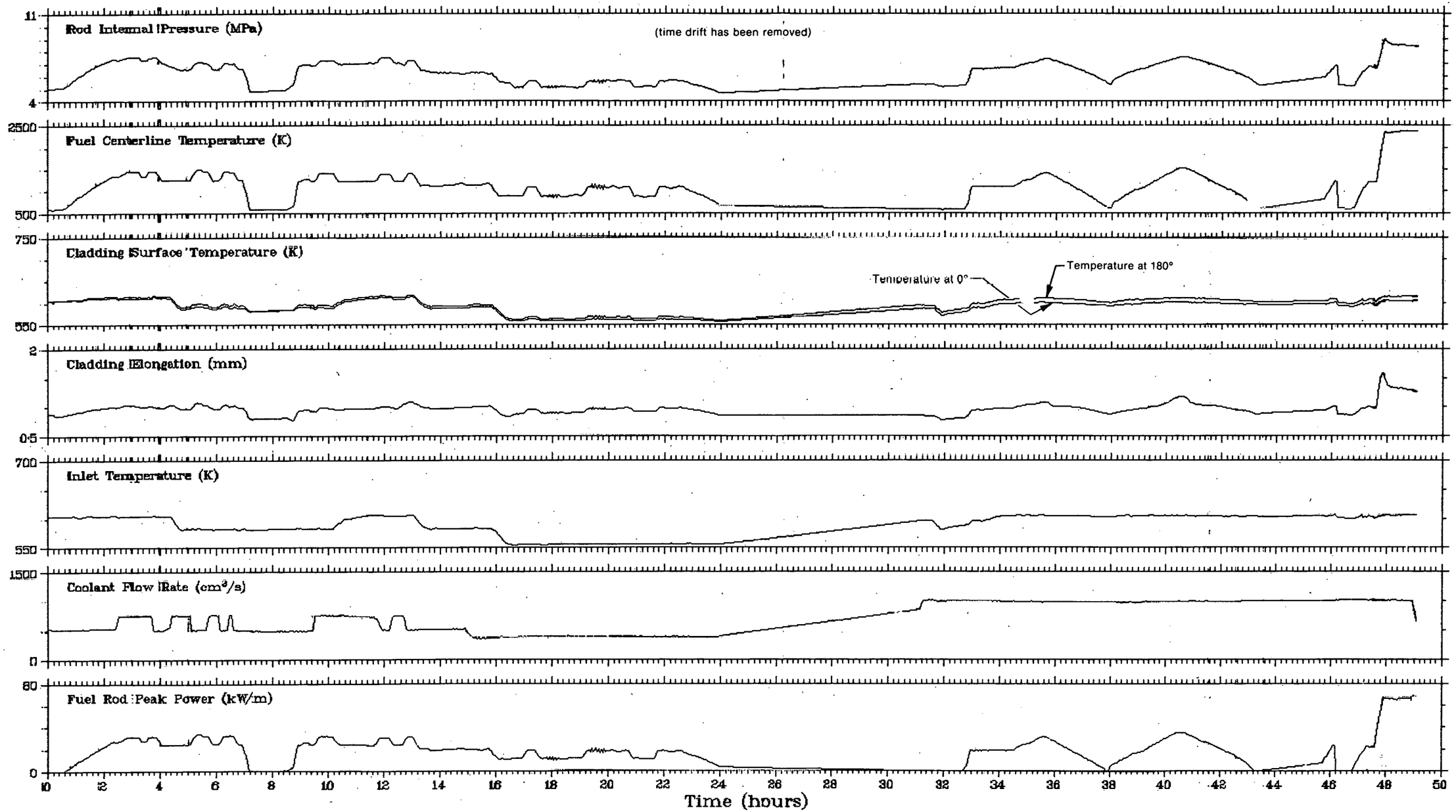

Fig. 11 Rod IE-012 behavioral data for pre-film boiling phase of Test IE-2.

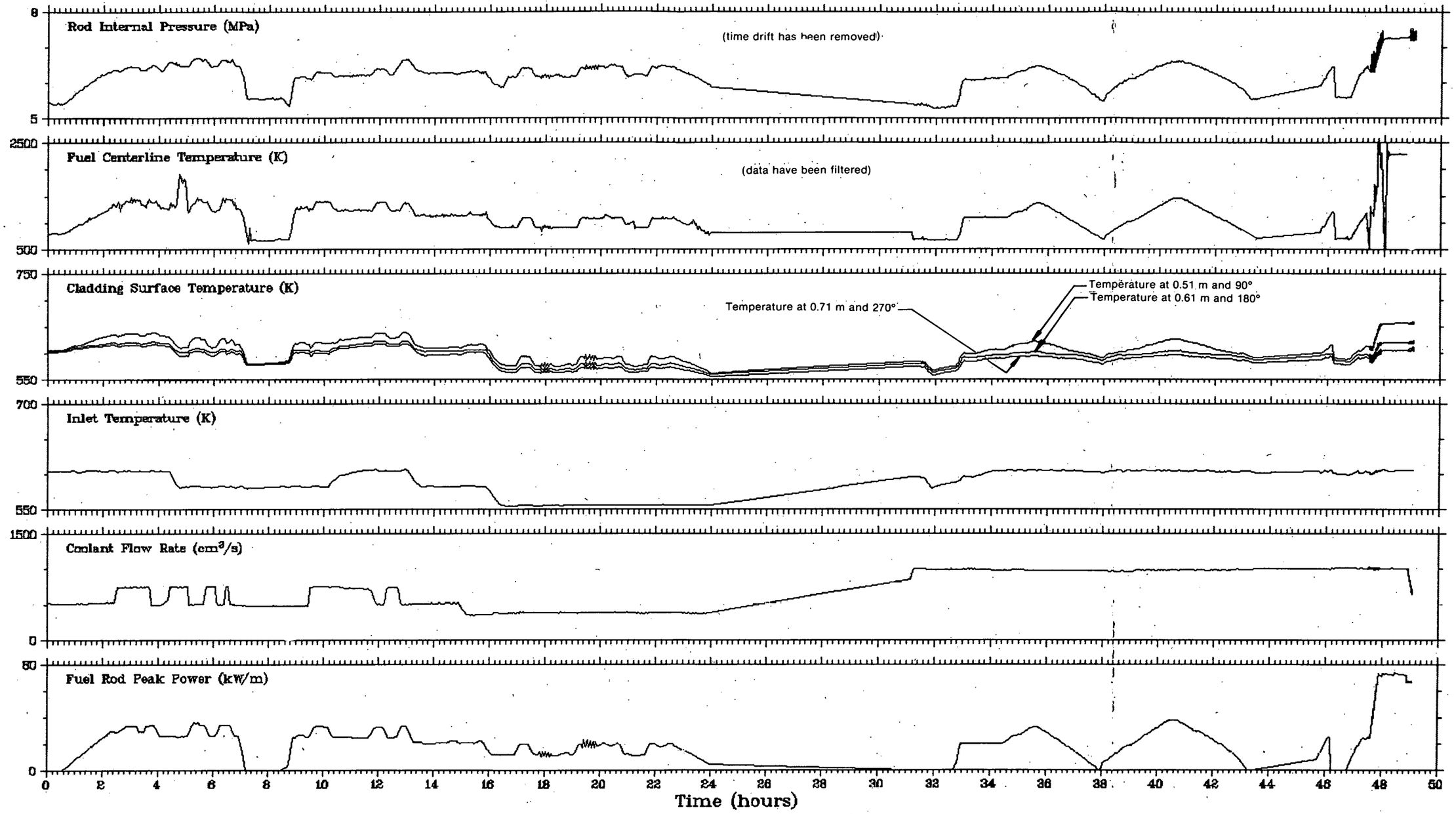

Fig. 12 Rod IE-013 behavioral data for pre-film boiling phase of Test IE-2.

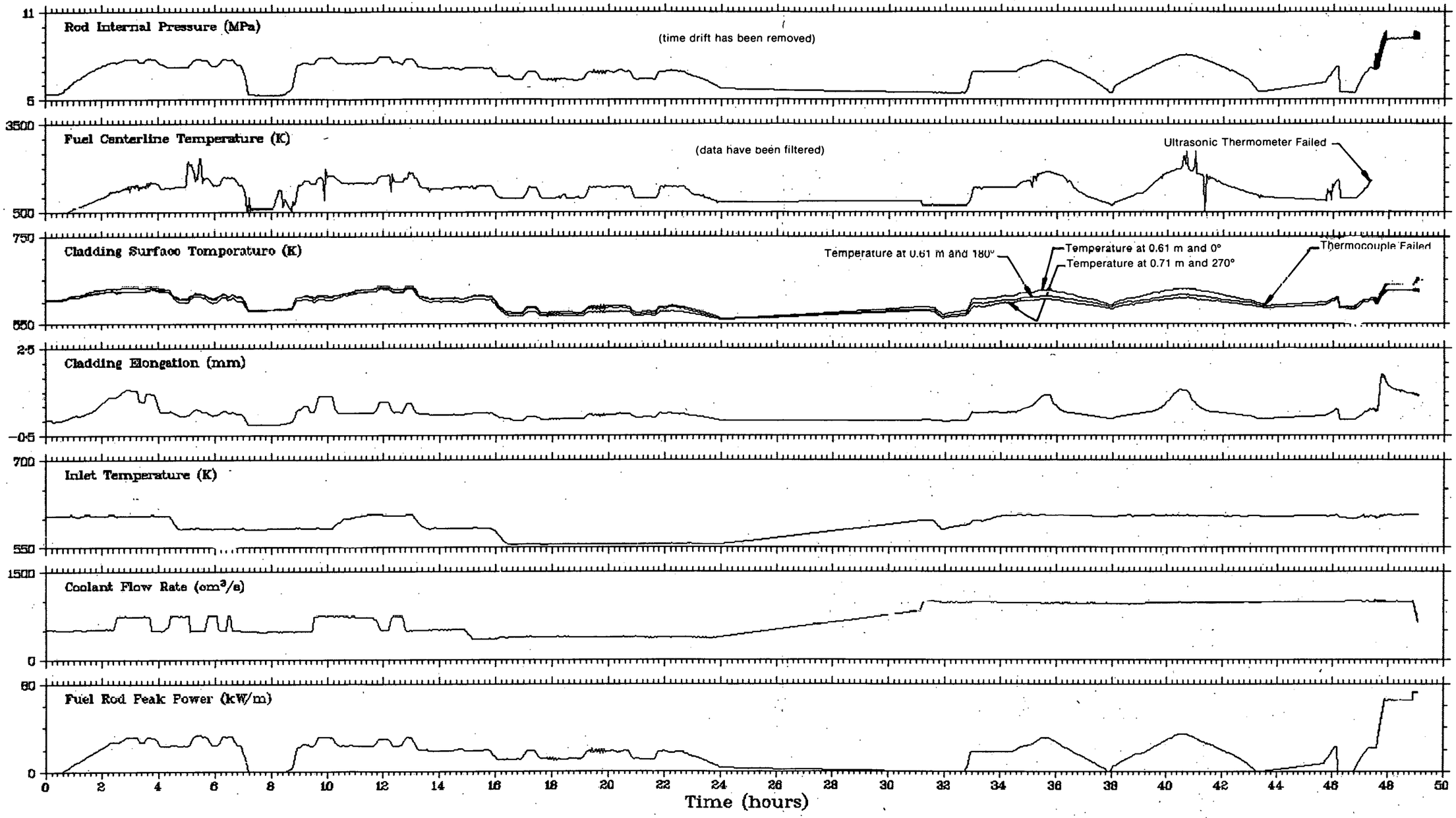

Fig. 13 Rod IE-014 behavioral data for pre-film boiling phase of Test IE-2.

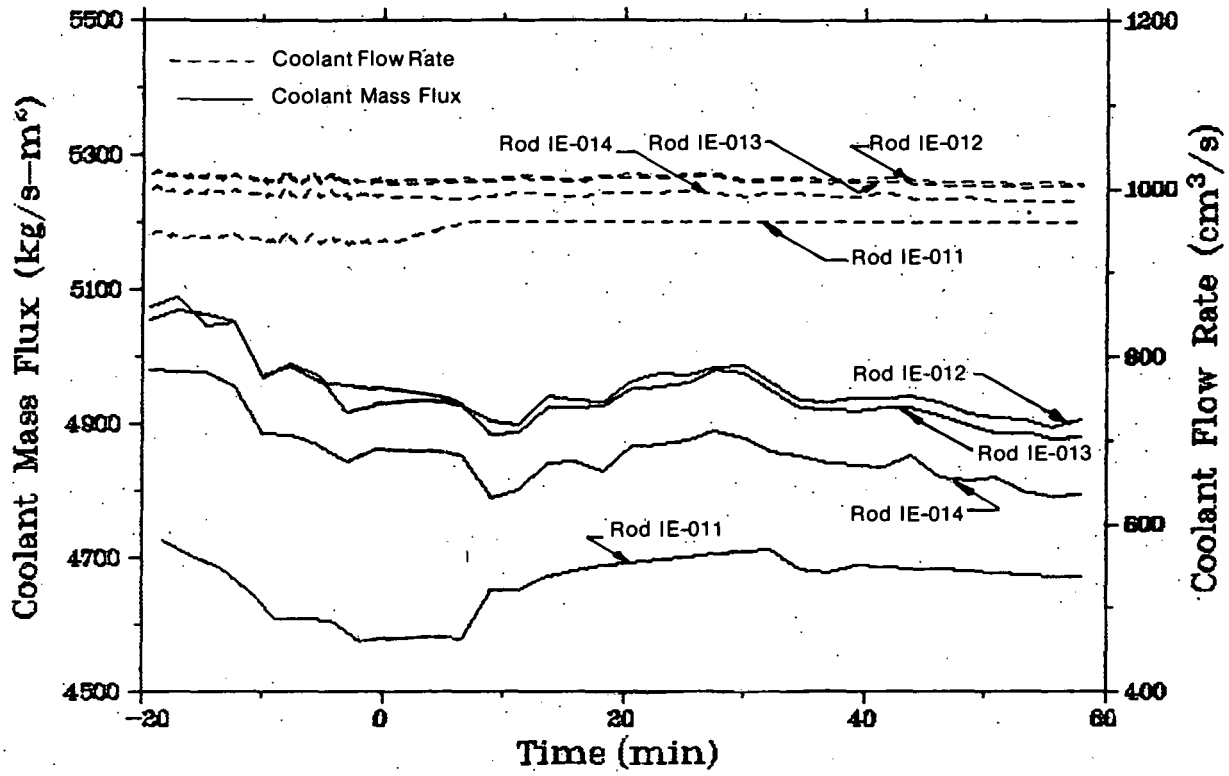

Fig. 14 Coolant flow rate and mass flux for all four rods during power ramp and steady-state operation.

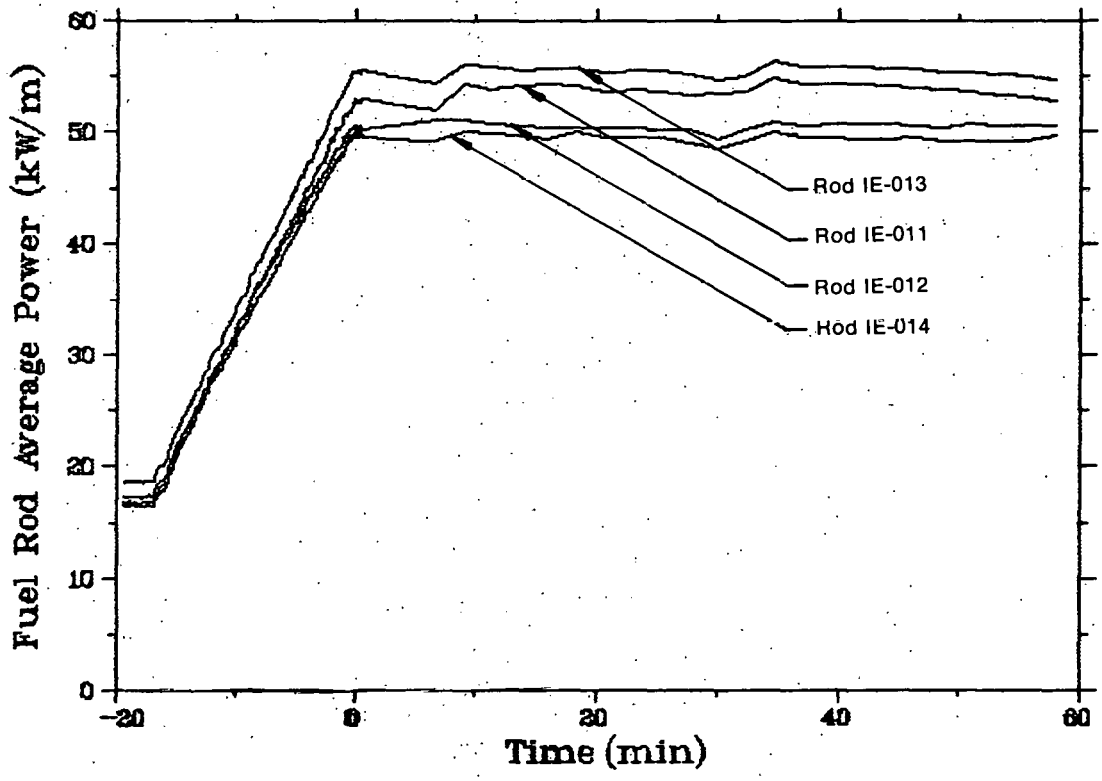

Fig. 15 Fuel rod average power for all four rods during power ramp and steady-state operation.

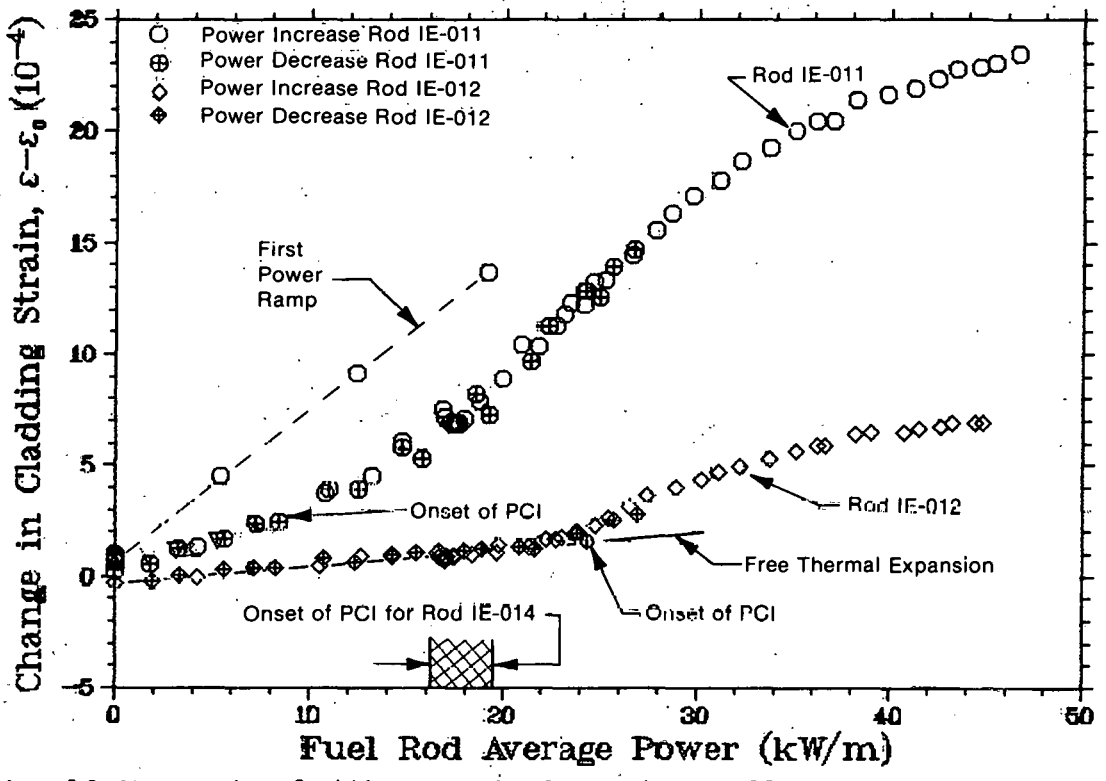

Fig. 16 Change in cladding strain for Rods IE-011 and IE-012 during pre-film boiling phase of Test IE-2. The power at the onset of PCI for Rod IE-014 is also indicated.

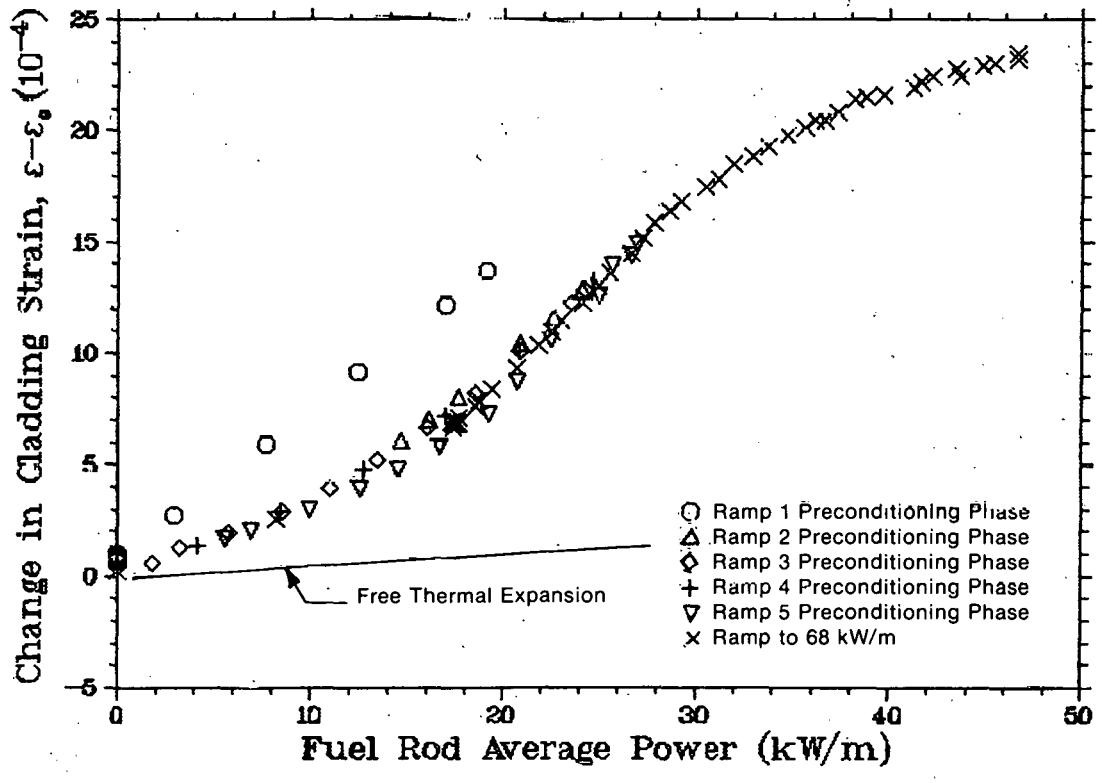

Fig. 17 Change in cladding strain for Rod IE-011 during power cycles.

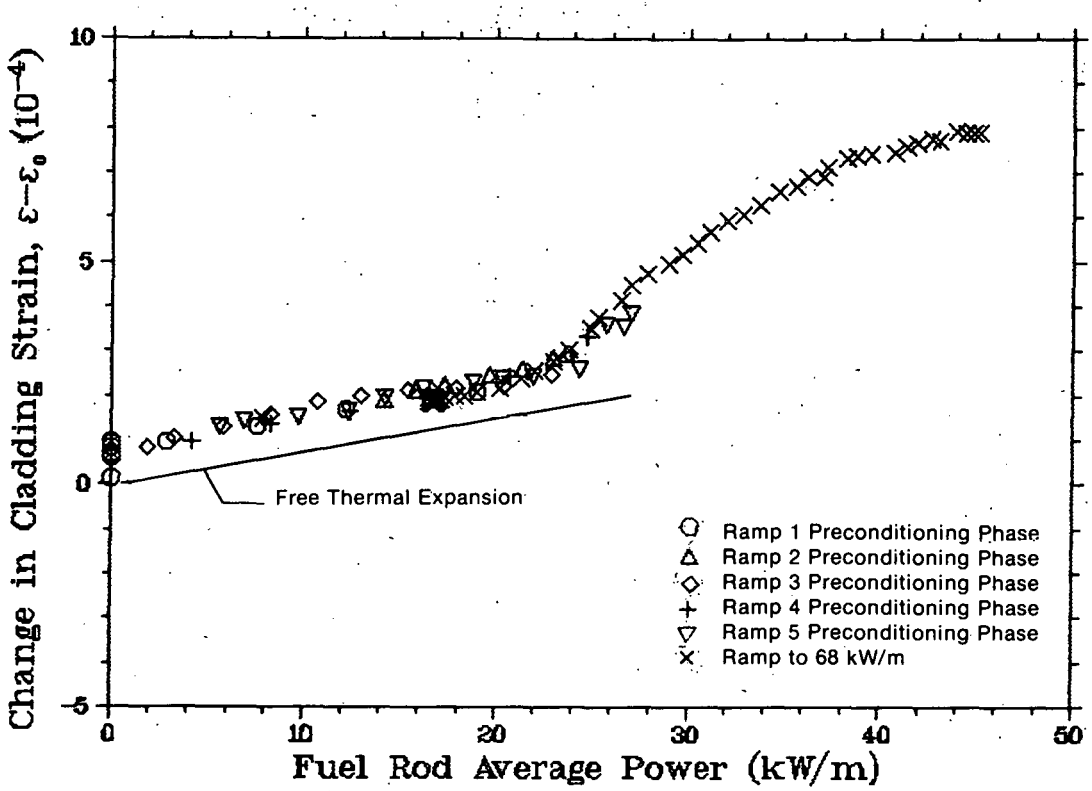

Fig. 18 Change in cladding strain for Rod IE-012 during power cycles.

As the fuel rods were subjected to continued power cycles (Figures 17 and 18), the relationship between strain and power became "saturated" or remained fixed, even for continued cycles. This constant relationship is due to the repositioning and deformation of the fuel. At the start of the test, because of the handling of the fuel rods, there is a non-uniform annular gap between the fuel pellets and the cladding. Off center, skewed, and chipped pellets produce a random annular gap with an average effective gap smaller than the designed diametral gap. The smaller effective gap causes PCI during the initial power cycles at low fuel rod powers. As the cycles continue, stresses between the cladding and the fuel column realign the pellets and pellet fragments, increasing the effective diametral gap. Once the fuel column has become aligned, PCI results from closure of the diametral gap by thermal expansion and cracking of the fuel. This type of PCI, often called "hard" PCI, happens at higher rod powers that are consistent from cycle to cycle. As the power is increased, "hard" PCI occurs first for Rod IE-011 at approximately 9 kW/m. The other two rods, IE-012 and IE-014, show PCI initiation at 23 kW/m and 18 kW/m, respectively. The power at which "hard"

PCI occurs is a function of the diametral gap and the previous maximum power level. Evidently, some PCI existed for Rod IE-011, during all power cycles even at rod powers close to zero (Figure 17), since the slope of strain versus power was higher than can be explained by thermal expansion of the cladding alone. The slope for Rod IE-012 is consistent with cladding thermal expansion. The differences in relative slopes between the two rods above the onset of "hard" PCI indicates that the axial extent of PCI was also much less for Rods IE-012 and IE-014 (large gaps) than for Rods IE-011 and IE-013 (small gaps).

The influence of prior irradiation damage to the cladding should make no difference in the elongation since no plastic deformation of the cladding was observed. Irradiation of zircaloy-4 raises the yield point, but has minimal effect on the modulus of elasticity and the thermal expansion coefficient[5]. Since the cladding of all three rods with LVDTs remained in the elastic region, except perhaps during the ramp to 68 kW/m, no differences were expected.

The influence of the diametral gap on elongation rate was also observed during the power ramp to and operation at 68 kW/m as shown in Figure 19. The cladding strain on Rod IE-011 showed evidence of hot pressing or creep of the fuel as the slope of strain versus time decreased above 34 kW/m even though the power increase versus time is constant. As the power ramp was terminated, the slope in strain versus time went from positive to negative with the strain decreasing in an exponential decay which is an indication of fuel creep[6]. The cladding strains in Rods IE-012 and IE-014 also showed evidence of fuel creep probably combined with some slippage because the level of PCI was low. The slope of the cladding strain for Rod IE-012 reached zero about the time the ramp was terminated. The difference in cladding strain behavior between the three rods is probably due to an interaction of two conditions. The larger initial gaps in Rods IE-012 and IE-014 would cause their average fuel temperatures to be higher, but the stress in their fuel would be less. Since fuel creep increases for both increasing fuel temperature and stress, the temperature must play the dominant role in this case resulting in higher creep rates for Rod IE-012 in comparison with Rod IE-011.

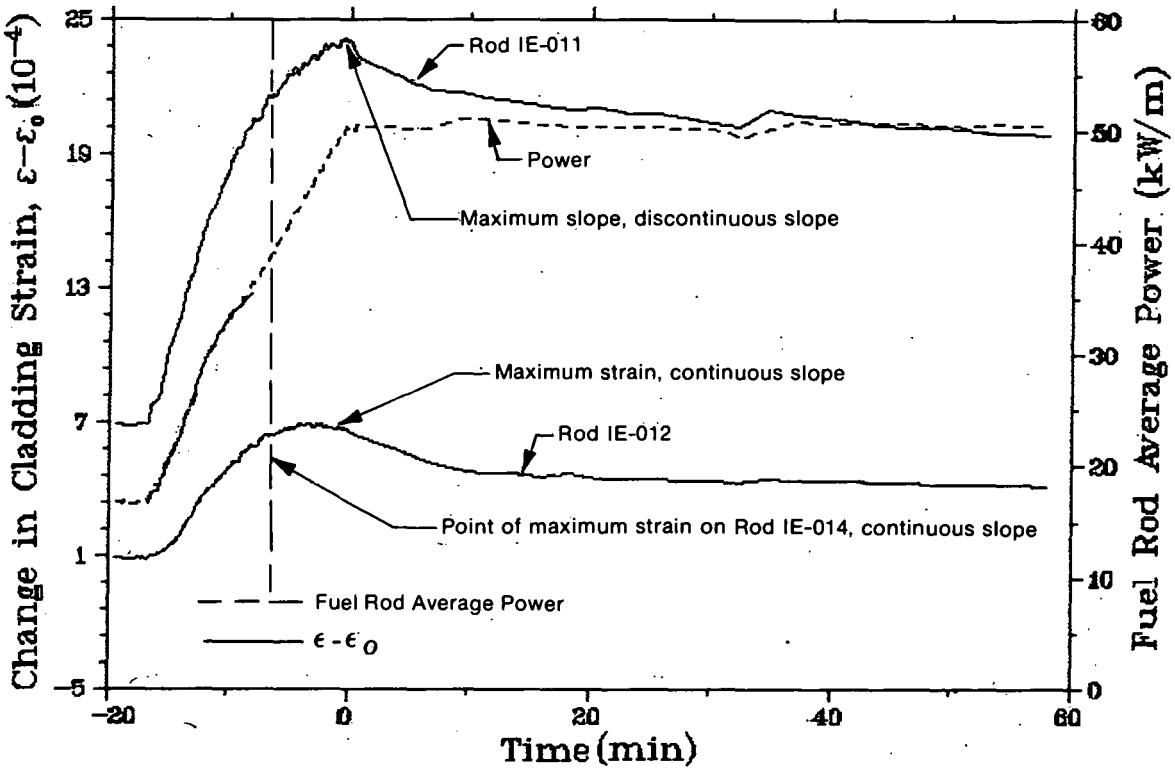

Fig. 19 Change in cladding strain for Rods IE-011 and IE-012 during power ramp and steady-state operation.

4.1.2 Fuel Rod Internal Pressure. The fuel rod internal pressure transducers showed sizable zero shifts before and during the tests. Prior to the test, all four transducers indicated changes in pressure from their "as-filled" pressure readings. These shifts are tabulated in Table C-V of Appendix C. During the test, the devices exhibited additional zero drifts. The data were corrected for these zero shifts using the results of a multiple regression analysis as discussed in Appendix C. When zero drifts were removed, effects of different gap sizes were readily apparent as shown in Figures 20 through 24. Rods IE-011 and IE-013, which had the smaller gaps of 0.102 and 0.100 mm, respectively, showed lesser increases in internal pressures than did Rods IE-012 and IE-014, which had gap sizes of 0.343 mm. This small pressure increase was expected, since the average gas temperatures in Rods IE-012 and IE-014 would be higher because of more gas contained in the larger nominal gaps and higher fuel surface temperature of the pellets.

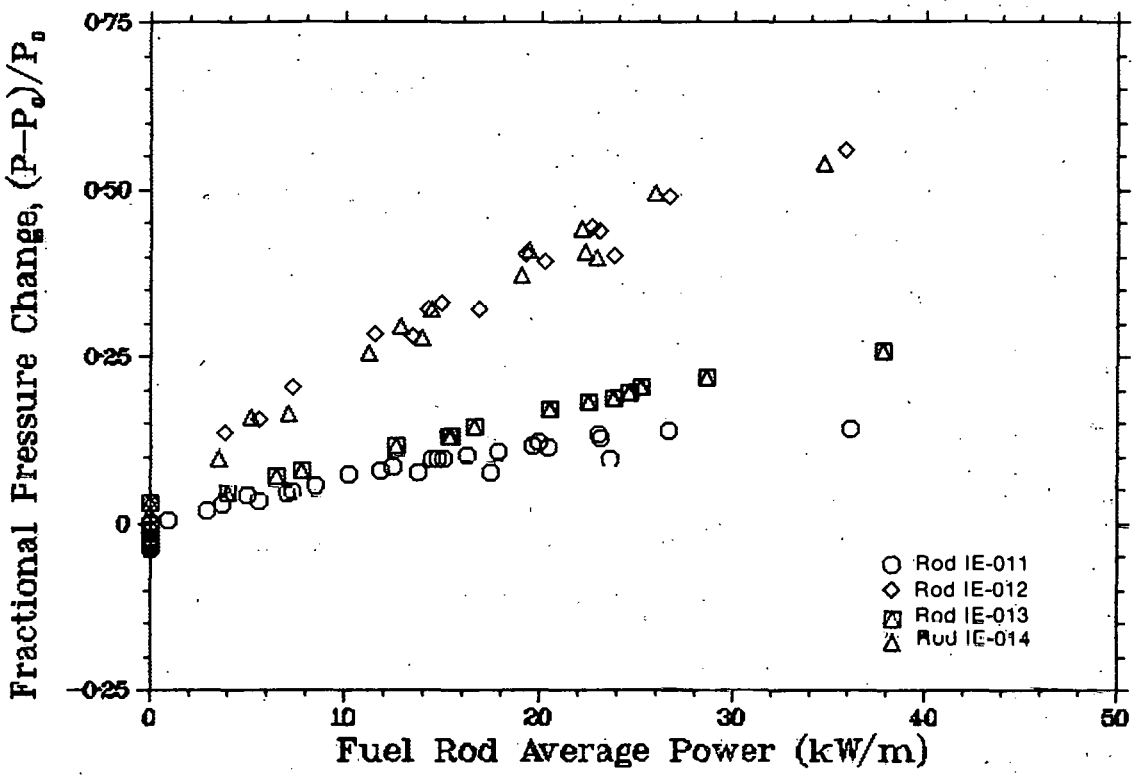

Fig. 20 Fractional change in rod internal pressure for all four rods during pre-film boiling phase of Test IE-2 (time drift has been removed).

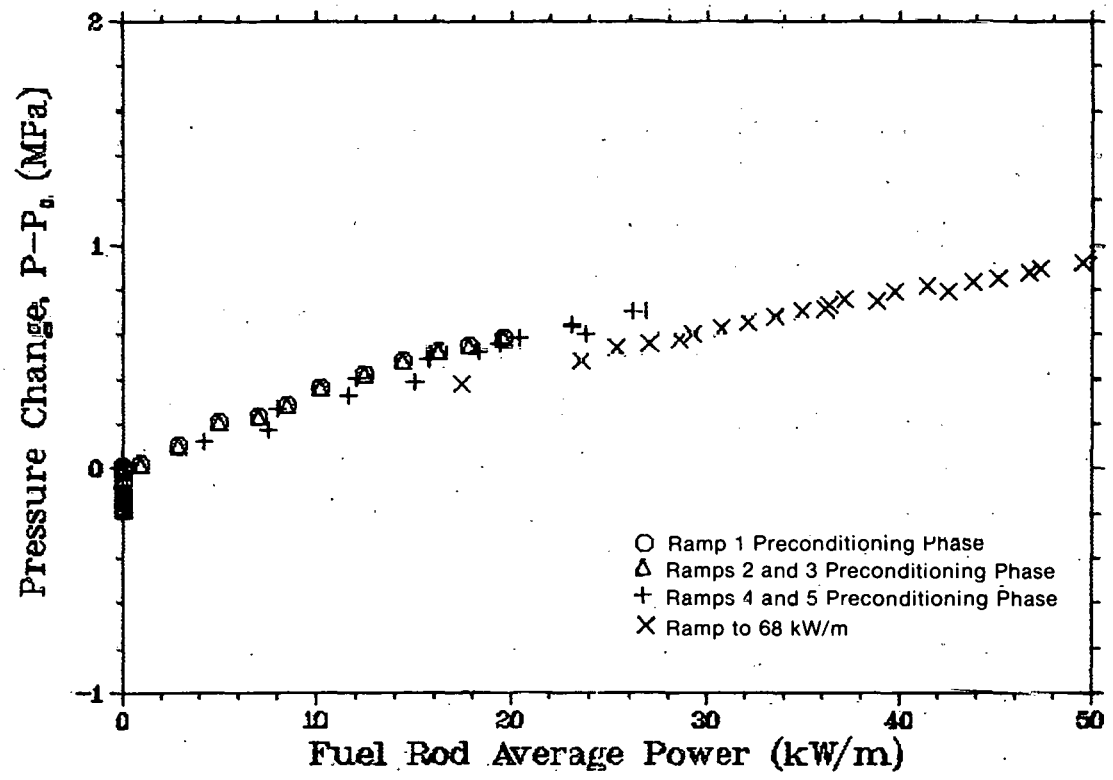

Fig. 21 Change in rod internal pressure for Rod IE-011 during power cycles (time drift has been removed).

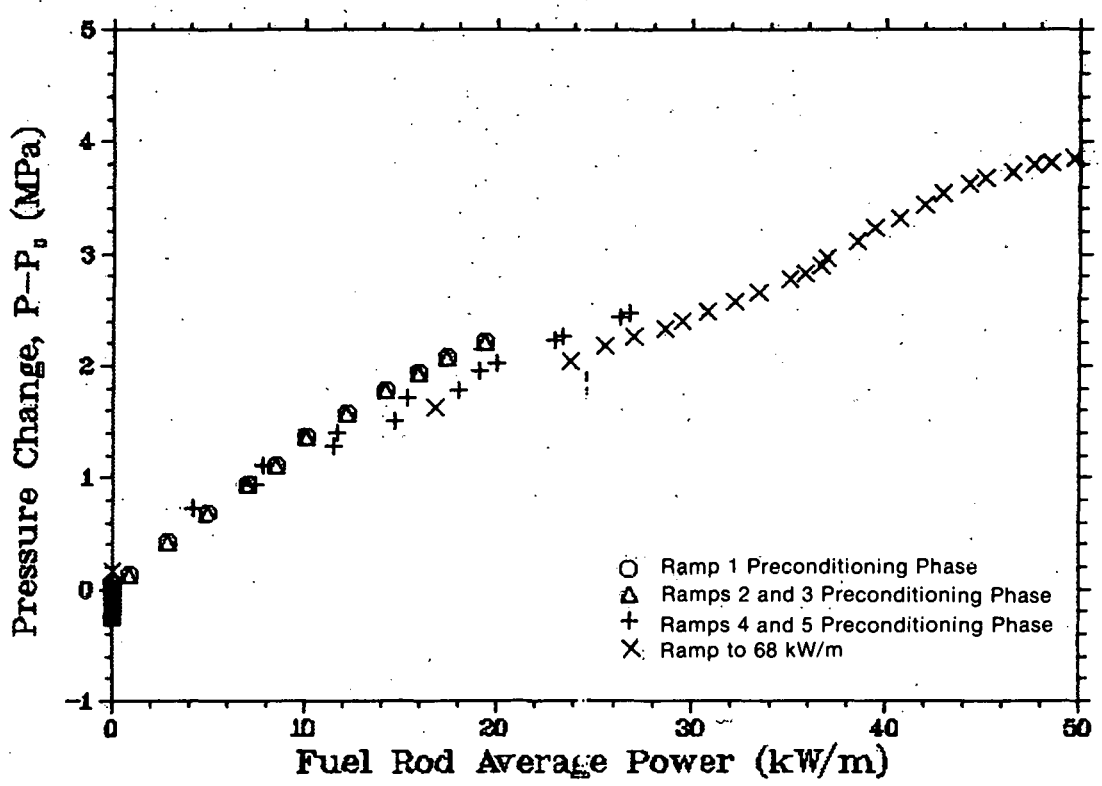

Fig. 22 Change in rod internal pressure for Rod IE-012 during power cycles (time drift has been removed).

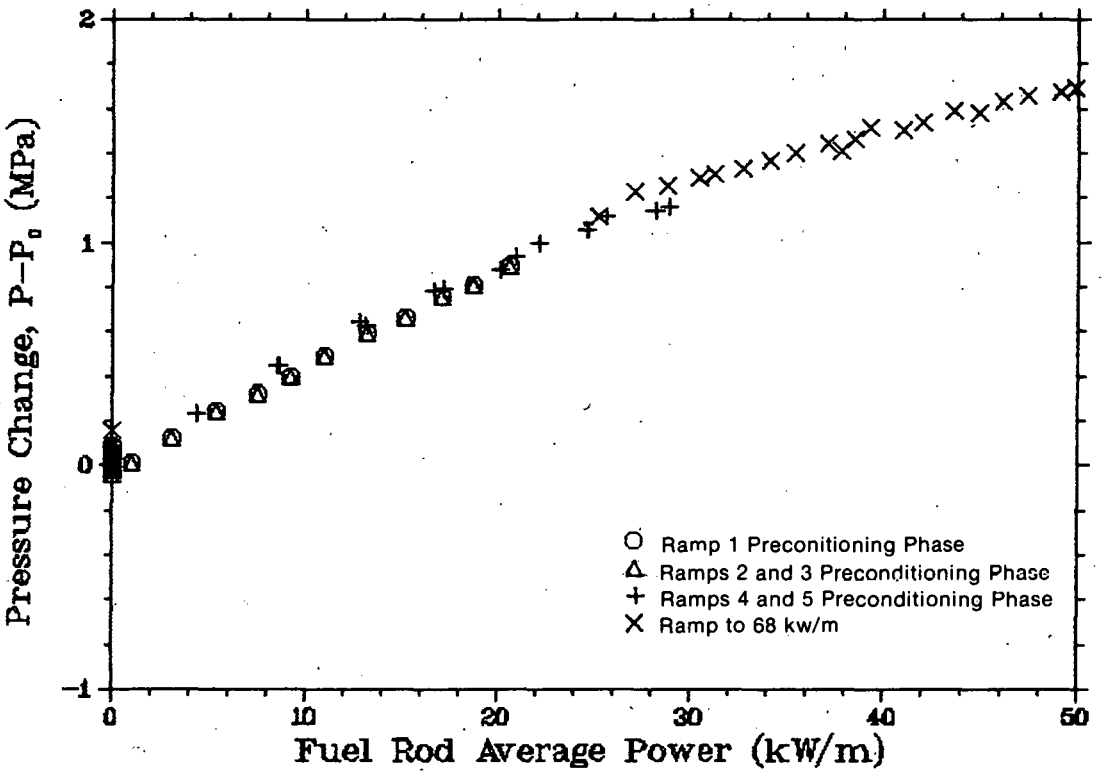

Fig. 23 Change in rod internal pressure for Rod IE-013 during power cycles (signal became extremely noisy during the later phases of the test so that additional filtering was necessary; time drift has been removed).

The pressure data in Figure 20 are presented in terms of fractional pressure change. As discussed in Appendix C, this transformation minimizes the slight differences in initial fill pressure or number of moles of fill gas. Thus, the differences in fractional pressure between large and small gap rods is dominated by the differences in the change of average gas temperature and void volume.

The power cycling had no discernible effect on the change in rod pressure (Figures 21 to 24). Since all the fuel rods had fresh fuel, no fission gases were released and no pressure changes were expected. The removal of the zero drift errors could bias these data. However, if a shift in the slope of pressure versus power had occurred, due perhaps to fuel cracking allowing more of the gas to see hotter interior pellet regions, this effect would not have been altered by the correction. Therefore, fuel cracking and other microstructural changes in the fuel pellets due to thermal cycling, had no observable effect on rod internal pressure.

A comparison of the data in Figure 25 shows that the internal pressure of Rod IE-011 remained constant during the steady-state operation at high power whereas the internal pressure of Rod IE-012 decreased. This trend is not seen in Rod IE-013 and IE-014; but, these signals were so noisy that this shift could have been concealed. Data for these two rods (Rods IE-013 and IE-014) were additionally filtered for the figure so the data do not appear to be noisy. However, the original noise had an amplitude of 1 MPa. Noise in the other two pressure signals was negligible.

The decrease in internal pressure for Rod IE-012 may have been due to accelerated drift of the transducer during this period. If so, that drift would not be removed by the previously mentioned drift correction. However, a comparison of the corrected rod pressure after shutdown and at the start of the test revealed no shift of this magnitude. As discussed in Sections 4.1.3 and 4.1.4, the centerline temperature and cladding surface temperature did not decrease appreciably during the steady power operation at high power so the gas temperature should have

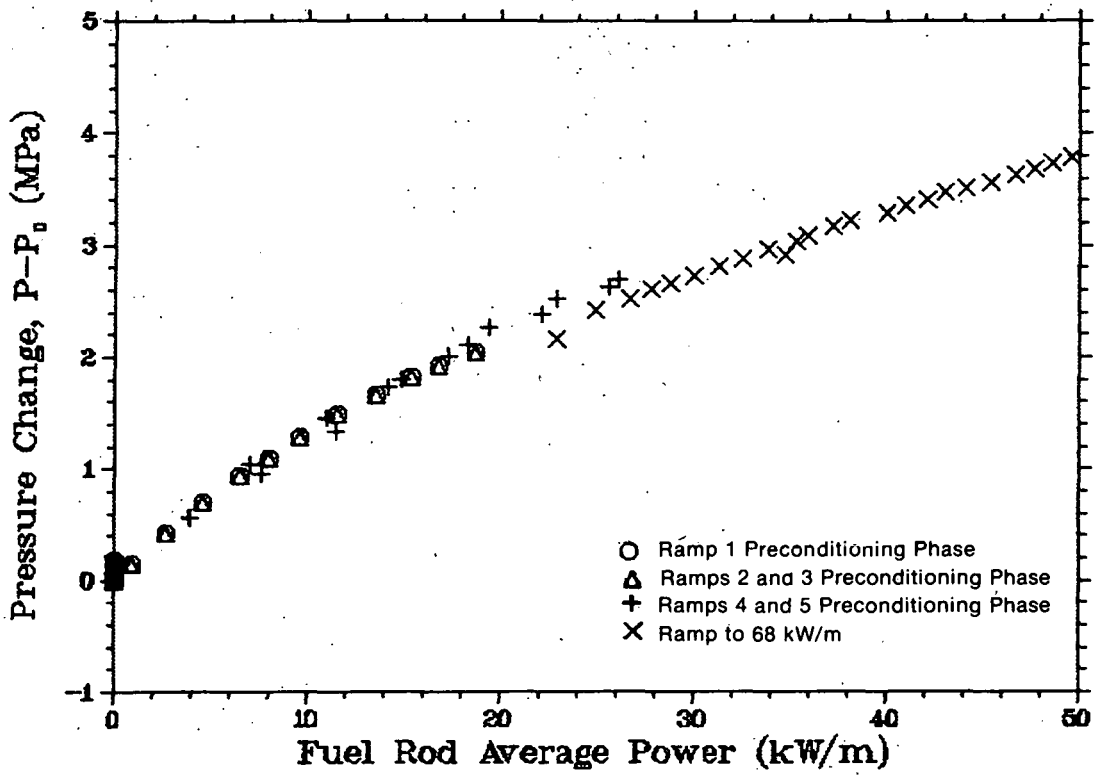

Fig. 24 Change in rod internal pressure for Rod IE-014 during power cycles (signal became extremely noisy during the later phases of the test so that additional filtering was necessary; time drift has been removed).

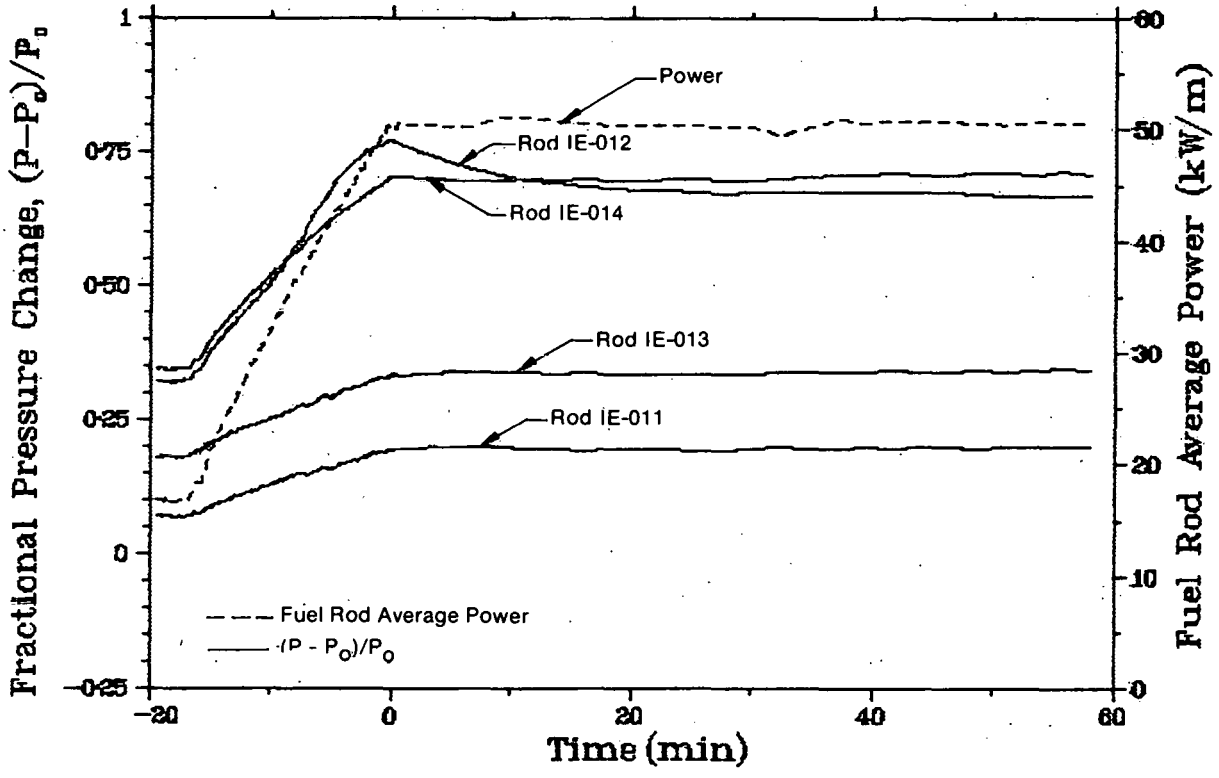

Fig. 25 Fractional change in rod internal pressure for all four rods during ramp and steady-state operation (time drift has been removed).

also remained fairly constant. If the decrease in pressure on Rod IE-012 is a true indication of the pressure during the steady-state period, the available void volume must have increased.

4.1.3 Fuel Centerline Temperature. All four centerline temperature measurements were valid through part of the ramp to 68 kW/m. The ultrasonic thermometers in Rods IE-013 and IE-014 produced extremely noisy data; so, the data for these rods were numerically filtered, as discussed in Appendix C. The data shown in Figures 10 to 13 and plots in this section have been filtered.

Both UTs on Rods IE-013 and IE-014 also exhibited drift during the test. (The drift of the UT on Rod IE-013 appeared to become negligible after the first power ramp). The results from a regression analysis (Appendix C) indicated the drift was probably a zero shift, which would indicate a drift in the signal conditioning equipment. This drift has not been removed because the reason for the drift is not fully understood. The reader is cautioned on the use of the UT data (see Section 6.2.3).

The differences in the centerline temperatures are apparent in Figure 26. At the same power levels, the rods with the smaller gaps (Rods IE-011 and IE-013) have lower centerline temperatures than does Rod IE-012. The greater centerline temperature of Rod IE-012 is due to the larger temperature drop across the large gap in this rod. No change occurs in the slope of centerline temperature versus power at powers well in excess of the powers at which PCI occurred. As discussed in the previous section, the onset of PCI occurred at average rod powers ranging from 9 to 23 kW/m. This range would correspond to a local power at the thermocouple locations of 7 to 19 kW/m on Rods IE-011 and IE-012 and 10 to 25 kW/m on Rods IE-013 and IE-014. This lack of a slope change implies that the PCI is due to localized, random fuel-cladding contact rather than uniform gap closure.

As shown in Figures 27 to 29, very little difference in the centerline temperatures is evident from cycle to cycle. During the first

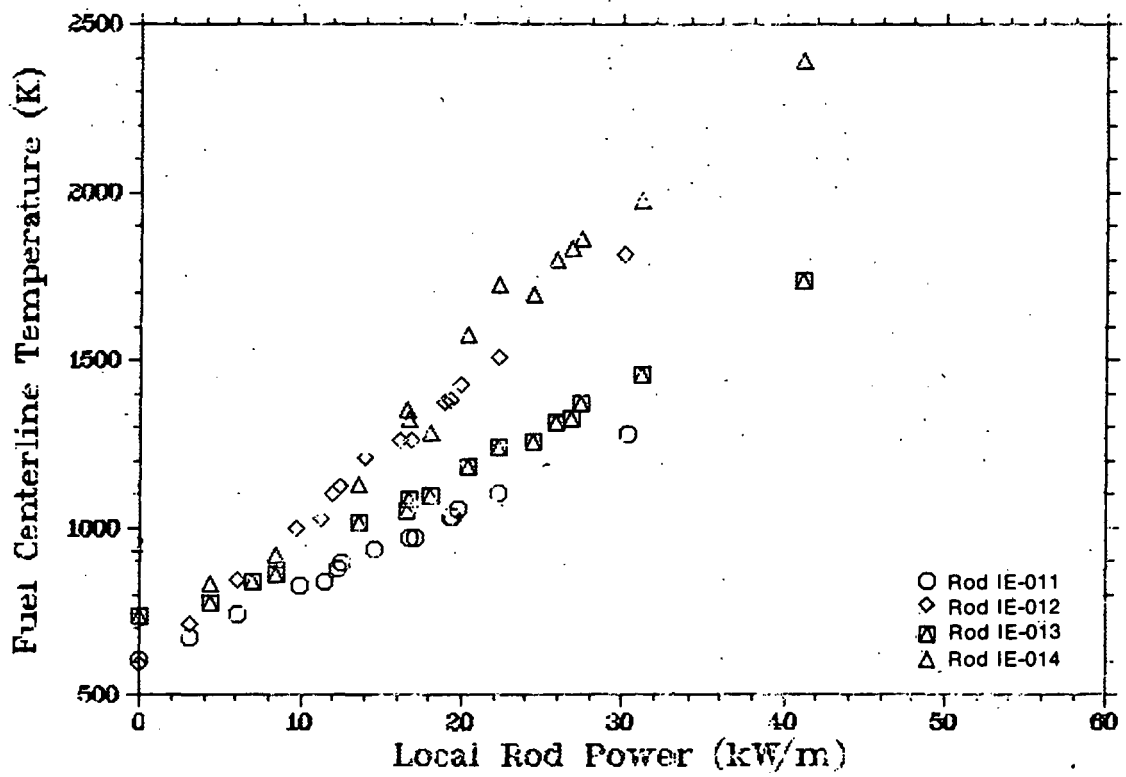

Fig. 26 Fuel centerline temperature for all four rods during pre-film boiling phase of Test IE-2 (the zero on the signal for Rod IE-014 drifted severely after the first power ramp so only the data for Ramp 1 are shown).

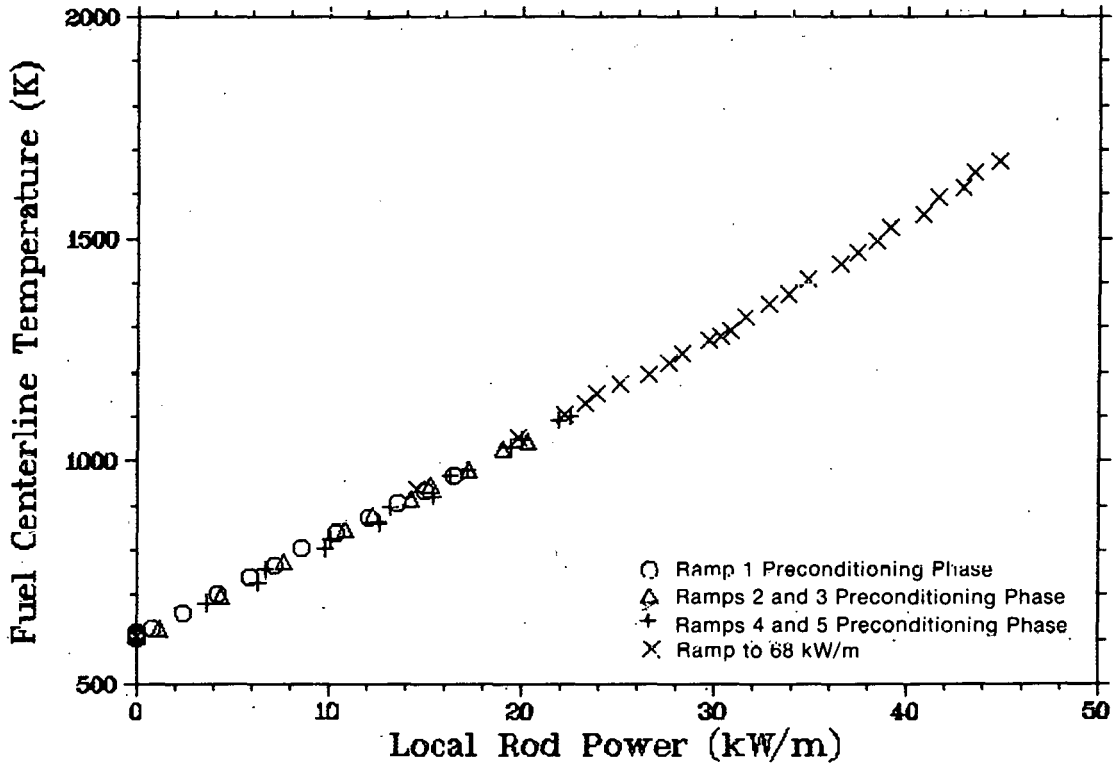

Fig. 27 Fuel centerline temperature for Rod IE-011 during power cycles.

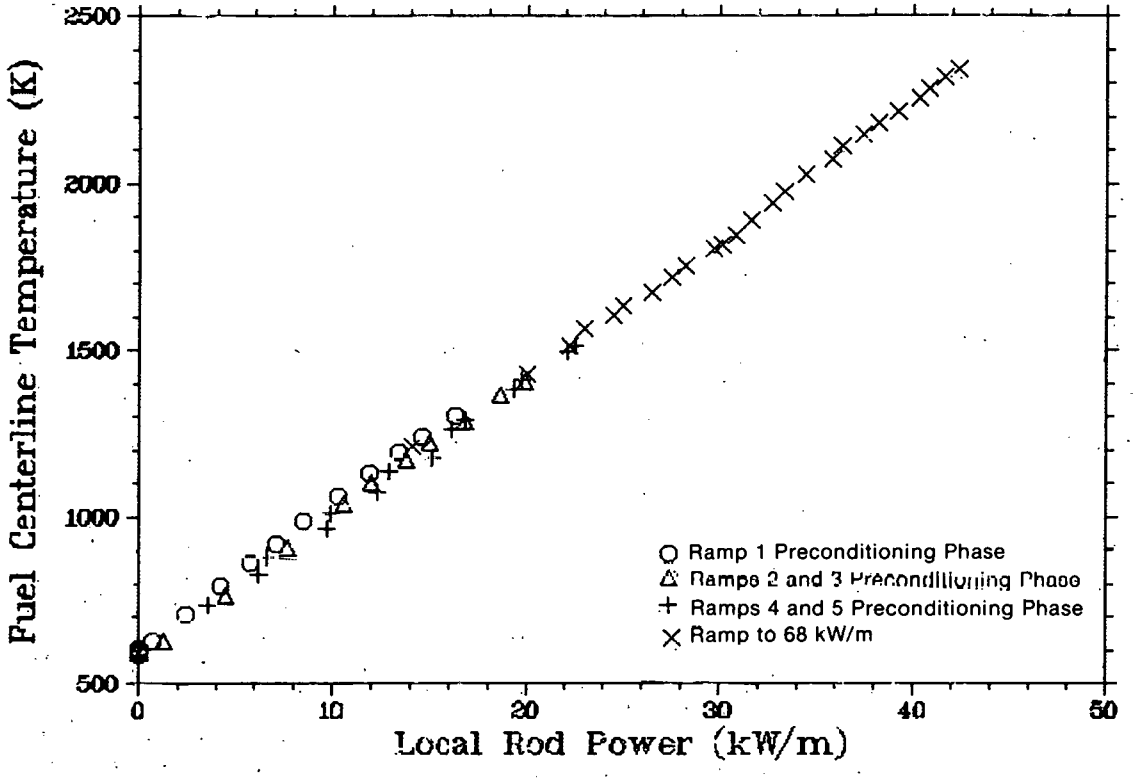

Fig. 28 Fuel centerline temperature for Rod IE-012 during power cycles.

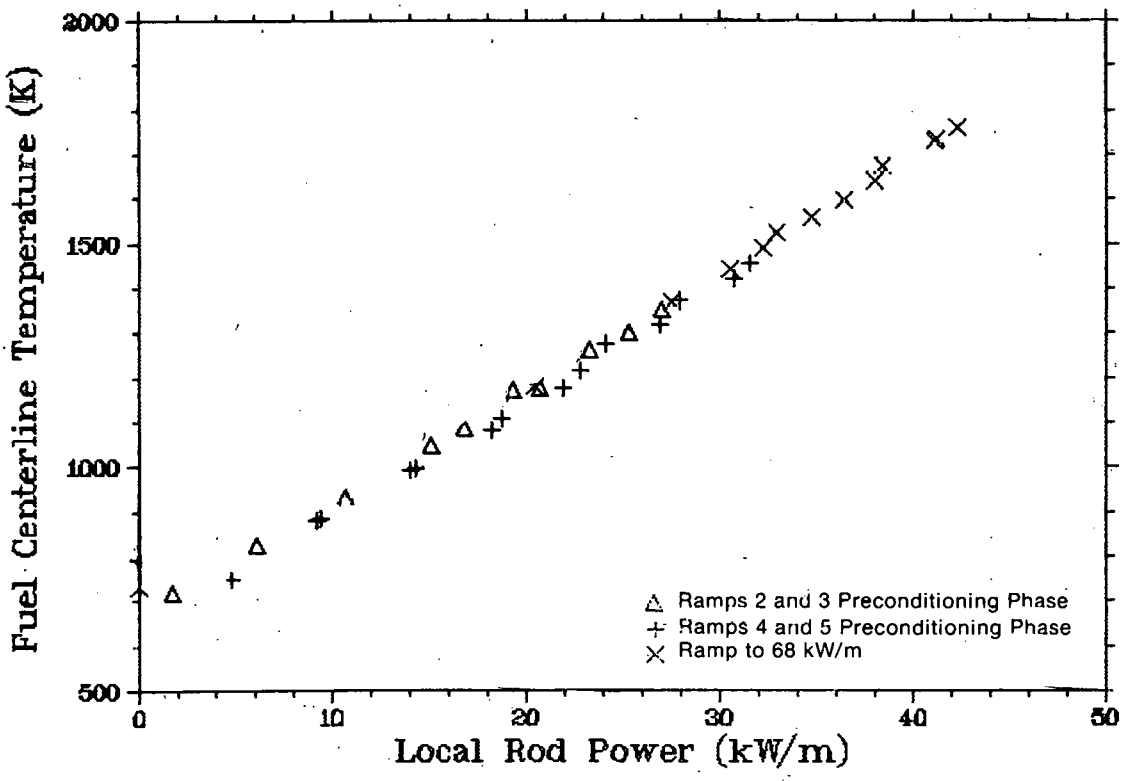

Fig. 29 Fuel centerline temperature for Rod IE-013 during power cycles (data have additionally been filtered).

ramp, the flow rate (which affects the surface temperature) was also reduced but this effect on centerline temperature is too small to be seen[a].

The differences in centerline temperature due to initial gap are also apparent during the power ramp to and hold at 68 kW/m as shown in Figure 30. The rods with the larger gaps have higher centerline temperatures than do the rods with the smaller gaps. The centerline temperatures did not change significantly during the steady operation at high power. The centerline temperatures exhibit a slight decrease, but this is probably due to the decrease in power rather than a change in the heat transfer through and from the fuel.

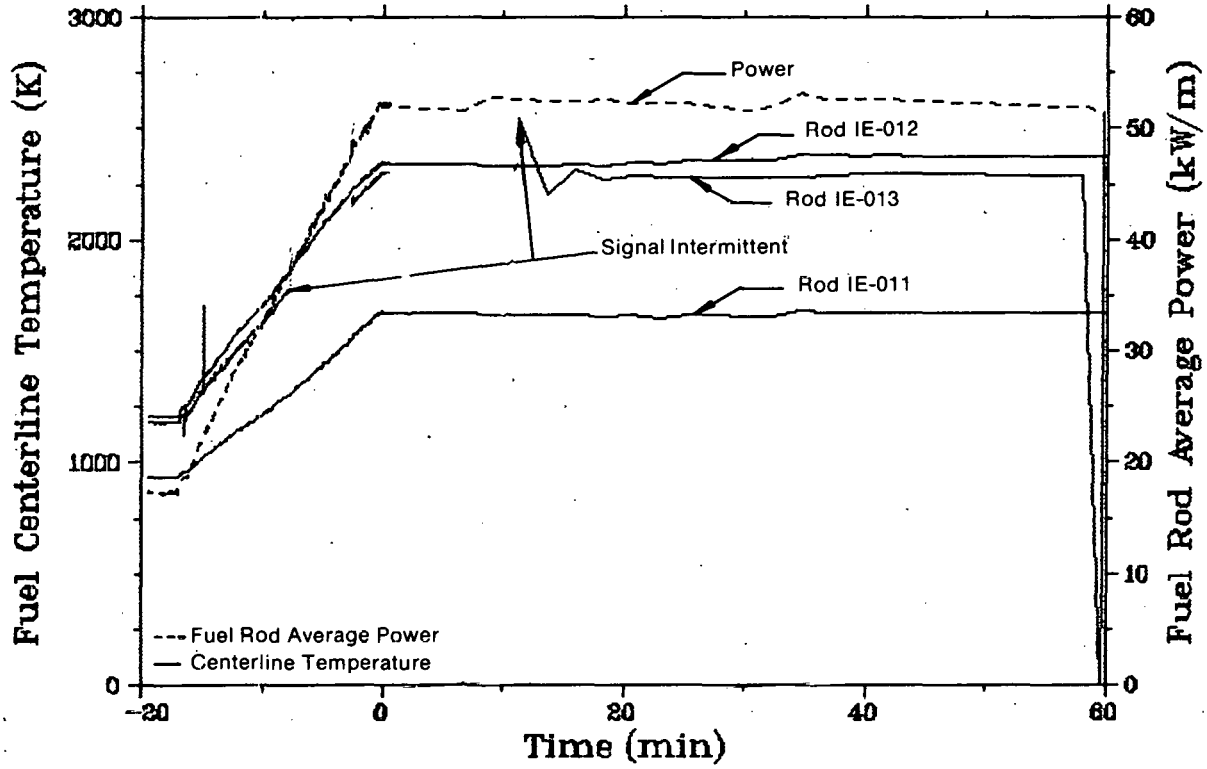

Fig. 30 Fuel centerline temperatures for Rods IE-011, IE-012, and IE-013 during power ramp and steady-state operation (data for Rod IE-013 have been additionally filtered).

[a] Fuel centerline temperatures have not been shown for Rod IE-014 because the drift was so severe that results after Ramp 1 would be misleading.

4.1.4 Cladding Surface Temperature. No reliable measurements of the absolute cladding surface temperature were made due to the dominance of systematic measurement uncertainty. The spring-loaded thermocouples used on the rods with irradiated cladding (Rods IE-011 and IE-012) have normally indicated lower temperatures than the absolute cladding surface temperatures. Because of their design, the cladding surface thermocouples act as fins perturbing the flow and the thermal symmetry of the fuel rods. The thermocouples on the other rods (Rods IE-013 and IE-014) were mounted in grooves by brazing or laser welding or both. These thermocouples generally indicate temperatures higher than the expected surface temperature due to their mid-wall location. The difference in temperature between a thermocouple mounted in a groove and the absolute cladding surface temperature is dependent upon the degree of bonding of the thermocouple to the cladding and exact radial location of the thermal junction within the thermocouple sheath. The plots of cladding surface temperature versus power are given in Section 6.2.4 along with the FRAP-T3 predictions.

4.2 Film Boiling Experimental Results

The PCM transient was initiated by a flow reduction at a constant average (all four rods) peak power of 68 kW/m. As shown in Figures 31 to 34, all four rods experienced an abrupt reduction in the heat transfer from their surfaces at the onset of film boiling. Immediately prior to the flow reduction, all four rods were in nucleate boiling. As the flow decreased, departure from nucleate boiling occurred, with the heat transfer going through a transition regime and reaching stable film boiling within 20 seconds. DNB was indicated by an abrupt increase in cladding elongation, fuel centerline temperature, rod internal pressure, and cladding surface temperatures (for part of the cladding thermocouple elevations). As seen in Figures 31 and 35, at a flow rate of 530 cm^3/s (2550 $kg/s\text{-}m^2$), cladding strain started to increase on Rod IE-011. There were no corresponding indications in centerline temperature, rod internal pressure, and cladding surface temperatures shown by Table II. At approximately the same time, there were slight indications of DNB on Rods IE-013 and IE-014 (Figures 33 and 34) at mass fluxes of 2750 $kg/s\text{-}m^2$

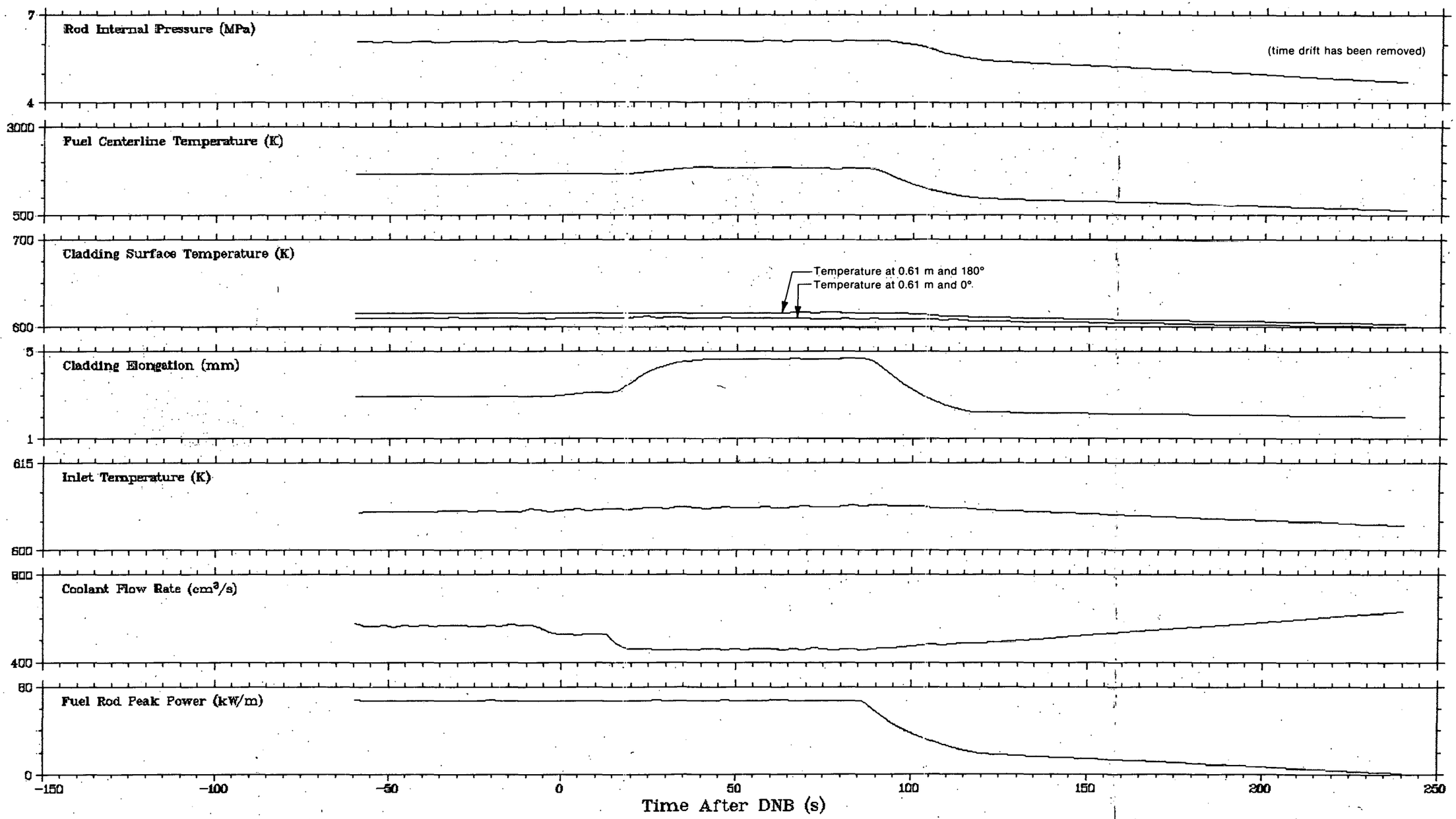

Fig. 31 Rod IE-011 behavioral data after DNB.

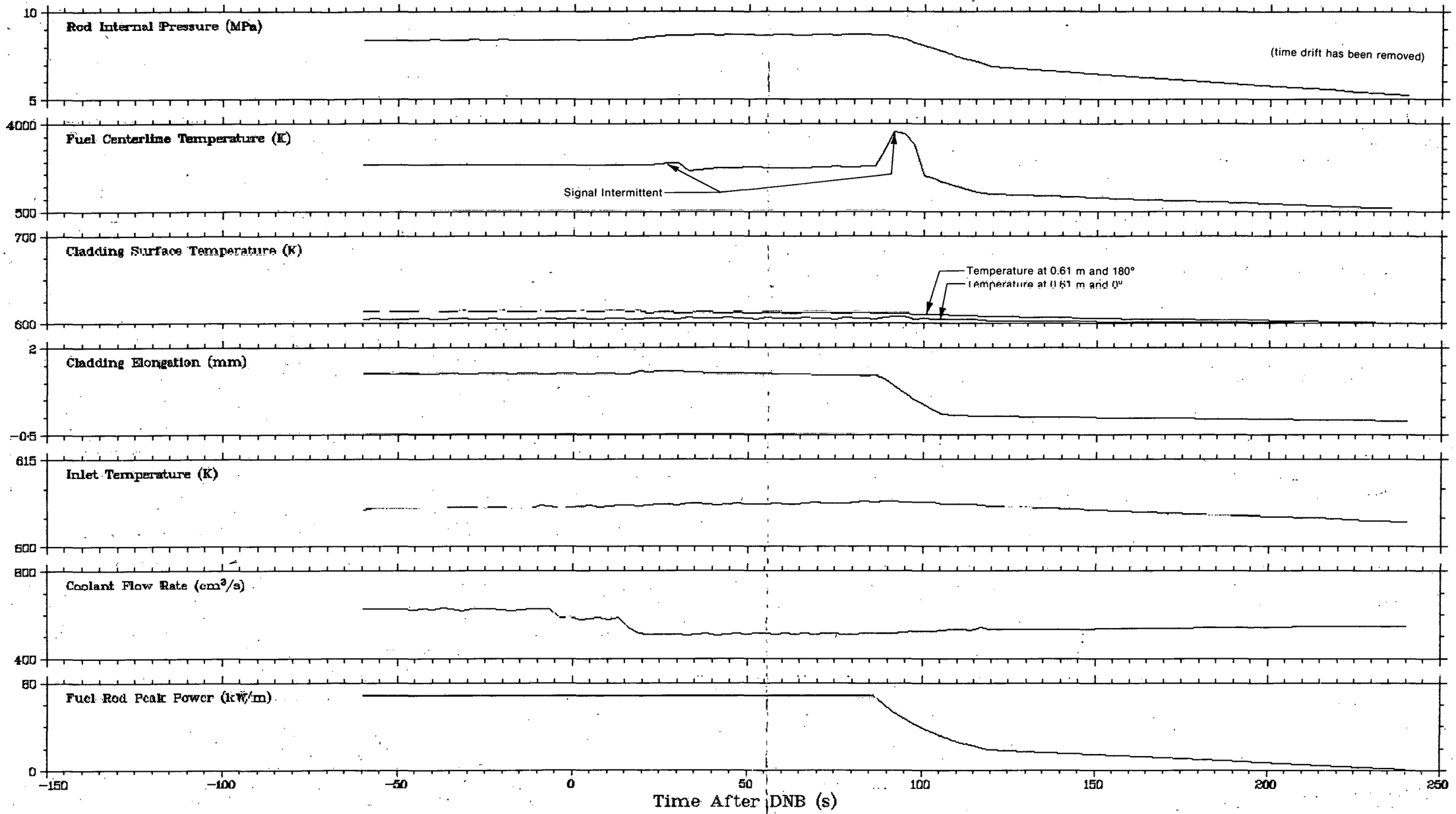

Fig. 32 Rod IE-012 behavioral data after DNB.

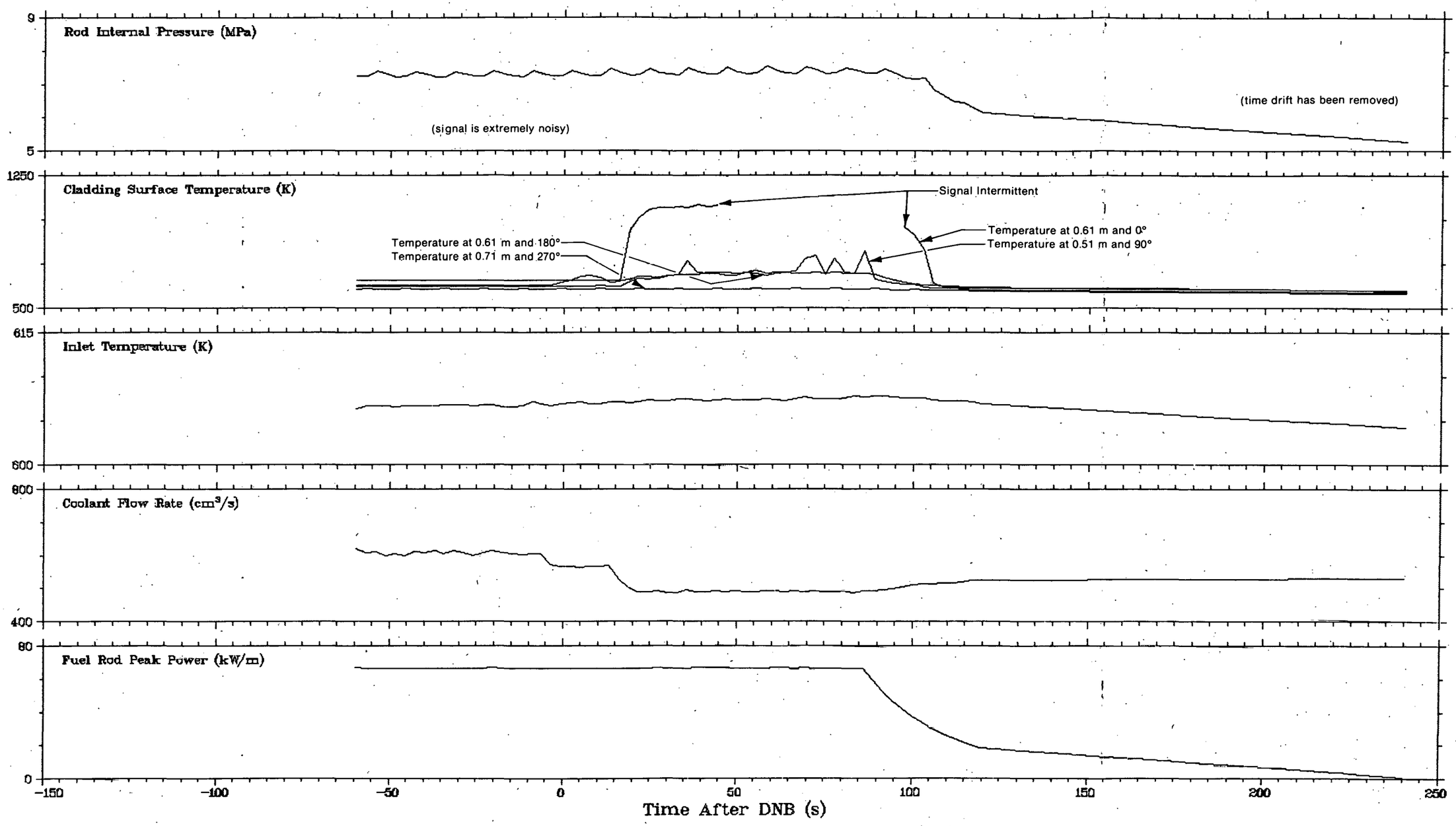

Fig. 33 Rod IE-013 behavioral data after DNB.

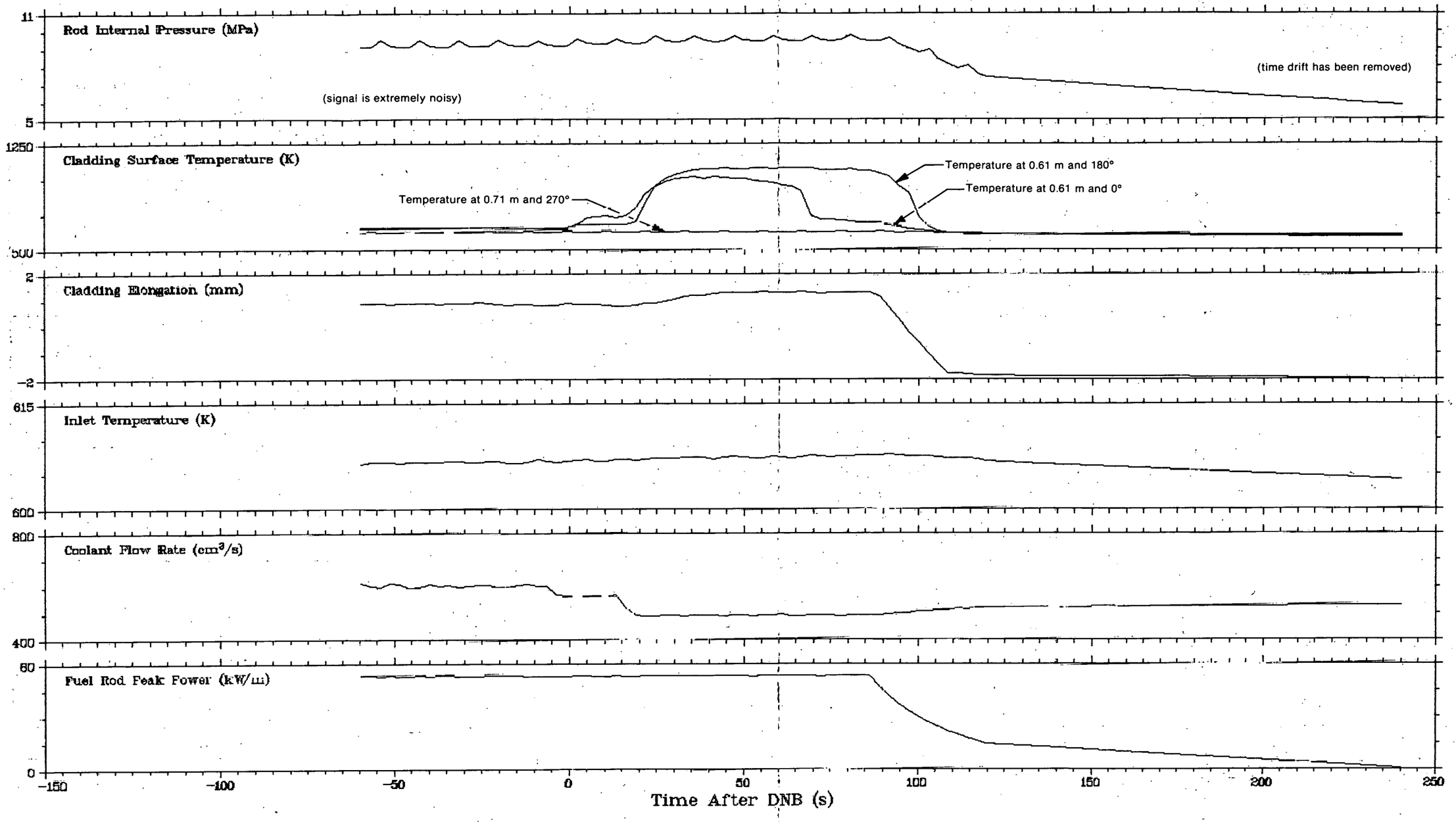

Fig. 34 Rod IE-014 behavioral data after DNB.

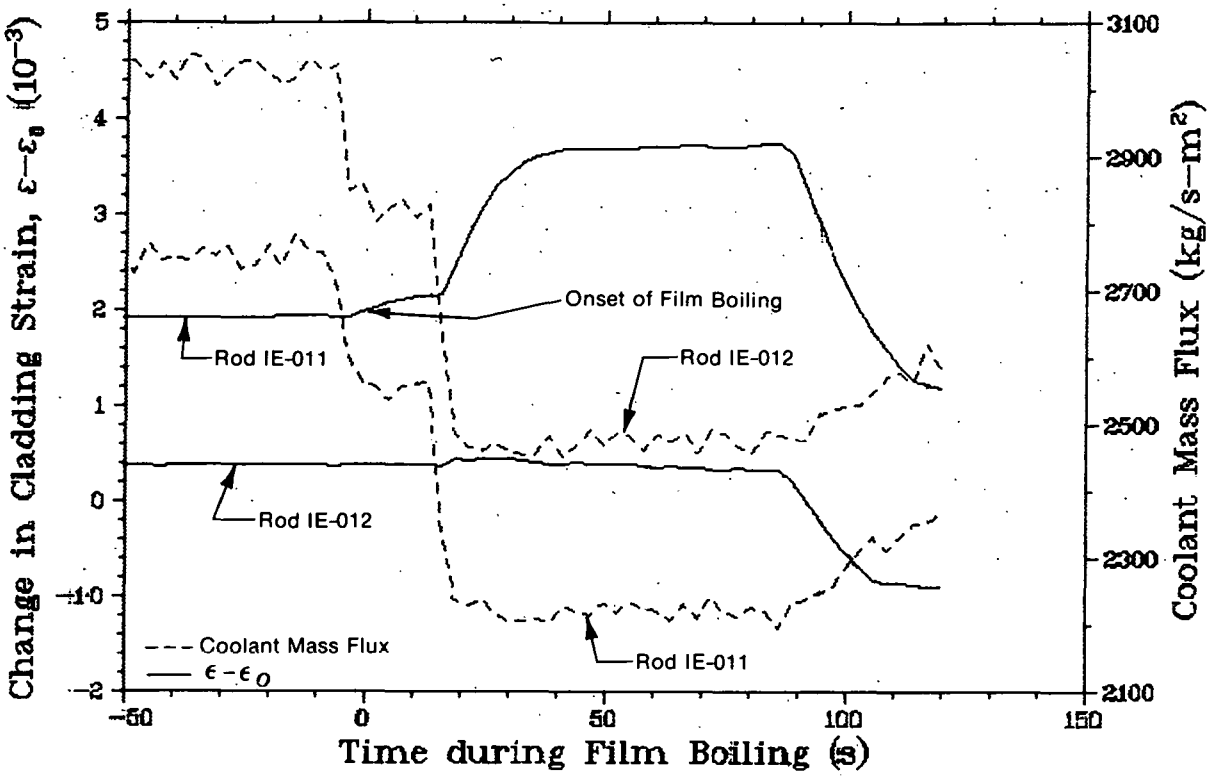

Fig. 35 Change in cladding strain for Rods IE-011 and IE-012 during film boiling.

for both. Rod pressures on both Rods IE-013 and IE-014 increased as shown in Figure 36. Centerline temperature of Rod IE-013 also increased as shown in Figure 37. Cladding surface temperatures at the 0.61-m elevation on Rods IE-013 and IE-014, both at 0° and 180°, and the 0.51 m elevation on Rod IE-013, at 90°, increased (Figure 38). After approximately 24 seconds the flow was further reduced; the resulting mass fluxes were (a) Rod IE-011 - 2220 kg/s-m^2, (b) Rod IE-012 - 2475 kg/s-m^2, (c) Rod IE-013 - 2360 kg/s-m^2, and (d) Rod IE-014 - 2370 kg/s-m^2. The heat transfer on all four rods then sharply decreased, reaching equilibrium in stable film boiling. All measured cladding strains and centerline temperatures increased. Rod internal pressure on Rods IE-012 and IE-014 and cladding surface temperature at elevations of 0.61 m and below also increased. The spring-loaded cladding surface thermocouples on Rods IE-011 and IE-012 gave no indication of film boiling, although PIE (Section 5) results indicated that these rods were in film boiling over essentially the same region. During film boiling, all of the measured

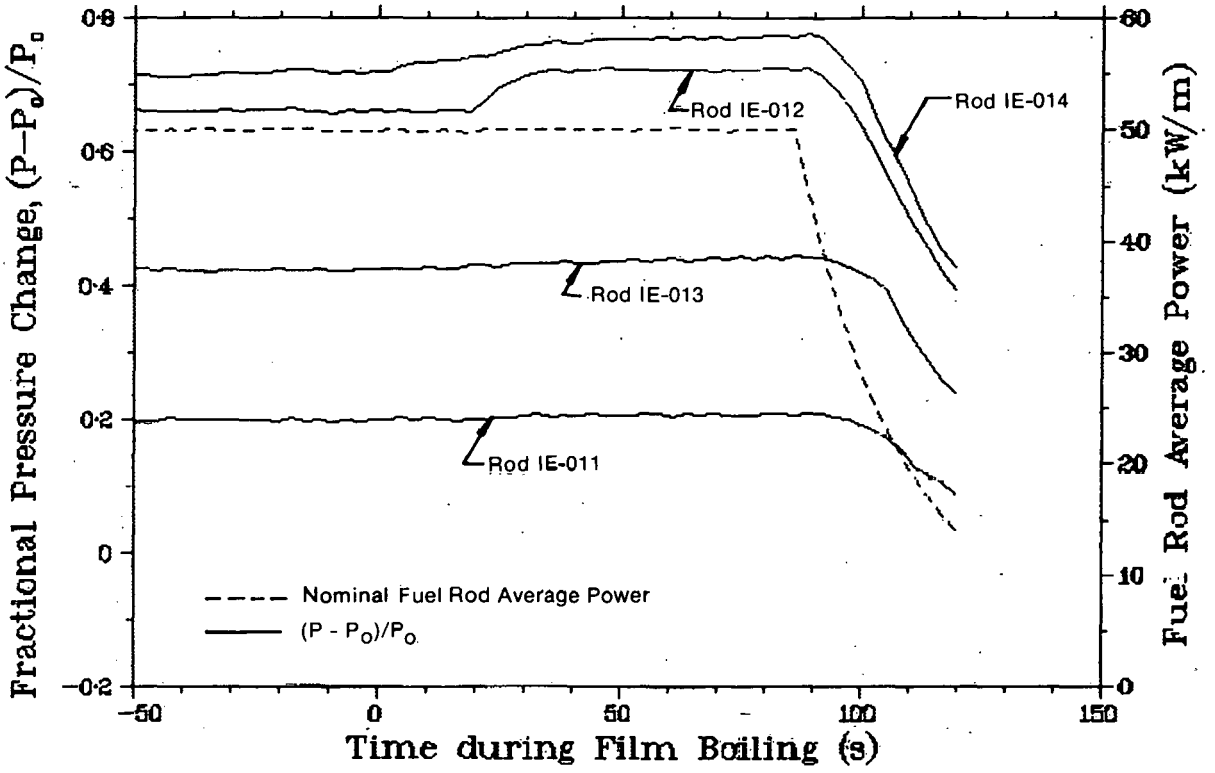

Fig. 36 Fractional change in pressure for all rods during film boiling.

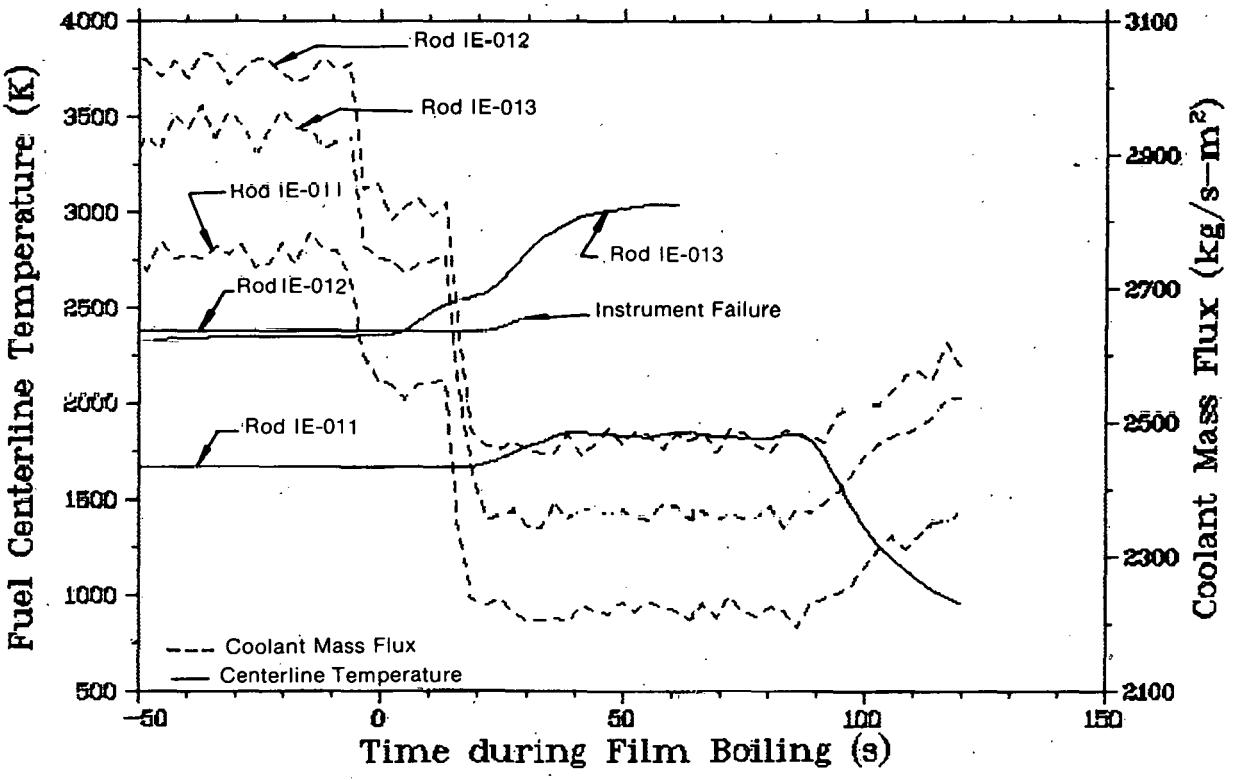

Fig. 37 Fuel centerline temperature for Rods IE-011, IE-012, and IE-013 during film boiling.

cladding surface temperatures on Rod IE-013 and IE-014 at elevations of 0.51 and 0.61 m appeared to reach equilibrium except for the temperature on Rod IE-013 at 0.51-m elevation (it exhibited fairly periodic oscillations in temperature until the complete collapse of the vapor layer at termination of the test).

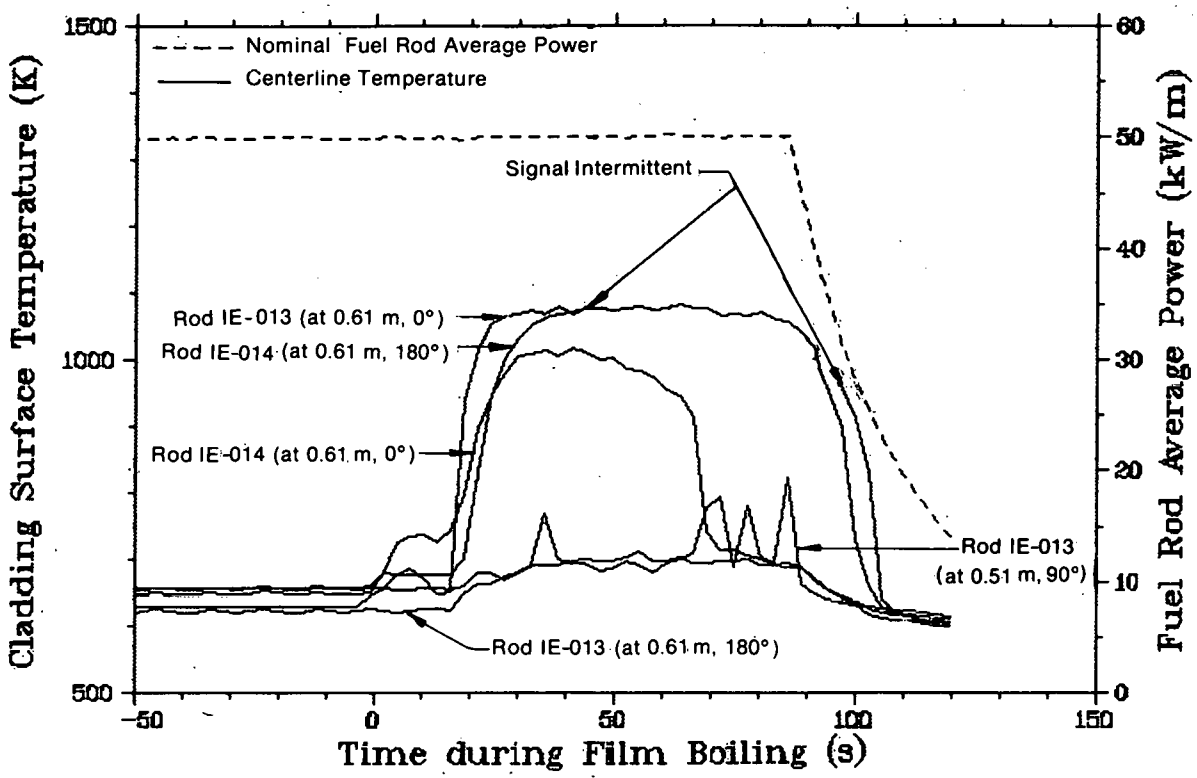

Fig. 38 Cladding surface temperatures which indicated film boiling during film boiling.

After one minute in film boiling on Rod IE-011, the cladding surface temperature at the 0.61-m elevation and 0-degree orientation on Rod IE-014 dropped sharply, indicating that the vapor layer collapsed over this part of the rod. The region of the vapor collapse must have been small since no corresponding decrease in cladding elongation on this rod was seen. After 1.5 minutes of film boiling on Rod IE-011, the rod power was decreased and the flow increased. Power was decreased at a rate of 1.4 kW/m per second from 60 kW/m down to 19 kW/m and at a rate of 0.2 kW/m per second down to 0 kW/m. The flow went up approximately 200 kg/s-m^2 over a 30-second period due to collapse of the voids, it then stabilized. At the beginning of the power decrease, cladding

strains, rod internal pressures, fuel centerline temperatures, and those cladding surface temperatures indicating film boiling started to decline. By the time the average rod power had reached 19 kW/m, all measurements were at pre-DNB readings.

The effects of different initial diametral gap sizes on rod behavior were readily apparent during this transient. Large differences in cladding strain of the rods were observed during the transition to and during film boiling (Figure 35). Rod IE-011 (0.102-mm gap) showed an elongation increase of approximately three to eight times that of Rods IE-012 and IE-014 (0.343 mm gap). Internal pressures (Figure 36) of Rods IE-012 and IE-014 showed larger increases than did the pressures of Rods IE-011 and IE-013. Centerline temperatures cannot be compared because the thermocouple on Rod IE-011 was the only centerline temperature measuring device to survive film boiling. Figure 37 shows this measurement with the other centerline measurements until the time of instrument failure. The cladding surface temperatures, for Rods IE-013 and IE-014, (the spring-loaded thermocouples on Rods IE-011 and IE-012 did not indicate film boiling) are shown in Figure 38. Additional discussions are contained in Section 6.

5. PRELIMINARY POSTIRRADIATION EXAMINATION RESULTS

After the completion of Test IE-2, test train hardware was disassembled in the PBF canal and the four rods, in their flow shrouds, were shipped to the hot cells. Preliminary results of the visual examinations and dimensional characterization are presented in this section. Complete postirradiation examination results, including detailed metallography, are to be published in a separate report.

5.1 Visual Examination

All four rods were intact. The film boiling zones were visually distinguishable by cladding collapse into pellet-to-pellet interfaces, cladding oxidation, and oxide spalling. Detailed observations on each rod are presented in the following sections; photographs of the rods through their film boiling zones are shown in Figures 39 to 42.

5.1.1 Rod IE-011. The film boiling zone on Rod IE-011 extended from the 0.546 to 0.679-m elevation, as measured from the bottom of the rod[a]. Oxide spalling and cladding collapse into pellet-to-pellet interfaces occurred throughout the film boiling zone, but were more pronounced on the 180 degree axis of the rod (Figure 40). The rod was intact with no obvious cladding failures.

5.1.2 Rod IE-012. The film boiling zone on Rod IE-012 extended from the 0.542 to 0.679-m rod elevation. The rod was intact with no obvious cladding perforations. Cladding collapse into pellet-to-pellet interfaces occurred over the entire zone, but was less pronounced than observed on Rod IE-011 (Figures 39 and 40). On the basis of pretest dimensional data in Appendix B, Rod IE-012 contained one fuel pellet with a diameter of 8.113 mm, slightly smaller than the nominal diameter of 8.390 mm. Cladding collapse onto this pellet was clearly distinguishable at the 0.584 to 0.597-m rod elevation (Figure 39). This elevation

---

[a] All elevations are referenced from the bottom of the fuel rod. The fuel column starts at 12.7 mm above the bottom of the rod.

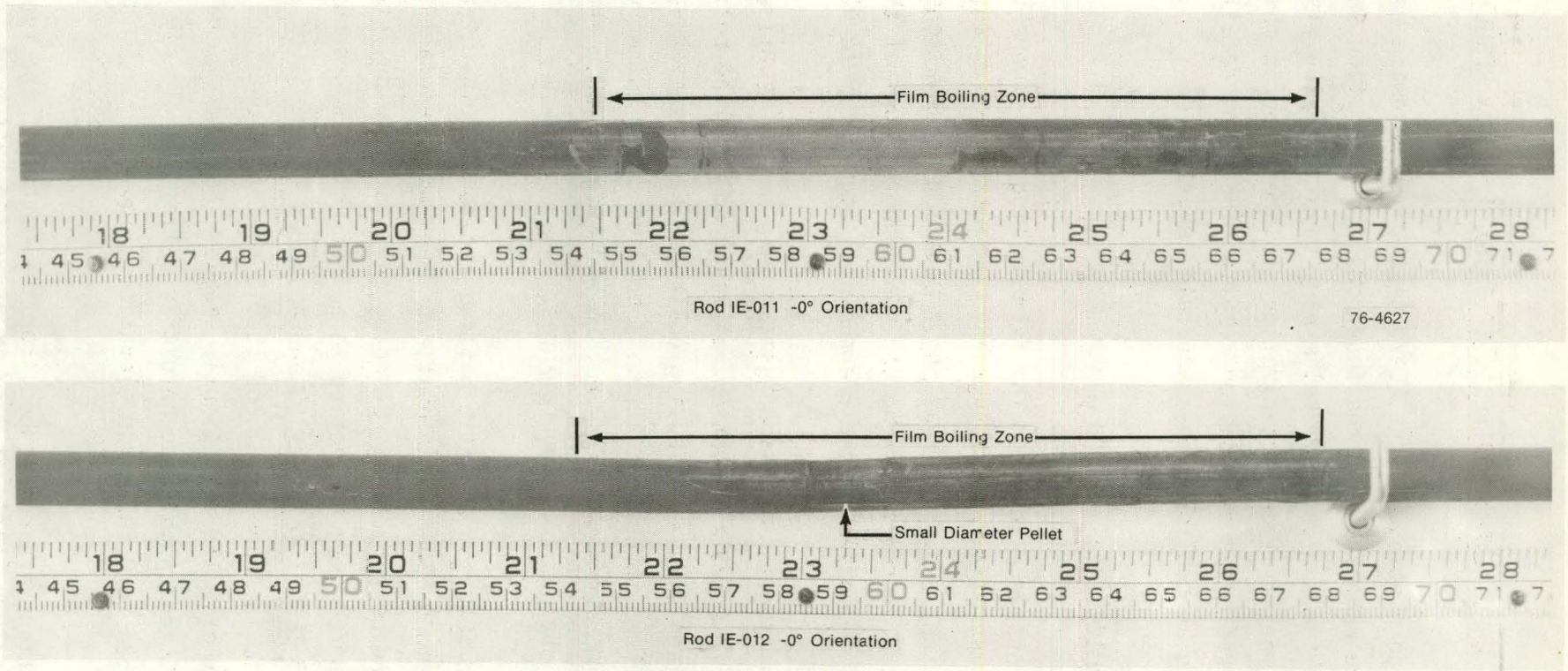

Fig. 39 Film boiling zones of Rods IE-011 and IE-012 at 0° orientation.

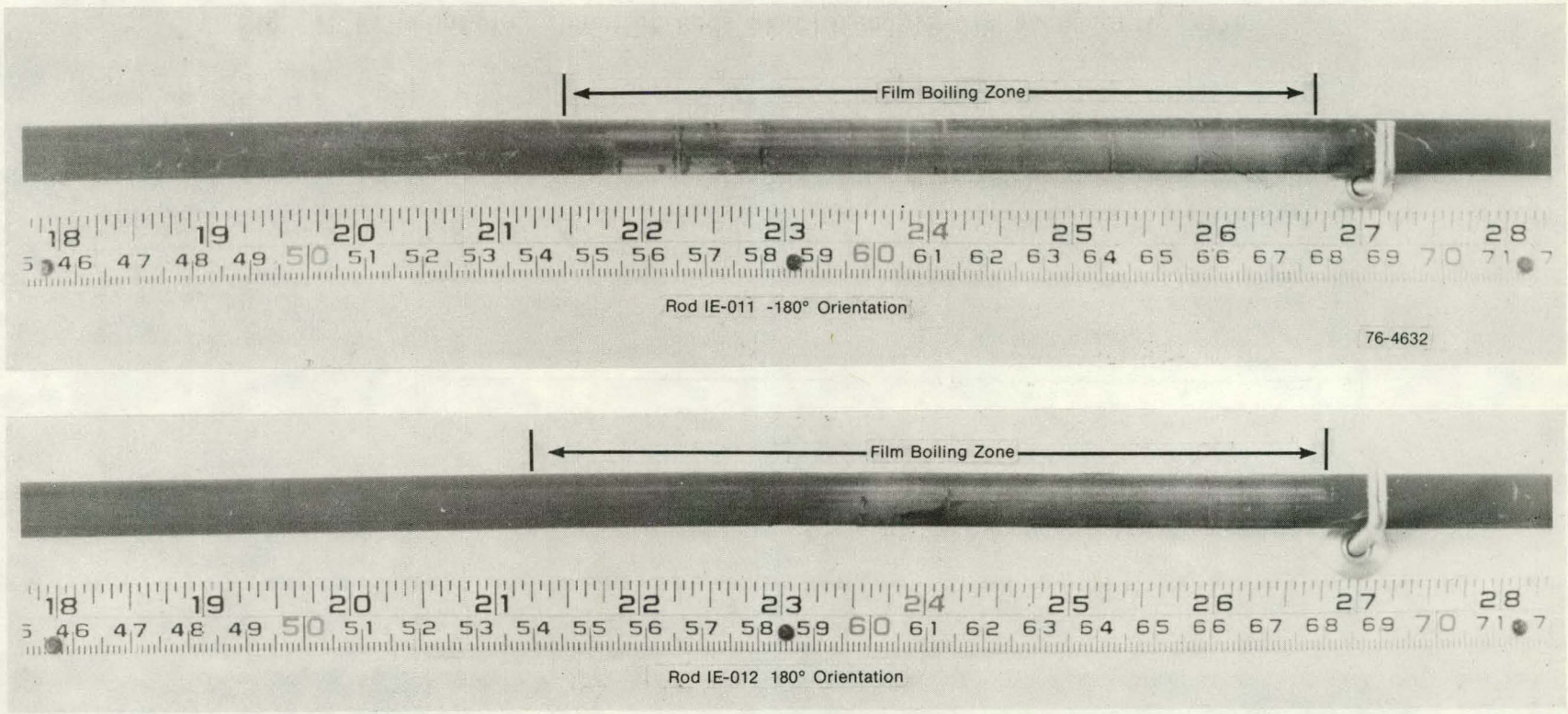

Fig. 40 Film boiling zones of Rods IE-011 and IE-012 at 180° orientation.

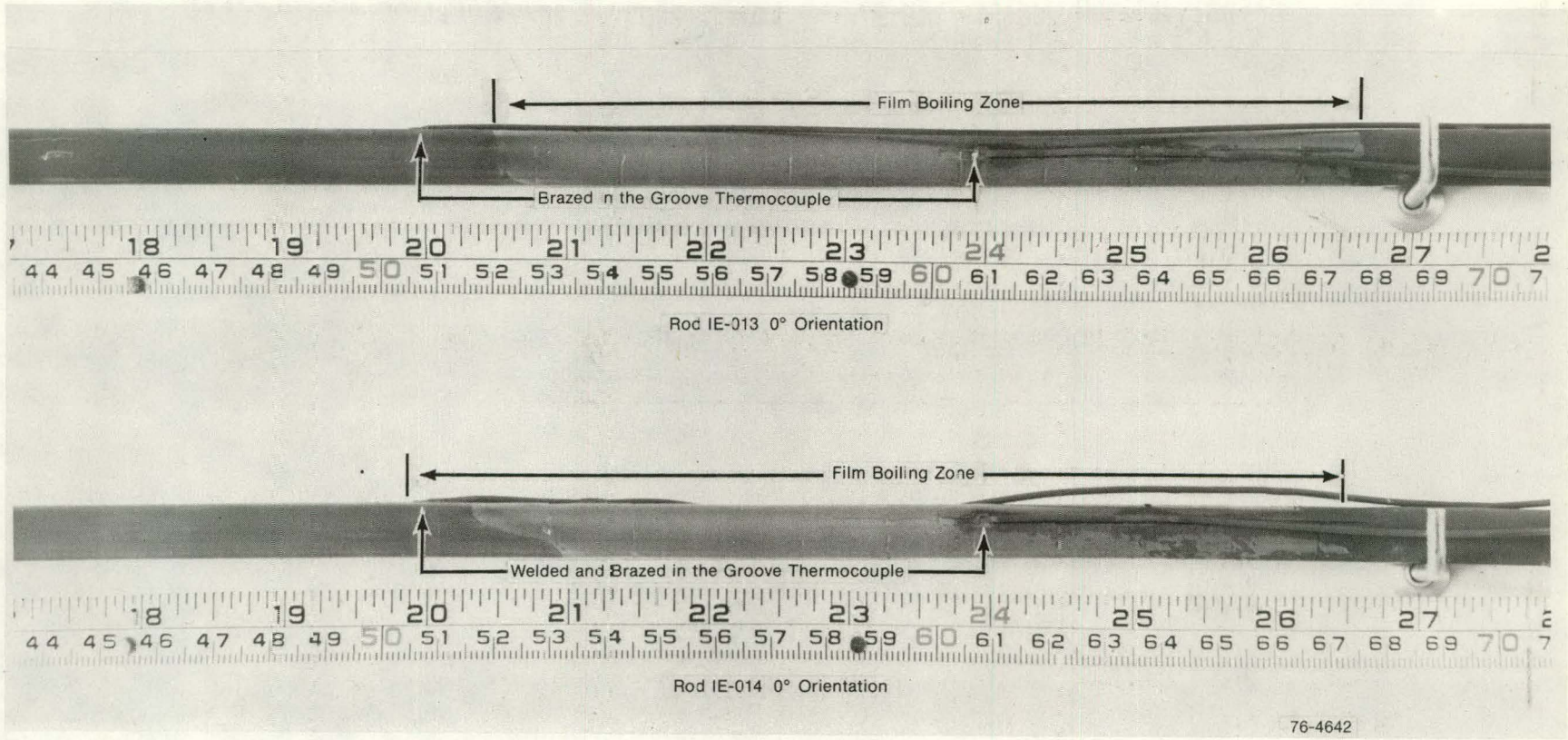

Fig. 41 Film boiling zones of Rods IE-013 and IE-014 at 0° orientation.

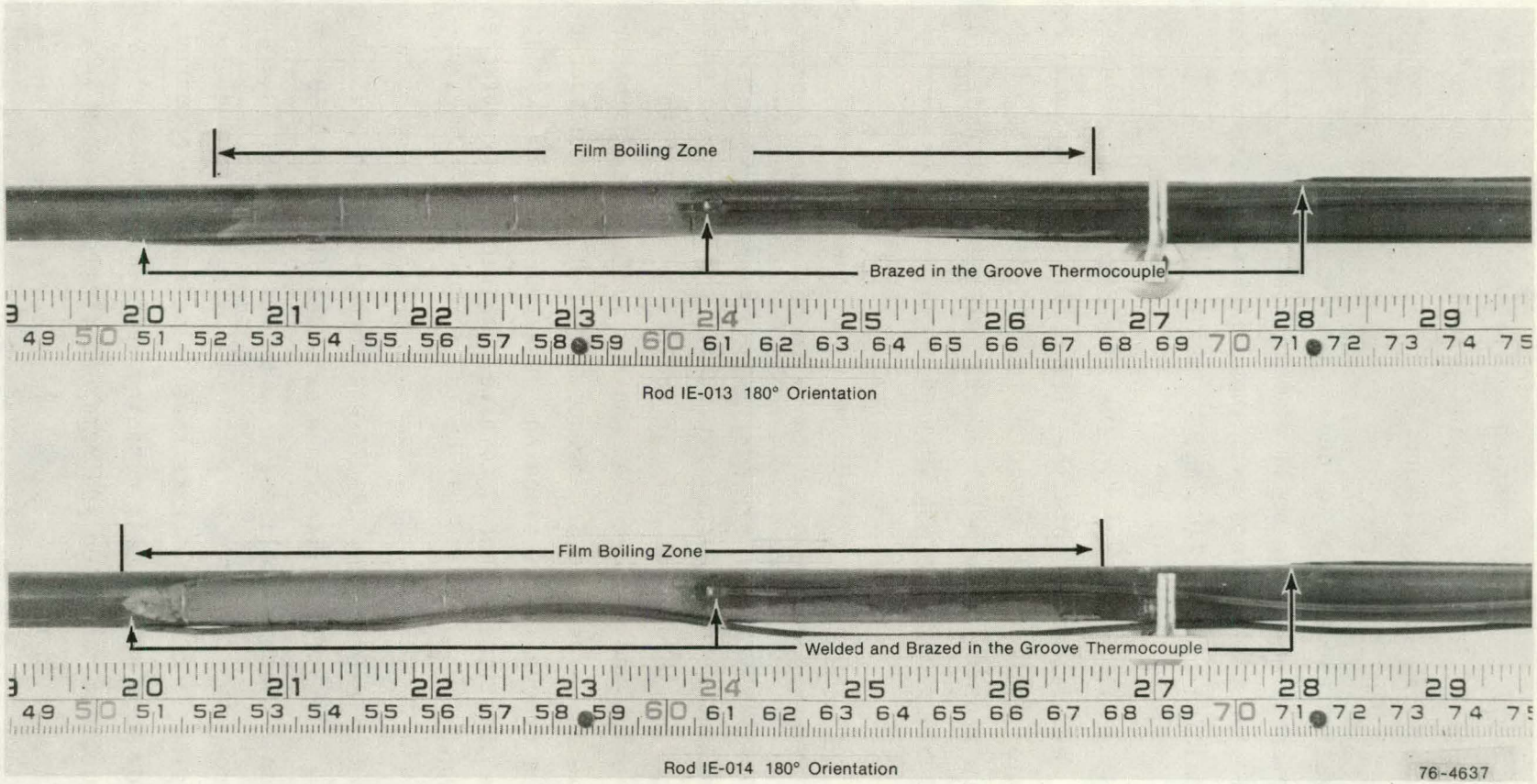

Fig. 42 Film boiling zones of Rods IE-013 and IE-014 at 180° orientation.

is approximately 7 mm higher than the elevation at which the pellet was loaded, which might indicate the axial growth of the fuel column below this pellet was 7 mm from cold conditions to film boiling conditions. Neutrographs of Rod IE-012 disclosed a 5-mm gap between pellets at the 0.567-m elevation and a 2-mm gap due to a transverse crack in the fuel pellet immediately below the small diameter pellet. No definite indications of cladding collapse into these gaps were observed during the visual examination of the cladding.

No oxide spalling occurred on the zero-degree axis of the rod. Black oxide was present in both the film boiling zone and the rest of the rod. Oxide spalling did occur on the 180-degree axis of the rod; however, bare zircaloy base metal was not exposed. Rather, a dark grey colored film was present on the spalled areas.

5.1.3 Rod IE-013. Rod IE-013 was intact with no obvious cladding perforation (Figures 41 and 42). The film boiling zone extended from the 0.521 to 0.676-m rod elevation. Cladding collapse into pellet-to-pellet interfaces which occurred throughout the zone appeared more pronounced on the 180-degree axis of the rod. In the film boiling zone, most of the oxide had spalled from the rod surface, exposing bare zircaloy base metal. The Type S thermocouples, which had a spaded junction brazed into a groove in the cladding, appeared to be in excellent condition. The junctions appeared to have remained firmly attached in the cladding groove.

5.1.4 Rod IE-014. Rod IE-014 was intact with no obvious cladding perforations. The film boiling zone extended from the 0.505 to 0.676-m rod elevation. Cladding collapse into pellet-to-pellet interfaces occurred throughout the zone with the collapse more pronounced on the 180-degree side of the rod. Extensive oxide spalling occurred, exposing bare zircaloy base metal. All cladding surface thermocouples appeared to be in excellent condition and remained firmly attached in their grooves in the cladding.

5.2 Dimensional Characterization

The results of diameter measurements made along the length of each rod are shown in Figures 43 through 46. For Rods IE-012, IE-013, and IE-014 the cladding uniformly collapsed throughout the film boiling zone. The diameter of Rod IE-011 may have slightly increased through the film boiling zone. As expected, the observed collapse strains for Rods IE-012 and IE-014 (initial diametral gaps of 0.343 mm) were greater than for Rods IE-011 and IE-013 (initial diametral gaps of 0.102 and 0.100 mm, respectively).

Estimates were made of the amount of bowing in each rod. Rod IE-011 bowed in the 180-degree direction from the 0.46 to 0.71-m rod elevation with an estimated maximum deflection of 4 mm. Rod IE-013 bowed in the 180-degree direction from 0.46 to 0.76-m rod elevation with an estimated maximum deflection of 6 mm. Rod IE-014 bowed in the zero-degree direction from the bottom of the rod to 0.62-m rod elevation with a deflection of approximately 4 mm. Rod IE-012 bowed in the 180-degree direction from 0.46 to 0.66-m rod elevation with an estimated maximum deflection of 10 mm. The bow on Rod IE-012 displayed an abrupt change in direction or "kinked" appearance at the 0.57-m location (Figure 39), 15 mm below the location of the undersized pellet and in the region of the 5-mm gap between pellet interfaces (Section 5.1.2).

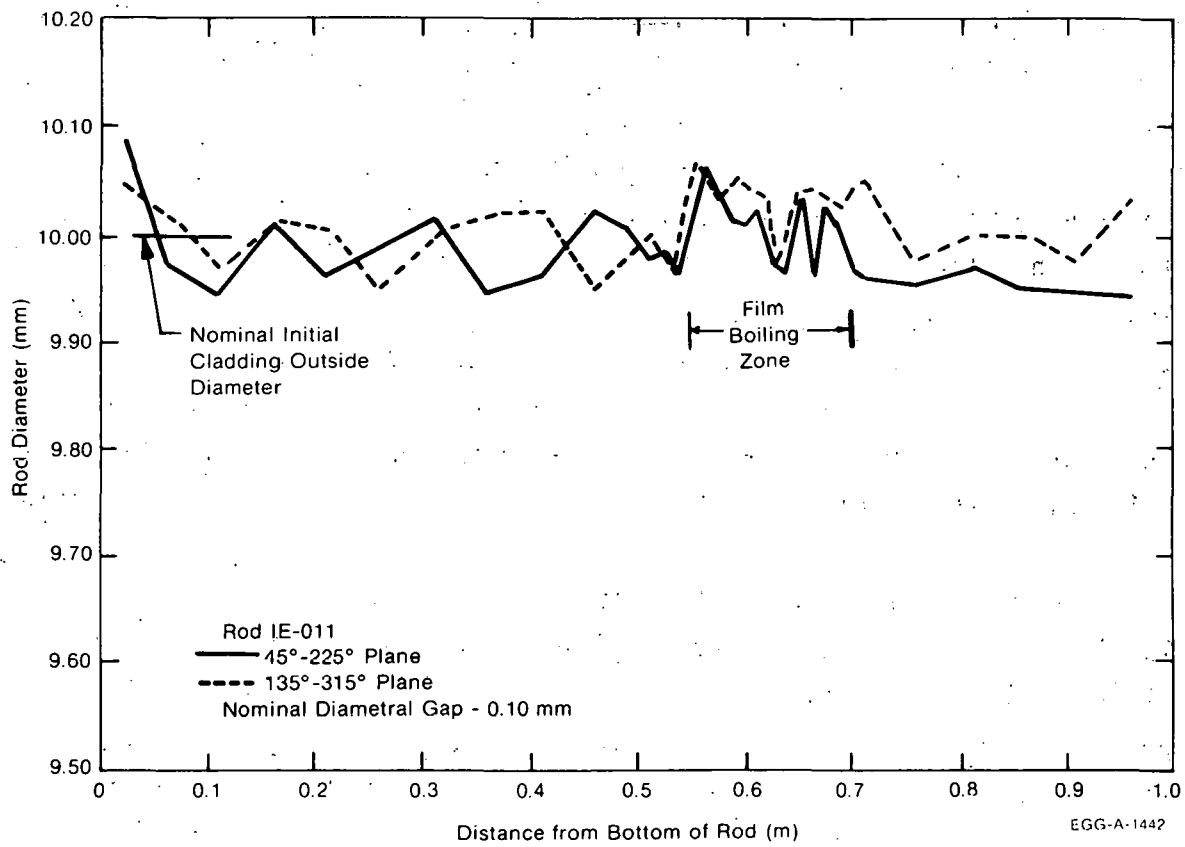

Fig. 43 Posttest diametral measurements on Rod IE-011.

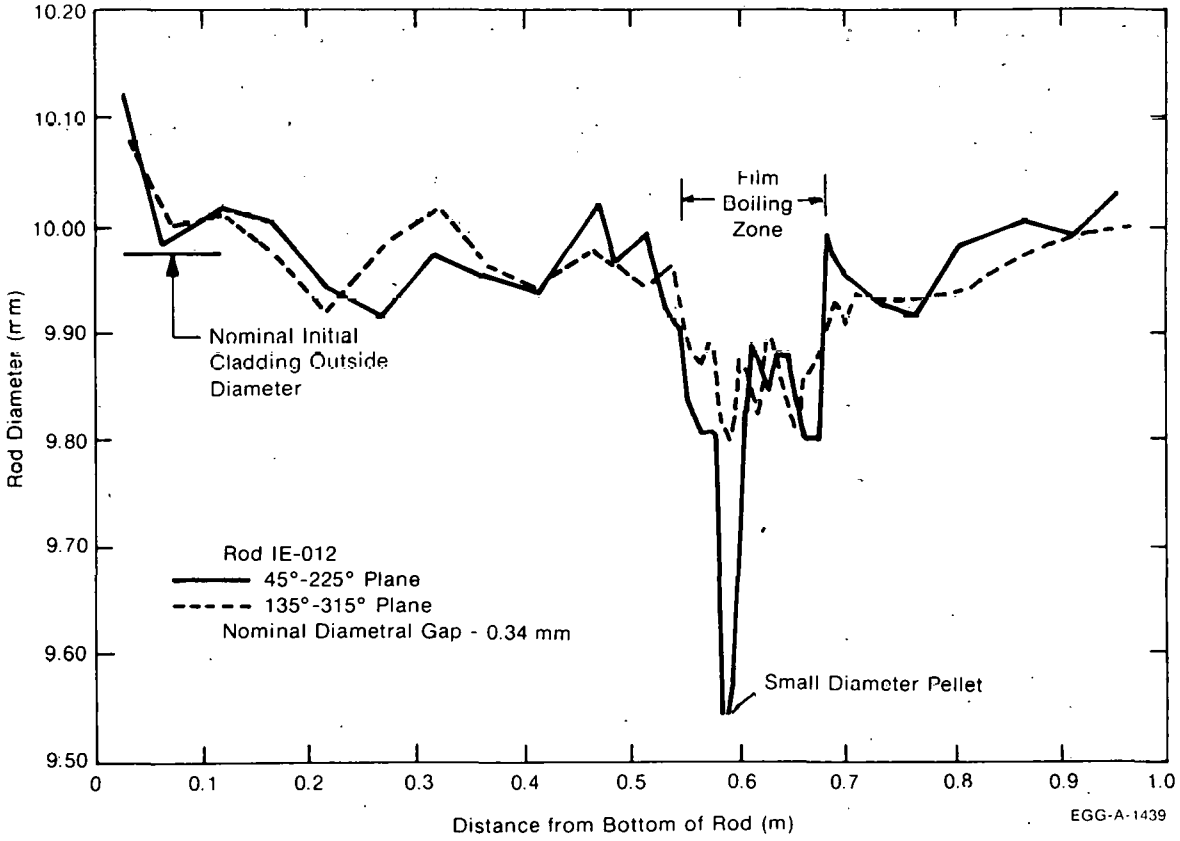

Fig. 44 Posttest diametral measurements on Rod IE-012.

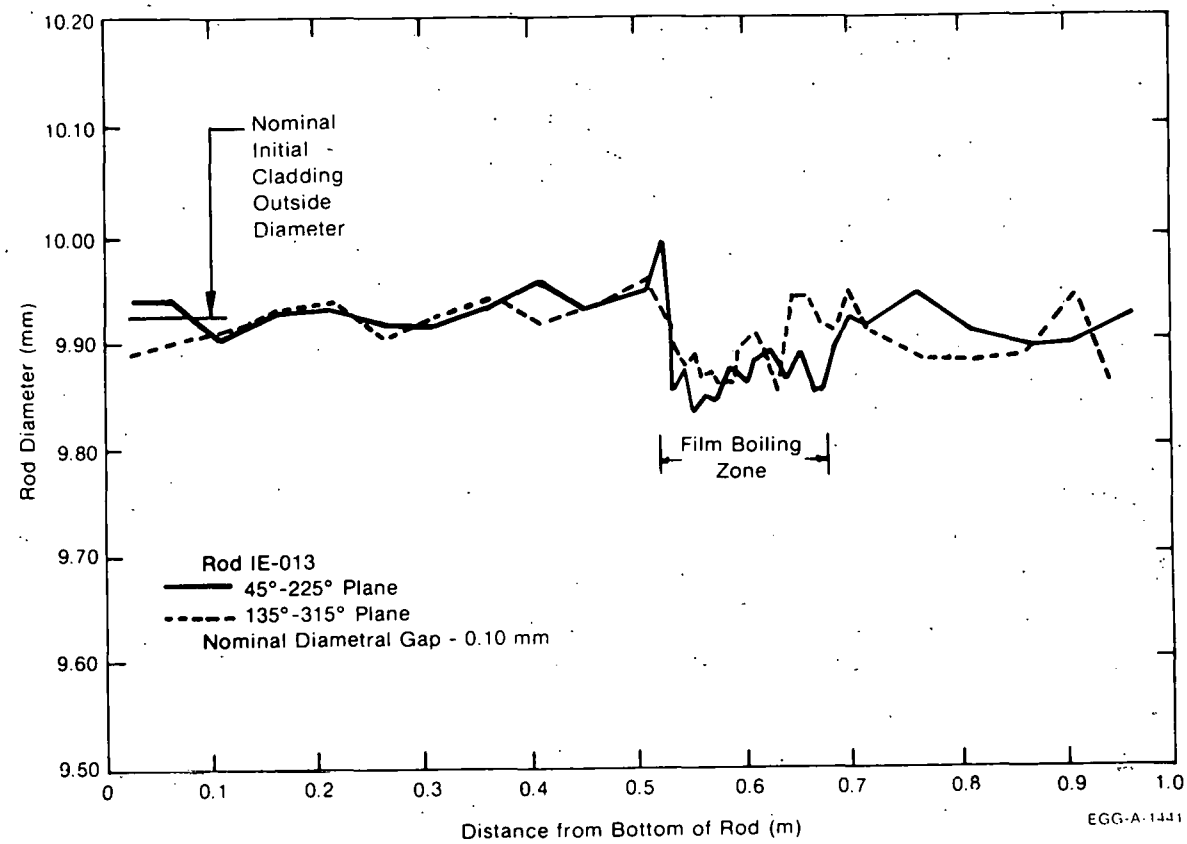

Fig. 45 Posttest diametral measurements on Rod IE-013.

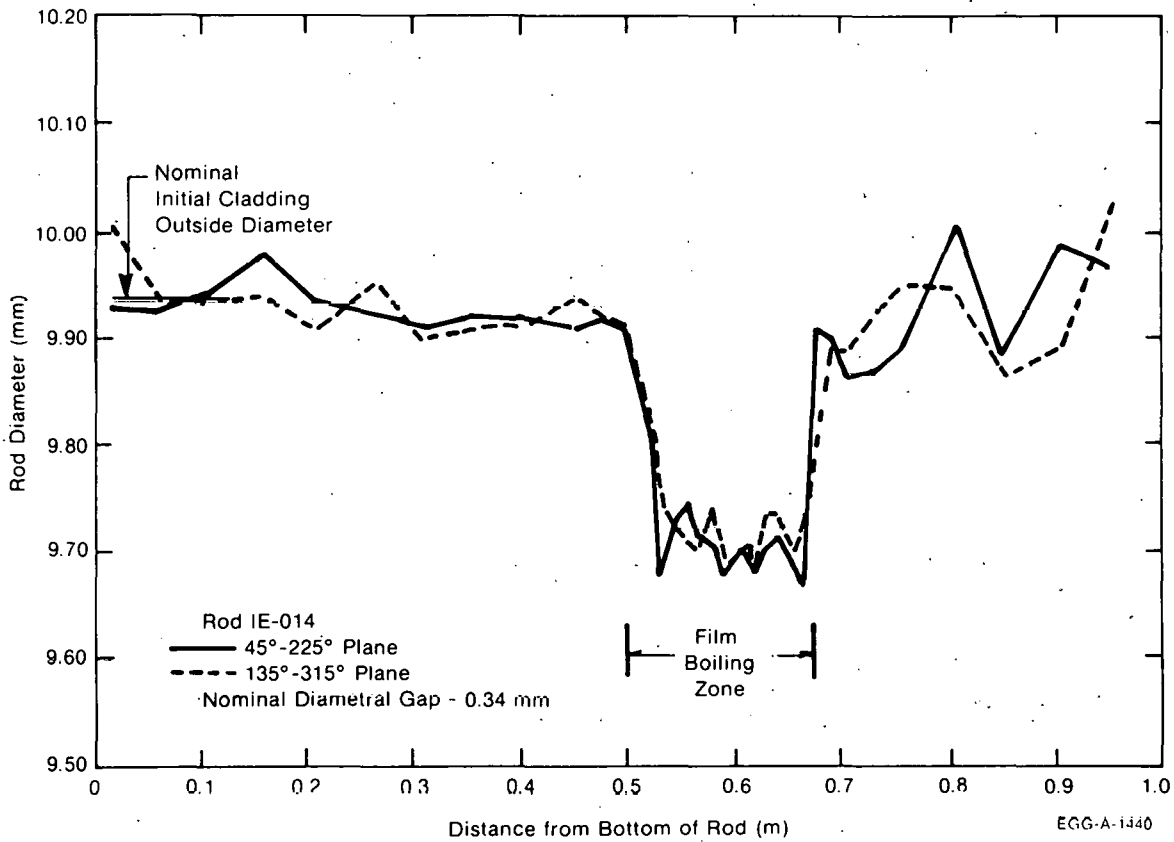

Fig. 46 Posttest diametral measurements on Rod IE-014.

6. COMPARISON OF EXPERIMENTAL AND FRAP-T3 CALCULATED RESULTS

As part of the posttest data evaluation, calculations of fuel rod behavior were made using FRAP-T3[a], a fuel behavior code, with input determined from test measurements. The FRAP-T3[8] code is under continued development incorporating improvements in fuel behavior models based upon comparisons between measured data and calculated results similar to those presented in this section.

Calculations from FRAP-T3 were compared with measured data from Test IE-2. Quasi-equilibrium calculations were performed for various power levels to analyze the quasi-equilibrium portion of the test as defined in Section 3. An analysis of the film boiling transient was performed with FRAP-T3 by modeling as closely as possible the measured fuel rod powers and mass fluxes versus time.

Rods IE-011 and IE-014 were specifically modeled using FRAP-T3 to study the effects of different gap sizes. Separate calculations were not made for Rods IE-012 and IE-013 because of their dimensional similarities to Rods IE-014 and IE-011, respectively. The effects of the irradiated cladding were not included for two reasons: first, the FRAP-T3 code does not include models for irradiated cladding, and second, fuel rod instrumentation indicated no significant measureable differences between the rods with and without irradiated cladding.

6.1 Analytical Model

The FRAP-T3 computer code is a composite of various subcodes that are used to calculate fuel rod behavior based on input power and flow conditions. The code is designed to allow the user to specify fuel behavior submodels, heat transfer correlations, axial and radial power distributions, and the physical characteristics of the fuel rod (for example, dimensions, fuel-cladding gap).

---

[a] FRAP-T3, MOD 003, Version 008 on tape T9P182 was used in conjunction with MATPRO MOD 008[7].

6.1.1 Fuel Rod Model. For this analysis, the fuel rods were modeled using 11 radial and 17 axial nodes. FRAP-T3 input included the nominal measured conditions of coolant flow, coolant inlet temperature, coolant pressure, fuel rod average power, and axial flux profile. The Westinghouse Electric Corporation W-3[9] critical heat flux (CHF) correlation (with the cold wall factor) and the Groeneveld tubes and annulus[10] film boiling heat transfer correlation (Version 5.9) were used. A free thermal expansion fuel deformation model which assumes that radial cracks extend from the fuel surface to the center and the Ross and Stoute[11] model for gap conductance were specified.

The axial and radial power profiles used in the calculations are shown in Tables IV and V. The radial profile was obtained from neutron transport calculations. The axial flux profile was determined from gamma scans of two cobalt wires as discussed in Appendix D.

Input to FRAP-T3 to model the fuel rods included the fresh fuel pellet nominal dimensions and the average cladding inside and outside diametral measurements taken prior to testing in the PBF reactor. These data are summarized in Section 2, Table I and in Appendix B.

6.1.2 Experiment Conduct Model. Steady-state analyses using FRAP-T3 were made using incremental steps in fuel rod average power of 6 kW/m, from zero to a maximum of 48 kW/m. At each step, the power was held constant, allowing the fuel rod parameters to equilibrate. These equilibrium fuel rod parameters (cladding surface temperatures, cladding elongation, etc.) at each 6 kW/m power step were compared with the quasi-equilibrium data presented in Section 4.1.

Transient fuel rod behavior during the flow reduction up to the point of DNB was calculated with FRAP-T3 to establish the proper initial conditions for film boiling transient calculations which were then compared with film boiling data presented in Section 4. FRAP-T3 did not calculate DNB well during the flow reduction using the experimentally determined fuel rod average power, coolant pressure, coolant inlet temperature, and coolant flow history during the flow reduction steps.

TABLE IV

AXIAL POWER PROFILE FOR TEST IE-2 FRAP-T3 CALCULATIONS

Elevation (m above bottom of fuel)	Local Power/Average Power
0.0	0.579
0.0555	0.732
0.1164	0.884
0.1545	0.991
0.1926	1.108
0.2536	1.204
0.2993	1.264
0.3527	1.311
0.4060	1.321
0.4517	1.306
0.4898	1.270
0.5508	1.169
0.6194	1.077
0.6651	1.006
0.7108	0.915
0.7565	0.785
0.8099	0.642
0.8403	0.564
0.8861	0.448

TABLE V

RADIAL POWER PROFILE FOR TEST IE-2 FRAP-T3 CALCULATIONS

Radial Location (mm from fuel centerline)	Local Power/Average Power
0.0 - 0.6178	0.870
0.6178 - 1.2355	0.880
1.2355 - 1.8533	0.896
1.8533 - 2.4711	0.928
2.4711 - 3.0888	0.970
3.0888 - 3.7066	1.030
3.7066 - 4.3243	1.130

The measured mass fluxes at which DNB occurred for Rods IE-011 and IE-014 were 2550 ± 30 and 2750 ± 30 kg/s-m^2, respectively, whereas the calculated mass fluxes were 3163 and 2924 kg/s-m^2, respectively, using the W-3 correlation with the cold wall factor. To improve the film boiling fuel behavior analysis, the FRAP-T3 code was modified to use the nucleate boiling heat transfer coefficients until the time DNB was measured to occur during the experiment. At the flow rate at which DNB occurred during the experiment, a logic switch was used in FRAP-T3 to force specific axial locations along the fuel rod into film boiling. The transient propagation of the film boiling zone cannot be modeled by this method, but equilibrium conditions during film boiling should be more correctly calculated. Visual postirradiation examination of the fuel rods provided measurements of the axial extent of the film boiling zones for input to the FRAP-T3 code. Table VI compares measured film boiling zones to those modeled in FRAP-T3. The film boiling zones were not modeled exactly because the node structure used in FRAP-T3 was selected to coincide with temperature measuring devices.

The coolant flow, inlet enthalpy (which corresponded to an inlet temperature of 605 K), system pressure of 14.8 MPa, and fuel rod power[a] that occurred in the experiment during film boiling were input to FRAP-T3. The coolant flows and rod powers that were used are shown in Figures 47 and 48. Results for Rods IE-011 and IE-013, both having initial diametral gaps of 0.10 mm, and for Rods IE-012 and IE-014, with gaps of 0.34 mm, are compared with FRAP-T3 results from Rods IE-011 and IE-014, respectively, in the figures in the remainder of this section.

---

[a] The FRAP-3 calculations were completed prior to the determination of final rod power levels at DNB. The analysis for the small gap rod, Rod IE-011, used a rod peak power of 68.9 kW/m, whereas the experimental powers were 66.0 and 70.6 kW/m for Rods IE-011 and IE-013, respectively. The calculations for the large gap rod, Rod IE-014, used a rod peak power of 65.1 kW/m, whereas the experimental powers were 64.2 and 64.4 kW/m for Rods IE-012 and IE-014, respectively. The differences between FRAP-T3 input and experimental powers are well within the confidence intervals of the data and should have no effect on the conclusions regarding comparisons of calculated and measured fuel rod behavior.

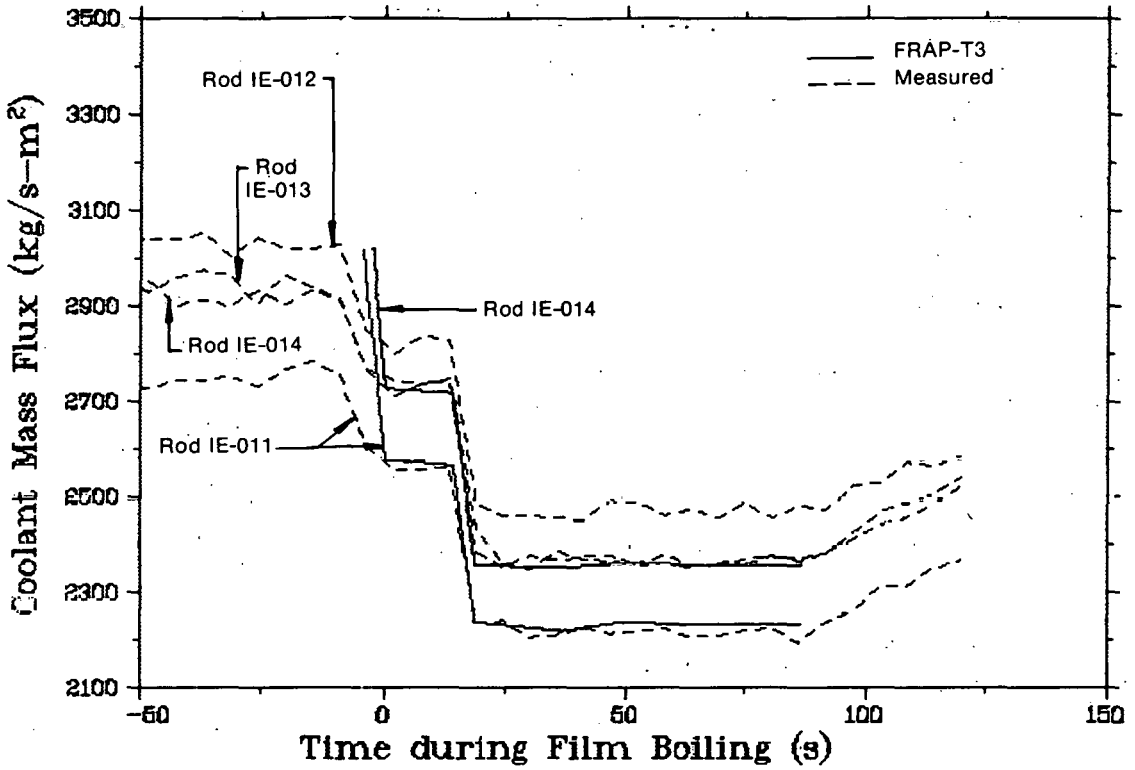

Fig. 47 Measured and FRAP-T3 modeled coolant mass fluxes during the flow reduction portion of the test.

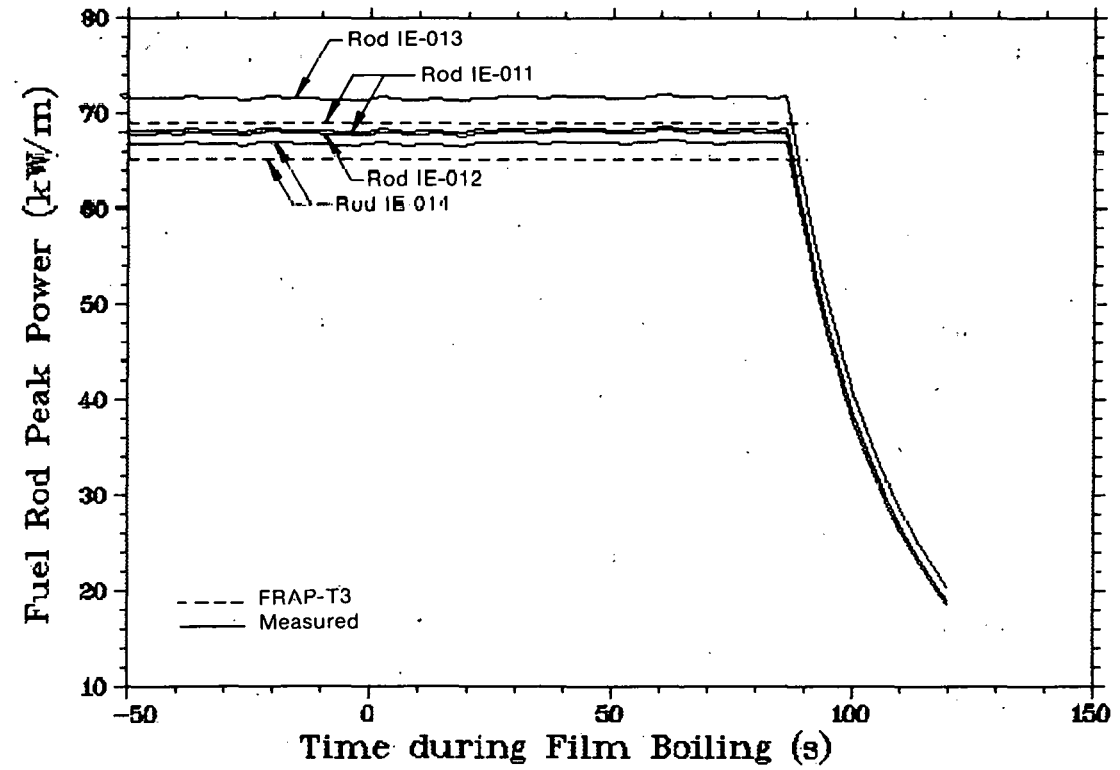

Fig. 48 Experimentally determined and FRAP-T3 modeled fuel rod peak powers during the flow reduction portion of the test.

TABLE VI

COMPARISON OF MEASURED FILM BOILING ZONES TO FILM BOILING ZONE MODELED IN FRAP-T3 FOR TEST IE-2

Rod	Lower Film Boiling Zone Boundary (m)	Upper Film Boiling Zone Boundary (m)	Length of Boiling Zone (m)	Ratio of Measured Film Boiling Zone to FRAP-T3 Modeled Zone
0.10 mm gap				
IE-011[a]	0.546	0.679	0.133	0.95
IE-013	0.521	0.676	0.155	1.11
FRAP-T3 (IE-011)	0.523	0.663	0.140	----
0.34 mm gap				
IE-012	0.542	0.679	0.137	0.83
IE-014[a]	0.505	0.676	0.171	1.04
FRAP-T3 (IE-014)	0.498	0.663	0.165	----

[a] Rod geometry explicitly modeled by FRAP-T3.

6.2 Comparison of Experiment and Analysis

In this section, FRAP-T3 results are compared with measurements for high power steady-state operation and film boiling operation for cladding elongation, fuel rod internal pressure, fuel centerline temperature, and cladding surface temperature. A summary of those comparisons is given in Table VII. Values of cladding elongation, fuel rod internal pressure, fuel centerline temperature, and cladding surface temperature immediately prior to the occurrence of film boiling are presented with the peak transient values prior to shutdown of the reactor. The increases in temperature, pressure, and elongation due to film boiling are also tabulated. A more extensive discussion of these results is presented in the following sections.

TABLE VII

COMPARISON OF MEASURED AND CALCULATED TRANSIENT VARIABLES FOR TEST IE-2

	Steady-State Pre-Film Boiling	Peak During Film Boiling	Maximum Increase due to Film Boiling
Cladding Elongation[a]	(mm)	(mm)	(mm)
Small Gap			
IE-011	3.86	5.63	1.77
IE-013[b]	----	----	----
FRAP (IE-011)	3.65	5.54	1.89
Large Gap			
IE-012	2.51	2.58	0.07
FRAP (IE-014)	1.78	1.95	0.17
Fuel Rod Internal Pressure	(MPa)	(MPa)	(MPa)
Small Gap			
IE-011	6.07	6.11	0.04
IE-013	7.32	7.42	0.10
FRAP (IE-011)	3.04	3.05	0.008
Large Gap			
IE-012	8.39	8.70	0.31
IE-014	9.30	9.60	0.30
FRAP (IE-014)	9.00	9.238	0.23
Fuel Centerline Temperature	(K)	(K)	(K)
0.61-m elevation UT			
IE-013	2300	3050	650
FRAP (IE-011)	2340	3010	670
IE-014[c]	----	----	---
FRAP (IE-014)	2870	2890	20
0.75-m elevation TC			
IE-011	1670	1850	180
FRAP (IE-011)	1873	1873	0
IE-012	2375	2445[d]	70
FRAP (IE-012)	2516	2519	3
Cladding Surface Temperature	(K)	(K)	(K)
0.51-m elevation			
IE-013	657	800[e]	143
FRAP (IE-011)	620	620[d]	0
IE-014	[f]	----	---
FRAP (IE-014)	620	1257	637
0.61-m elevation			
IE-011(0°)	611	[f]	---
IE-011(180°)	616	[f]	---
IE-013(0°)	625	1075	450
IE-013(180°)	620	700	80
FRAP(IE-011)	620	1250	630
IE-012(0°)	604	[f]	
IE-012(180°)	613	[f]	-----
IE-014(0°)	655	1010	355
IE-014(180°)	650	1080	430
FRAP(IE-014)	620	1190	570
0.71-m elevation			
IE-013	607	607	0
FRAP(IE-011)	619	619	0
IE-014	625	625	0
FRAP(IE-014)	619	619	0

[a] Absolute values of cladding elongation are not directly comparable. The steady-state measured elongation is a combination of the fuel rod expansion and the thermal expansion of the test train support hardware. FRAP-T3 calculates only the thermal expansion of the fuel rod.

[b] LVDT failed prior to test.

[c] Instrument failed prior to DNB.

[d] Film boiling not modeled at this location.

[e] Estimate from erratic signal; thermocouple possibly on edge of film boiling zone.

[f] Instrument failed at onset of DNB.

6.2.1 Cladding Elongation. Quasi-equilibrium cladding axial strains, $\varepsilon-\varepsilon_o$ as defined in Section 4, measured on Rods IE-011 and IE-012, and calculated by FRAP-T3 for Rods IE-011 and IE-014 are given in Figure 49[a]. FRAP-T3 calculated that the diametral gap of Rod IE-011 first closed at a rod average power of 24 kW/m and at 52.4 kW/m was closed over all but the top 7.4 cm of the fuel rod. Closure of the 0.343-mm diametral gap of Rod IE-014 was not calculated. Based on LVDT measurements during the preconditioning period, contact occurred at approximately 9 and 18 kW/m in Rods IE-011 and IE-014, respectively,

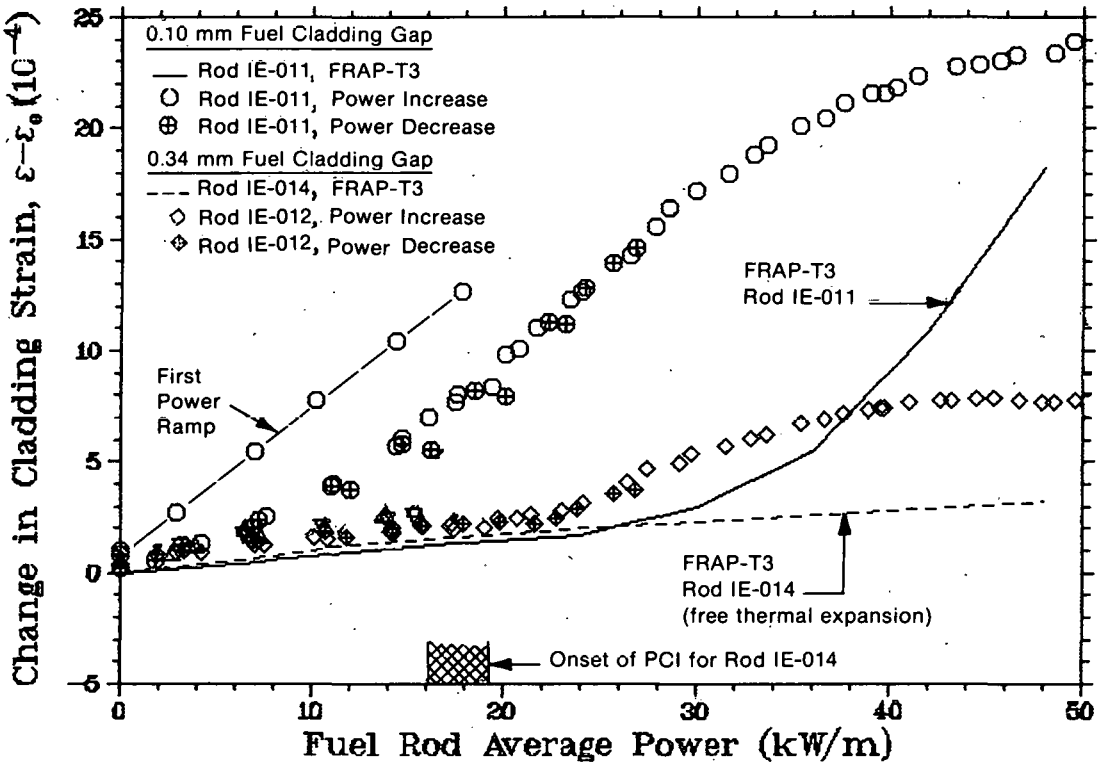

Fig. 49 Cladding elongation versus fuel rod average power for Rods IE-011 and IE-012.

[a] As noted in Section 4.1 the sensitivity of the LVDT on Rod IE-014 changed, therefore, only the onset of PCI is given in Figure 49 for this rod. Posttest FRAP-T3 calculations were performed for Rod IE-014 before the sensitivity change was realized. FRAP-T3 results for Rod IE-014 can generally be compared with data from Rod IE-012 because the fuel cladding gaps are similar. Cladding elongation during film boiling for Rod IE-012, however, should be approximately 25% less than the elongation for Rod IE-014 as a result of the difference in film boiling zone lengths.

after several power cycles had been conducted. Pellet-cladding mechanical interaction occurred at lower power levels during the first few cycles as discussed in Section 4.1. FRAP-T3 cannot calculate the effects of power cycling or creep by the fuel or cladding, so the comparisons of calculated and measured strains for each cycle and the steady-state operation at 68 kW/m average peak power are not presented.

Calculated and measured cladding axial strains during the film boiling transient are compared in Figures 50 and 51. Figure 50 shows results for Rod IE-011, a rod with a small gap, whereas, Figure 51 shows the strains for a rod with a large gap, measured on Rod IE-012 and calculated for Rod IE-014. LVDT measurements indicate that during film boiling operation, Rod IE-011, with an initial diametral gap of 0.102 mm, experienced a substantially greater elongation due to film boiling than did Rod IE-012 which had an initial diametral gap of 0.343 mm. Measured lengths of the film boiling zones on all the rods were not sufficiently different to account for the relatively large differences in length increase as a result of thermal expansion of the fuel or cladding. Diametral gaps in Rods IE-011 and IE-013 were probably closed through the film boiling zone during the hold at high power and during the flow reduction. Thermal expansion of the fuel during film boiling would then produce a large deformation in the cladding if there was no slippage between the fuel and cladding. Although quasi-equilibrium axial strain measurements indicated initial PCI at powers between 18 and 23 kW/m for Rods IE-014 and IE-012, it is probable that the PCI was weak and that slippage between the fuel and cladding occurred during the flow reduction prior to lock up between the fuel and cladding. Fuel creep during the steady-state period would reduce the severity of PCI prior to the flow reduction and shorten the axial extent of interaction. Weak PCI would account for the minimal lengthening of the cladding on Rods IE-012 and IE-014 during film boiling.

For Rod IE-011, FRAP-T3 calculated that the gap first closed at an average rod power of 24 kW/m and was closed over all but the top 7.4 cm of the fuel rod prior to the flow reduction. FRAP-T3, assuming no slippage between the fuel and cladding, calculated restrained expansions

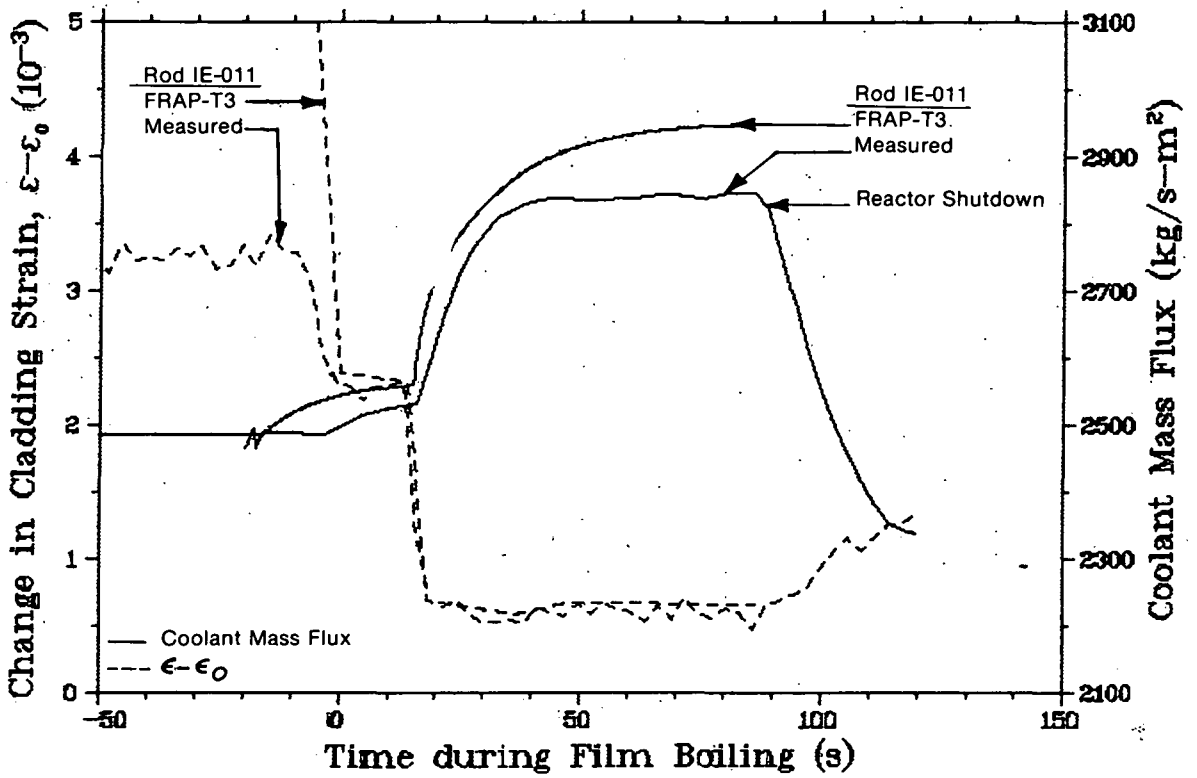

Fig. 50 Calculated and measured cladding elongation during film boiling for Rod IE-011.

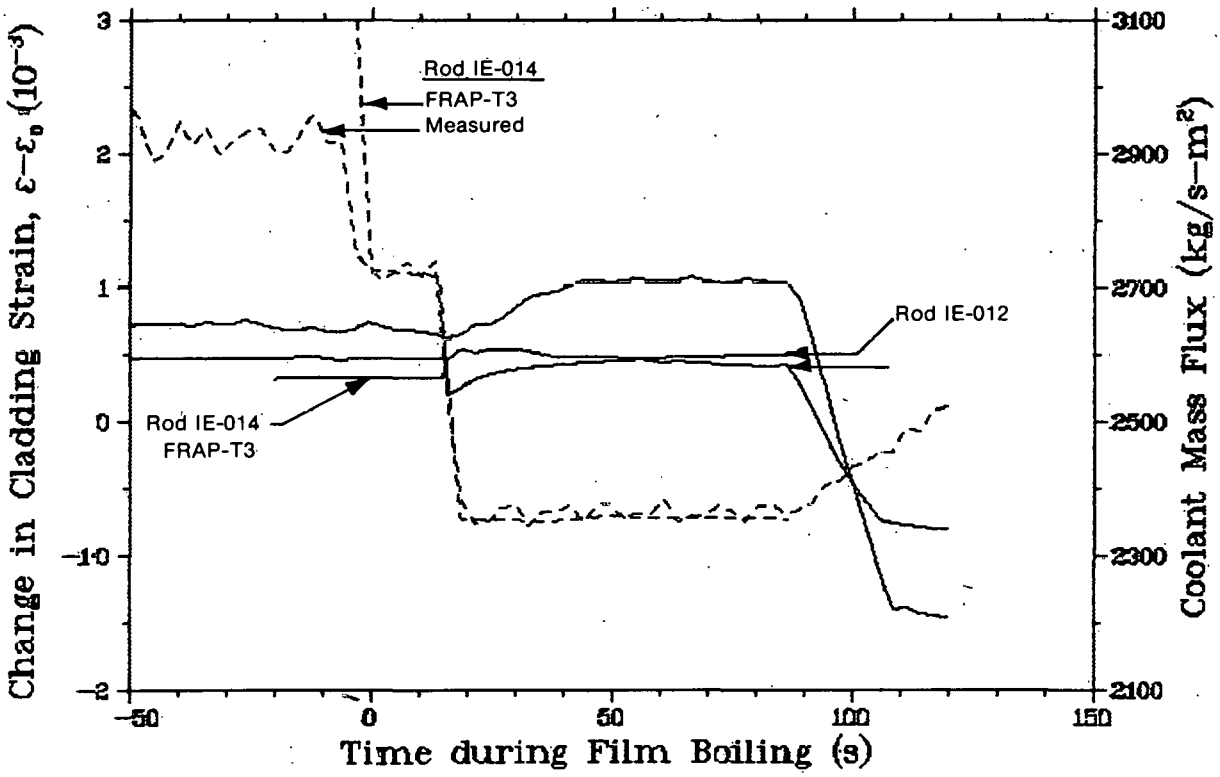

Fig. 51 Measured cladding elongation for Rod IE-012 and calculated strain for Rod IE-014 during film boiling.

for the fuel and cladding of 3.35 and 1.89 mm, respectively. Thus, plastic deformation of the cladding was calculated by FRAP-T3. If no slippage between the fuel and cladding occurs, the cladding will be deformed axially to accommodate the fuel expansion during film boiling. Since the film boiling zone length modeled in FRAP-T3 is only 5% larger than the measured film boiling zone length for Rod IE-011, the agreement between the calculated and measured cladding elongation is excellent. The calculated unrestrained fuel thermal expansion resulting from an estimated average fuel temperature increase due to film boiling of 700 K is approximately 1.5 mm for a film boiling zone equivalent to that measured on Rod IE-011. This length increase compares favorably with measured and FRAP-T3 calculated results which would indicate that plastic deformation of the cladding on Rod IE-011 did occur.

In the large gap fuel rod, Rod IE-014, FRAP-T3 calculated the fuel would lengthen by 8.7 mm by unrestrained thermal expansion whereas the cladding would lengthen by 0.17 mm. (FRAP-T3 indicated that the initial nominal diametral gap of 0.343 mm for Rod IE-014 did not close at any axial location prior to film boiling). Unrestrained axial thermal expansion of the cladding due to an estimated average temperature during film boiling over the measured film boiling zone lengths shown in Table VI would result in a cladding elongation of approximately 0.2 mm. Both of these calculated values compare favorably with the measured elongations for the large gap rod, Rod IE-012.

Permanent axial and radial cladding deformation was both measured and calculated for Test IE-2 fuel rods. The lengths of the rods were not measured during postirradiation examination of the fuel rods. However, in-reactor LVDT measurements made immediately following the flow reduction while the rod was at 605 K are compared in Table VIII with FRAP-T3 analyses of the permanent axial strain in the cladding. FRAP-T3 calculated the length change of Rod IE-011 within 5% of the measured value and correctly indicated a decrease in cladding length but not the magnitude for Rod IE-012 due to axial cladding collapse in the film boiling zone. The measured cladding radial strain in Rod IE-012 and the calculated radial strain in Rod IE-014 were substantially larger

TABLE VIII

COMPARISON OF MEASURED AND CALCULATED CLADDING PERMANENT AXIAL STRAIN FOR TEST IE-2

Rod	Cladding Permanent Axial Strain (mm)
0.10-mm gap	
Measured (Post-DNB)	
IE-011	0.82
IE-013	----
FRAP-T3(Rod IE-011)	
Pre-DNB	0.591
Post-DNB	0.860
0.34-mm gap	
Measured (Post-DNB)	
IE-012	-1.00
FRAP-T3(Rod IE-014)	
Pre-DNB	0.0
Post-DNB	-0.239

than either the measured or calculated radial strains in Rods IE-011 and IE-013. Permanent radial cladding deformation calculated by FRAP-T3 for Rod IE-011 is compared in Figure 52 with the cladding outer diameter measured during the PIE for Rods IE-011 and IE-013. Diametral growth[a] was measured in the film boiling zone of Rod IE-011. Collapse in the film boiling zone of Rod IE-013 was measured relative to the remainder of the rod. Growth in one rod and collapse in the other is attributed to variations in fuel swelling caused by fuel melting. FRAP-T3 calculated some radial growth prior to the flow reduction portion of the test.

[a] Postirradiation measurements of the cladding OD were performed remotely using a micrometer. Relative measurements on a given rod are generally accurate to within ±0.02 mm. A comparison of direct and remote micrometer measurements indicates that the remote measurements (posttest) may be offset by a maximum of -0.12 mm relative to the direct measurements (pretest) of the cladding OD. Since the cladding below the film boiling zone remained below approximately 620 K throughout the test, it was assumed that the cladding OD in this region had not been affected by operation in PBF. From this diameter measurement, the offset was determined and the percent strain was calculated. The standard deviation of the strain shown in Figures 52 and 53 is estimated to be ±0.026 mm or approximately ±0.26% strain for all of the rods.

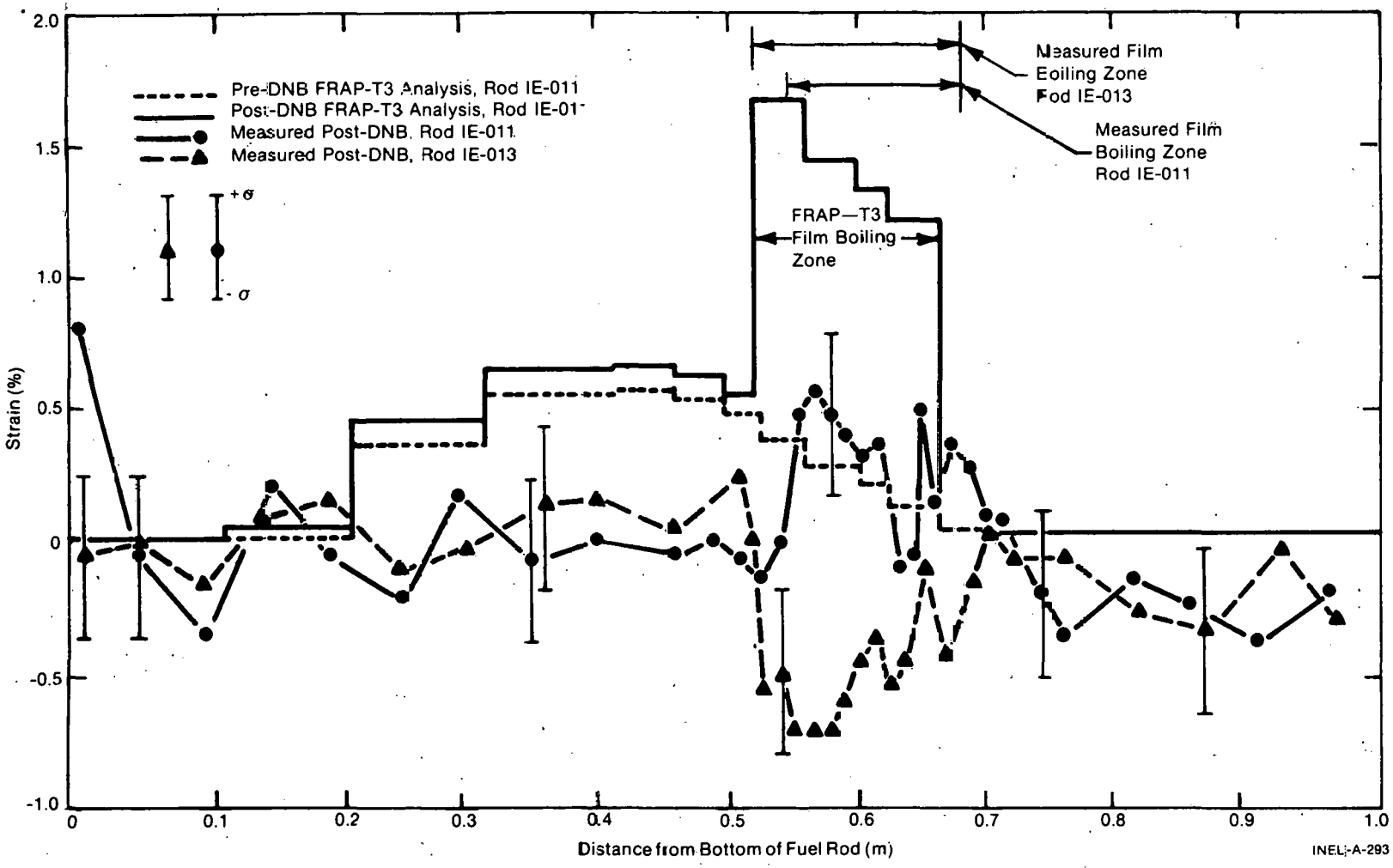

Fig. 52 Comparison of predicted plastic and measured cladding diametral strain for the fuel rods having an initial diametral gap of 0.10 mm.

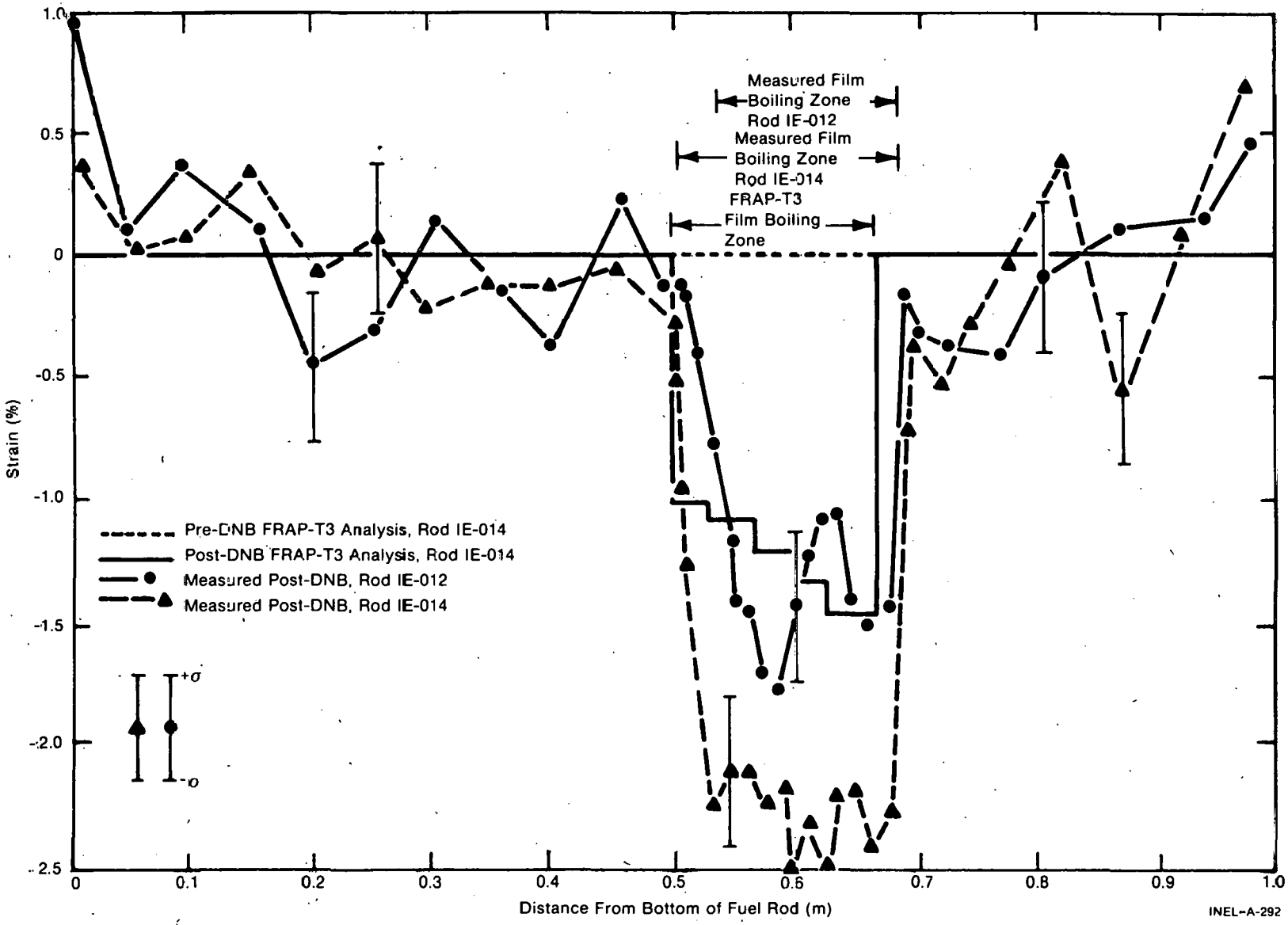

Fig. 53 Comparison of predicted plastic and measured cladding diametral strain for the fuel rods having an initial diametral gap of 0.34 mm.

Extensive cladding growth was calculated over the film boiling zone. (Although FRAP-T3 models the volume increase due to fuel melting, no molten fuel was calculated for these rods.) Figure 53 compares the strain determined from the measured postirradiation cladding OD of Rods IE-012 and IE-014 with the calculated strain in Rod IE-014. Collapse throughout the film boiling zone was measured on both rods and calculated by FRAP-T3. The difference between the collapse of irradiated cladding in Rod IE-012 and that of the unirradiated cladding in Rod IE-014 can be partially accounted for by creepdown of the cladding on Rod IE-012 during irradiation in the Saxton reactor prior to testing in PBF. In the region of the film boiling zone, the cladding outer diameter of Rod IE-012 is up to 0.03 mm smaller than that of Rod IE-014. Therefore, the cladding collapse strain of Rod IE-012 due to creepdown could be up to 0.3% less than the measured strain of -2.3% for Rod IE-014 which would result in a -2.0% strain. Since the measured strain for Rod IE-012 is approximately -1.4%, cladding creepdown prior to PBF testing does not account for all the differences between irradiated and unirradiated cladding.

6.2.2 Fuel Rod Internal Pressure. The calculated and measured quasi-equilibrium fuel rod internal pressure data from all four rods is presented in Figure 54. FRAP-T3 calculated pressures, evaluated by assuming instant pressure equilibrium throughout the rod are shown as a function of fuel rod average power. Pressures in the 0.10-mm diametral gap rods tend to be overestimated, whereas those in the 0.34-mm diametral gap rods are slightly underestimated. The difference in pressures between Rods IE-011 and IE-013 shown in Figure 54 represents a variation of approximately 10%. The reason for the overestimates of the rod internal pressure for the rods with the small gaps is not readily apparent, but may be related to gap closure.

Film boiling transient pressure transducer measurements for Rods IE-011 and IE-013 are compared with FRAP-T3 calculations of the fuel rod internal pressure for Rod IE-011 in Figure 55. Measurements for Rods IE-012 and IE-014 are compared to FRAP-T3 calculations for Rod IE-014 in Figure 56 (also Table VII.)

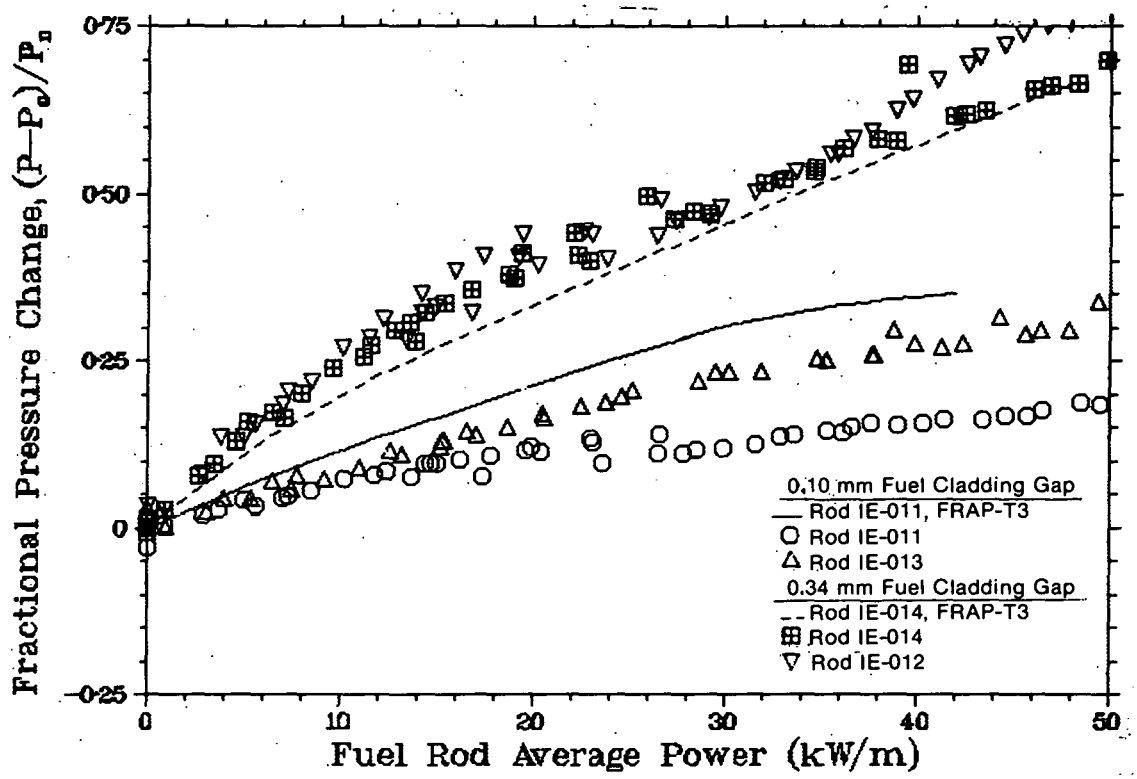

Fig. 54 Fuel rod internal pressure versus fuel rod average power for all rods during preconditioning.

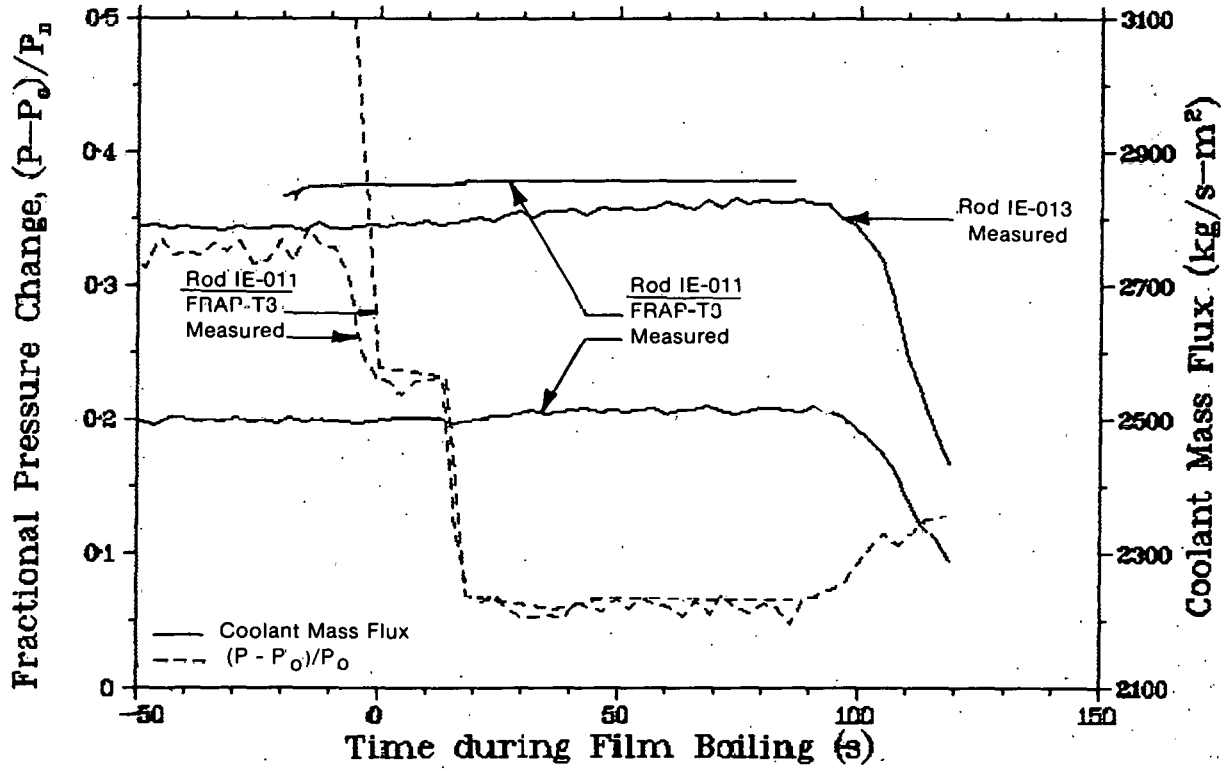

Fig. 55 Transient fuel rod internal pressure during film boiling for 0.10-mm diametral gap rods.

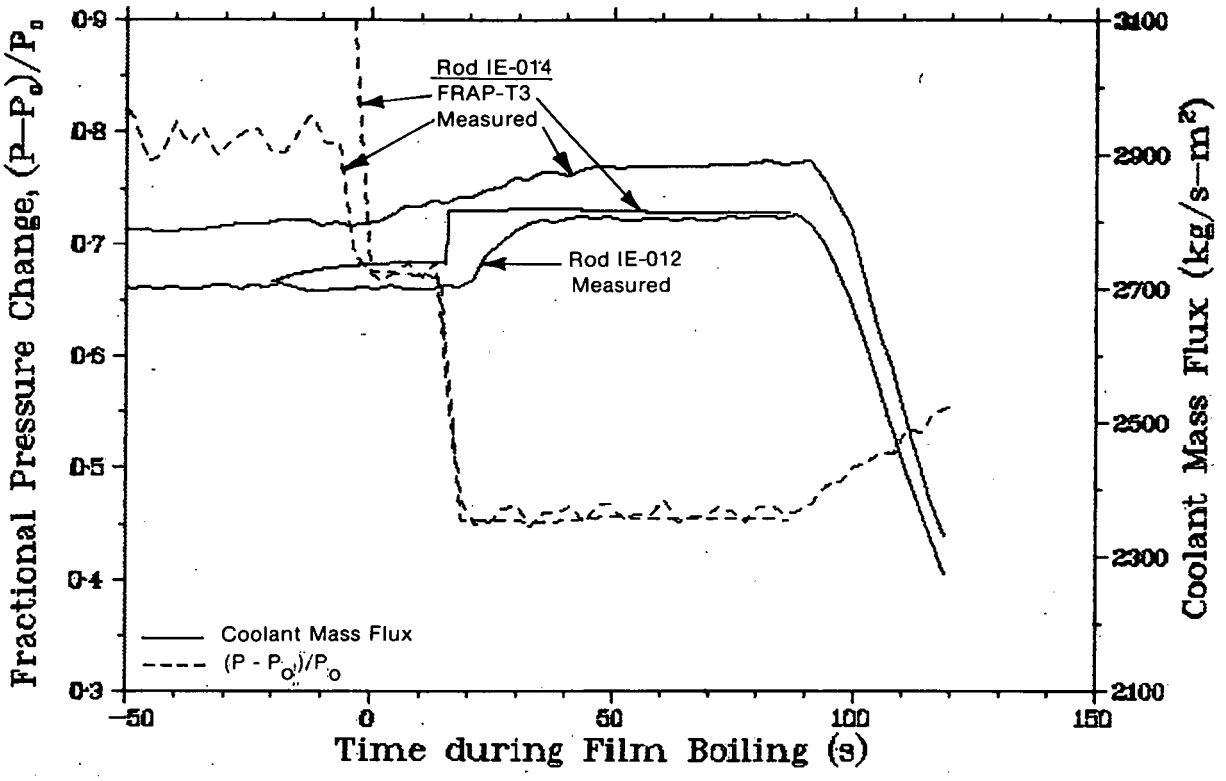

Fig. 56 Transient fuel rod internal pressure during film boiling for 0.34-mm diametral gap rods.

Transient pressure increases within the fuel rods were differentiated by the sizes of the initial diametral gaps. Rods IE-011 and IE-013 experienced small average pressure increases of 1.0% that are barely discernible on Figure 55. Rods IE-012 and IE-014 had average pressure increases of 3.5%. FRAP-T3 calculated pressure increases of 0.3% and 2.6%, respectively. The trends in terms of the difference in pressure increases due to gap differences were calculated, although the magnitude of the pressure increases was underestimated.

As discussed in Section 4.1.2, fractional change in pressure, $(P-P_o)/P_o$, is a function of the change in gas temperature and void volume. For the small gap rods, the gap was probably closed through the film boiling zone so that the transition into film boiling would not change the void volume appreciably. Thus an increase in gas temperature of 1%, i.e. 7 or 8 K, would account for the small pressure increase (the 7 or 8 K increase is based on a calculated average gas temperature of

720 and 820 K at 68 kW/m prior to DNB for Rods IE-011 and IE-013, respectively, which corresponds to the expected temperature increase from zero power conditions if void volume changes are neglected). Therefore, a slight difference in calculated and experimental gas temperature would explain the difference between FRAP-T3 calculated and measured pressure increases. For the large gap rods the situation is more complex because both gap thickness, thus void volume, and average gas temperature would change during transition to film boiling. In fact, measured cladding collapse onto the fuel in the film boiling zone would account for a 3% increase in pressure for Rods IE-012 and IE-014. When the average gas temperatures are also calculated for 68 kW/m prior to DNB assuming no change in void volume from zero power, the resulting temperatures are 1005 and 1044 K for Rods IE-011 and IE-013. These temperatures should be well in excess of the actual gas temperatures but they do establish an upper bound for the increase in temperature necessary to increase the pressure an additional 0.5%. Thus, a change in temperature of less than 5 K would increase the pressure 0.5%. Again slight differences in the calculated and measured cladding collapse and gas temperature would account for the difference in internal pressure.

6.2.3 Fuel Centerline Temperature. Fuel centerline thermocouple measurements during the quasi-equilibrium portion of the test are compared with FRAP-T3 calculations in Figures 57 and 58. The FRAP-T3 results for both the small and large gap rods are shown. A comparison of the data taken with ultrasonic thermometers (in Rods IE-013 and IE-014) and the thermocouples (in Rods IE-011 and IE-012) shows a significantly higher slope for the data from the ultrasonic thermometers. Although the FRAP-T3 calculations compare favorably with the UT generated data, this appears fortuitous. A comparison of the UT and thermocouple data from this test to data from two Irradiation Effects Scoping Tests (Test IE-ST-1[12] and IE-ST-2[13]), and Irradiation Effects Test 5[14] was made[a]. All data were obtained from thermocouples except for four

[a] Data from other tests were examined but not included because the fill gas composition and hence the thermal conductivity was not similar to that observed during the IE Test Series.

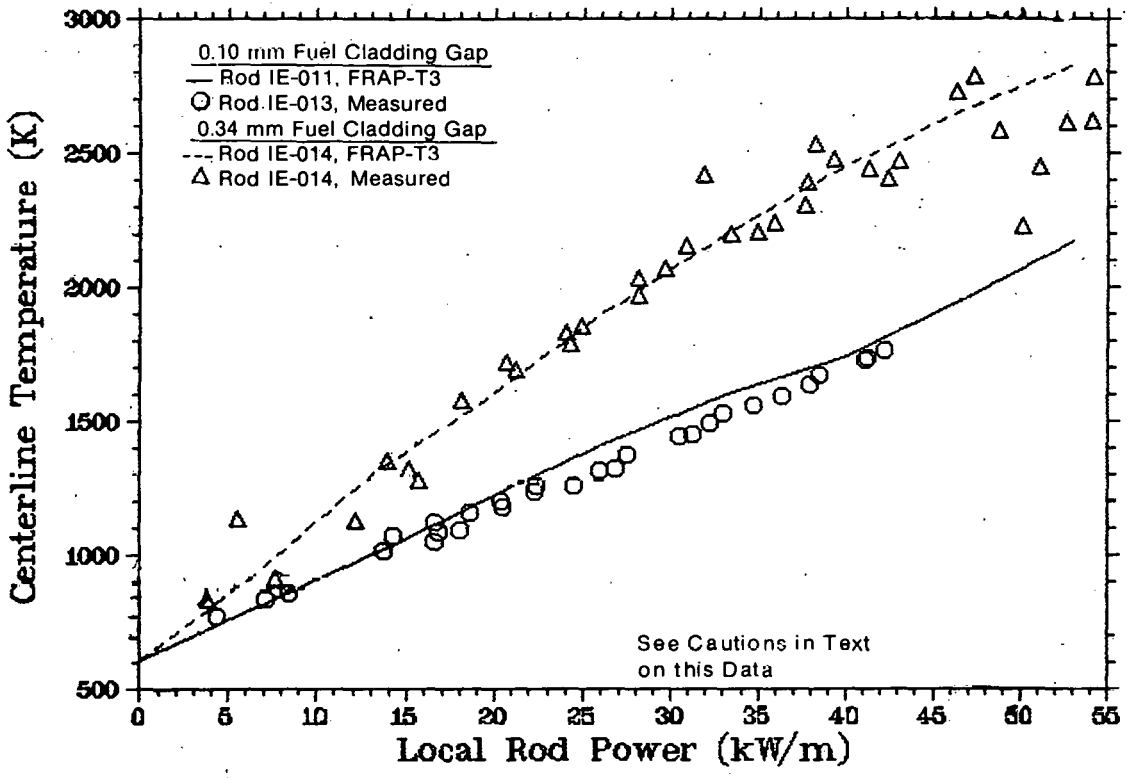

Fig. 57 Calculated fuel centerline temperatures and ultrasonic thermometer data at the 0.61-m elevation during quasi-equilibrium operation.

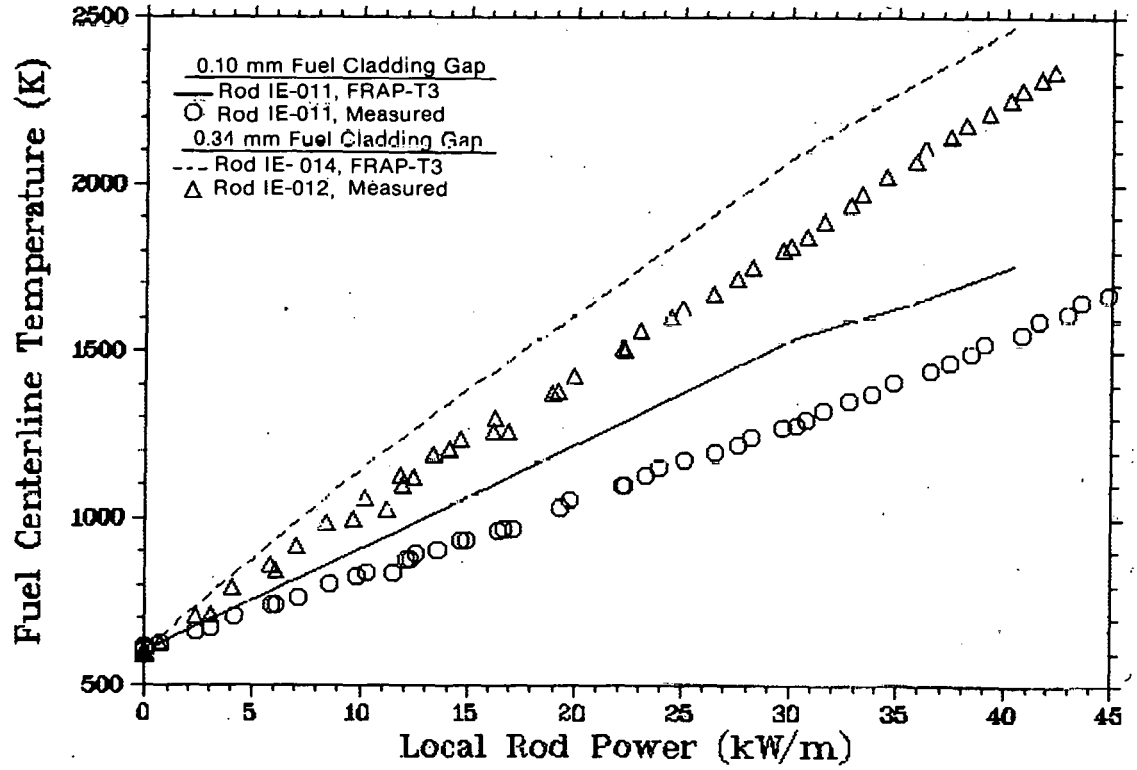

Fig. 58 Calculated fuel centerline temperatures and centerline thermocouple data at the 0.75-m elevation during quasi-equilibrium operation.

rods, two each in Tests IE-2 and IE-5, which used UTs. Since diametral gap has been a variable in these tests, temperature is plotted versus gap size with power as a parameter. The results are shown in Figures 59 and 60 for local powers of 18 and 40 kW/m. Apparently the UT data from Test IE-2 are significantly in error compared with similar data from thermocouples and the latter produce a more consistent trend. If this assessment of the data is correct, then as shown in Figure 58, FRAP-T3 overestimates the temperature at 40 kW/m by about 200 K.

Figure 61 compares the fuel centerline temperatures measured at an elevation of 0.61 m in Rod IE-013 and 0.75 m in Rod IE-011 with FRAP-T3 analyses of Rod IE-011 at the same elevations during the film boiling transient. Figure 62 compares temperature data for Rod IE-012 at an elevation of 0.75 m with FRAP-T3 analyses of fuel centerline temperatures in Rod IE-014.

Film boiling zones extended only up to the 0.68-m elevation so film boiling was not modeled at the 0.75-m elevation. Since these locations were above the film boiling zone, fuel centerline thermocouples at 0.75 m on Rods IE-011 and IE-012 should not have responded substantially to the occurrence of DNB. The fuel centerline thermocouple in Rod IE-011 indicated a temperature increase from 1670 K to 1850 K. An increase of approximately 70 K (2375 to 2445 K) was observed in Rod IE-012. FRAP-T3 calculations indicated that pre-film boiling temperatures would be 1873 and 2516 K, respectively, and that the temperature differences between the rods is due to the original diametral gap. Since axial heat conduction within the fuel is not modeled in FRAP-T3, an increase of less than 5 K was calculated for both rods during film boiling.

The ultrasonic thermometer at the 0.61-m elevation was in the central region of the film boiling zone on Rod IE-013. FRAP-T3 predicted a stable film boiling temperature of 3010 K which corresponds well to the measured temperature of 3050 K. (The same cautions apply to this measurement as previously discussed).

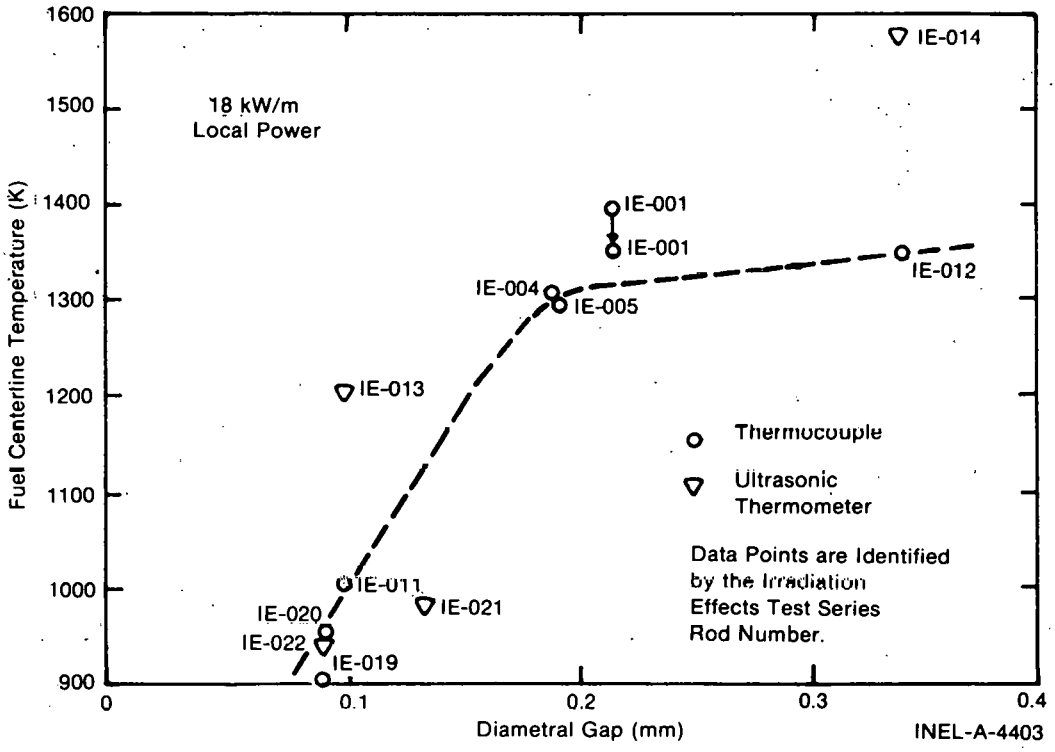

Fig. 59 Measured fuel centerline temperature at a local rod power of 18 kW/m versus initial cold fuel-cladding gap.

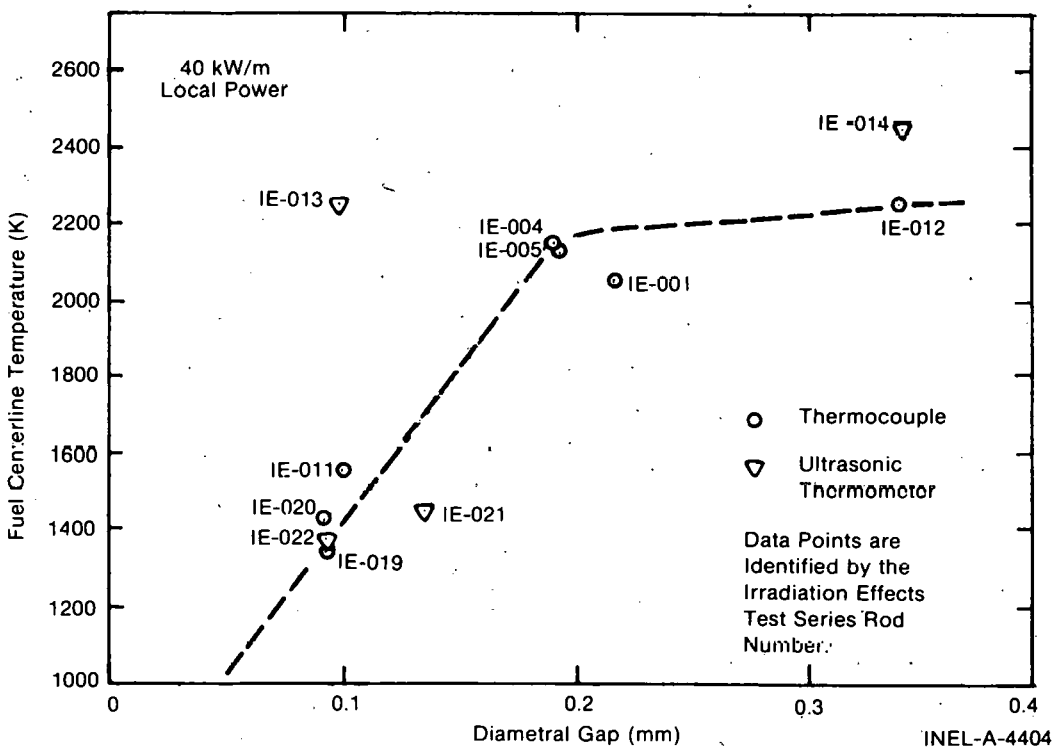

Fig. 60 Measured fuel centerline temperature at a local rod power of 40 kW/m versus initial cold fuel-cladding gap.

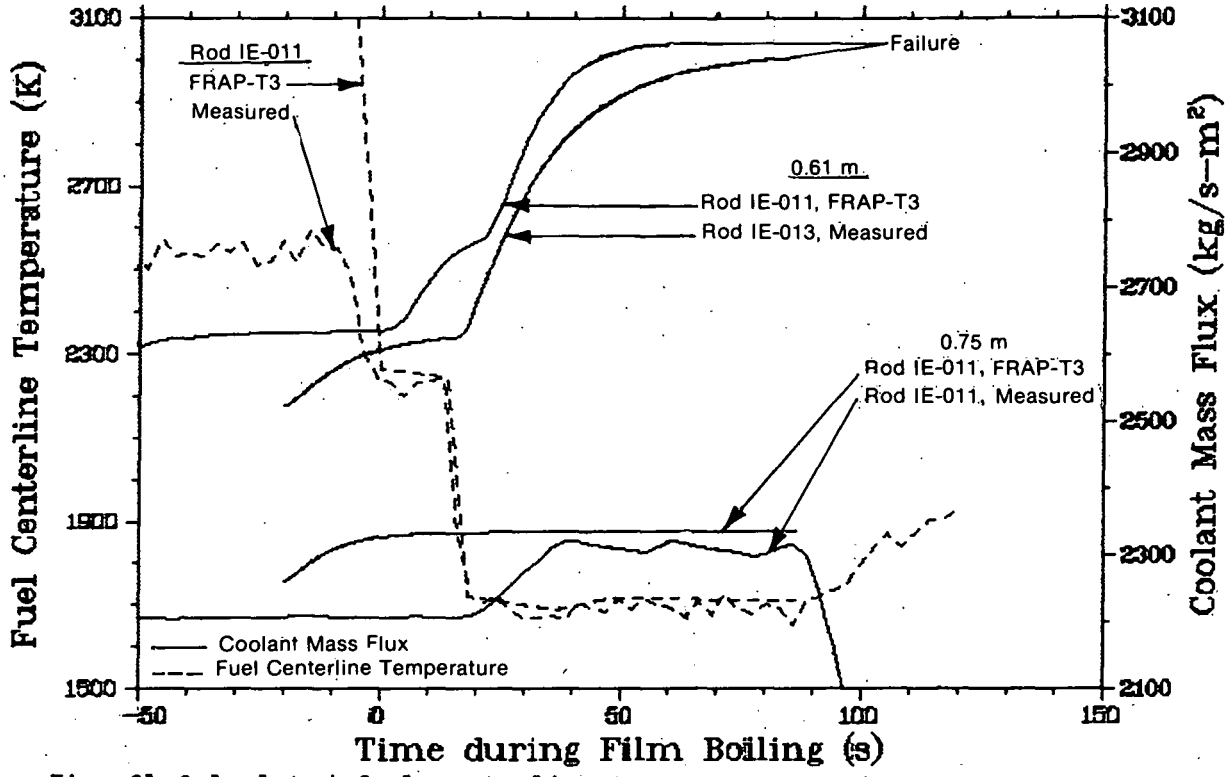

Fig. 61 Calculated fuel centerline temperatures and ultrasonic thermometer data for 0.10-mm diametral gap rods during film boiling.

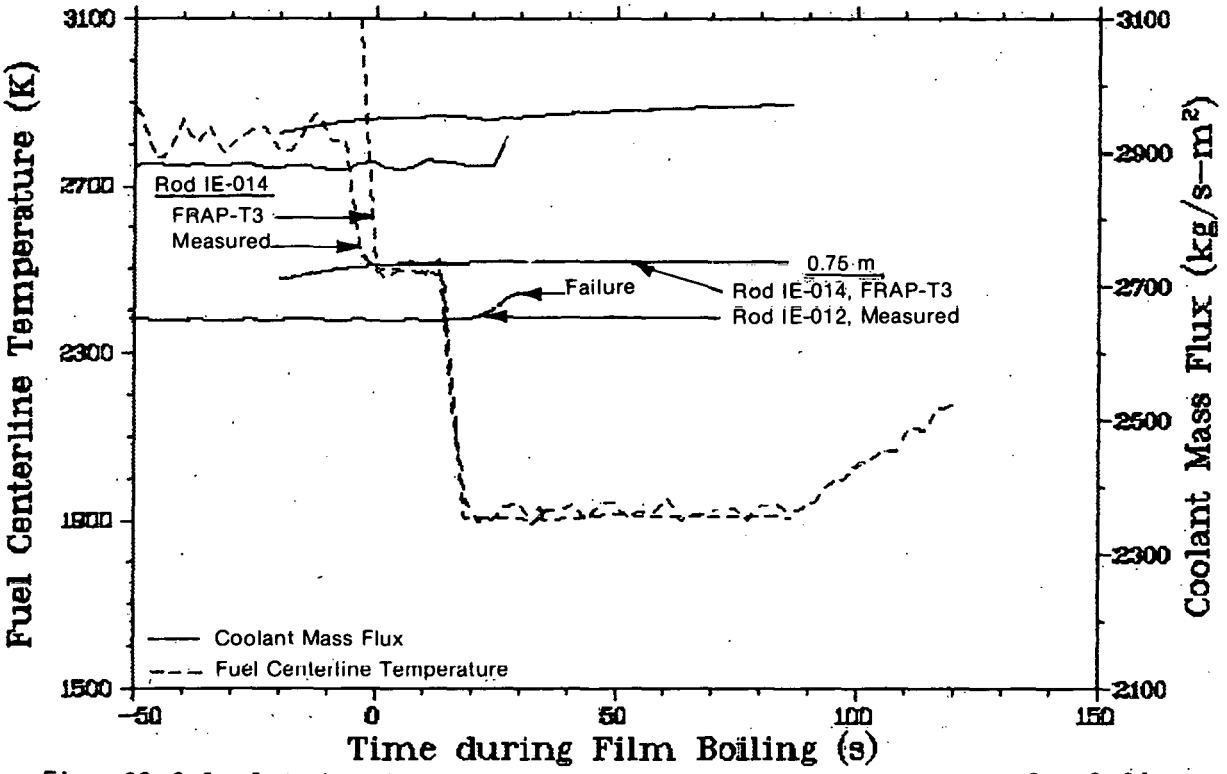

Fig. 62 Calculated and measured fuel centerline temperatures for 0.34-mm diametral gap rod during film boiling.

6.2.4 Cladding Surface Temperatures. Cladding surface temperatures were measured at one axial location, 0.61-m elevation, on Rods IE-011 and IE-012, and at three axial locations, 0.51, 0.61, and 0.71-m elevations, on Rods IE-013 and IE-014. Since the spring-loaded thermocouples generally have not provided good measurements of the cladding surface temperature during either quasi-equilibrium or transient conditions, their data are not presented. Type S thermocouples on the remaining rods were all placed in grooves in the cladding and either brazed or brazed and laser welded[a].

Figure 63 compares quasi-equilibrium data from cladding surface thermocouples located in grooves on Rods IE-013 and IE-014 at 0.51 m above the bottom of the fuel rod with FRAP-T3 calculated temperatures. Calculations of the cladding temperatures at both the surface and midradius are presented for both rods. Measured data fall in between these two calculated values at local rod powers greater than 30 kW/m since the thermocouples are embedded in the cladding. Data from thermocouples brazed in grooves on Rods IE-013 and IE-014 at an elevation of 0.61 m are compared with cladding surface and midradius temperatures calculated by FRAP-T3 in Figure 64. The high temperature from the thermocouple at 0° on Rod IE-014 may be a result of the groove being located deeper that at the mid wall radius. Cladding temperature measurements from Rods IE-013 and IE-014 at an elevation of 0.71 m are compared with FRAP-T3 calculations of the cladding surface and midradius temperatures in Figure 65.

Comparison of the data at the three elevations indicates that the temperatures measured on Rod IE-013 are consistently below those measured for Rod IE-014. The difference in power between the two rods is

---

[a] As discussed in Appendix A, the quasi-equilibrium data has been adjusted to reflect intercalibration with inlet temperature. No adjustment was made on the film boiling transient data because of the high temperature measured.

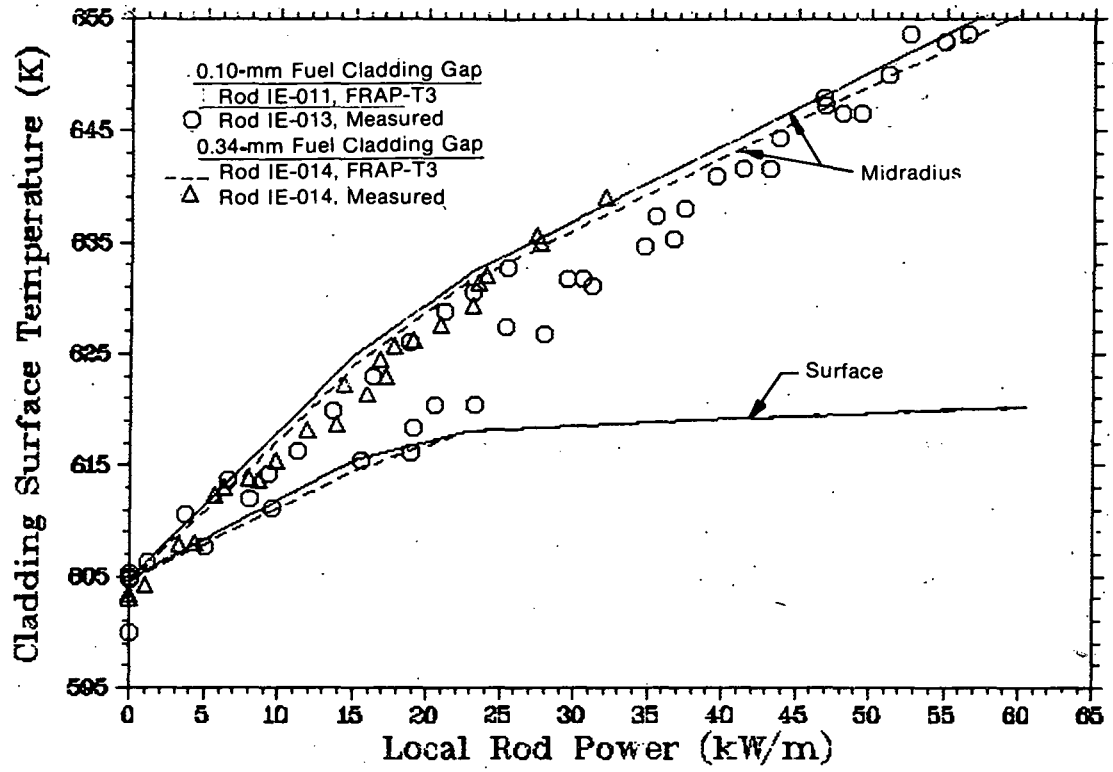

Fig. 63 Comparison of calculated and measured cladding surface temperatures and the predicted cladding midradius temperatures at the 0.51-m elevation versus fuel rod local power.

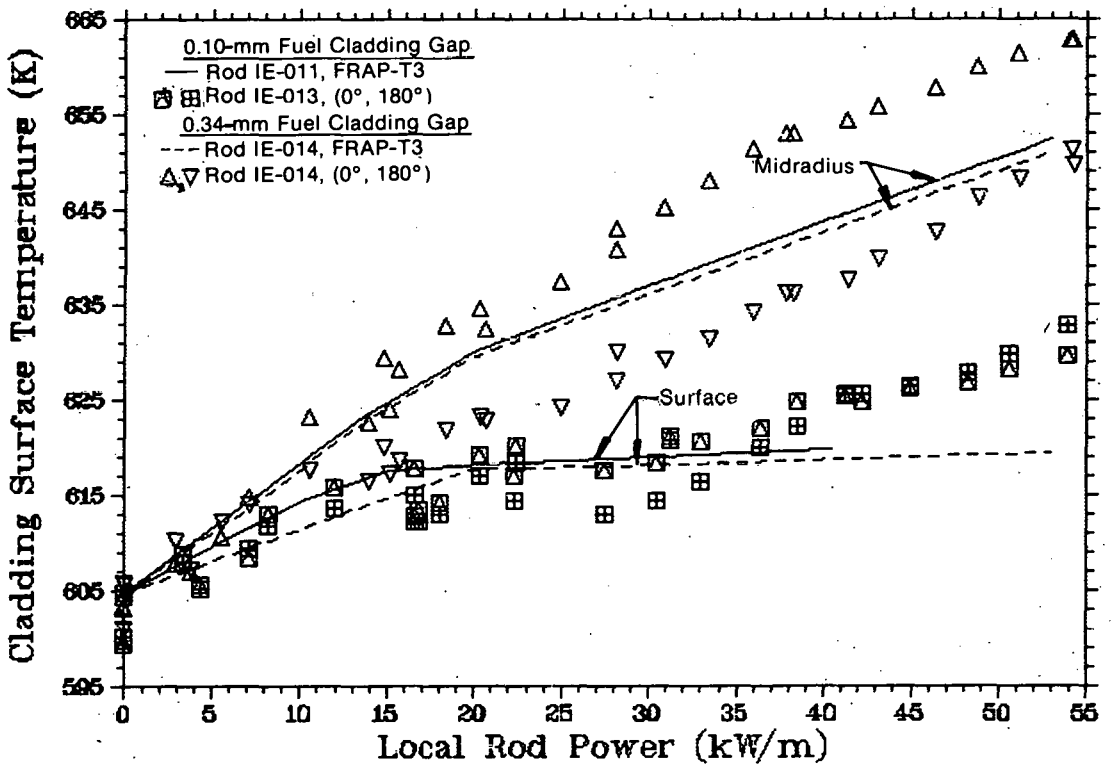

Fig. 64 Comparison of calculated and measured cladding surface temperatures and the predicted cladding midradius temperatures at the 0.61-m elevation versus fuel rod local power.

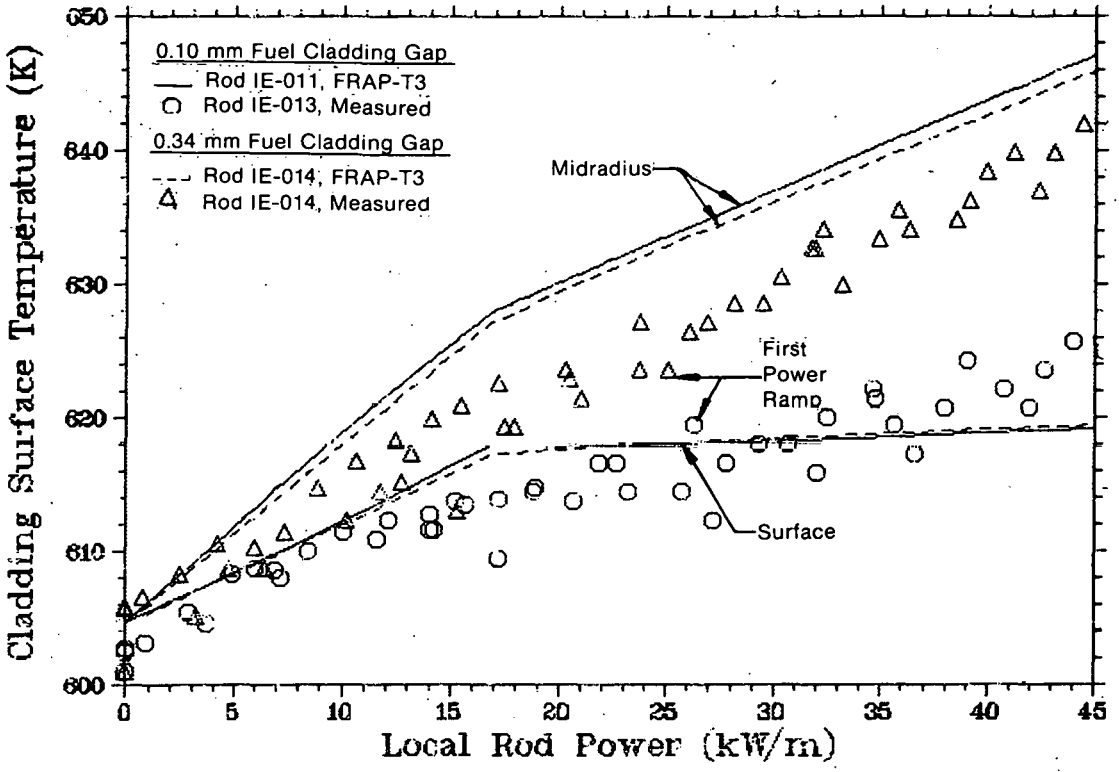

Fig. 65 Comparison of calculated and measured cladding surface temperatures and the calculated cladding midradius temperatures at the 0.71-m elevation fuel rod local power.

not responsible. The comparatively high temperature measured on Rod IE-014 cannot be attributed to the method of attaching the thermocouples, because the one brazed thermocouple was consistent with the three brazed and laser welded thermocouples on that rod. Circumferential variations in heat transfer may be partially responsible for the variations in measured temperature. Further, as evidenced by the FRAP-T3 calculations, the radial location of the thermocouple within the cladding wall would alter the temperature measured. The high power steady-state temperature gradient across the cladding at the 0.51, 0.61, and 0.71-m elevations varies from 60 to 120 K. A consistent variation in the cladding groove depth of approximately 0.15 mm (approximately 25% of cladding wall) between rods will produce the 15 to 25 K temperature differences seen in the data.

The cladding thermocouples located at the 0.61-m elevation on Rods IE-013 and IE-014 all responded to film boiling. Measured temperatures

on Rods IE-013 and IE-014 during the film boiling transient are compared with FRAP-T3 calculated values for Rods IE-011 and IE-014 in Figures 66 and 67, respectively. FRAP-T3 calculated peak temperatures of 1250 and 1198 K for Rods IE-011 and IE-014, respectively. Measured peak temperatures for three of the four thermocouple locations generally varied from 1010 to 1080 K. One thermocouple on Rod IE-013, however, recorded a peak value of only 700 K. The difference in measured and calculated values can be attributed to a fin-cooling effect on the thermocouple. The thermocouples act as fins to cool the cladding and actually measure temperatures between the coolant temperature and the actual cladding surface temperature.

Several of the cladding thermocouples recorded an increase in temperature of 50 to 100 K at time zero as shown on Figures 66 and 67. A subsequent decrease in temperature at approximately 15 seconds indicates collapse of the film boiling zone. An additional flow reduction reestablished film boiling on the rods. The time dependence of the film boiling zone length could not be adequately modeled by the current version of FRAP-T3. The onset of film boiling in FRAP-T3 was adjusted so that it would occur at the time stabilized film boiling occurred in the experiment.

One thermocouple on each of Rods IE-013 and IE-014 was located at 0.51 m above the bottom of the fuel rod. Only the thermocouple of Rod IE-013 operated during the flow reduction. The pre-film boiling measured temperature was 657 K. During film boiling, the signal was very erratic, reaching a peak of approximately 800 K, as shown in Figure 68. The bottom of the film boiling zone was determined to be at an elevation of 0.546 m from visual examination. FRAP-T3 predicted a pre-film boiling cladding surface temperature of 620 K and a peak temperature of 1257 K for full film boiling on Rod IE-014. Film boiling was not modeled at the 0.51-m elevation on Rod IE-011, the rod comparable to Rod IE-013, because it was apparently outside the film boiling zone. The measured temperatures for the 0.51-m elevation thermocouple on Rod IE-013 are attributed to the transition to film boiling with intermittent rewetting.

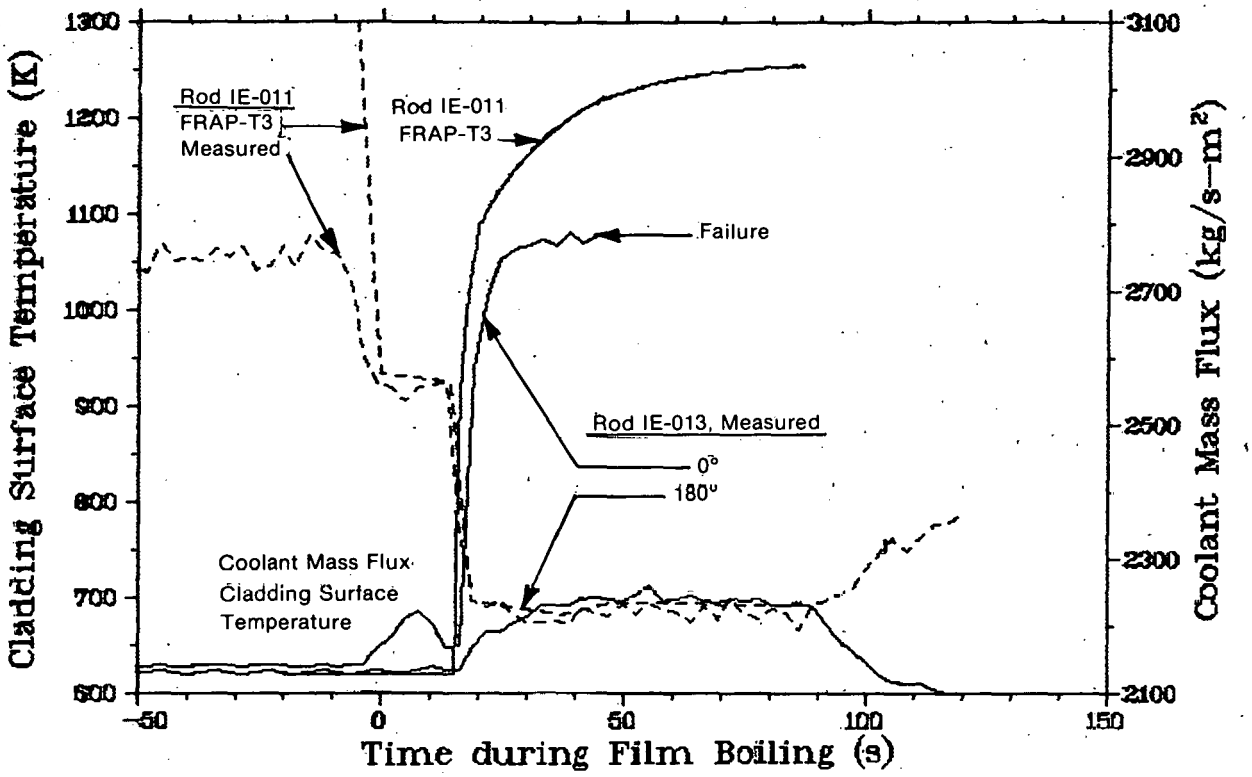

Fig. 66 Comparison of calculated and measured cladding surface temperatures at the 0.61-m elevation during film boiling on Rod IE-013.

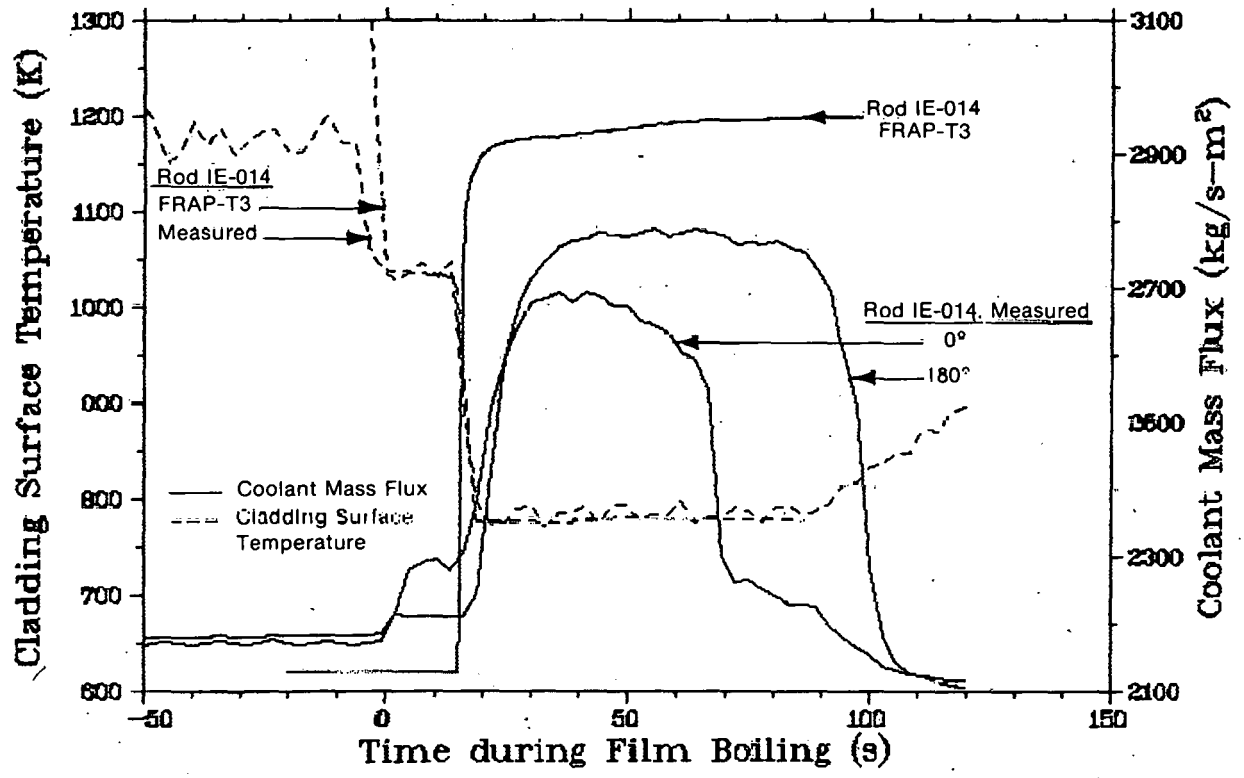

Fig. 67 Comparison of calculated and measured cladding surface temperatures at the 0.61-m elevation during film boiling on Rod IE-014.

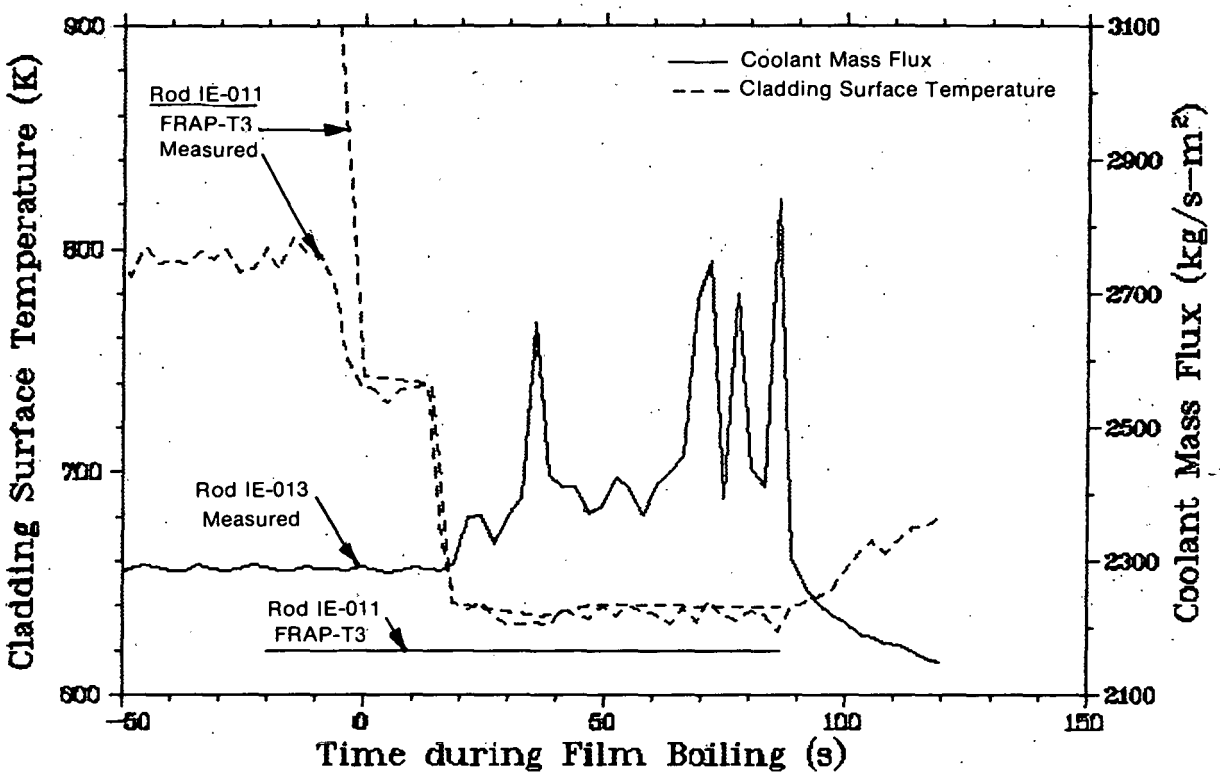

Fig. 68 Comparison of calculated and measured cladding surface temperatures at the 0.51-m elevation during film boiling on Rod IE-013.

7. DISCUSSION AND CONCLUSIONS

The purpose of Test IE-2 was to study the behavior of fuel rods with variations in diametral gap size and cladding irradiation damage state. The data from this test will be used in conjunction with data from other tests in the Irradiation Effects Test Series to establish the effects of differing design or operating conditions upon fuel rod behavior.

7.1 Effects of Gap and Cladding Irradiation

Of the four rods tested in Test IE-2, two had 0.10-mm diametral fuel-cladding gaps (Rods IE-011 and IE-013) and two had 0.34-mm gaps (Rods IE-012 and IE-014). One out of each pair of similar gap size rods had unirradiated cladding (Rods IE-013 and IE-014) and irradiated cladding (Rods IE-011 and IE-012). The remaining fuel rod design parameters were nominally the same among all four rods.

Comparison of the data as a function of gap size indicated that the rods with larger gaps experienced:

(1) Higher fuel centerline temperatures because of lower gap conductance;

(2) Onset of pellet-cladding mechanical interaction at higher rod powers because of the larger available volume for fuel expansion;

(3) Less total cladding elongation during both power cycling and film boiling because of reduced levels of pellet-cladding mechanical interaction;

(4) Increased rod relaxation strains at high power due to fuel creep or slippage or both because of reduced PCI friction force and increased average fuel temperature;

(5) Greater cladding collapse onto the fuel during film boiling with a resulting shortening of the cladding after shutdown;

(6) Larger pressure increases as a function of power due to larger number of moles of fill gas, increased gas temperature, and greater decrease in void volume due to fuel expansion with increasing power.

Because of cladding creepdown, fuel swelling, relocation, and densification, the effect of initial gap size should lessen as the irradiation time increases. This lessening of the initial gap size effect is shown by the results from Test IE-1 and Halden[a] tests that indicate the influence of gap size on irradiated fuel rod behavior was relatively minor[15 and 16].

The effect of prior cladding irradiation upon fuel rod behavior during Test IE-2 was minimal. The influence of prior irradiation damage on cladding behavior was expected to be significant only where the cladding strain and strain rates were high, such as in the power ramp to 68 kW/m. Plastic deformation resulting from the power ramp could not be measured by the LVDTs, since the power was not decreased to zero power after the power ramp and prior to film boiling which masks any effect of the ramp. The key result is that the rods with the irradiation damaged cladding did not fail as a result of PCI strain during the high power ramp. No discernible effect of prior cladding irradiation on fuel rod behavior during film boiling was observed.

7.2 FRAP-T3 Comparisons

The results from this and other tests in the IE Test Series are important for the development of verified analytical models for fuel rod behavior computer codes. A version of one of these codes, FRAP-T, has

---

[a] The OECD Halden Reactor Project, located in Halden, Norway.

been used throughout this test program for (a) prediction of fuel rod behavior to be expected during a test (for design and operation purposes), (b) comparisons of calculations with test data to determine whether any systematic errors in the data are present, and (c) to provide feedback for continued development of the code. The comparison made in Section 6 using FRAP-T3 shows that agreement between calculated and measured results is generally good. The comparisons are discussed in more detail in the following subsections, but the basic comparisons are as follows:

(1) Calculated fuel rod behavior generally agreed with measured behavior except that PCI was calculated at a higher power (or not at all) than was measured, resulting in less axial growth of the rods. This result was probably due to the differences in the annular gap modeled by FRAP-T3 and the actual gap.

(2) During the flow reduction phase, the calculation for the occurrence of DNB was the main discrepancy in FRAP-T3 results relative to the data. The consequences of this discrepancy were minimized in the calculations by forcing DNB to occur at a zone corresponding to the measured film boiling zone. This method yielded good agreement between calculated and measured film boiling fuel rod behavior for part of the measurements made. Correctly calculating the onset of DNB is only a function of using or having a DNB correlation applicable for these unique test conditions and geometries.

7.2.1 Pre-Film Boiling Behavior. During the pre-DNB phase of the experiment, the following were noted:

(1) Rods IE-011, IE-012 and IE-014 showed initiation of PCI at rod average powers of 9, 23, and 18 kW/m, respectively. The FRAP-T3 analyses indicated that PCI would occur on Rod IE-011 at 24 kW/m and PCI would not occur on either Rod IE-012 or IE-014 even during the ramp to 68 kW/m. Therefore, cladding elongation was also not well calculated.

(2) Calculated fuel rod pressures showed good agreement with the data.

(3) Quasi-equilibrium fuel centerline temperatures were overestimated.

(4) Comparisons of surface temperature calculations were limited by the scatter in the data.

7.2.2 Film Boiling Behavior

During the film boiling phase of the test the following were noted:

(1) Cladding elongation due to film boiling was generally well calculated. FRAP-T3 calculated the length increase of Rod IE-011 to within 8%. This agreement indicates that the fuel creep and probable cladding plastic deformation during the operation at 68 kW/m resulted in fuel and cladding stresses representative of a rod with a uniform gap width. Posttest axial permanent strains were also generally well calculated by FRAP-T3. The code correctly calculated a decrease in length of the large gap rods, but not the magnitude.

(2) Extensive radial cladding collapse due to film boiling operation was measured and calculated in the film boiling zone of the large gap rods. FRAP-T3 calculated cladding swelling for Rod IE-011 which did show some diameter increase in the film boiling zone.

(3) The magnitude of the rod internal pressure increases were not well calculated; however, the trends with regard to the different gap sizes were reasonably well calculated.

(4) On the basis of fuel centerline thermocouple data, FRAP-T3 overestimated fuel centerline temperature.

(5) FRAP-T3 generally calculated cladding temperatures that were higher than those measured. The measured values are probably low due to fin-cooling effects and other systematic errors. Overall assessment of the adequacy of the calculated versus measured temperature results during film boiling will depend on the results of the postirradiation examination.

8. REFERENCES

1. United States Nuclear Regulatory Commission, Reactor Safety Research Program *A Description of Current and Planned Reactor Safety Research Sponsored by the Nuclear Regulatory Commission's Division of Reactor Safety Research,* NUREG-75-1058 (June 1975).

2. L. B. Thompson et al., *Light Water Reactor Fuel Behavior Program Description: Irradiation Effects Experiment Requirements,* TFBP-TR-175 (February 1977).

3. R. W. Garner and D. T. Sparks, *Gap Conductance Test Series Test GC IE-2 Quick Look Report,* TFBP-TR-132 (October 1976).

4. G. W. Gibson et al., *Characteristics of UO_2-Zircaloy Fuel Rod Materials from the Saxton Reactor for Use in the Power Burst Facility*, ANCR-NUREG-1321 (September 1976).

5. K. Honnerz and G. Vesterlund, "Zircaloy Cladding Mechanical Properties" *Nuclear Engineering and Design, 33,2* (September 1975) pp 205-218.

6. R. Olander, *Fundamental Aspects of Nuclear Reactor Fuel Elements*, TID-26711-P1 (April 1976).

7. P. E. MacDonald and L. B. Thompson (eds.) *MATPRO Version 09 - A Handbook of Materials Properties for Use in the Analysis of Light Water Reactor Fuel Rod Behavior*, TREE-NUREG-1005 (December 1976).

8. J. A. Dearien et al., *FRAP-T3: A Computer Code for the Transient Analysis of Oxide Fuel Rods,* TFBP-TR-194 (August 1977).

9. L. S. Tong, *Boiling Crisis and Critical Heat Flux, AEC Critical Review Series,* TID-25887 (1972).

10. D. C. Groeneveld, *An Investigation of Heat Transfer in the Liquid Deficient Regime*, AECL-3281 (December 1968 Revised August 1969).

11. A. M. Ross and R. L. Stoute, *Heat Transfer Coefficient Between UO_2 and Zircaloy-2*, AECL-1552 (June 1962).

12. W. J. Quapp et al., *Irradiation Effects Test Series Scoping Test 1 Test Results Report*, TFBP-TR-110 (January 1976) (to be published as TREE-NUREG-1066).

13. W. J. Quapp et al., *Irradiation Effects Test Series Scoping Test 2 Test Results Report*, TFBP-TR-137 (September 1976) (to be published as TREE-NUREG-1044).

14. L. C. Farrar and D. W. Croucher, *Irradiation Effects Test Series Test IE-5 Quick Look Report*, TFBP-TR-163 (February 1977).

15. W. J. Quapp et al., *Irradiation Effects Test Series Test IE-1 Test Results Report*, TREE-NUREG-1046 (March 1977).

16. I. Ruyter, K. O. Vilpponen, and C. Vitanzu "Factors Affecting Cladding Elongation and Relaxation," *Enlarged Haldon Program Group Meeting, Sanderstolen, Norway, March 12-18, 1976.*

APPENDIX A

INSTRUMENTATION AND DATA ACQUISITION SYSTEM UNCERTAINTIES

The calibration equations that were used to convert the transducer output to engineering units during the data reduction process for Test IE-2 are presented in this appendix.

Data obtained during the conduct of the test are subjected to three significant sources of error: (a) instrument calibration error, (b) data system acquisition error, and (c) systematic measurement error. Estimates of both the instrument calibration error and data system acquisition error are provided in this appendix. The systematic measurement error is a consequence of the transducer design and installation. To quantify the effect of the measurement error it would be necessary, either by analysis or experiment, to simulate the in-use configuration of the transducer. Since this effort has not been made, an estimate of the systematic measurement error is not available. A qualitative assessment of the systematic measurement error indicates that this type of error is not significant except as stated below and that the measurements provided by the instruments should closely reflect values of the physical parameter measured, within the error estimates specified in this appendix. This assumption does not apply to the cladding surface temperature measurements. Also, this statement is made assuming that the instruments do not decalibrate prior to or during the experiment. As indicated by the test data from rod internal pressure transducers, ultrasonic thermometers, and the linear variable differential transformer (LVDT) on Rod IE-014, significant errors due to decalibration can occur. Data corrections or coordinate transformations were used to minimize these errors (Appendix C). Posttest calibrations were not performed on the test instrumentation to check for instrument decalibration due to the difficulties involved in handling irradiated components.

Calibration equations for each instrument are presented in a tabular form in Table A-I. Included in the table is the 95% confidence

TABLE A-I

SUMMARY OF CALIBRATION EQUATIONS AND UNCERTAINTIES IN TEST IE-2 EXPERIMENTAL MEASUREMENTS

Measurements	Transducer (serial number)	Fuel Rod Number	Calibration Equation	Output (% of Span)	Output (MPa)	Data System Error (MPa)	Calibration Error (MPa)	Total Error (MPa)
System Pressure	69-MPa Strain Post (SN 159)	[a]	MPa = -22.35 + 3.856(mV) $-4.583 \times 10^{-4}(mV)^2$ $+4.725 \times 10^{-2}(T)$	0	0	0.22	0.12	0.25
				25	10.3	0.27	0.08	0.28
				50	20.7	0.35	0.08	0.36
				75	31.0	0.46	0.09	0.47
				100	41.4	0.58	0.14	0.60
					(K)	(K)	(K)	(K)
Coolant Inlet and Outlet Temperature	Chromel-Alumel Thermocouple (all devices)	[a]	K = 343.6 + 24.05 (mV)	0	540	0.3	0.1	1.0
				25	568	0.3	1.1	1.1
				50	595	0.4	1.2	1.3
				75	623	0.5	1.3	1.4
				100	650	0.7	1.4	1.6
Cladding Surface Temperature	W5%/W26%Re Thermocouple	IE-011 IE-012	K = 351.2 +53.50(mV) $-0.5598(mV)^2$ $+0.02044(mV)^3$	0	540	10	2	10
				25	990	11	4	12
				50	1430	15	5	16
				75	1870	20	7	21
				100	2320	25	9	26
Cladding Surface Temperature	Platinum 10% Rhodium (Type S) Thermocouple	IE-013 IE-014	K = 381.2 +108.7(mV) $+0.7667(mV)^2$	0	500	7	1	7
				25	882	9	3	9
				50	1230	11	5	13
				75	1580	14	7	17
				100	2030	17	8	21

TABLE A-I (Continued)

SUMMARY OF CALIBRATION EQUATIONS AND UNCERTAINTIES IN TEST IE-2 EXPERIMENTAL MEASUREMENTS

Measurements	Transducer (serial number)	Fuel Rod Number	Calibration Equation	Output (% of Span)	Ouput (cm^3/s)	Data System Error (cm^3/s)	Calibration Error (cm^3/s)	Total Error (cm^3/s)
Coolant Flow	Turbine Flowmeter (SN 10094)	IE-011	cm^3/s = -0.6800 +0.1265(mV)	0	0	6.8	0.32	6.8
				25	210.3	7.9	0.27	7.9
				50	420.5	9.8	0.79	9.8
				75	630.8	11.5	0.27	11.5
				100	841.0	14.1	0.32	14.1
Coolant Flow	Turbine Flowmeter (SN 10092)	IE-012	cm^3/s = 0.3621 +0.1257(mV)	0	0	6.8	0.32	6.8
				25	209.1	7.9	0.27	7.9
				50	418.3	9.8	0.22	9.8
				75	627.4	11.5	0.28	11.5
				100	836.6	14.1	0.38	14.1
Coolant Flow	Turbine Flowmeter (SN 10095)	IE-013	cm^3/s = -0.6868 +0.1265(mV)	0	0	6.8	0.32	6.8
				25	211.2	7.9	0.24	7.9
				50	422.4	9.8	0.22	9.8
				75	633.6	11.5	0.28	11.5
				100	844.8	14.1	0.32	14.1
Coolant Flow	Turbine Flowmeter (SN 10093)	IE-014	cm^3/s = -0.0053 +0.1254(mV)	0	0.0	6.8	0.32	6.8
				25	213.6	7.9	0.28	7.9
				50	427.1	9.8	0.22	9.8
				75	640.7	11.5	0.28	11.5
				100	854.3	14.1	0.35	14.1

TABLE A-I (Continued)

SUMMARY OF CALIBRATION EQUATIONS AND UNCERTAINTIES IN TEST IE-2 EXPERIMENTAL MEASUREMENTS

Measurements	Transducer (serial number)	Fuel Rod Number	Calibration Equation	Output (% of Span)	Ouput (K)	Data System Error (K)	Calibration Error (K)	Total Error (K)
Coolant Temperature Differential	Copper-Constantan Thermocouple (Type T) (SN DTC-7)	IE-011	K = 16.10(nV)[b]	0	0	0.12	0.12	0.17
				25	5.60	0.11	0.14	0.18
				50	11.20	0.19	0.11	0.22
				75	16.80	0.25	0.11	0.27
				100	22.40	0.31	0.12	0.34
Coolant Temperature Differential	Copper-Constantan Thermocouple (Type T) (SN DTC-8)	IE-012	K = 16.08(nV)[b]	0	0	0.12	0.07	0.14
				25	5.60	0.14	0.07	0.16
				50	11.20	0.19	0.07	0.20
				75	0.25	0.25	0.07	0.26
				100	22.40	0.31	0.08	0.32
Coolant Temperature Differential	Copper-Constantan Thermocouple (Type T) (SN DTC-10)	IE-013	K = 16.12(nV)[b]	0	0	0.12	0.08	0.14
				25	5.60	0.14	0.08	0.16
				50	11.20	0.19	0.07	0.20
				75	16.80	0.25	0.08	0.26
				100	22.40	0.31	0.08	0.32
Coolant Temperature Differential	Copper-Constantan Thermocouple (Type T) (SN DTC-9)	IE-014	k = 16.08(nV)[c]	0	0	0.12	0.16	0.20
				25	5.60	0.14	0.15	0.21
				50	11.20	0.19	0.15	0.24
				75	16.80	0.25	0.16	0.30
				100	22.40	0.31	0.17	0.36

TABLE A-I (Continued)

SUMMARY OF CALIBRATION EQUATIONS AND UNCERTAINTIES IN TEST IE-2 EXPERIMENTAL MEASUREMENTS

Measurements	Transducer (serial number)	Fuel Rod Number	Calibration Equation	Output (% of Span)	Ouput (MPa)	Data System Error (MPa)	Calibration Error (MPa)	Total Error (MPa)
Fuel Rod	17.2-MPa Strain	IE-011	MPa = 5.699 + 3.389(mV)	0	0	0.11	0.18	0.21
Pressure	Post		$+3.616 \times 10^{-3}(mV)^2$	25	4.3	0.13	0.12	0.18
	(SN 301)		$-2.070 \times 10^{-2}(T)$	50	8.6	0.15	0.13	0.20
				75	12.9	0.17	0.12	0.21
				100	17.2	0.20	0.19	0.28
Fuel Rod	17.2-MPa Strain	IE-012	MPa =-6.128 + 3.470(mV)	0	0	0.11	0.18	0.21
Pressure	Post		$-4.789 \times 10^{-2}(mV)^2$	25	4.3	0.13	0.12	0.18
	(SN 222)		$+9.871 \times 10^{-3}(T)$	50	8.6	0.15	0.13	0.20
				75	12.9	0.17	0.12	0.21
				100	17.2	0.20	0.19	0.28
Fuel Rod	17.2-MPa Strain	IE-013	MPa = 3.945 + 3.450(mV)	0	0	0.11	0.12	0.16
Pressure	Post		$+3.046 \times 10^{-2}(mV)^2$	25	4.3	0.13	0.08	0.15
	(SN 257)		$-1.181 \times 10^{-2}(T)$	50	8.6	0.15	0.08	0.17
				75	12.9	0.17	0.08	0.19
				100	17.2	0.20	0.13	0.24
Fuel Rod	17.2-MPa Strain	IE-014	MPa = -3.297 + 3.232(mV)	0	0	0.11	0.04	0.12
Pressure	Post		$-1.603 \times 10^{-2}(mV)^2$	25	4.3	0.13	0.03	0.13
	(SN 305)		$+7.588 \times 10^{-3}(T)$	50	8.6	0.15	0.03	0.15
				75	12.9	0.17	0.03	0.17
				100	17.2	0.20	0.04	0.20

TABLE A-I (Continued)

SUMMARY OF CALIBRATION EQUATIONS AND UNCERTAINTIES IN TEST IE-2 EXPERIMENTAL MEASUREMENTS

Measurements	Transducer (serial number)	Fuel Rod Number	Calibration Equation	Output (% of Span)	Ouput (K)	Data System Error (K)	Calibration Error (K)	Total Error (K)
Fuel Centerline Temperature	W5%/W26%Re Thermocouple (SN 435)	IE-011	$K = 341.0 + 65.09(mV) - 0.9571(mV)^2 + 0.0237(mV)^3$	0	34C	14	[c]	[c]
				25	8EC	16	[c]	[c]
				50	14EC	19	[c]	[c]
				75	19EC	23	[c]	[c]
				100	25CC	28	[c]	[c]
Fuel Centerline Temperature	W5%/W26%Re Thermocouple (SN 434)	IE-012	$K = 346.2 + 59.92(mV) - 0.7595(mV)^2 + 0.0224(mV)^3$	0	3EC	14	[c]	[c]
				25	91C	16	[c]	[c]
				50	147C	19	[c]	[c]
				75	20EC	23	[c]	[c]
				100	25EC	28	[c]	[c]
Fuel Centerline Temperature	Ultrasonic Thermometer (SN 443)	IE-013	$K^{[e]} = -1156.9 + 408.96(mV) - 11.558(mV)^2 - 0.03448(mV)^3$	0	3CC	[c]	[c]	[c]
				25	10EC	[c]	[c]	[c]
				50	172C	[c]	[c]	[c]
			$K^{[f]} = 1736.1 + 193.44(mV) - 12.609(mV)^2 + 0.45201(mV)^3$	75	241C	[c]	[c]	[c]
				100	31CC	[c]	[c]	[c]
Fuel Centerline Temperature	Ultrasonic Thermometer (SN 442)	IE-014	$K^{[g]} = -1689.1 + 567.92(mV) - 11.347(mV)^2 - 0.7130(mV)^3$	0	3CC	[c]	[c]	[c]
				25	10EC	[c]	[c]	[c]
				50	172C	[c]	[c]	[c]
			$K^{[h]} = 2167.8 + 138.52(mV) - 7.110(mV)^2 + 0.21317(mV)^3$	75	241C	[c]	[c]	[c]
				100	31CC	[c]	[c]	[c]

TABLE A-I (Continued)

SUMMARY OF CALIBRATION EQUATIONS AND UNCERTAINTIES IN TEST IE-2 EXPERIMENTAL MEASUREMENTS

Measurements	Transducer (serial number)	Fuel Rod Number	Calibration Equation	Output (% of Span)	Ouput (mm)	Data System Error (mm)	Calibration Error (mm)	Total Error (mm)
Cladding Elongation	LVDT (SN 039)	IE-011	mm = 1.510 $+9.538 \times 10^{-3}$(mV) $+1.038 \times 10^{-6}$(mV)^2 -2.392×10^{-3}(T)	0	0	[c]	[c]	[c]
				25	3.81	[c]	[c]	[c]
				50	7.62	[c]	[c]	[c]
				75	11.43	[c]	[c]	[c]
				100	15.24	[c]	[c]	[c]
Cladding Elongation	LVDT (SN 433)	IE-012	mm = 1.777 $+1.070 \times 10^{-2}$(mV) $+2.319 \times 10^{-7}$(mV)^2 -2.871×10^{-3}(T)	0	0	[c]	[c]	[c]
				25	3.81	[c]	[c]	[c]
				50	7.62	[c]	[c]	[c]
				75	11.43	[c]	[c]	[c]
				100	15.24	[c]	[c]	[c]
Cladding Elongation	LVDT (SN 210)	IE-014	mm = -0.3090 $+1.974 \times 10^{-2}$(mV) -1.637×10^{-5}(mV)^2 $+9.706 \times 10^{-9}$(mV)[d]	0	0	[c]	[c]	[c]
				25	3.81	[c]	[c]	[c]
				75	7.62	[c]	[c]	[c]
				100	15.24	[c]	[c]	[c]

[a] Calibrations are not unique to a particular fuel rod.

[b] These equations are applicable to coolant inlet temperature at 600 K.

[c] Undefined, see Appendix A discussion.

[d] This equation is for a coolant temperature of 606 K.

[e] This equation applies over the range of 300 to 1750 K.

[f] This equation applies over the range of 1750 to 2800 K.

[g] This equation applies over the range of 300 to 2150 K.

[h] This equation applies over the range of 2150 to 2800 K.

interval estimate for each equation. The data system error and linear sum of the data system error and calibration instrument error are also provided.

The criterion for the 95% confidence interval estimate for those transducers that had a linear calibration equation was established using the following relation:

$$L_i = Y_i \pm t(1-\alpha/2) \quad S_{y \cdot x} \left[\frac{1}{n} + 1 + \frac{n(x_i - \bar{x})^2}{n\Sigma X^2 - (\Sigma X)^2} \right]^{1/2} \qquad \text{(A-1)}$$

where

L_i = the confidence interval estimate

Y_i = calculated value of the dependent variable from the regression equation

$t(1-\alpha/2)$ = value from a student's distribution for n-2 degrees of freedom

α = level of confidence (0.95 was used here)

$S_{y \cdot x}$ = standard error of the regression of y on x

n = number of points

X = independent variable

$\bar{x}$ = mean value of the independent variable

x_1 = value of the independent variable for which error estimate applies.

The evaluation for L_i for several x_i values established the 95% confidence interval estimate.

For those transducers that had functional relationships that were nonlinear or more multivariate, the 95% confidence interval estimate is given by:

$$L_i = Y_i \pm t(1 - \alpha/2)E \qquad (A\text{-}2)$$

where E is the standard error for the multivariate or polynomial relationship, and the other terms are as defined previously. The standard error term contains cross terms of the coefficients and independent variables. The preceding procedures were extracted from Reference A-1.

For those transducers that were not calibrated, the 95% confidence interval estimate is assumed to be specified by the accuracy limits as established by a manufacturer or an ANSI standard. The type of error estimate for each transducer is specified in the following discussions.

Test Train Instrumentation

(1) System Pressure. Two 69-MPa strain post pressure transducers were used to monitor the coolant pressure. One 69-MPa pressure transducer (SN 156) failed prior to the test, therefore only the calibration for the other (SN 159) is presented. As discussed in Section 3, this transducer drifted excessively.

(2) Coolant Inlet Temperature. Two Chromel-Alumel (Type K) thermocouples were used to measure the coolant inlet temperature. These devices were not calibrated. The 95% confidence interval estimate was taken to be 0.375% of reading, as stated by the manufacturer when using the standard calibration tables.

(3) Coolant Outlet Temperature. One Chromel-Alumel (Type K) thermocouple was provided to obtain the coolant outlet temperature of each fuel rod. Again, these devices were not calibrated and the error estimate for these devices was the same as for the inlet temperature thermocouples.

(4) Coolant Temperature Rise. One copper-constantan differential temperature measurement thermocouple pair was positioned in each flow shroud. Each thermocouple pair was calibrated for inlet temperatures of 583, 600, and 605 K for a 20 K temperature rise at each inlet temperature. All of the differential thermocouples correlated well.

(5) Coolant Flow. Four flowmeters with graphite journal bearings were used to measure the coolant flow rate through each flow shroud. These flowmeters were calibrated by the manufacturer (Flow Technology Incorporated). Although the calibrations were conducted with a slightly different inlet and outlet flow geometry than was used during the test, it has been established that these deviations do not affect the measured coolant flow accuracy.

(6) Cladding Elongation. A linear variable differential transformer (LVDT) was used on each fuel rod to measure the cladding elongation. The calibration equations for these devices are shown in Table A-I.

The output of each LVDT is sensitive to the transducer temperature, the lead wire resistance, and the electronic settings of the signal conditioner used. The transducers that were utilized for this experiment were not calibrated at the temperature and with the same lead wire and electronics settings that were used during the test. The procedure followed in determining a calibration function for the LVDTs was briefly described in the IE-1 Test Results Report[A-2].

Due to the nature of the calibration of these LVDTs, a formal estimate of the 95% confidence interval is not deemed appropriate; but, it is estimated that the calibrations described the cladding elongation changes within 5% (except for the LVDT on Rod IE-014). The calibration procedure used is not considered optimum, but practical limitations prevented correcting the deficiency for this test. (The LVDT on Rod IE-014 had decalibrated severely, so that the data were not presented).

Fuel Rod Instrumentation

(1) Fuel Rod Internal Pressure. Each fuel rod was fit with a 17-MPa strain post-type pressure transducer to measure the fuel rod internal pressure. The error estimates provided in this appendix represent the uncertainty associated with a multivariate (transducer case temperature and diaphragm pressure) fit to the calibration data. The design of these devices is such that they are occasionally subject to changes in the zero offsets between repeated pressure increase and decrease cycles. Sometimes this drift is excessive. A review of calibration data for several of these pressure transducers has shown that the calibration of the transducer generally does not shift during a pressure increase cycle and that any zero offset change usually occurs during the pressure decrease portion of a cycle. Consequently, the pressure differentials indicated during power increases are likely to be an accurate measure of the fuel rod internal pressure.

The reason for the zero shift is not fully understood, but it is most likely due to the strain gauges not being integrally attached to the strain post in the pressure transducer. Transducers SN 222 and SN 257 were not calibrated at temperatures above 590 K so they were expected to be less accurate than the remaining two transducers, calibrated at 606 K, the temperature at which the preconditioning and flow reduction portions of the test were conducted.

(2) Fuel Centerline Temperature. Tungsten-rhenium thermocouples were used to measure the fuel centerline temperature in Rods IE-011 and IE-012. The thermocouples used in the test consisted of a short, high temperature section spliced to a long lead-out cable. The lead-out cable was insulated with MgO, a stainless steel sheath, and wires (405/426 Hoskins alloys). These alloys match the standard calibration for W5%Re/W26%Re thermocouples. The high temperature zone had a tantalum sheath, BeO insulation, and stranded W5%Re/W26%Re wires. This high temperature portion for Rod IE-011 was calibrated prior to use, but the calibration of this zone did not match the standard calibration.

However, it did remain within 25 K of the standard calibration. The result is a thermocouple with a dual calibration which responds differently to temperature gradients along different parts of its length. This condition is discussed in IE Scoping Test 2 Test Results Report[A-3].

The high temperature portion of the thermocouple for Rod IE-012 was not calibrated, thus the standard calibration for a W5%Re/W26%Re thermocouple was used. The estimated uncertainty for these two thermocouples is ±30 K over the range from 600 to 2500 K.

Ultrasonic thermometers (UTs) were used to measure the fuel centerline temperature in Rods IE-013 and IE-014. The UTs were calibrated up to 2800 K using a combination of an optical pyrometer and a tungsten-rhenium thermocouple. The instrumentation for this device is set up such that a change of output range occurs during the DNB portion of the test. The UTs are expected to be accurate within ±5% but based on the arguments in Section 6.2.3 the error may be much larger.

(3) Cladding Surface Temperature. Uncalibrated tungsten-rhenium thermocouples, spring-loaded against the cladding, were used to measure the cladding surface temperature on Rods IE-011 and IE-012. The 95% confidence interval estimate was taken to be 0.375% of the reading, as stated by the manufacturer when using standard calibration tables. Type S thermocouples were used on Rods IE-013 and IE-014. Again, standard calibration tables were used to convert these data.

The uncertainties listed in Table A-I are for the test following the gap conductance phase. As discussed in Section 3.1, the recording range was switched from a small range to a large range at this point in the test. Because of the range changes, two separate calibration equations were used to evaluate the data. During the power calibration cycles, a calibration equation for the narrow range of 500 to 700 K was used. The instrument error was approximately ±1 K. During the preconditioning period and ramp to high power, an equation for a range of 500 to 2000 K was used in preparation for temperatures expected during

the flow reduction. The associated instrument error for this equation was ±10 K for the spring-loaded thermocouples and ±7 K for the Type S thermocouples. In an attempt to minimize this uncertainty in the absolute temperature, each cladding thermocouple was intercalibrated with the inlet temperature at zero power. After the data were adjusted using the inter-calibration results, the instrument uncertainties were estimated to be ±2 K for temperatures between 500 and 700 K. Above 700 K, the uncertainties given in Table A-I apply.

Another type of systematic error is also present in the cladding surface thermocouple data. Both spring-loaded and Type-S thermocouples measure temperatures other than cladding surface temperatures. The spring-loaded thermocouples measure temperatures between coolant and cladding surface temperature due to the coolant cooling the thermocouples which act as a fins in the flow. During film boiling operation, the errors are extreme with differences between actual and indicated temperatures on the order of several hundred degrees. The error in the Type S thermocouple data is apparently a function of the type of flow regime surrounding the rod. During forced convection and nucleate boiling, the Type S thermocouples measure temperatures between cladding midradius and surface because they are embedded in the cladding. During film boiling operation, these thermocouples indicate temperatures 100 to 200 K less than is calculated for the cladding surface temperatures. Because of the measurements during forced convection and nucleate boiling, it is felt that the thermocouples are indicating the actual temperature of the cladding somewhere between the midradius and surface, but have locally cooled the cladding due to the thermocouples acting as fins.

Data Acquisition System

A summary of the data recording system errors associated with decalibration and drift of the electronics used to record and reduce the data are given for each transducer in Table A-I. A thorough discussion of the source of these errors is given in Appendix B of the IE Scoping Test 1 Report[A-4].

The data system amplification, gain, and offset are such that the input signal (transducer output) and the output signal (recorded data signal) are related by the equation:

$$V_o = (V_i - V_z)\, G \qquad \text{(A-3)}$$

where

V_o = recorded data signal (volts)

V_i - transducer output signal (volts)

V_z = offset (volts)

G = gain.

The standard deviation of the recorded data signal, SV_o, can then be determined to be

$$SV_o = \left[\left(\frac{V_o}{G}\right)^2 S_G^{\,2} + G^2 S_{V_z}^{\,2} + G^2 S_{V_i}^{\,2}\right]^{1/2}. \qquad \text{(A-4)}$$

For the calibration, SV_i can be considered to be zero such that

$$S_{V_o} = \left[\left(\frac{V_o}{G}\right)^2 S_G^{\,2} + G^2 S_{V_z}^{\,2}\right]^{1/2} \qquad \text{(A-5)}$$

A test performed to evaluate the data system resulted in values of $\frac{S_G}{G}$ and GS_{V_z} to be 0.65% and 2.7 millivolts, respectively.

For a total span ($Y_{max} - Y_{min}$) on the recording channel of 1000 millivolts, Equation (A-5) can be simplified to

$$\frac{S_y}{Y_{max} - Y_{min}}\,\% = \left[\left(\frac{Y - Y_{min}}{Y_{max} - Y_{min}}\right)^2 \times (0.65\%)^2 + (0.27\%)^2\right]^{1/2} \qquad \text{(A-6)}$$

where

Y = measured signal in engineering units

S_Y = standard deviation of Y

Y_{max} = maximum output signal

Y_{min} = minimum output signal

$Y_{max}-Y_{min}$ = span of output signal.

The total transducer measurement uncertainty, excluding the systematic measurement error, can be estimated by combining the uncertainty in the calibration and the uncertainty associated with the data acquisition system. The "total error" is given to be the square root of the sum of the squares of these two errors. Table A-I summarizes the data system error, calibration error and the resultant total error for each of the transducers that functioned during the test.

REFERENCES

A-1. M. G. Natrella, *Experimental Statistics, National Bureau of Standards Handbook 91*, U. S. Government Printing Office, 1963.

A-2. W. J. Quapp et al., *Irradiation Effects Test Series Test IE-1 Test Results Report*, TREE-NUREG-1046 (March 1977).

A-3. W. J. Quapp et al., *Irradiation Effects Test Series Scoping Test 2 Test Results Report*, TFBP-TR-137 (September 1976).

A-4. W. J. Quapp et al., *Irradiation Effects Test Series Scoping Test 1 Test Results Report*, TFBP-TR-110 (January 1976).

APPENDIX B

FUEL ROD CHARACTERIZATION DATA

The pretest fuel rod characterization data for Test IE-2 are presented in this appendix to: (a) facilitate a comparison of fuel rod physical characteristics between IE experiments, (b) provide input for the analytical models used for prediction of fuel rod behavior during nuclear operations, and (c) provide data for posttest model verification activities. The amount and type of characterization data available are different for each fuel rod used in the test. All measurements, with the exception of mass and volume, were obtained using devices that are scaled for U. S. Customary Units. These values were then converted to SI units.

Rod IE-011 was constructed with cladding from a MAPI fuel rod (M-15) irradiated in the Saxton reactor to an approximate burnup of 5110 MWd/t and fresh fuel. Irradiated fuel within the MAPI rod was removed and replaced with unirradiated 12.5 wt% $^{235}UO_2$ fuel. The original end cap was replaced with an instrumented upper end cap. Characterization data for the Rod IE-011 are presented in Table B-I. The 95% population loaded value in the table refers to the dimensional range of a parameter within which 95% of the measurements were found. The void volume measurement includes the void found in the fueled region, the plenum, and the instrumented end cap. The measurement accuracy is $\pm$ 0.2 cm^3. The cladding mechanical properties are typical of MAPI fuel rod cladding prior to irradiation in the Saxton reactor. Table B-II contains characterization data for the fresh fuel pellets inserted into Rod IE-011. Pellet length measurements were obtained by measuring the length between the upper and lower dish shoulder of each pellet. Both the diameter and length measurements were performed using a Bausch and Lomb optical gauge, Model BR-25. The measurements are accurate to within $\pm$ 0.0005 cm. An analytical balance, accurate to within $\pm$ 1 milligram, was used to weigh the pellets. Table B-III contains cladding dimensions for Rod IE-011. An air gauge was used to

obtain measurements of the cladding inner diameter (ID) for the length of the rod. The accuracy of these measurements is estimated to be within ± 0.002 cm. Figure B-1 combines the fuel pellet outer diameter (OD) and cladding ID measurements to illustrate the diametral gap as a function of axial position.

Rod IE-012 is similar to Rod IE-011. Cladding from a MAPI fuel rod (M-19) irradiated in the Saxton reactor to an approximate burnup of 5610 MWd/t was filled with fresh 12.5 wt% $^{235}UO_2$ fuel and fitted with an instrumented upper end cap. Characterization data for the fuel rod is contained in Table B-IV. The fuel pellets, for which characterization is presented in Table B-V, were slightly smaller in diameter than those used in Rod IE-011 to create a larger diametral gap between the fuel and cladding. Measured cladding dimensions are presented in Table B-VI. Figure B-2 illustrates the diametral gap versus axial position for Rod IE-012. Two fuel pellets had an OD slightly different from the remainder of the pellets loaded in the rod.

Rod IE-013 was constructed using the cladding from an unirradiated Saxton fuel rod (925) and fresh 12.5 wt% $^{235}UO_2$ fuel pellets with the same OD as those pellets used in Rod IE-011. Characterization data for the fuel rod, fuel pellets, and cladding are presented in Tables B-VII, B-VIII, and B-IX, respectively. Figure B-3 contains the axial profile of the diametral gap for Rod IE-013.

Rod IE-014 was also manufactured with cladding from an unirradiated Saxton fuel rod (929). Fresh 12.5 wt% $^{235}UO_2$ fuel pellets having an OD similar to the pellets used in Rod IE-012 were inserted in Rod IE-014. Tables B-X, B-XI, and B-XII, respectively, contain characterization data for the fuel rod, fuel pellets, and cladding. Fuel pellet OD and cladding ID measurements are shown in Figure B-4 to illustrate the axial profile of the diametral gap.

A detailed characterization of these and other fuel rods used in the IE test series can be found in Reference B-1.

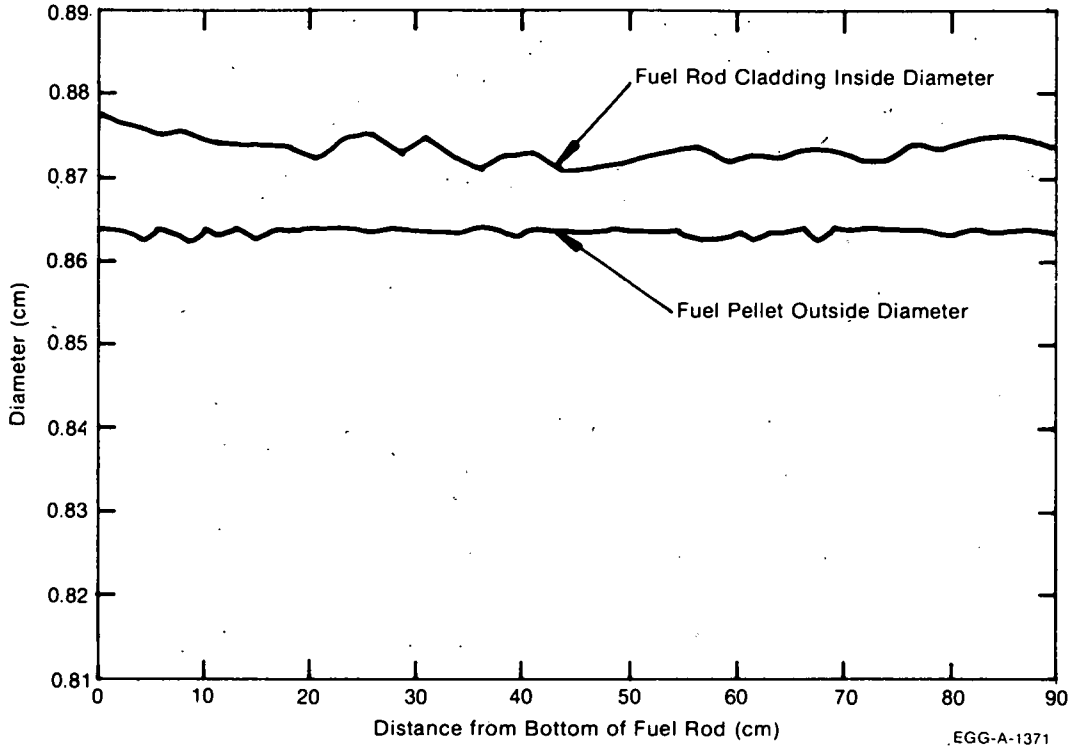

Fig. B-1 Diametral fuel-cladding gap versus axial position for Rod IE-011.

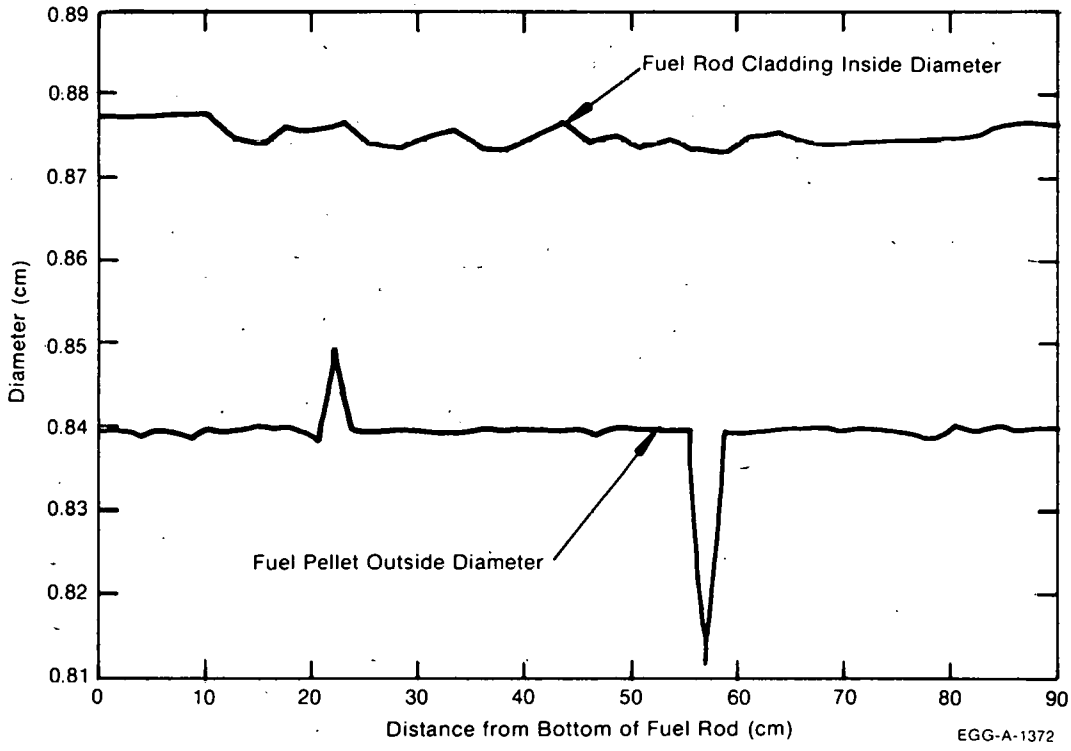

Fig. B-2 Diametral fuel-cladding gap versus axial position for Rod IE-012.

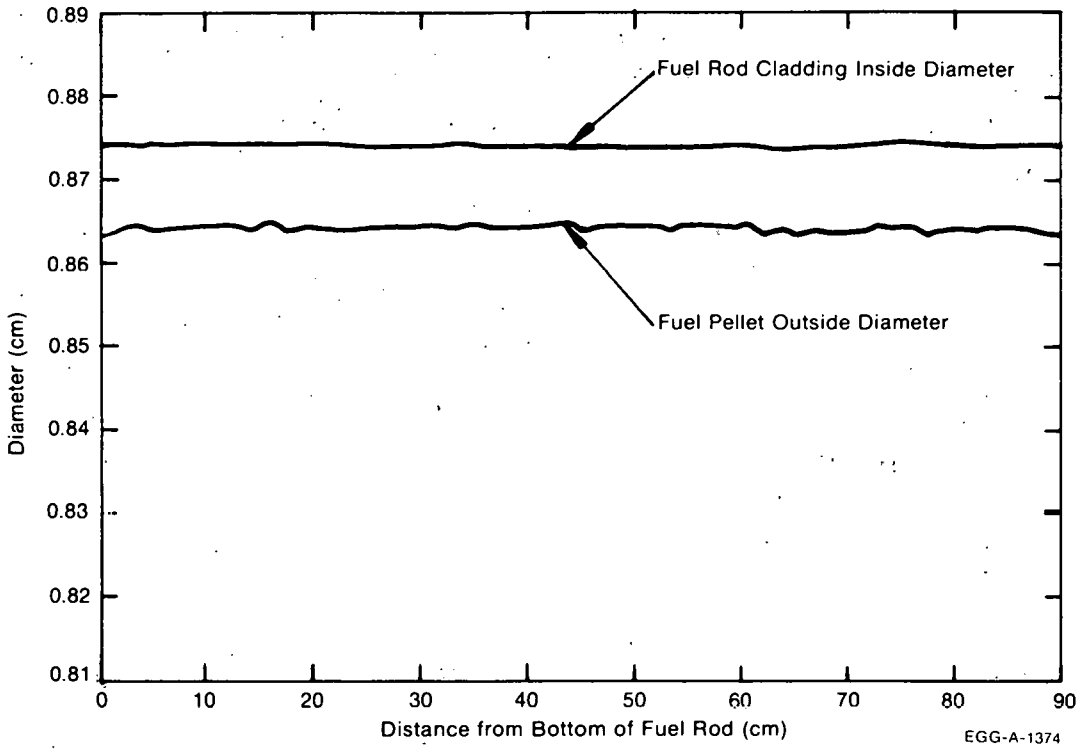

Fig. B-3 Diametral fuel-cladding gap versus axial position for Rod IE-013.

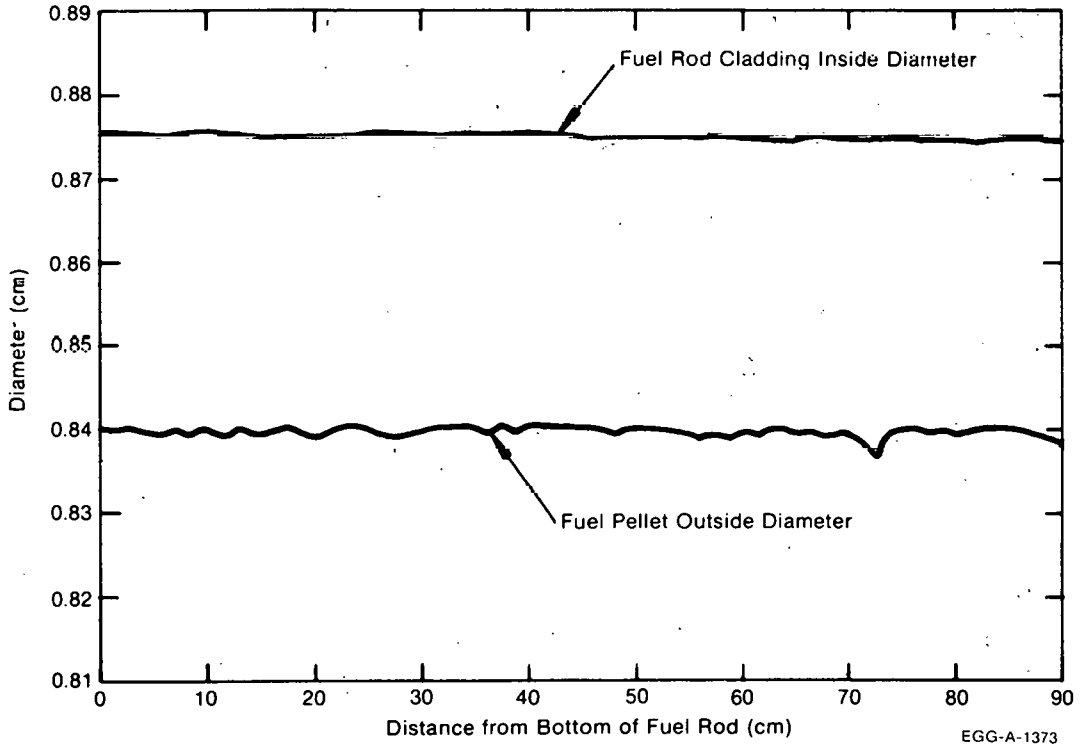

Fig. B-4 Diametral fuel-cladding gap versus axial position for Rod IE-014.

TABLE B-I

OVERALL PRETEST FUEL ROD AND CLADDING DATA FOR ROD IE-011

Finished Tube Data:		
Mean OD	-	0.9997 cm
Mean ID	-	0.8738 cm
Ovality (Max ID/Min ID)	-	1.0050
Cladding Length	-	96.949 cm
Overall Length	-	103.38 cm
Mechanical Properties Of Unirradiated Fuel Rod Cladding[a]:		
Yield Tensile Strength		
At Room Temperature	-	568.7 MPa
At 658 K	-	320.3 MPa
Ultimate Tensile Strength		
At Room Temperature	-	749.1 MPa
At 658 K	-	423.0 MPa
Fuel Data:		
Enrichment	-	12.49% ^{235}U
Mean Geometric Density	-	10.3661 gram/cm^3
95% Population Loaded	-	10.3661 (+ 1.3184, - 0.2059) gram/cm^3
Mean Diameter	-	0.8636 cm
95% Population Loaded	-	0.8636 (+0.0005, -0.0015) cm
Stack Mass	-	523.6631 gram
Measured Stack Length	-	88.3996 cm
Dish Dimensions		
Dish Chord	-	0.6604 cm
Dish Depth	-	0.0343 cm
Grain Size		
Grain Diameter	-	$22.5 \pm 6.5 \times 10^{-4}$ cm
Center Hole Length	-	18.2093 cm
Plenum Length	-	5.7404 cm
Mean Fuel-Cladding Gap	-	0.0102 cm
Measured Void Volume	-	6.6 ml
Fill Gas Data		
Pressure	-	2.51 MPa
Composition	-	76% He, 24% Ar

[a] Data supplied by Westinghouse Electric Corporation.

TABLE B-II

FUEL PELLET CHARACTERIZATION DATA FOR ROD IE-011

PELLET[a] NO.	DIAMETER (cm)				LENGTH (cm)			WEIGHT (GRAMS)	GEOMETRIC DENSITY (g/cm^3)	IMMERSION DENSITY (g/cm^3)
	TOP	CENTER	BOTTOM	AVERAGE	0°	90°	AVERAGE			
1	0.8633	0.8635	0.8636	0.8635	1.5403	1.5222	1.5312	9.1360	10.3236	0.0
2	0.8636	0.8633	0.8628	0.8633	1.5438	1.5400	1.5419	9.2181	10.3495	0.0
3	0.8623	0.8623	0.8623	0.8623	1.5433	1.5390	1.5411	9.2171	10.3762	0.0
4	0.8639	0.8639	0.8636	0.8638	1.5222	1.5174	1.5198	9.0904	10.3442	0.0
5	0.8636	0.8635	0.8631	0.8634	1.5573	1.5514	1.5544	9.2891	10.3405	10.3822
6	0.8616	0.8623	0.8626	0.8622	1.5220	1.5176	1.5198	9.0921	10.3853	0.0
7	0.8636	0.8639	0.8636	0.8637	1.5301	1.5265	1.5283	9.1731	10.3814	0.0
8	0.8626	0.8631	0.8631	0.8629	1.5154	1.5090	1.5122	9.0245	10.3422	0.0
9	0.8636	0.8639	0.8639	0.8638	1.5413	1.5367	1.5390	9.2372	10.3785	0.0
10	0.8623	0.8623	0.8631	0.8628	1.5629	1.5608	1.5618	9.3486	10.3726	10.3766
11	0.8636	0.8635	0.8639	0.8637	1.5189	1.5138	1.5164	9.0608	10.3362	0.0
12	0.8639	0.8633	0.8636	0.8636	1.5281	1.5207	1.5244	9.1222	10.3529	0.0
13	0.8636	0.8639	0.8641	0.8639	1.5423	1.5380	1.5401	9.2200	10.3493	0.0
14	0.8639	0.8639	0.8639	0.8639	1.5240	1.5207	1.5223	9.1063	10.3427	0.0
15	0.8639	0.8639	0.8639	0.8639	1.5187	1.5138	1.5163	9.0849	10.3604	10.3831
16	0.8639	0.8639	0.8639	0.8639	1.5187	1.5143	1.5165	9.0570	10.3629	0.0
17	0.8636	0.8635	0.8636	0.8636	1.5314	1.5276	1.5295	9.1339	10.3313	0.0
18	0.8639	0.8639	0.8639	0.8639	1.5357	1.5321	1.5339	9.2119	10.3828	0.0
19	0.8633	0.8639	0.8639	0.8637	1.5192	1.5123	1.5157	9.0653	10.3457	0.0
20	0.8639	0.8635	0.8636	0.8637	1.5314	1.5255	1.5284	9.1187	10.3190	10.3754
21	0.8633	0.8635	0.8636	0.8635	1.5530	1.5481	1.5505	9.3002	10.3766	0.0
22	0.8633	0.8633	0.8633	0.8633	1.5283	1.5217	1.5250	9.1264	10.3595	0.0
23	0.8639	0.8641	0.8636	0.8639	1.5194	1.3856	1.4525	9.0435	10.7722	0.0
24	0.8639	0.8635	0.8636	0.8637	1.3967	1.5197	1.4582	9.1316	10.8383	0.0
25	0.8633	0.8635	0.8633	0.8634	1.5121	1.3795	1.4458	8.9978	10.7791	10.2919
26	0.8631	0.8623	0.8626	0.8628	1.5489	1.5453	1.5471	9.2356	10.3441	0.0
27	0.8636	0.8639	0.8636	0.8637	1.5141	1.5113	1.5127	9.0685	10.3705	0.0
28	0.8633	0.8639	0.8633	0.8635	1.3820	1.3769	1.3795	9.0093	10.3170	0.0
29	0.8636	0.8639	0.8639	0.8638	1.5425	1.5367	1.5396	9.2380	10.3751	0.0
30	0.8636	0.8633	0.8631	0.8633	1.5207	1.5164	1.5185	9.0800	10.3514	10.4241

TABLE B-II (Continued)

FUEL PELLET CHARACTERIZATION DATA FOR ROD IE-011

PELLET[a] NO.	DIAMETER (cm) TOP	CENTER	BOTTOM	AVERAGE	LENGTH (cm) 0°	90°	AVERAGE	WEIGHT (GRAMS)	GEOMETRIC DENSITY (g/cm^3)	IMMERSION DENSITY (g/cm^3)
31	0.8633	0.8636	0.8633	0.8634	1.5321	1.5303	1.5312	9.1799	10.3753	0.0
32	0.8639	0.8641	0.8636	0.8639	1.5451	1.5377	1.5414	9.2033	10.3220	0.0
33	0.8639	0.8636	0.8633	0.8636	1.5230	1.5121	1.5175	9.0841	10.3569	0.0
34	0.8636	0.8633	0.8633	0.8634	1.5207	1.5174	1.5190	9.0806	10.3465	0.0
35	0.8636	0.8639	0.8636	0.8637	1.5182	1.5151	1.5166	9.0650	10.3392	10.3997
36	0.8639	0.8639	0.8636	0.8638	1.5113	1.5065	1.5089	9.0121	10.3303	0.0
37	0.8626	0.8628	0.8628	0.8628	1.5166	1.5154	1.5160	9.0373	10.3346	0.0
38	0.8628	0.8628	0.8628	0.8628	1.5151	1.5118	1.5135	9.0282	10.3397	0.0
39	0.8631	0.8628	0.8628	0.8630	1.5187	1.5146	1.5166	9.0362	10.3228	0.0
40	0.8636	0.8639	0.8633	0.8636	1.5070	1.4989	1.5029	9.0035	10.3661	10.4119
41	0.8626	0.8628	0.8626	0.8627	1.5428	1.5380	1.5404	9.2000	10.3539	0.0
42	0.8636	0.8636	0.8636	0.8636	1.5230	1.5146	1.5188	9.0672	10.3289	0.0
43	0.8633	0.8636	0.8639	0.8636	1.5220	1.5192	1.5206	9.0825	10.3341	0.0
44	0.8641	0.8641	0.8641	0.8641	1.5291	1.5263	1.5277	9.1344	10.3317	0.0
45	0.8626	0.8628	0.8628	0.8628	1.5306	1.3960	1.4633	9.1388	10.8323	10.4244
46	0.8639	0.8641	0.8641	0.8640	1.5126	1.5100	1.5113	9.0706	10.3744	0.0
47	0.8639	0.8641	0.8639	0.8639	1.5281	1.5225	1.5253	8.7298	10.3491	10.2935
48	0.8639	0.8641	0.8641	0.8640	1.5105	1.5067	1.5086	8.6282	10.3475	10.1772
49	0.8639	0.8641	0.8641	0.8640	1.5258	1.5199	1.5229	8.6888	10.3419	10.2101
50	0.8641	0.8641	0.8636	0.8639	1.5250	1.5212	1.5231	8.7157	10.3406	10.2988
51	0.8641	0.8641	0.8639	0.8640	1.5380	1.5326	1.5353	8.7641	10.3255	10.3160
52	0.8639	0.8636	0.8639	0.8638	1.5202	1.5149	1.5175	8.6948	10.3855	10.3058
53	0.8633	0.8639	0.8633	0.8635	1.5037	1.4956	1.4996	8.5646	10.3400	10.1963
54	0.8639	0.8639	0.8636	0.8638	1.5235	1.5182	1.5208	8.6820	10.3339	10.1602
55	0.8639	0.8641	0.8639	0.8639	1.5237	1.5189	1.5213	8.6735	10.3227	10.6845
56	0.8636	0.8639	0.8636	0.8637	1.5049	1.4994	1.5022	8.5823	10.3460	10.1556
57	0.8639	0.8639	0.8639	0.8639	1.5128	1.5083	1.5105	8.6299	10.3406	10.1720
58	0.8636	0.8639	0.8641	0.8639	1.5161	1.5126	1.5143	8.6476	10.3421	10.2486

[a] Pellets are numbered from bottom of fuel stack.

TABLE B-III

FUEL ROD CLADDING DIMENSIONS FOR ROD IE-011

Tube Inside Diameter Measurements			Tube Outside Diameter Measurements		
Location[a] (cm)	Inside Diameter (cm)		Location[a] (cm)	Outside Diameter (cm)	
	0°	90°		0°	90°
2.54	0.8768	0.8758	71.12	0.9967	1.0025
5.08	0.8755	0.8750	73.66	0.9980	1.0018
7.62	0.8755	0.8750	76.20	0.9992	1.0010
10.16	0.8740	0.8740	78.74	0.9977	1.0023
12.70	0.8735	0.8730			
15.24	0.8735	0.8735			
17.78	0.8735	0.8735			
20.32	0.8715	0.8722			
22.86	0.8745	0.8748			
25.40	0.8750	0.8748			
27.94	0.8730	0.8725			
30.48	0.8748	0.8750			
33.02	0.8725	0.8725			
35.56	0.8710	0.8710			
38.10	0.8733	0.8722			
40.64	0.8730	0.8727			
43.18	0.8710	0.8710			
45.72	0.8707	0.8717			
48.26	0.8715	0.8717			
50.80	0.8725	0.8725			
53.34	0.8738	0.8725			
55.88	0.8735	0.8738			
58.42	0.8722	0.8725			
60.96	0.8730	0.8725			
63.50	0.8722	0.8727			
66.04	0.8733	0.8738			
68.58	0.8733	0.8730			
71.12	0.8722	0.8720			
73.66	0.8725	0.8717			
76.20	0.8738	0.8743			
78.74	0.8740	0.8730			
81.28	0.8738	0.8750			
83.82	0.8750	0.8748			
86.36	0.8745	0.8750			
88.90	0.8745	0.8733			

[a] Distance from bottom of fuel rod.

TABLE B-IV

OVERALL PRETEST FUEL ROD AND CLADDING DATA FOR ROD IE-012

Finished Tube Data:		
Mean OD	-	0.9967 cm
Mean ID	-	0.8733 cm
Ovality (Max ID/Min ID)	-	1.0050
Cladding Length	-	96.954 cm
Overall Length	-	103.378 cm
Mechanical Properties Of Unirradiated Fuel Rod Cladding[a]:		
Yield Tensile Strength		
At Room Temperature	-	568.7 MPa
At 658 K	-	320.3 MPa
Ultimate Tensile Strength		
At Room Temperature	-	749.1 MPa
At 658 K	-	423.0 MPa
Fuel Data:		
Enrichment	-	12.49% ^{235}U
Mean Geometric Density	-	10.2776 gram/cm^3
95% Population Loaded	-	10.2776 (+01519, -0.8977) gram/cm^3
Mean Diameter	-	0.8390 cm
95% Population Loaded	-	0.8390 (+0.0104, -0.0277) cm
Stack Mass	-	493.2690 gram
Measured Stack Length	-	88.3768 cm
Dish Dimensions		
Dish Chord	-	0.6604 cm
Dish Depth	-	0.0343 cm
Grain Size		
Grain Diameter	-	$22.5 \pm 6.5 \times 10^{-4}$ cm
Center Hole Length	-	18.2677 cm
Plenum Length	-	5.7404 cm
Mean Fuel-Cladding Gap	-	0.0343 cm
Measured Void Volume	-	9.2 ml
Fill Gas Data		
Pressure	-	2.50 MPa
Composition	-	76% He, 24% Ar

[a] Data supplied by Westinghouse Electric Corporation.

TABLE B-V

FUEL PELLET CHARACTERIZATION DATA FOR ROD IE-012

PELLET[a] NO.	DIAMETER (cm)				LENGTH (cm)			WEIGHT (GRAMS)	GEOMETRIC DENSITY (g/cm^3)	IMMERSION DENSITY (g/cm^3)
	TOP	CENTER	BOTTOM	AVERAGE	0°	90°	AVERAGE			
1	0.8392	0.8397	0.8395	0.8395	1.5372	1.5397	1.5385	8.7112	10.3739	0.0
2	0.8390	0.8395	0.8395	0.8393	1.5270	1.5225	1.5248	8.5758	10.3100	0.0
3	0.8390	0.8392	0.8387	0.8390	1.5283	1.5316	1.5300	8.6524	10.3747	0.0
4	0.8390	0.8395	0.8395	0.8393	1.5443	1.5484	1.5464	8.6074	10.2015	0.0
5	0.8395	0.8392	0.8387	0.8391	1.5204	1.5176	1.5190	8.5725	10.3496	10.3904
6	0.8382	0.8385	0.8387	0.8385	1.5403	1.5448	1.5425	8.6899	10.3462	0.0
7	0.8392	0.8395	0.8397	0.8395	1.5367	1.5375	1.5371	8.6971	10.3666	0.0
8	0.8390	0.8392	0.8390	0.8390	1.5245	1.5278	1.5262	8.6077	10.3451	0.0
9	0.8392	0.8395	0.8395	0.8394	1.5016	1.5065	1.5041	8.4900	10.3473	0.0
10	0.8395	0.8397	0.8397	0.8396	1.5151	1.5207	1.5179	8.5518	10.3198	10.3813
11	0.8392	0.8395	0.8395	0.8394	1.5133	1.5176	1.5155	8.5600	10.3528	0.0
12	0.8395	0.8397	0.8397	0.8396	1.5337	1.5377	1.5357	8.6955	10.3700	0.0
13	0.8390	0.8395	0.8392	0.8392	1.5222	1.5278	1.5250	8.6189	10.3622	0.0
14	0.8379	0.8379	0.8379	0.8379	1.5283	1.5329	1.5306	8.6152	10.3512	0.0
15	0.8494	0.8496	0.8494	0.8495	1.5215	1.5245	1.5230	8.8182	10.3581	10.0975
16	0.8392	0.8392	0.8395	0.8393	1.5329	1.5367	1.5348	8.6583	10.3402	0.0
17	0.8392	0.8392	0.8395	0.8393	1.5100	1.5138	1.5119	8.5233	10.3351	0.0
18	0.8392	0.8397	0.8395	0.8395	1.4999	1.5075	1.5037	8.5074	10.3690	0.0
19	0.8395	0.8395	0.8395	0.8395	1.5060	1.5088	1.5074	8.5109	10.3476	0.0
20	0.8395	0.8395	0.8390	0.8393	1.5093	1.5141	1.5117	8.5011	10.3099	10.3829
21	0.8390	0.8392	0.8395	0.8392	1.5255	1.5288	1.5272	8.6113	10.3382	0.0
22	0.8392	0.8392	0.8392	0.8392	1.5255	1.5298	1.5277	8.7837	10.5416	0.0
23	0.8392	0.8395	0.8395	0.8394	1.5116	1.5199	1.5157	8.5340	10.3196	0.0
24	0.8395	0.8395	0.8397	0.8396	1.5293	1.5331	1.5312	8.6473	10.3429	0.0
25	0.8392	0.8395	0.8395	0.8394	1.5210	1.5240	1.5225	8.5844	10.3340	10.3880
26	0.8395	0.8395	0.8395	0.8395	1.4994	1.5039	1.5016	8.4709	10.3387	0.0
27	0.8395	0.8392	0.8392	0.8393	1.5403	1.5453	1.5428	8.6967	10.3314	0.0
28	0.8392	0.8395	0.8395	0.8394	1.5433	1.5469	1.5451	8.5679	10.1611	0.0
29	0.8392	0.8395	0.8395	0.8394	1.5088	1.5136	1.5112	8.5522	10.3733	0.0
30	0.8395	0.8395	0.8395	0.8395	1.5042	1.5090	1.5066	8.4845	10.3208	10.3678

TABLE B-V (Continued)

FUEL PELLET CHARACTERIZATION DATA FOR ROD IE-012

PELLET[a] NO.	DIAMETER (cm) TOP	CENTER	BOTTOM	AVERAGE	LENGTH (cm) 0°	90°	AVERAGE	WEIGHT (GRAMS)	GEOMETRIC DENSITY (g/cm^3)	IMMERSION DENSITY (g/cm^3)
31	0.8932	0.8392	0.8390	0.8391	1.5263	1.5156	1.5210	8.5868	10.3537	0.0
32	0.8395	0.8395	0.8395	0.8396	1.5039	1.5062	1.5051	8.5132	10.3642	0.0
33	0.8395	0.8395	0.8392	0.8394	1.5286	1.5334	1.5310	8.6589	10.3649	0.0
34	0.8392	0.8397	0.8392	0.8394	1.5329	1.5364	1.5347	8.6363	10.3127	0.0
35	0.8392	0.8397	0.8392	0.8394	1.5370	1.5405	1.5387	8.6682	10.3231	10.3898
36	0.8397	0.8397	0.8392	0.8396	1.5395	1.5438	1.5417	8.7100	10.3487	0.0
37	0.8392	0.8395	0.8395	0.8394	1.5161	1.5243	1.5202	8.6094	10.3799	0.0
38	0.8113	0.8113	0.8113	0.8113	1.5159	1.5199	1.5179	7.9232	10.2519	0.0
39	0.8392	0.8392	0.8395	0.8393	1.5189	1.5235	1.5212	8.5920	10.3540	0.0
40	0.8390	0.8392	0.8395	0.8392	1.5138	1.5169	1.5154	8.5510	10.3470	10.3516
41	0.8392	0.8395	0.8392	0.8393	1.5202	1.5151	1.5176	8.5779	10.3616	0.0
42	0.8392	0.8395	0.8395	0.8394	1.5334	1.5278	1.5306	8.6324	10.3358	0.0
43	0.8400	0.8397	0.8392	0.8396	1.5268	1.5220	1.5244	8.6147	10.3509	0.0
44	0.8397	0.8397	0.8395	0.8396	1.5194	1.5159	1.5176	8.5847	10.3613	0.0
45	0.8397	0.8397	0.8397	0.8397	1.5293	1.5240	1.5267	8.6183	10.3374	10.4076
46	0.8395	0.8395	0.8395	0.8395	1.5174	1.5136	1.5155	8.5717	10.3648	0.0
47	0.8397	0.8400	0.8395	0.8397	1.5174	1.5105	1.5140	8.1426	10.3384	10.3363
48	0.8395	0.8397	0.8395	0.8396	1.5255	1.5227	1.5241	8.2093	10.3549	10.2526
49	0.8392	0.8395	0.8397	0.8395	1.5184	1.5128	1.5155	8.1601	10.3559	10.2463
50	0.8390	0.8395	0.8392	0.8392	1.5215	1.5166	1.5190	8.1612	10.3402	10.3179
51	0.8397	0.8392	0.8385	0.8385	1.5138	1.5077	1.5108	8.0965	10.3472	10.3053
52	0.8372	0.8392	0.8397	0.8387	1.5326	1.5276	1.5301	8.2270	10.3606	10.3997
53	0.8400	0.8400	0.8400	0.8400	1.5344	1.5301	1.5323	8.2570	10.3501	10.2396
54	0.8395	0.8397	0.8392	0.8395	1.4986	1.4920	1.4953	8.0451	10.3650	10.4295
55	0.8395	0.8397	0.8397	0.8396	1.5349	1.5324	1.5337	8.2450	10.3488	10.0694
56	0.8397	0.8397	0.8400	0.8398	1.5273	1.5205	1.5237	8.1827	10.3348	10.3799
57	0.8392	0.8397	0.8397	0.8396	1.5184	1.5143	1.5164	8.1607	10.3491	10.4141
58	0.8395	0.8397	0.8397	0.8396	1.5337	1.5293	1.5315	8.2303	10.3307	10.2511

[a] Pellets are numbered from the bottom of the fuel stack.

TABLE B-VI

FUEL ROD CLADDING DIMENSIONS FOR ROD IE-012

Tube Inside Diameter Measurements			Tube Outside Diameter Measurements		
Location[a] (cm)	Inside Diameter (cm)		Location[a] (cm)	Outside Diameter (cm)	
	0°	90°		0°	90°
2.54	0.8766	0.8776	71.12	0.9944	0.9985
5.08	0.8771	0.8773	73.66	0.9957	0.9977
7.62	0.8773	0.8763	76.20	0.9957	0.9982
10.16	0.8778	0.8766	78.74	0.9959	0.9982
12.70	0.8748	0.8735			
15.24	0.8743	0.8735			
17.78	0.8760	0.8753			
20.32	0.8760	0.8750			
22.86	0.8768	0.8758			
25.40	0.8743	0.8730			
27.94	0.8740	0.8730			
30.48	0.8748	0.8740			
33.02	0.8760	0.8750			
35.56	0.8735	0.8730			
38.10	0.8735	0.8733			
40.64	0.8750	0.8748			
43.18	0.8766	0.8763			
45.72	0.8740	0.8740			
48.26	0.8748	0.8748			
50.80	0.8730	0.8743			
53.34	0.8738	0.8753			
55.88	0.8725	0.8738			
58.42	0.8728	0.8735			
60.96	0.8740	0.8753			
63.50	0.8753	0.8753			
66.04	0.8735	0.8755			
68.58	0.8745	0.8740			
71.12	0.8735	0.8753			
73.66	0.8738	0.8758			
76.20	0.8740	0.8758			
78.74	0.8745	0.8758			
81.28	0.8743	0.8763			
83.82	0.8753	0.8763			
86.36	0.8763	0.8766			
88.90	0.8766	0.8760			

[a] Distance from bottom of fuel rod.

TABLE B-VII

OVERALL PRETEST FUEL ROD AND CLADDING DATA FOR ROD IE-013

Finished Tube Data:		
Mean OD	-	0.9925 cm
Mean ID	-	0.8741 cm
Ovality (Max ID/Min ID)	-	1.0017
Cladding Length	-	[a]
Overall Length	-	103.51 cm
Mechanical Properties Of Unirradiated Fuel Rod Cladding[b]:		
Yield Tensile Strength		
At Room Temperature	-	571.4 MPa
At 658 K	-	388.9 MPa
Ultimate Tensile Strength		
At Room Temperature	-	772.8 MPa
At 658 K	-	489.5 MPa
Fuel Data:		
Enrichment	-	12.49% ^{235}U
Mean Geometric Density	-	10.3725 gram/cm^3
95% Population Loaded	-	10.3725 (+0.792, -01.207) gram/cm^3
Mean Diameter	-	0.8641 cm
95% Population Loaded	-	0.8641 (+0.0005, -0.0005) cm
Stack Mass	-	521.6914 gram
Measured Stack Length	-	88.6079 cm
Dish Dimensions		
Dish Chord	-	0.6604 cm
Dish Depth	-	0.0343 cm
Grain Size		
Grain Diameter	-	$22.5 \pm 6.5 \times 10^{-4}$ cm
Center Hole Length	-	36.6116 cm
Plenum Length	-	5.7404 cm
Mean Fuel-Cladding Gap	-	0.100 cm
Measured Void Volume	-	7.7143 ml
Fill Gas Data		
Pressure	-	2.69 MPa
Composition	-	76% He, 24% Ar

[a] Not obtained.
[b] Data supplied by Westinghouse Electric Corporation.

TABLE B-VIII

FUEL PELLET CHARACTERIZATION DATA FOR ROD IE-013

PELLET[a] NO.	DIAMETER (cm) TOP	CENTER	BOTTOM	AVERAGE	LENGTH (cm) 0°	90°	AVERAGE	WEIGHT (GRAMS)	GEOMETRIC DENSITY (g/cm^3)	IMMERSION DENSITY (g/cm^3)
1	0.8636	0.8636	0.8636	0.8636	1.5347	1.5408	1.5377	9.1972	10.3463	0.0
2	0.8644	0.8644	0.8644	0.8644	1.5022	1.5047	1.5034	9.0060	10.3469	0.0
3	0.8646	0.8646	0.8646	0.8646	1.5342	1.5408	1.5375	9.2241	10.3536	0.0
4	0.8639	0.8639	0.8639	0.8639	1.4983	1.5037	1.5010	9.0109	10.3818	0.0
5	0.8639	0.8639	0.8639	0.8639	1.5499	1.5524	1.5512	9.3068	10.3714	10.4054
6	0.8639	0.8639	0.8639	0.8639	1.5380	1.5438	1.5409	9.2308	10.3563	0.0
7	0.8641	0.8641	0.8641	0.8641	1.5466	1.5512	1.5489	9.3230	10.3988	0.0
8	0.8644	0.8644	0.8644	0.8644	1.5083	1.5133	1.5108	9.0536	10.3502	0.0
9	0.8641	0.8641	0.8641	0.8641	1.5067	1.5136	1.5102	9.0171	10.3190	0.0
10	0.8639	0.8639	0.8639	0.8639	1.5055	1.5093	1.5074	9.0243	10.3528	10.4081
11	0.8646	0.8646	0.8646	0.8646	1.5189	1.5245	1.5217	9.1480	10.3759	0.0
12	0.8636	0.8636	0.8636	0.8636	1.5189	1.5225	1.5207	9.1291	10.3862	0.0
13	0.8644	0.8644	0.8641	0.8643	1.5273	1.5321	1.5297	9.2011	10.3890	0.0
14	0.8641	0.8641	0.8641	0.8641	1.5204	1.5245	1.5225	9.1423	10.3765	0.0
15	0.8639	0.8639	0.8639	0.8639	1.5524	1.5568	1.5546	9.3446	10.3902	10.4313
16	0.8641	0.8641	0.8641	0.8641	1.5296	1.5380	1.5338	9.2131	10.3788	0.0
17	0.8641	0.8641	0.8641	0.8641	1.5392	1.5448	1.5420	9.2715	10.3879	0.0
18	0.8641	0.8641	0.8641	0.8641	1.5428	1.5469	1.5448	9.2747	10.3725	0.0
19	0.8644	0.8644	0.8644	0.8644	1.5047	1.5080	1.5063	9.0450	10.3713	0.0
20	0.8644	0.8644	0.8644	0.8644	1.5197	1.5225	1.5211	9.1317	10.3680	10.4056
21	0.8641	0.8641	0.8641	0.8641	1.5347	1.5377	1.5362	9.2092	10.3579	0.0
22	0.8641	0.8641	0.8641	0.8641	1.5143	1.5123	1.5133	9.1032	10.3954	0.0
23	0.8646	0.8646	0.8646	0.8646	1.5270	1.5316	1.5293	9.1982	10.3802	0.0
24	0.8641	0.8641	0.8641	0.8641	1.5212	1.5278	1.5245	9.1393	10.3591	0.0
25	0.8641	0.8641	0.8641	0.8641	1.5385	1.5443	1.5414	9.2425	10.3598	10.4012
26	0.8641	0.8641	0.8641	0.8641	1.5108	1.5131	1.5119	9.0775	10.3758	0.0
27	0.8641	0.8641	0.8641	0.8641	1.5494	1.5532	1.5513	9.3149	10.3734	0.0
28	0.8646	0.8646	0.8646	0.8646	1.5390	1.5425	1.5408	9.2645	10.3764	0.0
29	0.8646	0.8646	0.8646	0.8646	1.5276	1.5234	1.5300	9.1699	10.3439	0.0
30	0.8636	0.8636	0.8636	0.8636	1.5197	1.5240	1.5218	9.1401	10.3908	10.4205

TABLE B-VIII (Continued)

FUEL PELLET CHARACTERIZATION DATA FOR ROD IE-013

PELLET[a] NO.	DIAMETER (cm) TOP	CENTER	BOTTOM	AVERAGE	LENGTH (cm) 0°	90°	AVERAGE	WEIGHT (GRAMS)	GEOMETRIC DENSITY (g/cm^3)	IMMERSION DENSITY (g/cm^3)
31	0.8644	0.8644	0.8644	0.8644	1.5138	1.5189	1.5164	9.1058	10.3710	0.0
32	0.8644	0.8644	0.8644	0.8644	1.5370	1.5420	1.5395	9.2542	10.3797	0.0
33	0.8644	0.8644	0.8644	0.8644	1.5276	1.5334	1.5305	9.1903	10.3701	0.0
34	0.8641	0.8641	0.8641	0.8641	1.5423	1.5464	1.5443	9.2909	10.3941	0.0
35	0.8639	0.8639	0.8639	0.8639	1.5210	1.5253	1.5231	8.7155	10.3491	10.3933
36	0.8646	0.8646	0.8646	0.8646	1.5083	1.5135	1.5109	8.6410	10.3310	10.4002
37	0.8646	0.8646	0.8646	0.8646	1.5192	1.5237	1.5215	8.7274	10.3486	10.4123
38	0.8644	0.8644	0.8644	0.8644	1.5278	1.5311	1.5295	8.7849	10.3681	10.3253
39	0.8641	0.8641	0.8641	0.8641	1.5248	1.5303	1.5276	8.7427	10.3444	10.3686
40	0.8646	0.8646	0.8646	0.8646	1.5080	1.5121	1.5100	8.6760	10.3867	10.4108
41	0.8636	0.8636	0.8636	0.8636	1.5278	1.5334	1.5306	8.7378	10.3440	10.3785
42	0.8641	0.8641	0.8641	0.8641	1.5133	1.5199	1.5166	8.6919	10.3727	10.4073
43	0.8636	0.8636	0.8636	0.8636	1.5171	1.5215	1.5193	8.7107	10.3762	10.3429
44	0.8639	0.8639	0.8639	0.8639	1.4928	1.4968	1.4948	8.5461	10.3428	10.3849
45	0.8636	0.8636	0.8636	0.8636	1.5154	1.5199	1.5176	8.6908	10.3572	10.3911
46	0.8639	0.8639	0.8639	0.8639	1.5458	1.5502	1.5480	8.8854	10.3790	10.4274
47	0.8639	0.8639	0.8639	0.8639	1.5222	1.5265	1.5244	8.7510	10.3758	10.3747
48	0.8644	0.8644	0.8644	0.8644	1.5286	1.5321	1.5303	8.7751	10.3504	10.3713
49	0.8641	0.8641	0.8641	0.8641	1.5095	1.5143	1.5119	8.6641	10.3521	9.1655
50	0.8641	0.8641	0.8641	0.8641	1.5105	1.5141	1.5123	8.6626	10.3745	10.3860
51	0.8636	0.8636	0.8636	0.8636	1.5377	1.5423	1.5400	8.7962	10.3287	10.3593
52	0.8641	0.8641	0.8641	0.8641	1.5339	1.5370	1.5354	8.7929	10.3564	10.3782
53	0.8641	0.8641	0.8641	0.8641	1.5143	1.5184	1.5164	8.7069	10.3856	10.3792
54	0.8639	0.8639	0.8639	0.8639	1.5169	1.5232	1.5201	8.7038	10.3629	10.3557
55	0.8641	0.8641	0.8641	0.8641	1.5385	1.5428	1.5406	8.8691	10.4240	9.6781
56	0.8641	0.8641	0.8641	0.8641	1.5326	1.5370	1.5348	8.8047	10.3680	11.1645
57	0.8641	0.8641	0.8641	0.8641	1.5507	1.6845	1.6176	8.9024	9.9397	10.3838
58	0.8636	0.8636	0.8636	0.8636	1.5182	1.5222	1.5202	8.7165	10.3769	10.9676

[a] Pellets are numbered from bottom of fuel stack.

TABLE B-IX

FUEL ROD CLADDING DIMENSIONS FOR ROD IE-013

Tube Inside Diameter Measurements			Tube Outside Diameter Measurements		
Location[a] (cm)	Inside Diameter (cm)		Location[a] (cm)	Outside Diameter (cm)	
	0°	90°		0°	90°
2.54	0.8741	0.8742	2.54	0.9944	0.9931
5.08	0.8744	0.8741	30.48	0.9931	0.9931
7.62	0.8745	0.8739	58.42	0.9906	0.9925
10.16	0.8744	0.8739	86.36	0.9919	0.9925
12.70	0.8743	0.8739			
15.24	0.8743	0.8742			
17.78	0.8744	0.8742			
20.32	0.8744	0.8739			
22.86	0.8744	0.8738			
25.40	0.8743	0.8738			
27.94	0.8744	0.8738			
30.48	0.8743	0.8739			
33.02	0.8743	0.8740			
35.56	0.8743	0.8739			
38.10	0.8743	0.8738			
40.64	0.8744	0.8736			
43.18	0.8742	0.8736			
45.72	0.8743	0.8736			
48.26	0.8745	0.8736			
50.80	0.8742	0.8737			
53.34	0.8741	0.8738			
55.88	0.8740	0.8740			
58.42	0.8743	0.8737			
60.96	0.8742	0.8733			
63.50	0.8740	0.8737			
66.04	0.8741	0.8738			
68.58	0.8741	0.8738			
71.12	0.8741	0.8747			
73.66	0.8741	0.8748			
76.20	0.8741	0.8747			
78.74	0.8740	0.8746			
81.28	0.8739	0.8747			
83.82	0.8738	0.8747			
86.36	0.8739	0.8746			
88.90	0.8739	0.8745			

[a] Distance from bottom of fuel rod.

TABLE B-X

OVERALL PRETEST FUEL ROD AND CLADDING DATA FOR ROD IE-014

Finished Tube Data:		
Mean OD	-	0.9939 cm
Mean ID	-	0.8738 cm
Ovality (Max ID/Min ID)	-	1.0023
Cladding Length	-	[a]
Overall Length	-	103.51 cm
Cladding Mechanical Properties Of Unirradiated Fuel Rod Cladding[b]:		
Yield Tensile Strength		
At Room Temperature	-	571.4 MPa
At 658 K	-	388.9 MPa
Ultimate Tensile Strength		
At Room Temperature	-	772.8 MPa
At 658 K	-	489.5 MPa
Fuel Data:		
Enrichment	-	12.49% ^{235}U
Mean Geometric Density	-	10.4127 gram/cm^3
95% Population Loaded	-	10.4127 (+0.0831, -0.0791) gram/cm^3
Mean Diameter	-	0.8395 cm
95% Population Loaded	-	0.8395 (+0.0076, -0.0102) cm
Stack Mass	-	489.7859 gram
Measured Stack Length	-	88.4022 cm
Dish Dimensions		
Dish Chord	-	0.6604 cm
Dish Depth	-	0.0343 cm
Grain Size		
Grain Diameter	-	$22.5 \pm 6.5 \times 10^{-4}$ cm
Center Hole Length	-	36.5176
Plenum Length	-	5.7404 cm
Mean Fuel-Cladding Gap	-	0.0343 cm
Measured Void Volume	-	10.2497 ml
Fill Gas Data		
Pressure	-	2.67 MPa
Composition	-	76% He, 24% Ar

[a] Not obtained.
[b] Data supplied by Westinghouse Electric Corporation.

TABLE B-XI

FUEL PELLET CHARACTERIZATION DATA FOR ROD IE-014

PELLET[a] NO.	DIAMETER (cm) TOP	CENTER	BOTTOM	AVERAGE	LENGTH (cm) 0°	90°	AVERAGE	WEIGHT (GRAMS)	GEOMETRIC DENSITY (g/cm^3)	IMMERSION DENSITY (g/cm^3)
1	0.8397	0.8397	0.8397	0.8397	1.5227	1.5273	1.5250	8.6337	10.3673	0.0
2	0.8400	0.8400	0.8400	0.8400	1.5387	1.5453	1.5420	8.7304	10.3597	0.0
3	0.8395	0.8395	0.8395	0.8395	1.5260	1.5314	1.5287	8.6404	10.3563	0.0
4	0.8392	0.8392	0.8392	0.8392	1.5202	1.5237	1.5220	8.6108	10.3735	0.0
5	0.8397	0.8397	0.8397	0.8397	1.5415	1.5471	1.5443	8.7271	10.3466	10.3835
6	0.8390	0.8390	0.8390	0.8390	1.5049	1.5093	1.5071	8.4685	10.3104	0.0
7	0.8400	0.8400	0.8400	0.8400	1.5149	1.5179	1.5164	8.6087	10.3906	0.0
8	0.8390	0.8390	0.8390	0.8390	1.5342	1.5390	1.5366	8.6810	10.3636	0.0
9	0.8400	0.8400	0.8400	0.8400	1.5281	1.5359	1.5320	8.6721	10.3589	0.0
10	0.8390	0.8390	0.8390	0.8390	1.5248	1.5286	1.5267	8.6229	10.3620	10.3697
11	0.8397	0.8397	0.8397	0.8397	1.4948	1.4989	1.4968	8.4512	10.3420	0.0
12	0.8400	0.8400	0.8400	0.8400	1.4996	1.5047	1.5022	8.5032	10.3618	0.0
13	0.8392	0.8392	0.8392	0.8392	1.5481	1.5502	1.5491	8.7938	10.4055	0.0
14	0.8390	0.8390	0.8390	0.8390	1.5138	1.5194	1.5166	8.5817	10.3817	0.0
15	0.8397	0.8397	0.8397	0.8397	1.5070	1.5118	1.5094	8.5500	10.3745	10.3923
16	0.8400	0.8400	0.8400	0.8400	1.5136	1.5187	1.5161	8.5562	10.3290	0.0
17	0.8397	0.8397	0.8397	0.8397	1.5161	1.5212	1.5187	8.5860	10.3537	0.0
18	0.8390	0.8390	0.8390	0.8390	1.5375	1.5408	1.5391	8.7046	10.3744	0.0
19	0.8392	0.8392	0.8392	0.8392	1.5263	1.5316	1.5290	8.6457	10.3673	0.0
20	0.8395	0.8395	0.8395	0.8395	1.5403	1.5453	1.5428	8.7089	10.3417	10.3336
21	0.8400	0.8400	0.8400	0.8400	1.5230	1.5281	1.5255	8.6257	10.3478	0.0
22	0.8400	0.8400	0.8400	0.8400	1.5367	1.5418	1.5392	8.7306	10.3790	0.0
23	0.8400	0.8400	0.8400	0.8400	1.5342	1.5390	1.5366	8.6861	10.3443	0.0
24	0.8392	0.8392	0.8392	0.8392	1.5235	1.5309	1.5272	8.6313	10.3622	0.0
25	0.8402	0.8402	0.8402	0.8402	1.5309	1.5359	1.5334	8.6884	10.3624	10.3660
26	0.8397	0.8397	0.8397	0.8397	1.5293	1.5324	1.5309	8.6236	10.3151	0.0
27	0.8402	0.8402	0.8402	0.8402	1.5347	1.5400	1.5373	8.7037	10.3537	0.0
28	0.8400	0.8400	0.8400	0.8400	1.5215	1.5248	1.5231	8.6398	10.3814	0.0
29	0.8397	0.8397	0.8397	0.8397	1.5202	1.5258	1.5230	8.6042	10.3458	0.0
30	0.8397	0.8397	0.8397	0.8397	1.5255	1.5316	1.5286	8.6497	10.3620	10.3769

TAELE B-XI (Continued)

FJEL PELLET CHARACTERIZATION DATA FOR ROD IE-014

PELLET[a] NO.	DIAMETER (cm)				LENGTH (cm)			WEIGHT (GRAMS)	GEOMETRIC DENSITY (g/cm^3)	IMMERSION DENSITY (g/cm^3)
	TOP	CENTER	BOTTOM	AVERAGE	0°	90°	AVERAGE			
31	0.8397	0.8397	0.8397	0.8397	1.5476	1.5405	1.5441	8.7252	10.3461	0.0
32	0.8395	0.8395	0.8395	0.8395	1.5270	1.5298	1.5284	8.6331	10.3493	0.0
33	0.8400	0.8400	0.8400	0.8400	1.5199	1.5255	1.5227	8.6169	10.3565	0.0
34	0.8400	0.8400	0.8400	0.8400	1.4935	1.4976	1.4956	8.4578	10.3527	0.0
35	0.8397	0.8397	0.8397	0.8397	1.5108	1.5156	1.5132	8.360	10.3425	10.3839
36	0.8392	0.8392	0.8392	0.8392	1.5202	1.5240	1.5221	8.1791	10.3418	10.3594
37	0.8385	0.8385	0.8385	0.8385	1.4953	1.5004	1.4978	8.9441	10.3511	10.3639
38	0.8390	0.8390	0.8390	0.8390	1.5314	1.5359	1.5337	8.2753	10.3902	10.4792
39	0.8387	0.8387	0.8387	0.8387	1.5324	1.5367	1.5345	8.2703	10.3846	10.4464
40	0.8395	0.8395	0.8395	0.8395	1.5034	1.5072	1.5053	8.0962	10.3460	10.4298
41	0.8390	0.8390	0.8390	0.8390	1.5339	1.5377	1.5358	8.2748	10.3748	10.4389
42	0.8397	0.8397	0.8397	0.8397	1.5278	1.5324	1.5301	8.2128	10.3090	10.4107
43	0.8392	0.8392	0.8392	0.8392	1.5192	1.5240	1.5216	8.1650	10.3275	10.4175
44	0.8392	0.8392	0.8392	0.8392	1.5171	1.5212	1.5192	8.1643	10.3433	10.4958
45	0.8387	0.8387	0.8387	0.8387	1.5222	1.5250	1.5236	8.1942	10.3710	10.4255
46	0.8395	0.8395	0.8395	0.8395	1.5164	1.5215	1.5189	8.1955	10.3779	10.4592
47	0.8385	0.8385	0.8385	0.8385	1.5075	1.5126	1.5100	8.1087	10.3559	10.4096
48	0.8362	0.8362	0.8362	0.8362	1.4986	1.5032	1.5009	8.0519	10.4073	10.4441
49	0.8397	0.8397	0.8397	0.8397	1.5204	1.5230	1.5217	8.2055	10.3645	10.4332
50	0.8400	0.8400	0.8400	0.8400	1.5243	1.5309	1.5276	8.2016	10.3128	10.4152
51	0.8395	0.8395	0.8395	0.8395	1.5182	1.5225	1.5203	8.1951	10.3677	10.4561
52	0.8395	0.8395	0.8395	0.8395	1.5143	1.5197	1.5170	8.1650	10.3524	10.4311
53	0.8390	0.8390	0.8390	0.8390	1.5288	1.5334	1.5311	8.2557	10.3688	10.4400
54	0.8395	0.8395	0.8395	0.8395	1.5118	1.5161	1.5140	8.1324	10.3321	10.3907
55	0.8397	0.8397	0.8397	0.8397	1.5377	1.5410	1.5394	8.2833	10.3411	10.4247
56	0.8397	0.8397	0.8397	0.8397	1.5037	1.5095	1.5066	8.1006	10.3290	10.4101
57	0.8392	0.8392	0.8392	0.8392	1.5055	1.5083	1.5069	8.1253	10.3792	10.4019
58	0.8387	0.8387	0.8387	0.8387	1.5321	1.5352	1.5337	8.2602	10.3708	10.3906

[a] Pellets are numbered from bottom of fuel stack.

TABLE B-XII

FUEL ROD CLADDING DIMENSIONS FOR ROD IE-014

Tube Inside Diameter Measurements			Tube Outside Diameter Measurements		
Location[a] (cm)	Inside Diameter (cm)		Location[a] (cm)	Outside Diameter (cm)	
	0°	90°		0°	90°
2.54	0.8750	0.8755	2.54	0.9938	0.9944
5.08	0.8752	0.8748	30.48	0.9930	0.9931
7.62	0.8757	0.8740	58.42	0.9919	0.9950
10.16	0.8759	0.8750	86.36	0.9957	0.9944
12.70	0.8755	0.8752			
15.24	0.8753	0.8754			
17.78	0.8752	0.8755			
20.32	0.8752	0.8754			
22.86	0.8754	0.8752			
25.40	0.8757	0.8752			
27.91	0.8754	0.8750			
30.48	0.8752	0.8750			
33.02	0.8754	0.8751			
35.56	0.8750	0.8751			
38.10	0.8753	0.8745			
40.64	0.8755	0.8749			
43.18	0.8750	0.8752			
45.72	0.8748	0.8749			
48.26	0.8750	0.8745			
50.80	0.8753	0.8741			
53.34	0.8753	0.8745			
55.88	0.8750	0.8747			
58.42	0.8745	0.8747			
60.96	0.8744	0.8747			
63.50	0.8743	0.8744			
66.04	0.8744	0.8744			
68.58	0.8743	0.8745			
71.12	0.8743	0.8740			
73.66	0.8743	0.8741			
76.20	0.8743	0.8743			
78.74	0.8738	0.8745			
81.28	0.8736	0.8745			
83.82	0.8742	0.8741			
86.36	0.8742	0.8742			
88.90	0.8743	0.8739			

[a] Distance from bottom of fuel rod.

REFERENCES

B-1. G. W. Gibson et al., *Characteristics of UO_2 - Zircaloy Fuel Rod Materials from the Saxton Reactor for Use in the Power Burst Facility*, ANCR-NUREG-1321 (September 1976).

APPENDIX C

DATA REDUCTION AND EVALUATION

All data for Test IE-2 were recorded on the PBF Surveillance System[a] in an analog format and then were digitized by the PBF PDP-15 data reduction facility. The resulting digital data were processed on an IBM 360, using the MAC/RAN Time Series Analysis Program[C-2], and permanently stored on seven-track magnetic tapes in the MAC/RAN SIDU (Standard Input Data Unit) format.

During the processing on the IBM 360, several data reduction steps were completed:

(1) Data were converted from data system volts to engineering units (SI) using the calibration equations presented in Appendix A.

(2) Any wild points were removed.

(3) Zero power offsets due to data system drift were removed from coolant ΔT and SPND data channels.

(4) SPND data channels were converted from detector nanoamps to neutron flux, using the results from a special calibration test[C-3].

(5) Ultrasonic thermometer data were numerically filtered to remove excessive wild points.

(6) Rod internal pressure data were corrected for large drifts in zero due to instrument decalibration.

---

[a] The Surveillance System is an FM multiplexed data recording system that records channels of analog data plus a standard time code (IRIG-A) on magnetic tape[C-1].

Reduced Data Format

Three separate sets of the data are stored on tape. These sets are

(1) A complete set with the data in the form of data system volts

(2) A complete set with the data in engineering units (SI) obtained by applying calibration equations tabulated in Appendix A

(3) A set decimated from (2) with calculated parameters such as rod power added for additional calculations and plotting.

Each data channel on the two complete sets contains approximately 28,000 data values with variable digitizing intervals ranging from 10 seconds down to 0.25[a] seconds. Table C-I shows the digitizing intervals used.

TABLE C-I

DIGITIZING INTERVALS USED FOR DATA REDUCTION IN TEST IE-2

Time[a] Period (sec)	Test Phase	Digitizing Interval (sec)
-14,700 - 170,577	Preconditioning	10.0
170,940 - 172,440	Power Ramp	0.2
172,440 - 175,980	Steady-State Operation at 68 kW/m	10.0
175,980 - 176,880	Flow Reduction	0.2
176,880 - 178,020	After Shutdown	10.0

[a] The time corresponds to time on Figure 9 where time of zero designates the beginning of the first power increase.

[a] As the data were digitized, they were filtered with a low pass filter whose cutoff frequency corresponds to the Nyquist frequency ($1/2\Delta T$).

The third set of data contains data that were numerically filtered and decimated by a factor of 14 to give approximately 2000 points per channel. Several calculated parameters were added to the original data channels including

(1) Results from SPND data: (a) axial local power, (b) average neutron flux, (c) peak elevation, and (d) peak to average (see Appendix D).

(2) Average rod power for each rod, calculated thermal-hydraulically (Appendix D).

(3) Coolant mass flux for each rod, calculated using ASTEM[C-4] water properties and inlet temperature.

In the SIDU format, each data channel has a unique number and name of eight characters. All of the data channels available are listed in Table C-II. The data channels are also shown in Figures C-1 through C-11.

Data Reduction

Corrections were applied to some of the channels to eliminate obvious errors in the data. Some of the corrections were straightforward, such as removal of wild points, while others were not. Each of the corrections are discussed below.

The first correction to be applied to the data was wild point removal. During the digitizing process, particularly at the end or beginning of an analog tape which contains four hours of data, wild points were sometimes introduced into the data. Most of these points were removed using the MAC/RAN processor following conversion to engineering units.

The second step was elimination of zero power offsets in coolant ΔT and SPND data. These transducers have a very small output. Therefore, the signals must be recorded through high gain amplifiers. For this

TABLE C-II

DATA CHANNEL FORMAT FOR TEST IE-2

Comments	Transducer Name	Rod Number	Elevation (m)	Serial Number	Azimuthal (degrees)	Data System Channel Number	Reduced Tape No.	Channel ID	Units
Corrected for zero shift --	Fuel Rod PxD	IE-011	--	301	--	8-1	32	RODPRS11	MPa
	Centerline TC	IE-011	.75	435		9-1	20	FULTMP11	K
	Cladding TC (spring)	IE-011	.61	--	180	10-1	36	CLDTMP11	K
	Cladding TC (spring)	IE-011	.61	--	0	10-2	37	CLDTMP12	K
Corrected for zero shift --	Coolant ΔT	IE-011	--	DTC-7	--	6-3	26	DELTMP11	K
	Flowmeter	IE-011	--	10094	--	5-3	18	FLORAT11	cm^3/s
	LVDT	IE-011	--	039	--	14-1	49	CLDDSP11	mm
Corrected for zero shift --	Fuel Rod PxD	IE-012	--	222	--	8-2	33	RODPRS21	MPa
	Centerline TC	IE-012	.74	434	--	9-2	21	FULTMP21	K
	Cladding TC (spring)	IE-012	.61	--	180	10-3	38	CLDTMP21	K
	Cladding TC (spring)	IE-012	.61	--	0	10-4	40	CLDTMP22	K
Corrected for zero shift --	Coolant ΔT	IE-012	--	DTC-8	--	7-1	28	DELTMP21	K
	Flowmeter	IE-012	--	10092	--	6-1	24	FLORAT21	cm^3/s
	LVDT	IE-012	--	433	--	14-3	19	CLDDSP21	mm

TABLE C-II (continued)

DATA CHANNEL FORMAT FOR IE-2

Comments	Transducer Name	Rod Number	Elevation (m)	Serial Number	Azimuthal (degrees)	Data System Channel Number	Reduced Tape No.	Channel ID	Units
Corrected for zero shift --	Fuel Rod PxD	IE-013	--	257	--	8-3	34	RODPRS31	MPa
Failed at onset of film boiling (UT has decalibrated) --	Centerline UT	IE-013	.60	443	--	9-3	22	FULTMP31	K
	Cladding TC (Type S)	IE-013	.51	--	90	11-2	42	CLDTMP31	K
	Cladding TC (Type S)	IE-013	.61	--	0	11-1	41	CLDTMP32	K
	Cladding TC (Type S)	IE-013	.61	180	180	11-3	43	CLDTMP33	K
	Cladding TC (Type S)	IE-013	.71	--	270	11-4	44	CLDTMP34	K
Corrected for zero shift --	Coolant ΔT	IE-013	--	DTC-10	--	6-4	27	DELTMP31	K
	Flowmeter	IE-013	--	10095	--	5-4	39	FLORAT31	cm^3/s
Failed at beginning of test --	LVDT	IE-013	--	--	--	--	--	--	mm

TABLE C-II (continued)

DATA CHANNEL FORMAT FOR TEST IE-2

Comments	Transducer Name	Rod Number	Elevation (m)	Serial Number	Azimuthal (degrees)	Data System Channel Number	Reduced Tape No.	Channel ID	Units
Corrected -- for zero shift	Fuel Rod PxD	IE-014	--	306	--	8-4	35	RODPRS41	MPa
Failed -- during power ramp (UT has decalibrated)	Centerline UT	IE-014	.60	442	--	9-4	23	FULTMP41	K
	Cladding TC (Type S)	IE-014	.51	--	90	13-2	46	CLDTMP41	K
	Cladding TC (Type S)	IE-014	.61	--	0	13-1	45	CLDTMP42	K
	Cladding TC (Type S)	IE-014	.61	--	180	13-3	47	CLDTMP43	K
	Cladding TC (Type K)	IE-014	.71	--	270	13-4	48	CLDTMP44	K
Corrected -- for zero shift	Coolant ΔT	IE-014	--	DTC-9	--	7-2	29	DELTMP41	K
	Flowmeter	IE-014	--	10093	--	6-2	25	FLORAT41	cm^3/s
LVDT has -- decalibrated	LVDT	IE-014	--	210	--	14-4	50	CLDDSP41	mm

TABLE C-II (continued)

DATA CHANNEL FORMAT FOR TEST IE-2

Comments	Transducer Name	Rod Number	Elevation (m)	Serial Number	Azimuthal (degrees)	Data System Channel Number	Reduced Tape No.	Channel ID	Units
Unreliable -- (All were corrected for zero shift)[a]	SPND 2	--	0.319	53977	225	3-3	10	NTFLUX02	$n/cm^2 \cdot s$
	SPND 3	--	0.475	53973	225	3-4	11	NTFLUX03	$n/cm^2 \cdot s$
	SPND 4	--	0.627	53971	225	4-1	12	NTFLUX04	$n/cm^2 \cdot s$
	SPND 5	--	0.791	53980	225	4-2	13	NTFLUX05	$n/cm^2 \cdot s$
	SPND 6	--	0.627	53975	315	4-3	14	NTFLUX06	$n/cm^2 \cdot s$
	SPND 7	--	0.627	53967	45	4-4	15	NTFLUX07	$n/cm^2 \cdot s$
	SPND 8	--	0.627	53976	135	5-1	16	NTFLUX08	$n/cm^3 \cdot s$
	Loop Flowmeter	--	--	--	--	5-2	17	LOPFL001	cm^3/s
Range Changes--not removed for reactor power less than 1 MW $0-1.78 \times 10^5$	SLP-1	--	--	--	--	1-4	3	RECPOW01	MW
	Fission Break Monitor	--	--	--	--	2-2	5	FISREL01	$Log_{10}(R/hr)$
	PPS #1	--	--	--	--	1-3	2	RECPOW02	MW
	PPS #2	--	--	--	--	2-1	4	RECPOW03	MW
	(Time)	--	--	--	--	12-1 thru 12-4	1	TIME	sec
Decalibrated	Coolant Pressure (10K)	--	--	--	--	2-4	7	SYSPRS01	MPa
Decalibrated	Coolant Pressure (10K)	--	--	--	--	3-2	9	SYSPRS02	MPa
	Inlet TC	--	--	--	--	2-3	6	INTEMP01	K
	Inlet TC	--	--	--	--	3-1	8	INTEMP02	K
	Outlet TC	--	--	--	--	7-3	30	OUTEMP01	K
	Outlet TC	--	--	--	--	7-4	31	OUTEMP02	K

[a] Polarity reversed during power calibration and gap conductance. Working during rest of test.

TABLE C-II (continued)

DATA CHANNEL FORMAT FOR TEST IE-2

Comments	Transducer Name	Rod Number	Elevation (m)	Serial Number	Azimuthal (degrees)	Data System Channel Number	Reduced Tape No.	Channel ID	Units
	(Local Peaking Factor)	--	0.013	--	--	--	51	AXFLUX01	--
	(Loca Peaking Factor)	--	0.159	--	--	--	52	AXFLUX02	--
(Calculated data, available on decimated set only)	(Local Peaking Factor)	--	0.306	--	--	--	53	AXFLUX03	--
	(Local Peaking Factor)	--	0.452	--	--	--	54	AXFLUX04	--
	(Local Peaking Factor)	--	0.521	--	--	--	55	AXFLUX05	--
	(Local Peaking Factor)	--	0.599	--	--	--	56	AXFLUX06	--
	(Local Peaking Factor)	--	0.662	--	--	--	57	AXFLUX07	--
	(Local Peaking Factor)	--	0.724	--	--	--	58	AXFLUX08	--
	(Local Peaking Factor)	--	0.745	--	--	--	59	AXFLUX09	--
	(Local Peaking Factor)	--	0.892	--	--	--	60	AXFLUX10	--
	(Average Neutron Flux)	--	--	--	--	--	61	FLUXAVER	$n/cm^2 \cdot s$
	(Elevation or Peak)	--	--	--	--	--	62	FLXMXELV	m
	(Peak to Average)	--	--	--	--	--	63	FLUXMAX	--

TABLE C-II (continued)

DATA CHANNEL FORMAT FOR TEST IE-2

Comments	Transducer Name	Rod Number	Elevation (m)	Serial Number	Azimuthal (degrees)	Data System Channel Number	Reduced Tape No.	Channel ID	Units
Peak = 1.307 x Average	(Average Rod Power)	011	--	--	--	--	64	RODPWR01	kW/m
	(Average Rod Power)	012	--	--	--	--	65	RODPWR02	kW/m
	(Average Rod Power)	013	--	--	--	--	66	RODPWR03	kW/m
	(Average Rod Power)	014	--	--	--	--	67	RODPWR04	kW/m
(Average of all four rods)	(Average Rod Power)	--	--	--	--	--	68	RODPWRAV	kW/m
	(Standard deviation of rod power)	--	--	--	--	--	69	RODPWRSD	kW/m
	(Mass flux)	011	--	--	--	--	70	MASFLX01	$kg/m^2 \cdot s$
	(Mass flux)	012	--	--	--	--	71	MASFLX02	$kg/m^2 \cdot s$
	(Mass flux)	013	--	--	--	--	72	MASFLX03	$kg/m^2 \cdot s$
	(Mass flux)	014	--	--	--	--	73	MASFLX04	$kg/m^2 \cdot s$

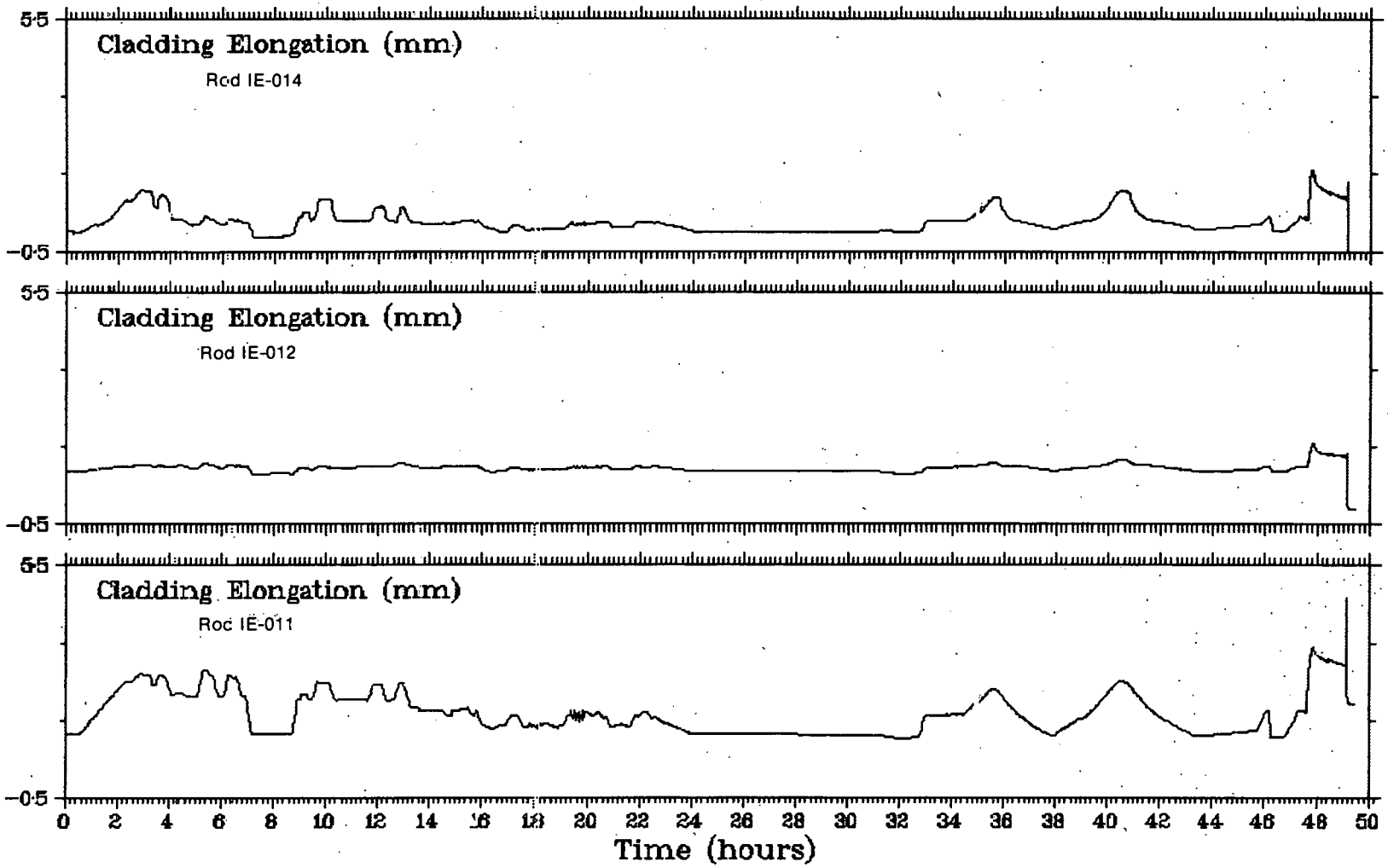

Fig. C-1 Cladding elongation for Test IE-2.

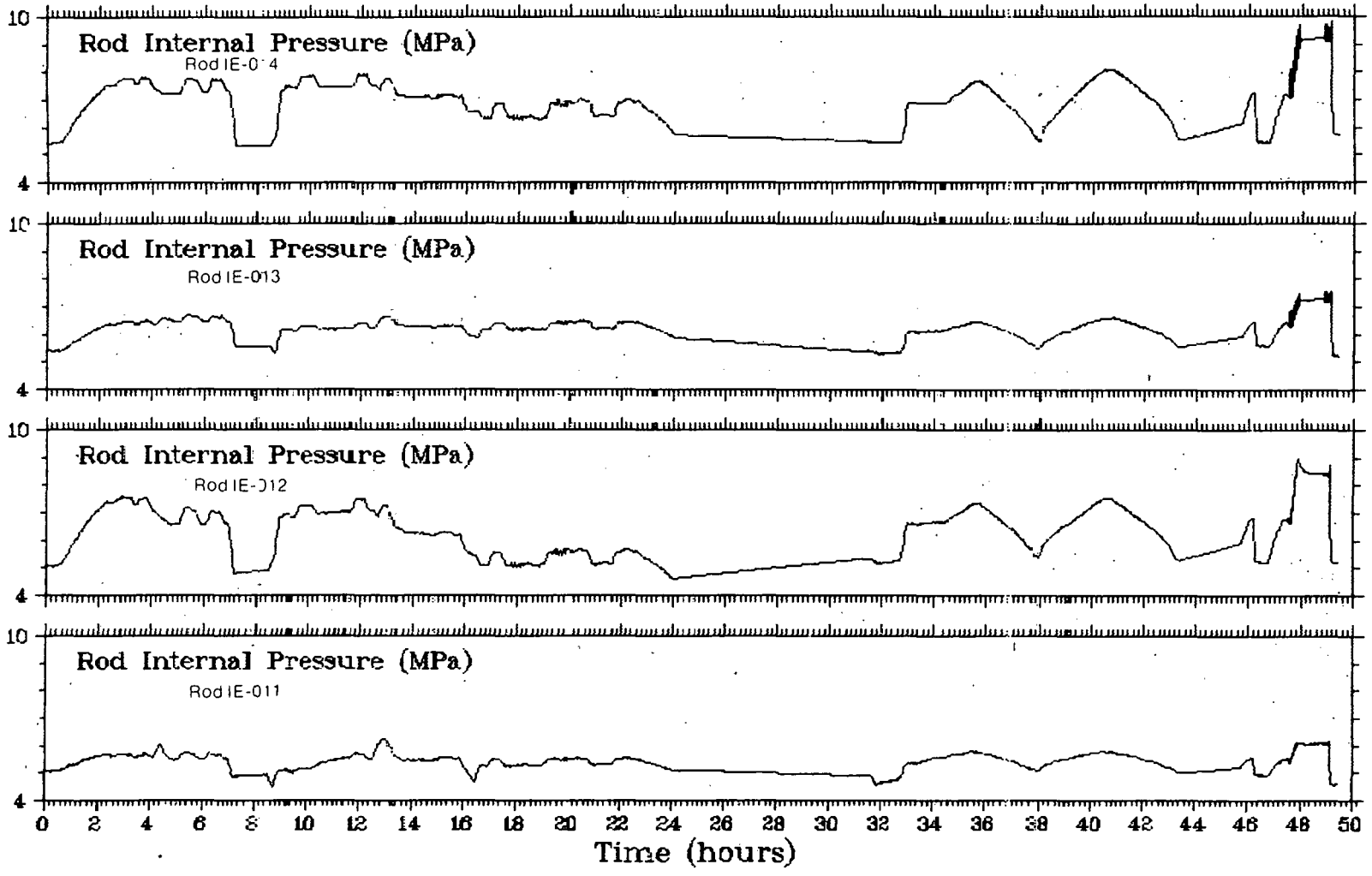

Fig. C-2 Rod irternal pressure for Test IE-2 (data have been corrected for drift).

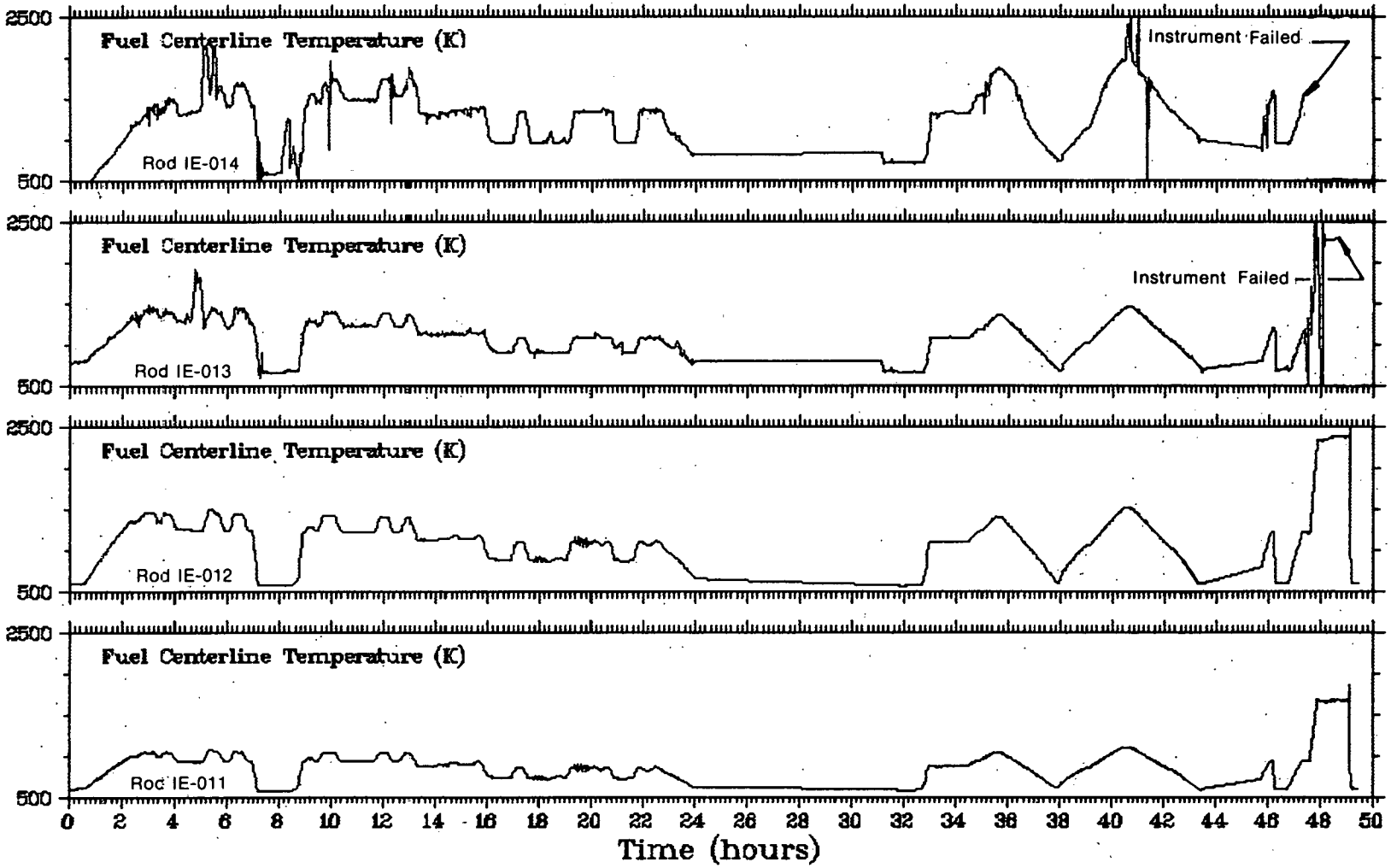

Fig. C-3 Fuel centerline temperature for Test IE-2.

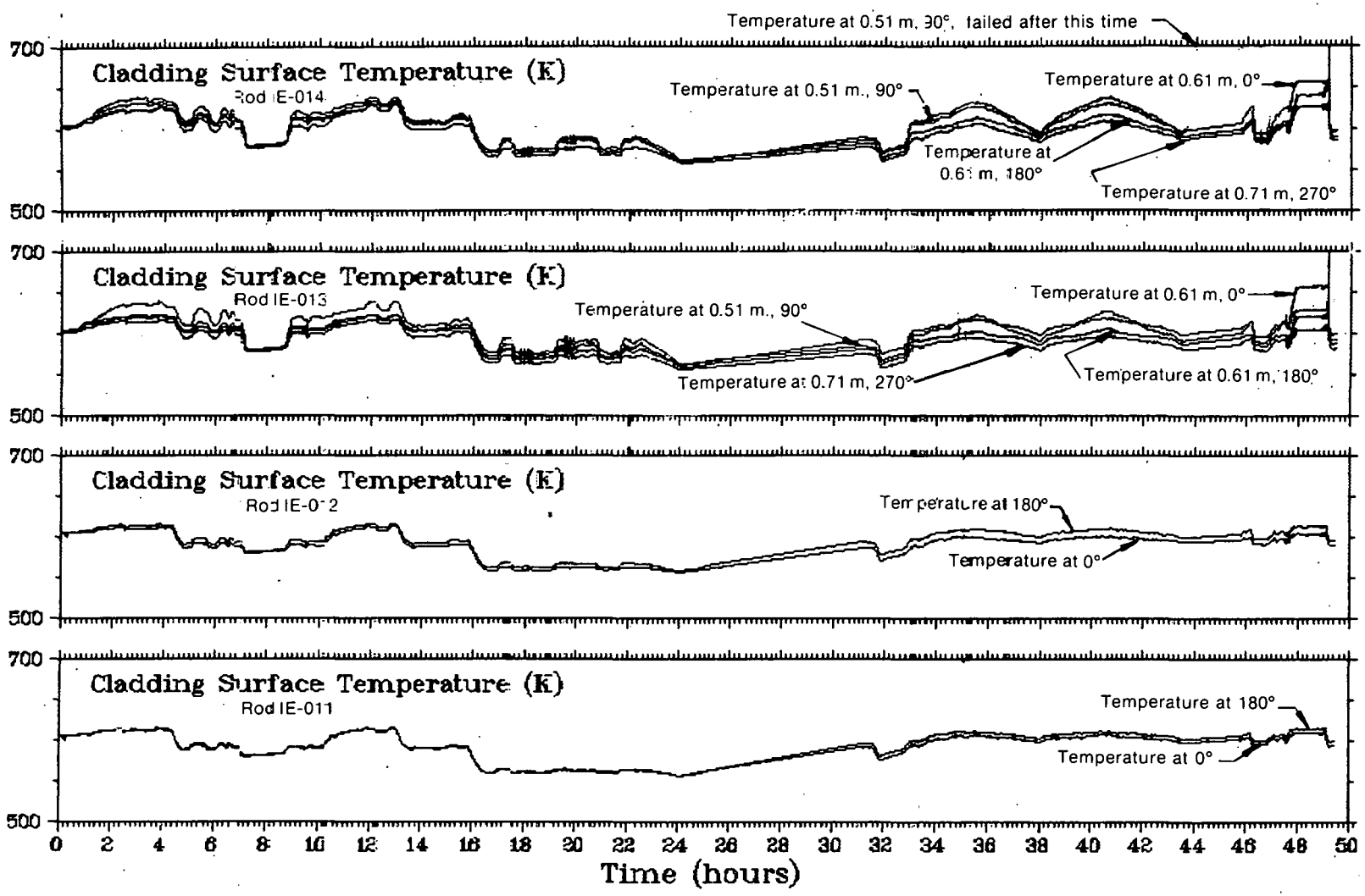

Fig. C-4 Cladding surface temperature for Test IE-2.

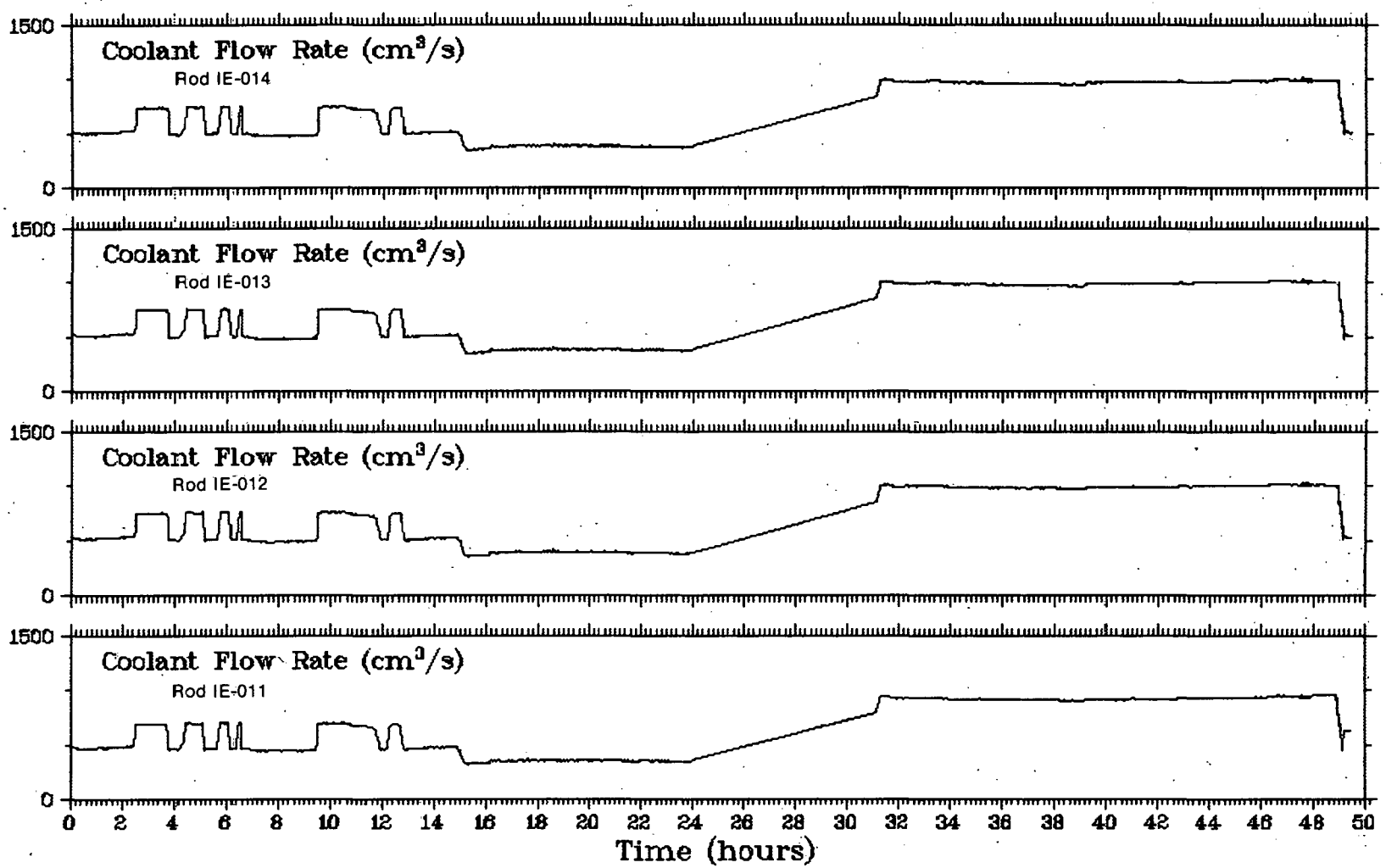

Fig. C-5 Coolant flow rate for Test IE-2.

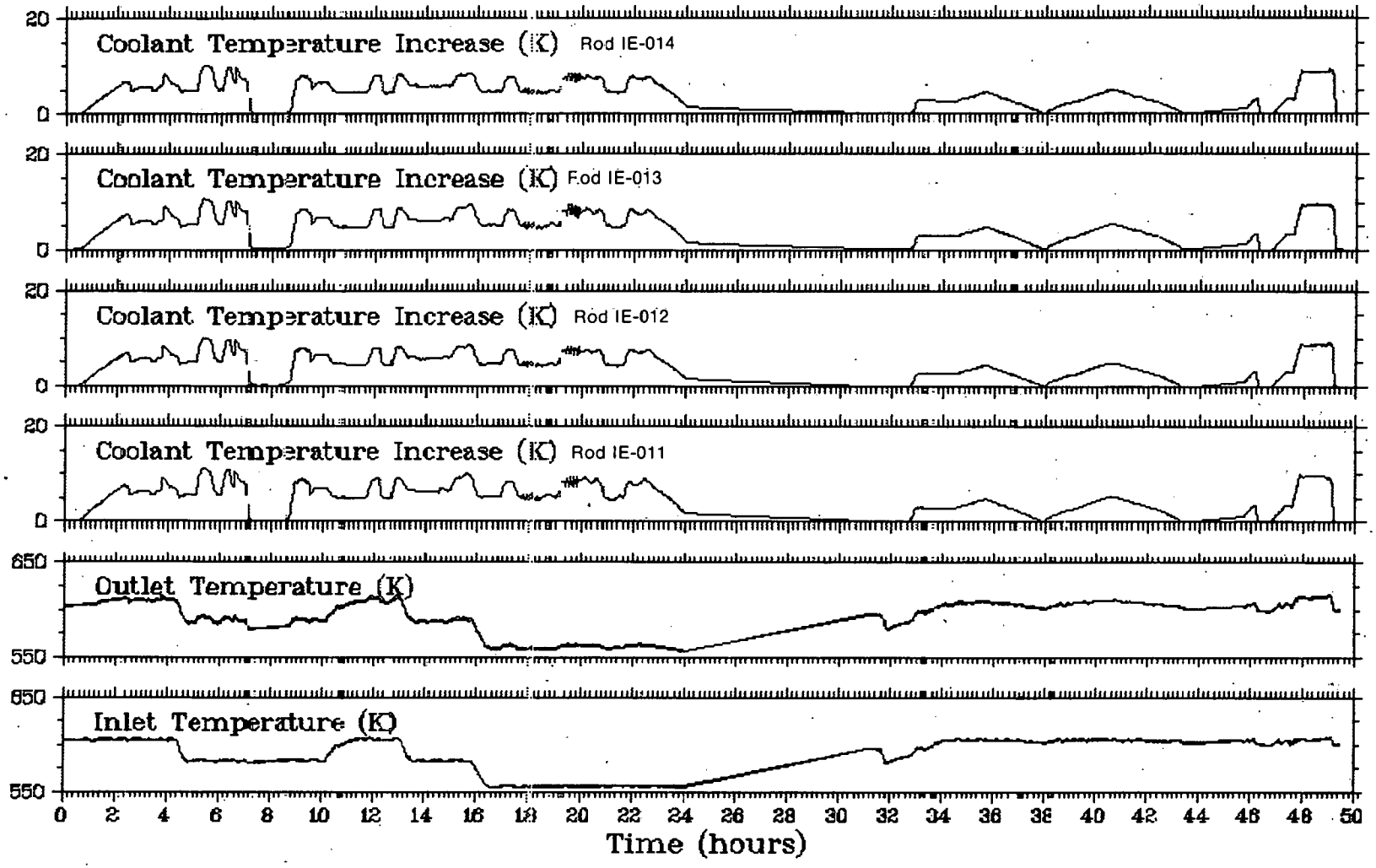

Fig. C-6 Coolant inlet and outlet temperature and coolant temperature increase for Test IE-2.

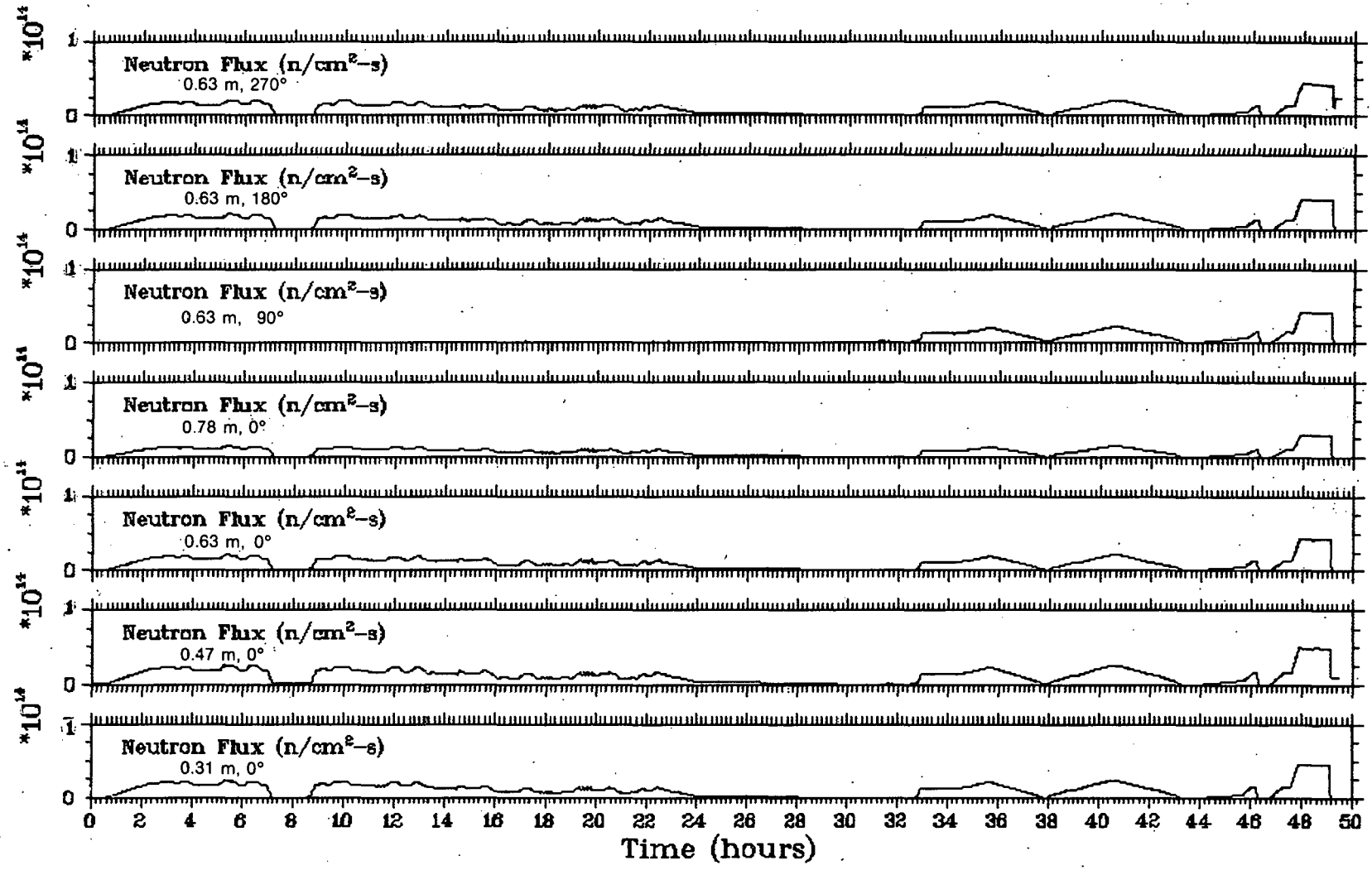

Fig. C-7 Neutron flux for Test IE-2.

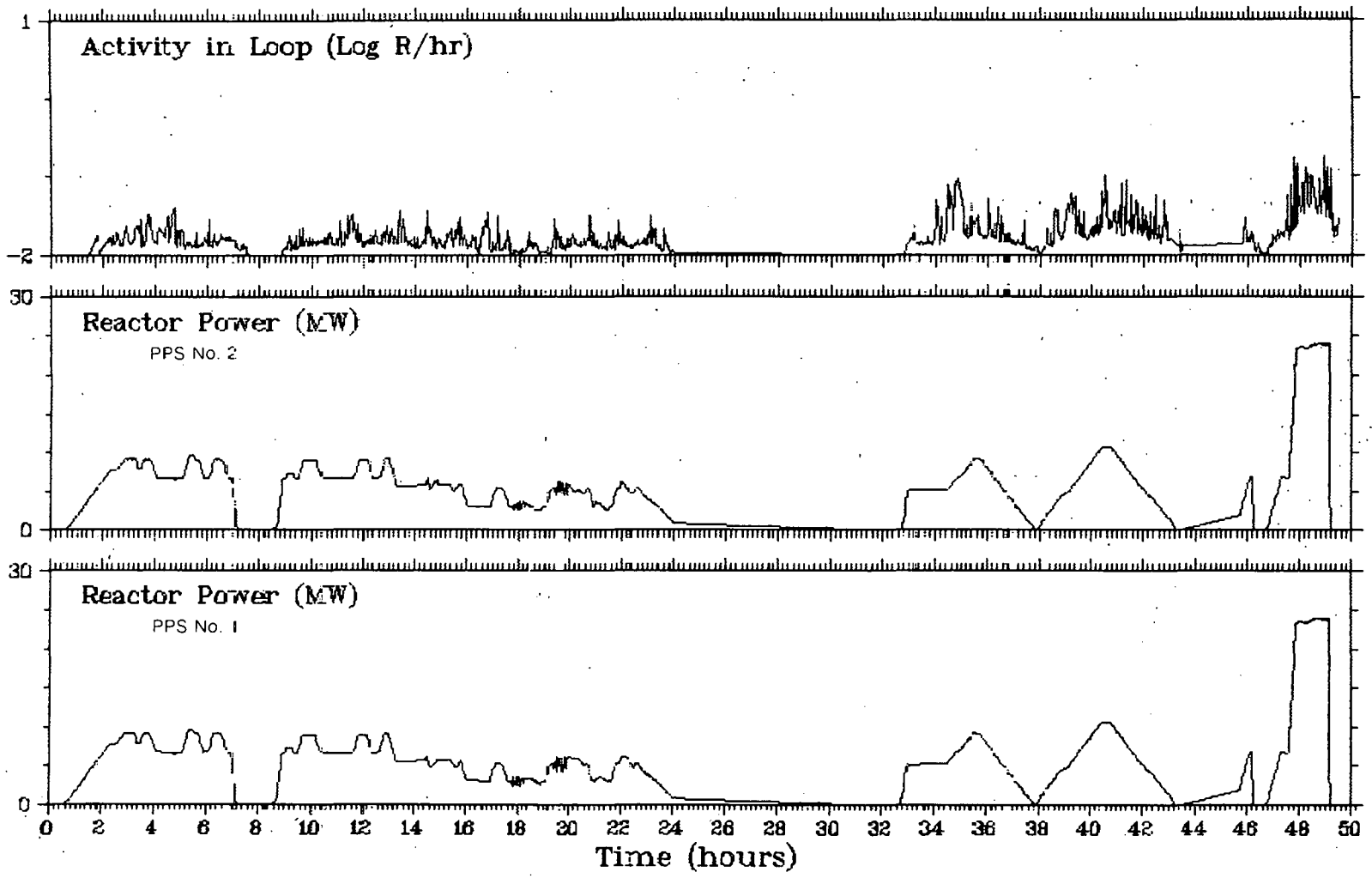

Fig. C-8 Reactor power and activity in loop for Test IE-2 (reactor power measured by SLP-1 not included because of range changes).

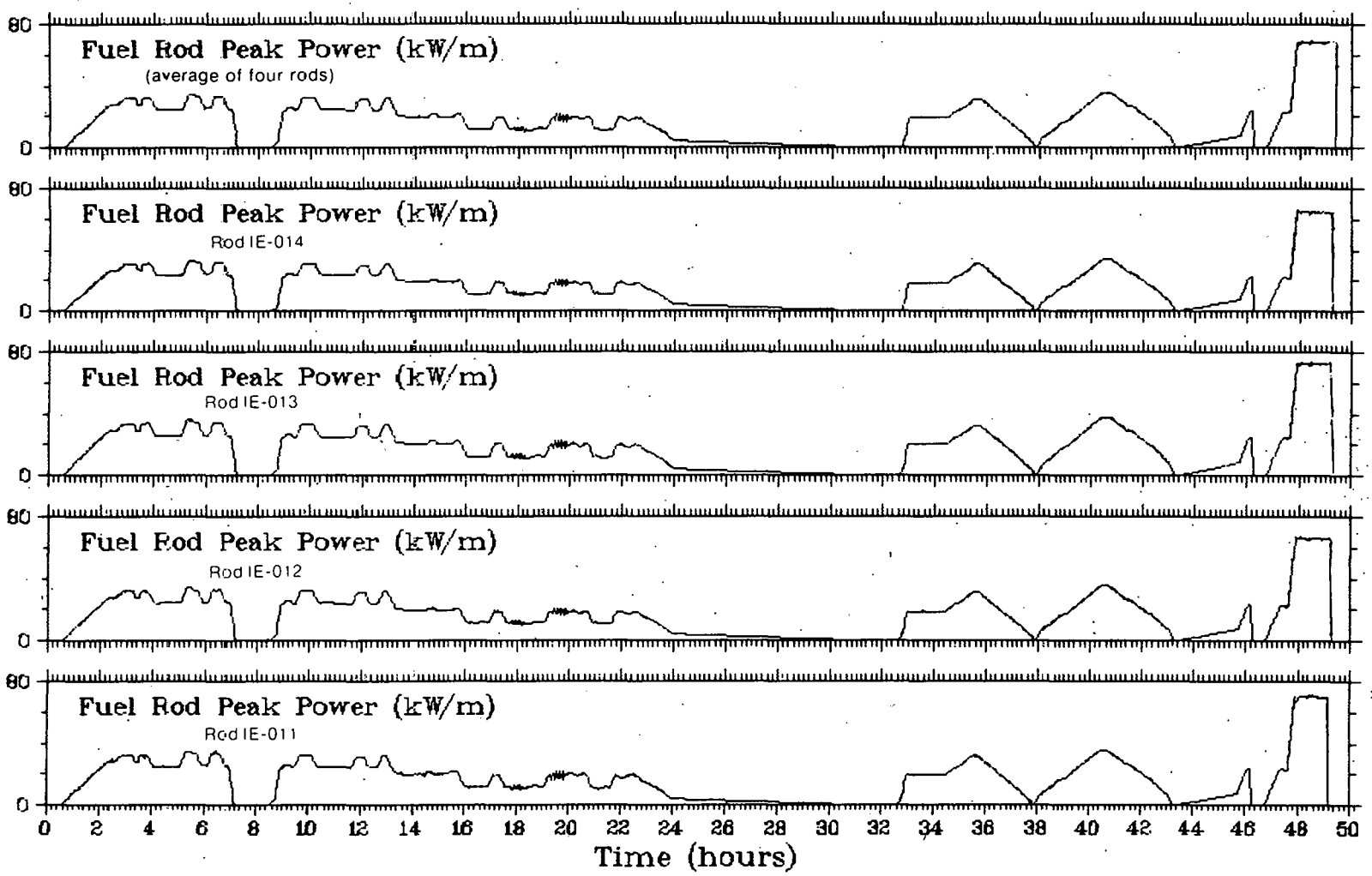

Fig. C-9 Fuel rod peak power for Test IE-2.

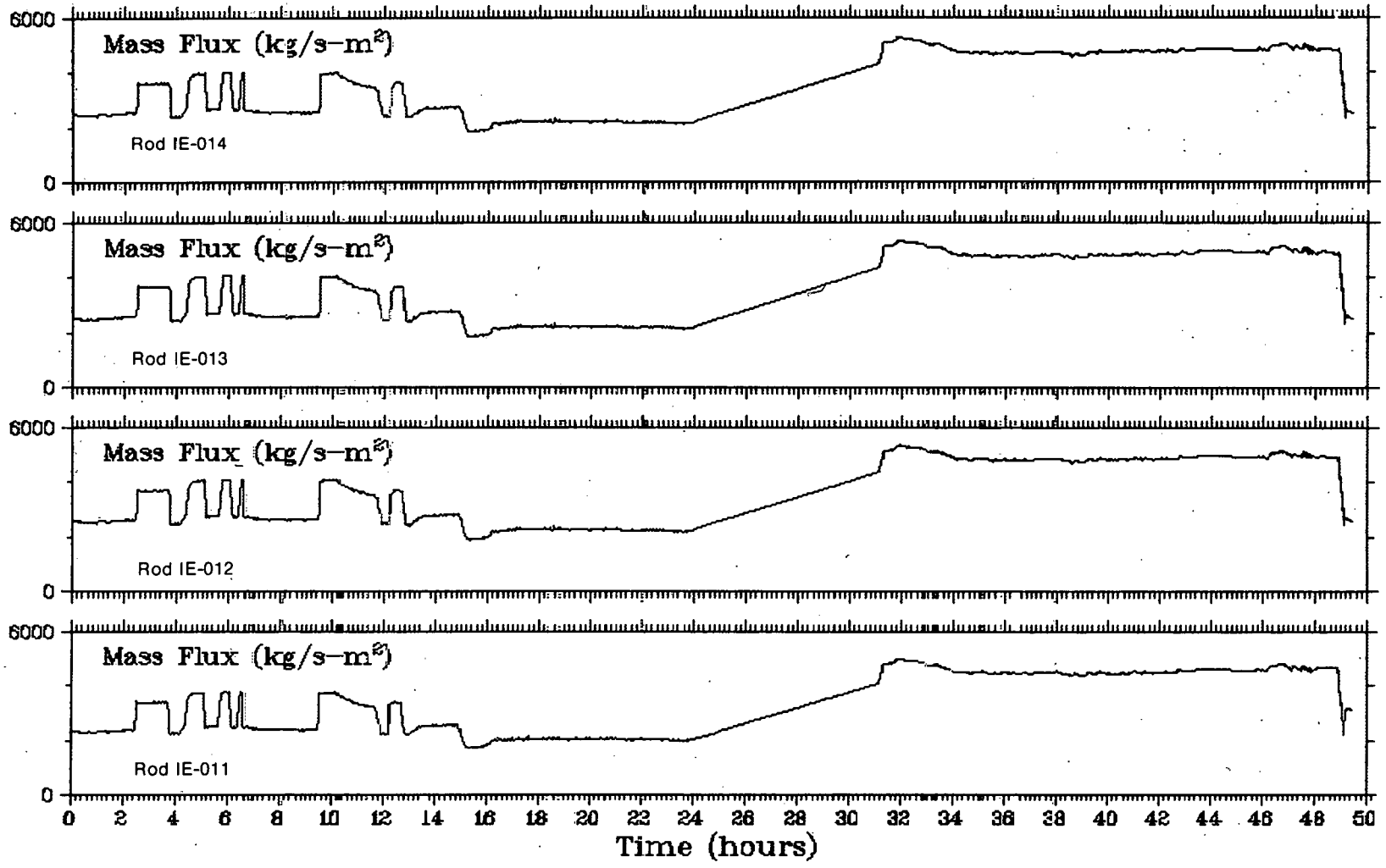

Fig. C-10 Mass flux for Test IE-2.

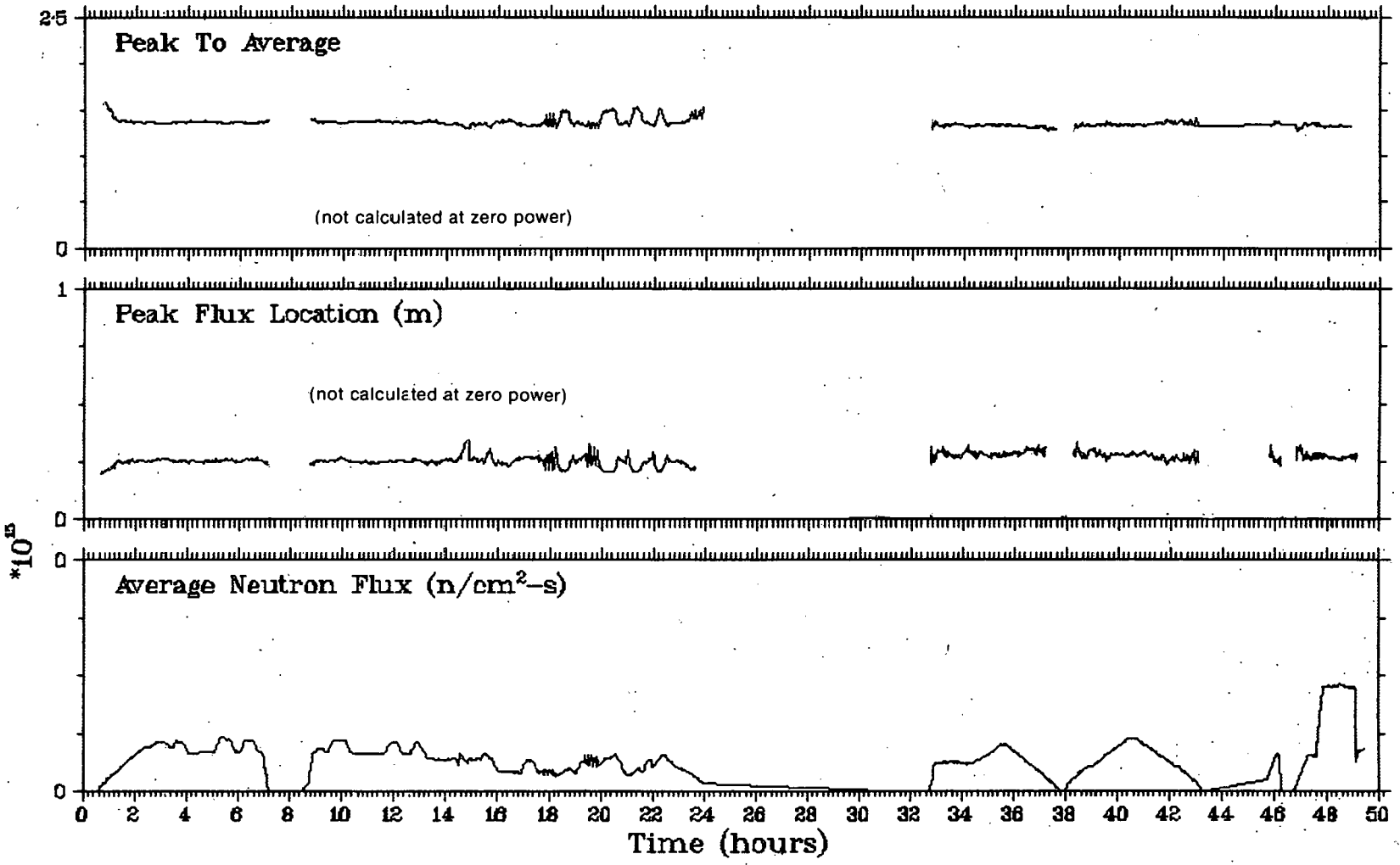

Fig. C-11 Peak to average, peak flux location and average neutron flux for Test IE-2.

reason, these transducers are more subject to small electronic zero drifts than are the other transducers which use low to moderate gains. This zero shift was corrected by adding an offset to the data so that the temperature rise and SPND current was zero at zero reactor power. The constants that were applied are shown in Table C-III.

TABLE C-III

ZERO POWER OFFSET CORRECTIONS APPLIED TO DIFFERENTIAL THERMOCOUPLE AND SPND CHANNELS IN TEST IE-2

Instrument	Rod	Correction[a]
DTC-7	IE-011	-0.3123 K
DTC-8	IE-012	0.4065 K
DTC-10	IE-013	0.3648 K
DTC-9	IE-014	-0.1042 K
SPND 2	--	0.0150 nanoamps
SPND 3	--	0.0231 nanoamps
SPND 4	--	0.0085 nanoamps
SPND 5	--	0.0156 nanoamps
SPND 6	--	0.0622 nanoamps
SPND 7	--	0.0241 nanoamps
SPND 8	--	0.0150 nanoamps

[a] This correction was added to the data so that the average instrument signal at zero power was zero.

The SPND data were then converted from detector nanoamps to neutron flux. The conversion factors were determined from the results of a special in-pile SPND calibration test using the PBF reactor[C-3]. In this test the SPNDs and a cobalt wire were mounted in the IE-2 hardware minus the fuel rods and shrouds. The reactor was operated in a square

wave fashion with rapid increases to and decreases from a constant power. The reactor power was held constant at 13 MW (50% of the maximum reactor power in Test IE-2) for one hour. The fluence was then determined from a gamma scan of the cobalt wire. Neutron flux was calculated by dividing the fluence by the time at power. A conversion between individual SPND output and neutron flux was found by dividing the neutron flux at each SPND elevation by a corresponding SPND current. The conversion factors are tabulated in Table C-IV.

TABLE C-IV

TEST IE-2 CONVERSION FACTORS RELATING SPND CURRENT AND NEUTRON FLUX

Instrument	Conversion Factor[a] (10^{20} $n/cm^2 \cdot s$ per ampere)
SPND 2	3.1726
SPND 3	3.2457
SPND 4	3.3117
SPND 5	3.3055
SPND 6	3.2033
SPND 7	3.2924
SPND 8	3.1435

[a] The SPND data were multipled by this constant to produce neutron flux.

The ultrasonic thermometer data was also further reduced. These data were extremely noisy with an excessive number of wild points. To eliminate these points, a numerical low pass filter (six-pole tangent Butterworth with half power point at the Nyquist frequency) was applied to these data using the MAC/RAN processor[C-2]. The ultrasonic thermometer on Rod IE-014 also showed a possible zero shift. The cause for the shift could not be determined. The shift was erratic and could have involved a change in the sensitivity of the device. Therefore, attempts

to remove the shift were unsatisfactory[a]. The data presented in this report have not been corrected for this problem.

Rod internal pressure data were also corrected for zero shifts due to decalibration of the pressure transducers. The correction was determined using the results of a multiple regression analysis of the data. The model chosen for the regression was determined as follows.

The pressure of the fill gas should be described fairly well using the ideal gas equation.

$$P = \rho RT \qquad \text{(C-1)}$$

where

P = gas pressure
ρ = gas density
R = gas constant
T = Temperature (absolute scale).

The measured pressure (P_m) was assumed to be

$$P_m = P + bt + b_1 t^2 + C \text{ (MPa)} \qquad \text{(C-2a)}$$

or

$$P_m = \rho RT + bt + b_1 t^2 + C \qquad \text{(C-2b)}$$

where

b and b_1 = quadratic time drift coefficients
t = time from start of test (seconds)
C = zero shift from the time of pressurization of the the rod to the start of the test.

---

[a] A multiple regression analysis to determine a trend gave results that were meaningless. It is felt that the worsening of the one-sided noise in the signal (Figure C-3) as the test progressed biased the results.

Since the average temperature of the gas cannot be measured, it is approximated as quadratic function of average fuel rod power as

$$T = T_{in} + d\Phi + d_1\Phi^2 \qquad \text{(C-3)}$$

where

Φ = average fuel rod power (kW/m)
d and d_1 = quadratic power coefficients
T_{in} = inlet temperature (K).

When Equation (C-3) is substituted into Equation (C-2b) and a general set of coefficients applied, measured pressure is

$$P_m = a_o + a_1\Phi + a_2\Phi^2 + a_3T_{in} + a_4t + a_5t^2 \qquad \text{(C-4)}$$

where

$a_o = C$
$a_1 = \rho Rd$
$a_2 = \rho Rd_1$
$a_3 = \rho R$
$a_4 = b$
$a_5 = b_1$

The first coefficient, a_o, was determined by using the cold (300 K) fill pressure adjusted to hot (606 K) conditions at the start of the test,

$$a_o = P_m - P = P_m - P_{cold} \cdot \frac{606}{300} \qquad \text{(C-5)}$$

A multiple regression analysis was then used to determine the remainder of the coefficients. The analysis was made using data from the first power ramp and the last two cycles of the preconditioning phase. This was done to avoid highly transient data such as the gap conductance segment and the power ramp. The results of this analysis are given in Table C-V.

TABLE C-V

TEST IE-2 MULTIPLE REGRESSION ANALYSIS RESULTS FOR FUEL ROD INTERNAL PRESSURE

	Regression Equation Coefficients[a]					
Rod	a_o	a_1	a_2	a_3	a_4	a_5
IE-011	-3.29	0.324×10^{-1}	-0.244×10^{-3}	0.838×10^{-2}	-0.833×10^{-5}	0.276×10^{-10}
IE-012	-0.23	0.127	-0.143×10^{-2}	0.847×10^{-2}	-0.161×10^{-4}	0.553×10^{-10}
IE-013	-0.97	0.510×10^{-1}	-0.384×10^{-3}	0.915×10^{-2}	0.372×10^{-5}	-0.251×10^{-10}
IE-014	-0.22	0.141	-0.166×10^{-2}	0.904×10^{-2}	0.894×10^{-5}	-0.279×10^{-11}

[a] The regression analysis model was $P_m = a_1 \Phi + a_2 \Phi^2 + a_3 T_{in} + a_4 t + a_5 t^2$ where a_c was determined using cold fill pressure.

The corrected pressure (P) was then calculated for the entire test using

$$P = P_m - a_o - a_4 t - a_5 t^2. \qquad \text{(C-6)}$$

The corrected pressure is presented in the text.

Cladding elongation was also corrected to account for slight differences in mounting the LVDTs in the test hardware. When these devices are calibrated, displacement is defined as zero when the core is centered in the device. When the LVDTs are mounted in the hardware the core is not necessarily centered. Therefore, to define cladding elongation in terms of the actual length of the cladding, the elongation must be set to zero at this point. This could have been handled in the equation to convert data system volts to engineering units by a suitable transformation. However, it was more convenient to apply the zero correction as a separate step. The elongation zero shifts applied to the data are given in Table C-VI.

TABLE C-VI

CORRECTIONS APPLIED TO CLADDING ELONGATION DATA IN TEST IE-2

Rod	Correction[a] (mm)
IE-011	0.00
IE-012	-1.53
IE-014	1.02

[a] This correction was added to the data so that the elongation would be zero at cold (300 K) conditions.

Coordinate Transformation

Coordinate transformations were used in some of the plots for cladding elongation and rod internal pressure. These were not really

data corrections because no changes were made to the data. They were made, particularly in the case of comparisons with FRAP-T3[C-5] results, to minimize the effects of small uncertainties in transducer output or to eliminate the effect of heating the fuel rods up to test conditions prior to the test.

For the pressure transducer, the transformations were made to minimize the uncertainties in correcting for transducer zero shift prior to the test [a_o in equation (C-4)] and to minimize the slight differences in fill gas pressure between the rods. The first transformation was applied as follows. At operating temperatures, prior to an increase in fuel rod power (at time = 0) the corrected pressure is

$$P_o = \rho_o R T_o + a_o^* - a_o \qquad \text{(C-7)}$$

where

a_o^* = actual difference between measured and hot pressure
T_o = rod temperature at the start of the test (605 K)
P_o = corrected pressure at start of the test
$a_o^* - a_o$ = should be zero if the hot pressure is determined exactly in Equation C-5.

If pressure data is presented in terms of pressure differences, i.e.

$$P - P_o = \rho R T - \rho_o R T_o \qquad \text{(C-8)}$$

the offset prior to the test ($a_o^* - a_o$) is eliminated. Therefore, the difference in corrected pressure is equal to the difference in actual pressure. Of course, if there were no uncertainties involved in calculating in Equation (C-5), this would be unnecessary since P_m [Equation (C-6)] would equal the actual pressure. However with this transformation all the pressure differences are equal,

$$P_m - P_o(\text{measured}) = P\ (\text{actual}) - P_o(\text{actual}) = P - P_o \qquad \text{(C-9)}$$

The second transformation minimizes the effects of slight differences in the initial fill gas pressure of the rods. If Equation (C-8) is divided by P_o, the following is obtained when $a_o^* - a_o$ is zero

$$\frac{P - P_o}{P_o} = \frac{P\,T}{P_o T_o} - 1 \qquad \text{(C-10a)}$$

If written in terms of void volume (V_o) and change in void volume (ΔV_o) it is

$$\frac{P - P_o}{P_o} = \frac{V_o}{V_o + \Delta V_o} \frac{T}{T_o} - 1 \qquad \text{(C-10b)}$$

Therefore, if the void volume or initial fill gas pressure is slightly different for each rod (P_o and V_o for each rod) that difference is minimized. Using the coordinate transformation of Equation (C-10b), only the changes in gas temperature and void volume are important. The P_o's for each rod are given in Table III in Section 4.1.

A transformation was also applied to the cladding elongation data. Cladding thermal strain, referenced to the cold rod temperatures, can be written

$$\varepsilon = \alpha\,(T - T_{in}) + \alpha_o\,(T_{in} - T_{cold}) \qquad \text{(C-11)}$$

where

- ε = strain = cladding elongation divided by initial cladding length
- α = expansion coefficient of the cladding during the test (During PCI it will be a combination of both the fuel expansion and cladding expansion coefficients)
- α_o = expansion coefficient of the cladding during heat up and changes in inlet temperature.
- T = temperature of the cladding
- T_{in} = inlet temperature
- T_{cold} = cold temperature (300 K)

Defining an initial strain at the start of the test,

$$\varepsilon_o = \alpha_o (T_o - T_{cold}) \qquad \text{(C-12)}$$

the difference is

$$\varepsilon - \varepsilon_o = \alpha (T - T_{in}) + \alpha_o (T_{in} - T_o) \qquad \text{(C-13)}$$

In this form, effects of growth during heatup have been eliminated and the effects of changes in inlet temperature $[\alpha_o (T_{in} - T_o)]$ have been isolated. For actual cladding growth, α_o is the expansion coefficient for the cladding, but for the measured growth it is not. The LVDTs are mounted in the test assembly which also grows during heatup and inlet temperature increases. The hardware is mostly zircaloy so that the measured growth is approximately zero. Thus, for the measured values of strain, α_o is approximately zero. If it is not exactly zero, expressing cladding strain in terms of Equation (C-13) minimizes the effect of hardware growth, since $(T_{in} - T_o)$ is small (<10 K), except for the gap conductance testing. Expressing strain in this manner is particularly important in the case of comparisons with FRAP-T3 since α_o is not zero in the calculations. The test assembly is not modeled in FRAP so the α_o used in the calculations is the actual expansion coefficient.

REFERENCES

C-1. W. J. Quapp et al., *Irradiation Effects Test Series Scoping Test 1 Test Results Report*, TFBP-TR-110 (January 1976).

C-2. R. K. Otnes (ed.), *Reference Manual: MAC/RAN III-Time Series Data Analysis System*, Agababian Associates (1973).

C-3. C. M. Allison, *Irradiation Effects Test Series SPND Calibration Test 3 Test Results Report*, TFBP-TR-142 (October 1976).

C-4. K. V. Moore, *ASTEM-A Collection of FORTRAN Subroutines to Evaluate the 1967 ASME Equations of State for Water/Steam and Derivatives of these Equations*, ANCR-1026 (October 1971).

C-5. J. A. Dearien et al., *FRAP-T3: A Computer Code for the Transient Analysis of Oxide Fuel Rods*, TFBP-TR-194 (August 1977).

APPENDIX D

POWER CALIBRATION RESULTS

Fuel rod power, expressed in terms of linear heat rating, is calculated using a combination of several techniques. Fuel rod average power is determined by a thermal balance. Fuel rod local powers, based on axial peaking factors, are determined from the neutron fluence measured by cobalt flux wires mounted parallel to the rods and/or a sine function fit to the output of axially distributed SPNDs. Individual fuel rod peak power (average power times a constant peaking factor of 1.307), as presented in the body of this report, was found using the decimated data for flow rate, inlet temperature, etc. (Appendix C). For the flow reduction phase of the test, where saturated conditions existed at the shrouds' outlets, power was determined by using a linear regression between SPND 4 and individual rod powers (Table D-I).

Fuel Rod Average Power

The thermal balance calculations are dependent upon thermal equilibrium conditions between the fuel rod and the coolant, i.e., the energy generated in the rods is equal to the energy transferred to the coolant. For all phases of the test, except during the flow reduction phase, equilbrium exists. Rod power can then be found, by calculating the change in energy of the coolant between the outlet and inlet of an individual flow shroud. This calculation is made with a computer code which uses experimentally measured coolant flow rate, temperature rise, inlet temperature, and pressure. The code incorporates the equations presented in Reference D-1 with water properties determined from the ASTEM subroutines[D-2].

A thermal balance was calculated for each of the four rods since they were contained in individual flow shrouds. Each rod had a differential thermocouple pair to measure the temperature rise of the coolant within its shroud and a flowmeter to measure the flow rates.

TABLE D-I

LINEAR REGRESSION EQUATIONS RELATING

NEUTRON FLUX MEASURED BY SPND 4 AND FUEL ROD AVERAGE POWER

Rod Number	Test[a] Phase	Regression[b] Equation	95% Confidence Intervals (kW/m)
IE-011	Preconditioning Period	$y = 9.836 \cdot x + 0.04$	$\pm$ 0.86
	Power Ramp, Steady-State Operation and Flow Reduction	$y = 9.370 \cdot x + 0.29$	$\pm$ 0.38
IE-012	Preconditioning Period	$y = 9.794 \cdot x + 0.06$	$\pm$ 0.80
	Power Ramp, Steady-State Operation and Flow Reduction	$y = 9.451 \cdot x + 0.08$	$\pm$ 0.38
IE-013	Preconditioning Period	$y = 9.678 \cdot x + 0.02$	$\pm$ 0.78
	Power Ramp, Steady-State Operation and Flow Reduction	$y = 9.239 \cdot x + 0.18$	$\pm$ 0.71
IE-014	Preconditioning Period	$y = 10.368 \cdot x + 0.17$	$\pm$ 1.27
	Power Ramp, Steady-State Operation and Flow Reduction	$y = 9.798 \cdot x + 0.61$	$\pm$ 0.36
Average of all four	Preconditioning Period	$y = 9.505 \cdot x - 0.09$	$\pm$ 0.71
	Power Ramp, Steady-State Operation and Flow Reduction	$y = 8.997 \cdot x + 0.28$	$\pm$ 0.59

[a] The gap conductance data was not included in the "Preconditioning Phase" regression.

[b] y = Average rod power (kW/m)

x = Neutron flux ($n/cm^2 \cdot s$), measured by SPND 4 divided by 10^{14}.

Both coolant inlet temperature and pressure were also measured. All of these instruments were available throughout the test except for the system pressure transducers. No usable pressure data were recorded. For these calculations, a constant pressure of 14.8 MPa was assumed based upon PBF plant instrumentation data.

Since individual fuel rod power was available throughout the test, a comparison of the power in each rod was made. This was done to check for any unexpected variations in power due to instrument drift or asymmetry in the neutron flux due to control rod changes. No asymmetry or drift were found. The slight variations in power between rods due to rod design or assembly remained consistent during the test.

The ratios of individual fuel rod power to fuel rod average power, shown in Table D-II, remained constant within the listed uncertainties.

TABLE D-II

TEST IE-2 RATIOS OF INDIVIDUAL FUEL ROD POWER TO FUEL ROD AVERAGE POWER

Power Ratios	Mean	95% Confidence Interval
Rod IE-011/Average	0.997	±0.015
Rod IE-012/Average	0.981	±0.019
Rod IE-013/Average	1.060	±0.027
Rod IE-014/Average	0.958	±0.019

The uncertainties in rod power for Rod IE-011 through IE-014 were calculated using both instrument calibration errors and data acquisition errors. These results are shown in Table D-III.

TABLE D-III

TEST IE-2 UNCERTAINTIES IN FUEL ROD POWER[a]

Average Rod Power (kW/m)	95% Confidence Level (kW/m)
0.0	± 1.58
29.2	± 1.65
60.7	± 1.79

[a] At system conditions of: pressure, 14.8 MPa; inlet temperature, 600 K; and flow rate, 1000 cm^3/s. The tabulated results for rod power and total error are for the average coolant differential temperature and total error presented in Appendix A. The variation of the error between the rods was insignificant.

Local Power

A local power profile (power as a function of the elevation above the bottom of the rod) was obtained using the data from SPNDs and cobalt flux wires. The SPND results were used to determine the instantaneous peaking factors. These factors were then multiplied by average rod power to obtain an instantaneous local power. The instantaneous peaking factors were calculated by fitting a sine function to the output from SPND 3 - SPND 5[a] (elevations from the bottom of the rod; 0.48 m, 0.63 m, and 0.79 m, respectively) and dividing by the integral average of the fit over the length of the fuel (see Reference D-1 for a discussion of the technique). The sine fit is forced to zero at 0.1 m above and below the fuel column. This gives the best agreement between the fit and flux wire data taken from this and previous tests with these types of rods[D-2,D-3]. However, since the bottom SPND's were unusable some caution must be applied when using instantaneous local power for the bottom half of the rod because of the uncertainties of extrapolating

[a] SPND 1 (0.16-m elevation) was failed prior to the beginning of the test and SPND 2 (0.31-m elevation) was unreliable.

a fit over a region where no data points exist. These effects are expected to be negligible based upon comparison with the flux wire data and results from previous tests[D-1, D-2].

Even through the instantaneous peaking factors could have small systematic errors due to the extrapolation of the fit, any shift or skewing in the peaking factors and local powers due to control rod changes can be determined. When these results were analysed, it was found that any appreciable skewing in local power due to changes in control position was limited to a rod power less than 10 kW/m. Above that level, any changes in local power were minor. In going from a rod power of less than 30 kW/m up to 68 kW/m, the peak to average changed from 1.31 to 1.29, a change of less than 2%. Even this small change is limited to the lower half of the rod; so the normalized local power on the upper half of the rod remained fixed.

During Test IE-1, voiding in the flow shrouds during the flow reduction caused a skewing of the local power profile[D-3]. In this test no such effects were apparent. Peak to average, average flux, and peak elevation showed no changes during film boiling.

Local power versus axial elevation determined from both the SPND's and an average of the flux wires are shown in Figure D-1 and tabulated in Table D-III. There is fairly close agreement between the results, particularly for the upper half of the rods. There is an obvious difference in the locations of the peak, although the peak to averages agree. This is due to two points.

The first concerns the SPNDs. The uncertainties in the "SPND local power, as shown in the Table D-IV and Figure D-1, are due to control rod changes, differences in SPND's sensitivities, and the effective length[a] that was chosen. Control rod changes will cause a

---

[a] The sine fit uses a functional form $f(x) = \sum_{n=1}^{3} b_n \sin \frac{n\pi x}{L}$. L is the effective length (see Reference D-1).

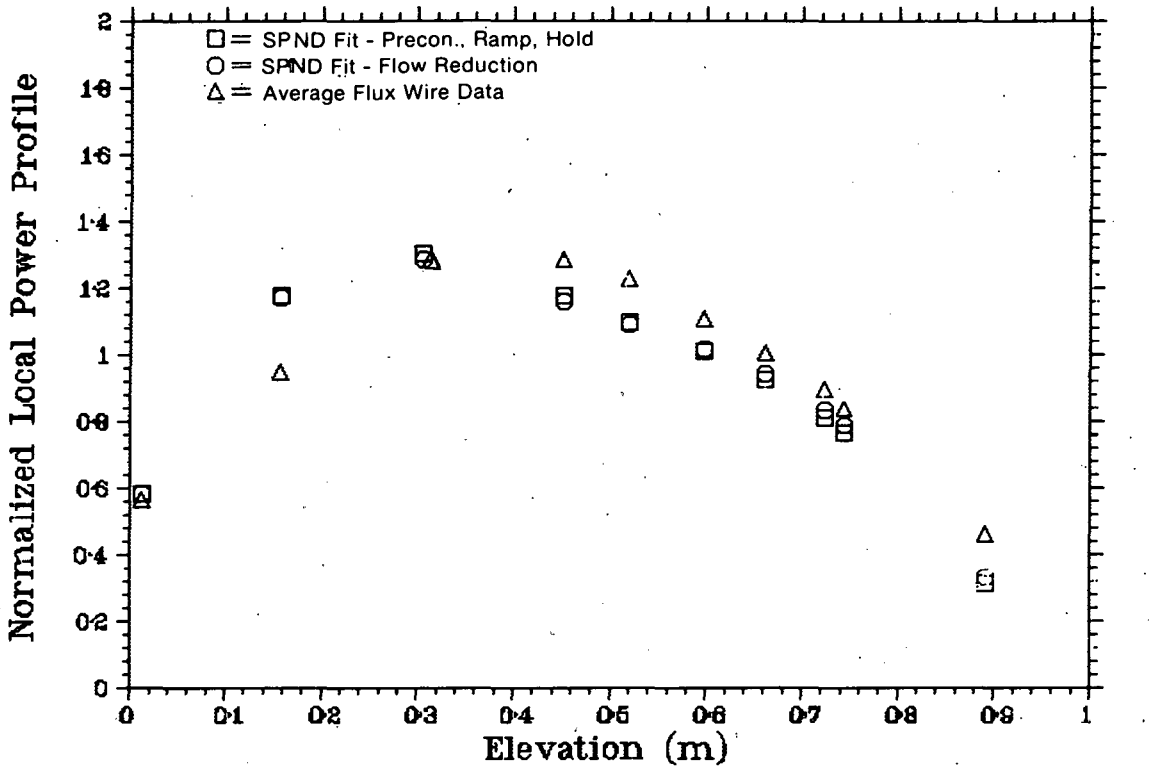

Fig. D-1 Local power profile for preconditioning period, power ramp and steady-state operation, flow reduction (based on SPND signals), and entire test (based on average flux wire data).

TABLE D-IV

TEST IE-2 LOCAL POWER PROFILE WITH UNCERTAINTIES

	Instantaneous Local Power From SPNDs				Integrated Profile	
	Preconditioning,[a] Power Ramp and Steady-State Operation At High Power[e]		Flow Reduction[b]		From an Average of Flux Wires[c]	
Elevation	Normalized Local Power	95% Confidence Intervals	Normalized Local Power	95% Confidence Intervals	Normalized Local Power	Estimate of Standard Deviation[d]
0.013	0.583	±0.055	0.584	±0.049	0.567	0.056
0.159	1.175	±0.062	1.169	±0.049	0.948	0.041
0.306	1.305	±0.016	1.288	±0.023	1.240	0.003
0.452	1.178	±0.027	1.163	±0.02	1.289	0.013
0.521	1.100	±0.033	1.094	±0.029	1.230	0.031
0.599	1.010	±0.043	0.017	±0.033	1.1075	0.001
0.662	0.925	±0.042	0.9406	±0.033	1.006	0.007
0.724	0.813	±0.033	0.836	±0.024	0.900	0.016
0.745	0.768	±0.032	0.791	±0.024	0.838	0.0204
0.892	0.317	±0.026	0.331	±0.024	0.465	

[a] Excluding Gap Conductance segment

[b] Average Peak Elevation: 0.251 ± 0.008
Average Peak to Average: 1.288 ± 0.022

[c] Average of the two wires
Average Peak Elevation: 0.3953 ± 0.038 (estimate of standard deviation)
Average Peak to Average: 1.307 ± 0.235 (estimate of standard deviation)

[d] The estimate of the standard deviation is given only for reference and is due to an unknown shift in the axial locations of the wires

[e] Average Peak Elevation: 0.294 ± 0.011
Average Peak to Average: 1.307 ± 0.016

spread in the peaking factors, and the differences in the SPND sensitivities and the choice of an effective length will cause consistent systematic errors in the peaking factors. Therefore, the uncertainties shown in Table D-IV take into account both errors.

The second point concerns the flux wires. It was discovered that the results from the two wires had nearly identical shapes, but were shifted by approximately 0.05 m. Therefore, their exact reference elevations are unknown. Based on previous flux data from tests of this type[D-2, D-3], exact elevations should be within 0.05 m from the elevations given. Table D-IV shows the integrated flux profile calculated from the average of the two wire's results. The 95% confidence interval is not given because only two sample points are available at each elevation. The presentation of the confidence intervals would be misleading because of the low number of points. The profile from this average, even with the uncertainty in axial location, is believed to be the best indication of the actual local power profile in the fuel rods. For this reason this average flux was used for the FRAP-T3[D-4] calculations discussed in Section 5.1.1.

REFERENCES

D-1. W. J. Quapp et al., *Irradiation Effects Test Series Scoping Test 1 Test Results Report*, TFBP-TR-110 (January 1976).

D-2. K. V. Moore, ASTEM - *A Collection of FORTRAN Subroutines to Evaluate the 1967 ASME Equations of State for Water/Steam and Derivatives of these Equations*, ANCR-1026 (October 1971).

D-3. W. J. Quapp et al., *Irradiation Effects Test Series Test IE-1 Test Results Report*, TREE-NUREG-1046 (March 1977).

D-4. J. A. Dearien et al., *FRAP-T3: A Computer Code for the Transient Analysis of Oxide Fuel Rods*, TFBP-TR-194 (August 1977).

DISTRIBUTION RECORD FOR TREE-NUREG 1074

Internal Distribution

1 - Chicago Patent Group
9800 South Cass Avenue
Argonne, Illinois 60439

2 - CA Benson
Idaho Operations Office-ERDA
Idaho Falls, ID 83401

3 - RJ Beers, ID

4 - PE Litteneker, ID

5 - RE Tiller, ID

6 - RE Wood, ID

7 - HP Pearson, Supervisor
Technical Information

8-17 - INEL Technical Library

18-37 - Authors

38-151 - Special Internal

External Distribution

152-153 - Saul Levine, Director
Office of Nuclear Regulatory Research, NRC
Washington, DC 20555

154-473 - Distribution under NRC-3, Water Reactor Safety Research
Fuel Behavior

bcc: Special Tree
Distribution - 80
TFBP Standard
C. M. Allison
D. W. Croucher DWC
A. S. Mehner
S. A. Ploger
W. J. Quapp file
Central File
R. A. DaBell

December 19, 1977

Mr. R. E. Tiller, Director
Reactor Operations & Programs Division
Idaho Operations Office - DOE
Idaho Falls, ID 83401

ERRATA TO TREE-NUREG-1074, "IRRADIATION EFFECTS TEST SERIES, TEST IE-2 TEST RESULTS REPORT" - Zan-390-77

Dear Mr. Tiller:

Errata to TREE-NUREG-1074, Irradiation Effects Test Series, Test IE-2 Test Results Report, August 1977, C. M. Allison, D. W. Croucher, S. A. Ploger, A. S. Mehner.

On page 95, the first reference has an incorrectly typed number. Change to "75/058".

I will be happy to discuss any questions or comments you may have regarding the above change.

Very truly yours,

Original

J. O. Zane, Manager
Thermal Fuels Behavior Program

sj

Attachment:
Errata

cc: R. W. Barber, DOE-RSRC - 2
R. B. Foulds, NRC-RSR
W. V. Johnston, NRC-RSR - 2
R. Rossi/J. E. Humphreys, NRC-OMPIC
P. O. Strom, NRC-ID
L. S. Tong, NRC-RSR
R. W. Kiehn, EG&G Idaho, w/o enc.

ERRATA

Errata to TREE-NUREG-1074 "Irradiation Effects Test Series, Test IE-2 Test Results Report, August 1977, C. M. Allison, D. W. Croucher, S. A. Ploger, A. S. Mehner.

On page 95, the first reference has an incorrectly typed number. Change to "75/058".